Novel approaches to absolute structure

Pedersen, Katja Desiree

Publication date:
2021

Document Version
Publisher's PDF, also known as Version of record

Novel approaches to absolute structure

PhD thesis

Katja Desiree Pedersen

Department of Chemistry

Technical University of Denmark

November 2021

Preface

The work presented in this thesis is the result of my three years of research as a PhD student at the Department of Chemistry, Technical University of Denmark. The project was supervised by Associate Professor Charlotte Held Gotfredsen.

This project was designed as an interdisciplinary collaboration between the fields of NMR spectroscopy and nanochemistry, with Professor Jindong Zhang as co-supervisor. Her passing halfway through the project forced a revision of the scope of the work, and the loss of her enthusiasm and knowledge in the field was felt.

In lieu of a full external stay, which was prevented due to Covid-19 lockdown, a collaborative study was conducted together with the group of Associate Professor Thomas Tørring at Aarhus University. I am grateful for the invitation to participate in the study of a fascinating compound.

The results included in Chapter 5 contain contributions from Bsc students. Under my co-supervision they participated in the synthesis of graphene oxide and functionalized products hereof. Thanks to Christian Falck Jørgensen and Mads Marquard Nielsen for daring to be part of a project with no certain results.

I am grateful to the Department of Chemistry for the awarded Academic Excellence Scholarship that have funded my studies. NMR center • DTU and the Villum Foundation are gratefully acknowledged for access to the 600 and 800 MHz spectrometers. Access to instruments at the Danish Center for Ultrahigh-Field NMR Spectroscopy funded by the Danish Ministry of Higher Education and Science (AU-2010-612-181) is acknowledged.

I am beyond grateful to Lotte for her guidance over the last many years, which has shaped the way I think of science and seeing the perspectives in the research. I look forward to many more discussions in the future.

I want to thank the entire NMR group, both current and previous members for fruitful discussions and great company. Here an extra thank you is owed to Kasper for running ^{13}C MAS NMR spectra for me and for answering my many questions regarding analysis and simulation of spectra. Thank you to Casper Hoeck for feedback on my discussion of triculamin and valuable input throughout my studies.

I would like to thank Morten Meldal for taking the time to discuss click chemistry in relation to GO functionalization with me. His great advice will have an impact on future experiments.

I am indebted to Jing Tang for helping me obtain AFM images and letting me shadow her in the laboratory during synthesis of graphene oxide.

Thank you to Tim Booth and Kristian S. Mølhave for rewarding discussions on GO analysis, which has been a confirmation of the benefits of cooperation across fields. A thank you is also extended to Jens Ulstrup and Christian Engelbrekt for valuable discussions.

Thank you to colleagues at DTU Chemistry for all the little things every day that make this a great place to work. I am grateful for all my office- and lunch mates over the years for good discussions about chemistry, but especially for talks about everything else. Thanks to Charlotte for support and great friendship.

I am thankful for all the friends I have made during my entire time at DTU. I have had a wonderful time here and a lot of that is owed to you.

Thanks to my family and friends (some have been around for so long that they feel like family) for their unwavering support. I am aware of my tendency to disappear into my DTU bubble and I am so grateful for you insisting that I sometimes have to join the rest of the world too.

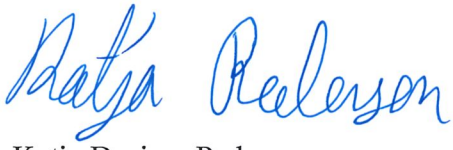

Katja Desiree Pedersen,

November 2021

Abstract

The function, activity and specificity of natural- and other organic compounds are decided by their 3D structure in solution, and accurate characterization methods are of great value in e.g. drug discovery. Nuclear magnetic resonance (NMR) spectroscopy is a powerful analytical technique in structure elucidation of organic compounds and have been used to identify countless compounds as well as their interactions. This thesis covers work related to expanding the applicability of NMR structural analysis towards compounds, whose 3D structure still represent a challenge for the structure elucidation process.

As an example of the structure elucidation process based on conventional NMR analysis, the 3D structure of the lasso peptide triculamin was elucidated using internuclear distances derived from NOE data. The analysis resulted in a structural ensemble, which displays both the conformational stability of the macrolactam ring and the flexibility of the tail region.

Graphene oxide (GO) has risen as a novel material with numerous attractive properties and potential applications. GO spontaneously forms liquid crystals in aqueous solution, which induces a degree of order for dissolved compounds, when placed in a magnetic field. This makes GO applicable as alignment media for acquisition of NMR spectra under anisotropic conditions. Additional structural information can be extracted from these spectra and used in structure elucidation of organic compounds. The alignment properties of GO were explored by measuring residual dipolar couplings (RDCs) of model compounds, resulting in many observations for sample preparation and stability of GO solutions, among these discussions related to the effects of GO concentration and solvent composition for the degree of alignment.

Multiple methods of GO functionalization was pursued to expand its applicability toward a broader range of compounds and enable enantiodiscrimination. Synthesis strategies based on amide coupling and increasing the amount of carboxylic acids on the GO sheets were carried out, producing modified GO materials that preserved the alignment properties. The synthesized materials were analyzed using AFM, IR and ^{13}C MAS NMR spectroscopy. However, the analysis could not unambiguously prove the covalent functionalization, when compared to a control sample. The results highlight the need for a critical approach when characterizing functionalized GO materials.

An alternative approach based on click (CuAAC) chemistry was pursued. Azide groups were successfully introduced on the GO sheets, and subsequent reactions strived to further functionalize GO by coupling with a small alkyne. The functionalized products obtained from initial testing revealed incomplete reaction by the continued presence of azides, thus future effort will focus on finding optimal reaction conditions and accurate characterization methods.

Resumé

Funktion, aktivitet og specificitet af naturstoffer er bestemt af deres 3D struktur i opløsning, og nøjagtige metoder til at karakterisere dem har stor værdi bl.a. i drug discovery. NMR (nuclear magnetic resonance) spektroskopi er et alsidigt og vigtig analytisk værktøj i strukturopklaringen af organiske stoffer og har været brugt til at identificere utallige stoffer og deres funktion. Denne afhandling omhandler arbejdet med at udvide anvendeligheden af NMR baseret struktur analyse til at inkludere stoffer, hvis 3D struktur stadig er en udfordring i strukturopklaringsprocessen.

Som et eksempel på hvordan konventionel NMR analyse bruges til struktur opklaring blev 3D strukturen af lassopeptidet triculamin kortlagt ved hjælp af internukleare afstande udregnet fra NOE data. Analysen resulterede i et ensemble af strukturer, som udviser den konformationelle stabilitet af makrolactam ringen og fleksibiliteten i peptidets hale.

Grafen oxid (GO) er trådt frem som et nyt materiale med mange attraktive egenskaber og potentielle anvendelsesmuligheder. GO former spontant flydende krystaller i vandig opløsning, hvilket inducerer en grad af orden for opløste stoffer, når det placeres i et magnetisk felt. Dette gør GO anvendelig som et såkaldt ”alignment” medie til at optage NMR spektre under anisotropiske betingelser. Fra disse spektre kan man opnå yderligere information til brug i strukturopklaringsprocessen. GO’s alignment egenskaber blev udforsket ved at måle residuale dipolære koblinger af model stoffer, hvilket resulterede i adskillige observationer relateret til prøve forberedelse og stabilitet af GO opløsninger, heriblandt var der diskussioner omhandlende effekten af GO’s koncentration og kompositionen af solvent på graden af orden i opløsningen.

Adskillige metoder til at funktionalisere GO blev afprøvet for at udvide dets anvendelighed til at inkludere en bredere klasse af stoffer og gøre det muligt at skelne imellem enantiomerer. Synteser baseret på amid koblinger og forøgelsen af carboxylsyrer på overfladen af GO blev udført og resulterede i modificerede GO materialer, som havde bibeholdt evnen til at fungere som alignment medie. De syntetiserede materialer blev analyseret ved hjælpe af AFM, IR og ^{13}C MAS NMR spektroskopi. Dog var analysen ikke i stand til at utvetydigt bevise dannelsen af kovalente bindinger til nye stoffer, når der blev sammenlignet med en kontrol prøve. Resultaterne understreger nødvendigheden af en kritisk tilgang når GO materialer skal karakteriseres.

En alternativ tilgang til funktionaliseringen af GO baseret på klik (CuAAC) kemi blev herefter afprøvet. Azid grupper blev indført på GO’s overflade og efterfølgende reaktioner efterstræbte at funktionalisere GO yderligere ved at koble det med en lille alkyn. Den fortsatte tilstedeværelse af azid i produkterne af initielle forsøg viste at klik reaktionen ikke var komplet. Derfor vil den fremtidige indsats fokusere på at finde optimale reaktionsbetingelser og nøjagtige karakteriseringsmetoder.

Publications

I **Pedersen, Katja D**; Zhang, Jingdong; Gotfredsen, Charlotte H. "Practical considerations for working with graphene oxide as alignment media for RDC measurements." *Magn Reson. Chem*. 2021; 1–8.

II F. D. Andersen; **Pedersen, Katja D**; Juhl, Dennis W; Mygind, Tobias; Chopin, Paul; Svenningsen, Esben B; Poulsen, Thomas B; Lund, Marie B; Schramm, Andreas; Gotfredsen, Charlotte H; Tørring, Thomas. "Triculamine: an unusual lassopeptide with potent anti-mycobacterial activity" (draft).

Abbreviations

1D	One dimensional
2D	Two dimensional
3D	Three dimensional
AFM	Atomic force microscopy
AcCN	Acetonitrile
B3LYP	Becke Three Parameter Hybrid Functionals
cGO	GO from a commercial source
CLIP	Clean in-phase
CSA	Chemical shift anisotropy
CuAAC	Cu(I) catalyzed azide-alkyne cycloaddition
DFT	Density Functional Theory
DIC	*N,N'*-diisopropylcarbodiimide
DIPEA	*N,N*-diisopropylethylamine
DMF	*N,N'*-dimethylformamide
DMSO	Dimethyl sulfoxide
DTU	Technical University of Denmark
E	Energy
EDC	1-ethyl-3-(3-dimethylaminopropyl) carbodiimide
EtOAc	Ethyl acetate
F1	Indirect dimension
F2	Direct dimension
FF	Force field
FID	Free induction decay
GIAO	Gauge invariant atomic orbitals
GO	Graphene oxide
GO-base	base-treated GO
GO-COOH	Carboxylated GO
GO-PEG	Pegylated GO
GO-Tyr	GO functionalized with tyrosine
GO-N_3	GO functionalized with azide
HMBC	Heteronuclear multiple bond correlation
HPLC	High-performance liquid chromatography
HRMS	High-resolution MS
HRTEM	High-resolution TEM
HSQC	Heteronuclear single quantum coherence
IR	Infrared
LC	Liquid crystal
MAS	Magic angle spinning
Me-α-Glc	methyl-α-D-glucopyranoside
MM	Molecular mechanics
MDR-TB	multidrug resistant *M. tuberculosis*
MS	Mass spectrometry
NMR	Nuclear magnetic resonance
NHS	*N*-hydroxysuccinimide
NOE	nuclear Overhauser effect
NOESY	nuclear Overhauser effect spectroscopy
NUS	Non-uniform sampling
Oxyma	Ethyl (2Z)-2-cyano-2-(hydroxyimino)acetate
PANIC	peak amplitude normalization for improved cross-relaxation
PBS	phosphate-buffered saline
ppm	parts per million
Q	Quality (factor)
RCSA	Residual chemical shift anisotropy
RDC	Residual dipolar coupling constant
RDC_{max}	Maximum experimental RDC
RF	Radio frequency
rGO	reduced graphene oxide
RQC	Residual quadrupolar coupling
RT	Room temperature
S/N	Signal-to-noise
SAG	Strain-induced Alignment in a Gel
SEM	Scanning electron microscopy
sGO	GO synthesized in-house
Si-alk	4-(tertbutyldimethylsilyloxy)-1-butyne
SP	Stretched polymer
ssNMR	solid state NMR
SVD	Singular value decomposition
TEM	Transmission electron microscopy
Tf	triflate

TGA	Thermogravimetric analysis	B_0	Magnetic field
THF	Tetrahydrofuran	D	Dipolar coupling constant
TMS	Tetramethylsilane	I	Spin quantum number
TOCSY	Total correlation spectroscopy	J	J-coupling constant
UV-Vis	Ultraviolet-visible	T	Total coupling constant
XPS	X-ray photoelectron spectroscopy		

Content

1 Introduction 1
2 NMR structure elucidation 4
2.1 Information available and limitations 4
2.2 Anisotropy 7
2.2.1 Residual dipolar coupling 9
2.2.2 Alignment media 10
2.3 Computational methods 12
2.3.1 Force field methods 13
2.3.2 Density functional theory 14
3 Graphene oxide background 15
3.1.1 History and synthesis 15
3.2 Characterization of graphene oxide 16
3.2.1 Infrared spectroscopy 17
3.2.2 Solid state ^{13}C NMR spectroscopy 18
3.2.3 Atomic force microscopy 19
3.3 Structure of graphene oxide 20
3.4 Dispersibility and liquid crystal formation 22
4 GO synthesis, behavior, and NMR properties 23
4.1 Menthol: sample preparation, modelling and alignment 23
4.2 Factors affecting GO alignment 28
4.2.1 GO source 28
4.2.2 Time dependent stability 29
4.2.3 Concentration 31
4.2.4 Solvent 33
4.2.5 Resdispersion of dried GO 34
4.3 Other properties affecting GO 35
4.3.1 Temperature 35
4.3.2 Salts and acids 36
4.3.3 Two phase systems 37
4.3.4 Ultrasonication 38
4.4 GO alignment of other test compounds 39
4.4.1 Alignment and recovery of Me-α-Glc 39
4.4.2 No enantiodiscrimination of pinanediol 40
4.5 Conclusion 41
4.6 Experimental 42
5 GO functionalization part 1: Amidation 44
5.1 GO-Tyr 45
5.1.1 Results and discussion 45
5.2 GO-PEG 47
5.2.1 Results and discussion 48
5.3 Discussion of experimental aspects and techniques 51

5.3.1 Purification 51
5.3.2 Solid state ^{13}C NMR spectroscopy 52
5.3.3 X-ray photoelectron spectroscopy 53
5.3.4 Raman spectroscopy 54
5.3.5 Design of experiments 55
5.4 Conclusion 56
5.5 Experimental 57
6 GO functionalization part II: Carboxylation 59
6.1 Results 60
6.2 Effect of base on the GO structure 63
6.3 Discussion 64
6.4 Conclusion 65
6.5 Experimental 66
7 GO functionalization part III: Click chemistry 68
7.1 GO-N_3 68
7.1.1 Synthesis 69
7.1.2 Results and discussion 70
7.2 Click chemistry on GO-N_3 72
7.2.1 Synthesis strategy 73
7.2.2 Results and discussion 74
7.3 Conclusion 76
7.4 Experimental: 77
8 Structure elucidation of Triculamin – a lasso peptide 79
8.1 Assignment 80
8.2 Introduction to NOEs 83
8.3 Finding the conformational fit 84
8.4 Conclusion 87
8.5 Experimental 88
9 Overall conclusion and outlook 89
10 References 92

1 Introduction

Natural products and their analogues remain a constant source of novel therapeutics.[1][2] They further provide ample inspiration for synthetic chemists and drug discovery researchers seeking new structural scaffolds to explore for biological activity. Nature provides a diverse range of natural products from small organic molecules to large biologics, with each type requiring different analytical methods for characterization of their structure and properties. The interaction between a drug and its therapeutic target are governed by its 3D structure, thus it is essential for the drug discovery process to have accurate methods to fully elucidate the absolute structure of compounds. For complex structures, this may require extensive studies using several analytical techniques. A major barrier towards 3D structure elucidation may arise when chirality is present in the molecule as many commonly applied analytical techniques are not capable of distinguishing between enantiomers.

X-ray crystallography can provide 3D structures at high accuracy, however it requires the generation of a crystal, which may be very challenging for some compounds. For organic compounds, the mass can be found by mass spectrometry (MS) and analysis of high-resolution MS spectra may reveal the molecular formula. However, no other technique besides nuclear magnetic resonance (NMR) spectroscopy will be as information-rich regarding the structure of the compound and NMR is routinely used to identify organic and bioorganic molecules in solution. Structural information from NMR spectroscopy can be in the form of isotropic parameters as chemical shifts, spin-spin *J*-coupling constants and nuclear Overhauser effect (NOE) derived distances. Nevertheless, for some compounds additional information is needed to fully elucidate the structure, e.g. in cases of hydrogen deficient regions and to resolve relative and absolute stereochemistry. If anisotropic conditions can be created within the sample by the use of an alignment media, the compound no longer moves freely in solution and consequently, may display an average preferred orientation relative to the magnetic field. Partial orientation of a compound can introduce additional effects in NMR spectra that are not observed under isotropic conditions. From analysis of the acquired spectra, new information may be gained, providing orthogonal knowledge in the pursuit of the fully elucidated structure. The use of anisotropic information has been used to assign relative and absolute configuration of compounds, and to revise earlier structures.[3–6]

Graphene oxide (GO) was recently described as a new, tunable alignment media that promised easy sample preparation and produced high quality spectra.[7] GO is dispersible in aqueous solution and certain polar organic solvents due to its hydrophilic nature, which makes GO easy to process and enables chemical manipulation.[8] It has already been shown that functionalizing GO widened its dispersibility and thus its utility as alignment media, promising further potential for GO based materials for NMR purposes.[9][10] GO is perhaps best known due to its structural connection to graphene as illustrated in Figure 1.1.

Graphene is a 2D material of sp^2-hybridized carbon atoms in a hexagonal lattice being only one atom thick, giving it unique electronic properties. Graphene related studies saw a boom since single layer graphene was isolated and characterized in 2004 by Geim and Novoselov, research that in 2010 was awarded the Nobel prize in physics.[11–13] Graphene has been used for e.g. biosensors, transparent conductors and coatings.[14] Ever since, GO has received special attention as a processable stepping-stone towards single layer graphene, with the benefits of GO being cheap and the production possible at large scale. Other routes to single layer graphene include micromechanical cleavage (scotch tape)[12], chemical vapor deposition[15] and liquid-phase exfoliation[16]. GO is converted to graphene by reduction, and numerous reduction agents have been reported.[17] As an intermediate on the road to graphene, GO and graphene discoveries and research are tightly linked, although GO was first described more than 160 years ago from oxidation of graphite.[18][19]

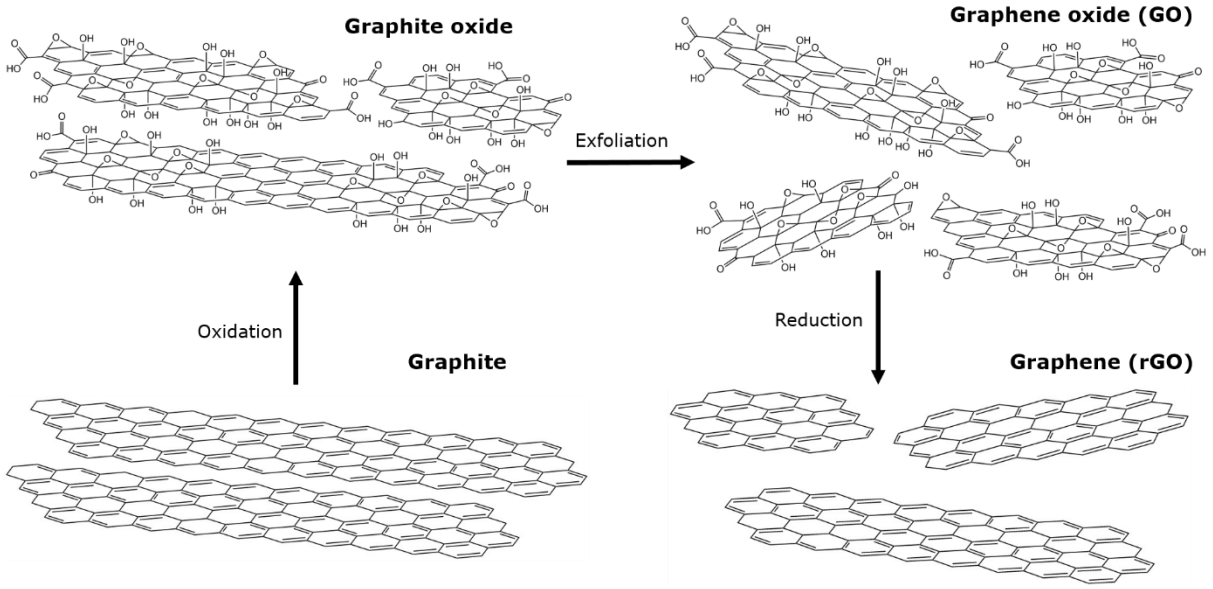

Figure 1.1. Illustration of the major synthetic steps from graphite to graphene via graphene oxide. Graphite consists of double bonded carbon in a honeycomb lattice in multiple layers, which stack due to van der Waals attractive forces. Oxidation forms graphite oxide, where the introduction of oxygen functionalities increase the interlayer spacing with subsequent exfoliation into single layer graphene oxide (GO) typically achieved by dispersion in water aided by sonication. Ideally, reduction of GO results in graphene. However, graphene obtained by reduction of GO does not fully recover the electronic properties of graphene obtained by e.g. mechanical cleavage and are therefore often referred to as reduced GO (rGO).

This project is thus a combination of two separate chemical research fields; structure analysis by NMR spectroscopy and the fascinating opportunities of graphene oxide (GO) as used in nanochemistry. The hope is that researchers working with nanochemistry, organic synthesis, or NMR spectroscopy will find interest in this multidisciplinary project and see potential for future cross-collaborations. As such, the reactions, techniques, and observations in the following span a wide array of chemistry, but the discussions are aimed at being understandable across the fields.

The aim was to explore GO as alignment media in NMR structural studies by functionalizing GO sheets, creating new materials with advantageous properties such as increased dispersibility, simple sample preparation, and no interference from background signals from the media. A potential achievement would be the functionalization of GO with chiral entities to introduce stereospecific interactions with solutes and thus enable the determination of absolute structure, which is not possible in conventional NMR analysis.

The theoretical background is divided into two chapters covering a description of NMR spectroscopic methods in structure analysis and an introduction to GO with focus on the structure, respectively. A chapter is devoted to expanding on discoveries regarding GO as alignment media, which is also described in the publication "Practical considerations for working with graphene oxide as alignment media for RDC measurements"[20], included in appendix.

Functionalization of GO utilizing different reaction strategies based on amide coupling, carboxylation, and click chemistry are described in three separate chapters, which are linked by a general discussion on characterization of functionalized GO materials.

NMR structural analysis was applied for the lasso peptide triculamin in collaboration with the group of Associate Professor Thomas Tørring. A structural ensemble expressing the 3D structure of triculamin was found by detailed analysis of nuclear Overhauser effect (NOE) NMR data. This project is an example of how conventional NMR structural analysis can be applied for peptides, where knowledge of the amino acid sequence can be supplied from other analytical methods. The scaffold of a novel natural compound might be extremely challenging to elucidate, especially for compounds with proton deficiency or unknown stereochemistry. Thus the need for supplementary methods to obtain additional structural information.

2 NMR structure elucidation

Across scientific fields such as chemistry, biotechnology, and material science, nuclear magnetic resonance (NMR) spectroscopy is utilized routinely due to the wealth of information it provides. The history of this technology spans decades with the introduction of Fourier transformation, superconducting magnets and cryoprobes as key milestones. An ongoing effort to develop high field magnets and instrumentation has greatly broadened the utility of NMR spectroscopy and established it as its own field of research. Today, ultra-high field spectrometers up to 1.2 GHz are available, while low field benchtop NMR instruments has grown in popularity as a lower cost alternative.[21]

This chapter presents the types of information gained from conventional NMR spectra and how it may be used in structure elucidation, before introducing how anisotropic interactions can be a source of additional structural information. The discussion mainly relates to small-to-medium sized organic compounds in solution. Most details are also true in other cases, though some aspects may change in relevance. For a brief introduction to the theoretical background of NMR and relevant experimental parameters, see appendix.

The chapter ends with an introduction to computational methods of generating and optimizing 3D structures for modelling of structural ensembles to evaluate against experimental data.

2.1 Information available and limitations

From NMR spectra, a variety of information can be gained.[22][23] The following discussion is centered on ^{1}H NMR spectroscopy, as it is most commonly employed, but ^{13}C, ^{15}N, ^{19}F, and ^{31}P NMR spectroscopy are also used in analysis of organic compounds.

The resonances are distributed in the NMR spectrum according to their chemical environment, expressed by the chemical shift δ. Numerous, detailed empirical rules about how different functional entities influence the chemical shift, goes back to the start of NMR spectroscopy.[24] Today, computational methods can calculate the expected chemical shift of a given nuclei with great precision as an orthogonal method of comparison.

The area under the curve of each resonance is related to the amount of chemically equivalent protons giving rise to the peak. Thus, the relative number of nuclei can be surmised from their integral. The integrals in Figure 2.1 correspond to two methylene groups, two CH, and two methyl group, the latter being chemically equivalent resulting in a combined integral of 6 protons.

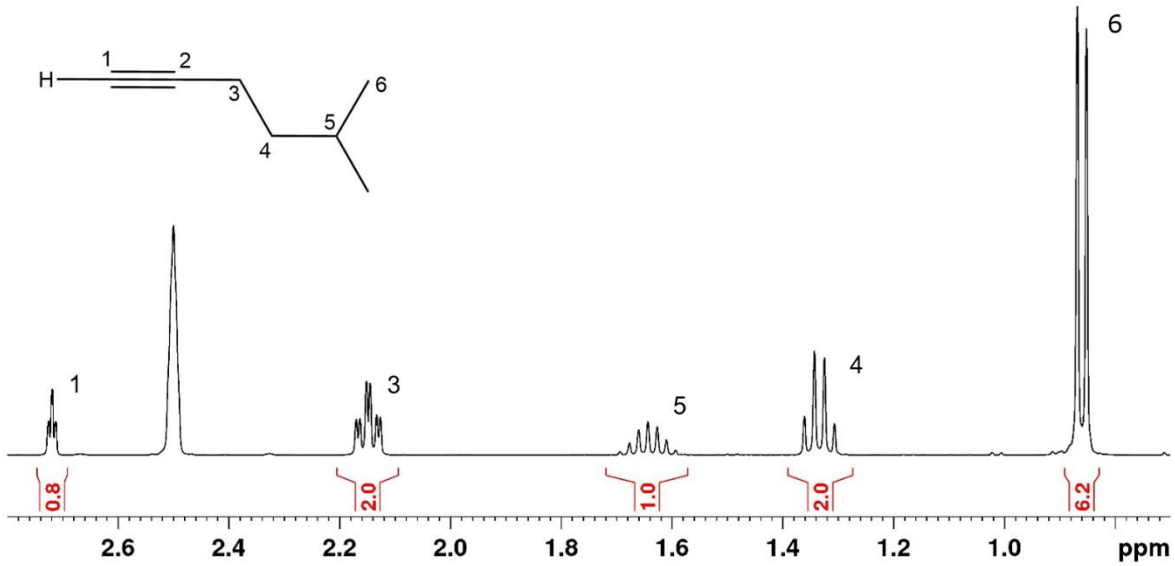

Figure 2.1. 1D ^{1}H NMR spectrum of 5-methyl-1-hexyne in DMSO-*d*6 at 400 MHz.

Bonded nuclei in close proximity influence each other in various ways beyond just chemical shielding effects. A given nucleus is affected by the spin of the nuclei in its surroundings, thus experiencing a slightly different chemical environment depending on whether the neighboring nuclei possess α- or β-spin. There is an equal chance for each spin and therefore the resonance signal of the nucleus will split into two peaks due to the α- and β-spin of the neighboring nuclei. The measured distance between the split peaks is called the scalar spin-spin *J*-coupling constant and is normally given in Hz. For each additional neighboring NMR active nuclei, the signal will split into additional peaks. The size of the *J*-coupling constant between nuclei depends on the type of nuclei, structural properties, and their relative bond angle as illustrated in Figure 2.2. The resonance of a nucleus, which couples to several neighboring nuclei with different *J*-coupling constants, may show a complex pattern of multiple peaks, making quick interpretation difficult. However, a thorough analysis can be valuable as it may add substantial structural information.

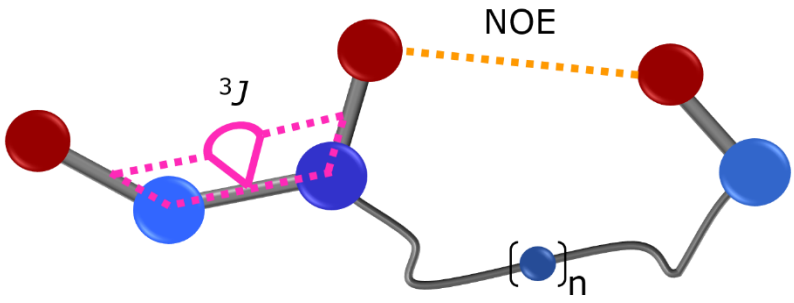

Figure 2.2. The ^{3}J-coupling constant acts through bonds and depends on the dihedral angle (shown in pink). NOE correlations act through space with the strength depending on the internuclear distance (orange), here illustrated to act intramolecularly. However, intermolecular NOE correlations can also be observed.

In contrast to the *J*-coupling that acts through bonds, the nuclear Overhauser effect (NOE) interacts through space as indicated in Figure 2.2. NOE correlations may be seen at internuclear distances up to app. 5 Å. Analysis of NOE data is an important tool in the elucidation of 3D structures as correlations between nuclei placed within different structural regions, are clues on the conformational folding in solution. An example of how NOE analysis can be utilized in the structure elucidation process is presented in Chapter 8.

In addition to the effects mentioned above, experimental factors also influence the obtained spectra. Changing solvent, temperature and pH may cause changes in the spectra as the chemical environment within the sample is altered. As most solvents add resonances to the spectra, overlap may obscure signals of interest. Varying the temperature may alter the relative ratio of structural conformers for flexible compounds. Particularly for loosely bound protons, pH can have major effects as the exchange rate with the solvent may change drastically.

Especially for ^{1}H NMR spectra, overlap of resonances occur often, as the window of their corresponding frequencies is relatively narrow. Some overlap may be resolved at higher field spectrometers as spectral resolution directly depends on magnetic field strength. Two-dimensional (2D) NMR spectra may resolve overlap of resonances in the indirect dimension. 2D NMR experiments can be either homonuclear (e.g. ^{1}H-^{1}H) or heteronuclear (e.g. ^{1}H-^{13}C), and utilize different internuclear interactions e.g. through one or more bonds ($^{1}J_{CH}$, $^{n}J_{HH}$, $^{n}J_{CH}$). With 2D (or higher dimension) experiments, the information that can be accessed through NMR spectra is extensive and is part of why NMR spectroscopy has been employed across many scientific fields.

With the multitude of structural information available, an immense number of structures have been elucidated via NMR spectroscopy. However, the elucidation process might be challenged when trying to distinguish diastereomers and conventional NMR based analysis is incapable of distinguishing enantiomers as the NMR observables are identical.

2.2 Anisotropy

Even with the wealth of structural information gained from an NMR spectroscopic structural analysis described above, for some compounds this is insufficient to definitively determine the complete structure. For compounds with proton deficiency, structural information may be scarce, making analysis difficult or leading to misinterpretations with incorrect structures as a result.[25][5] Many NMR experiments utilize homo- or heteronuclear proton correlations to attain structural information. Structures with several quaternary chiral carbons in the core may represent an enormous challenge, requiring a combination of analytical methods to solve. In addition, structural flexibility may hamper a full 3D structural elucidation, as conformational averaging can eliminate distinct signals, which are needed when distinguishing e.g. stereocenters.

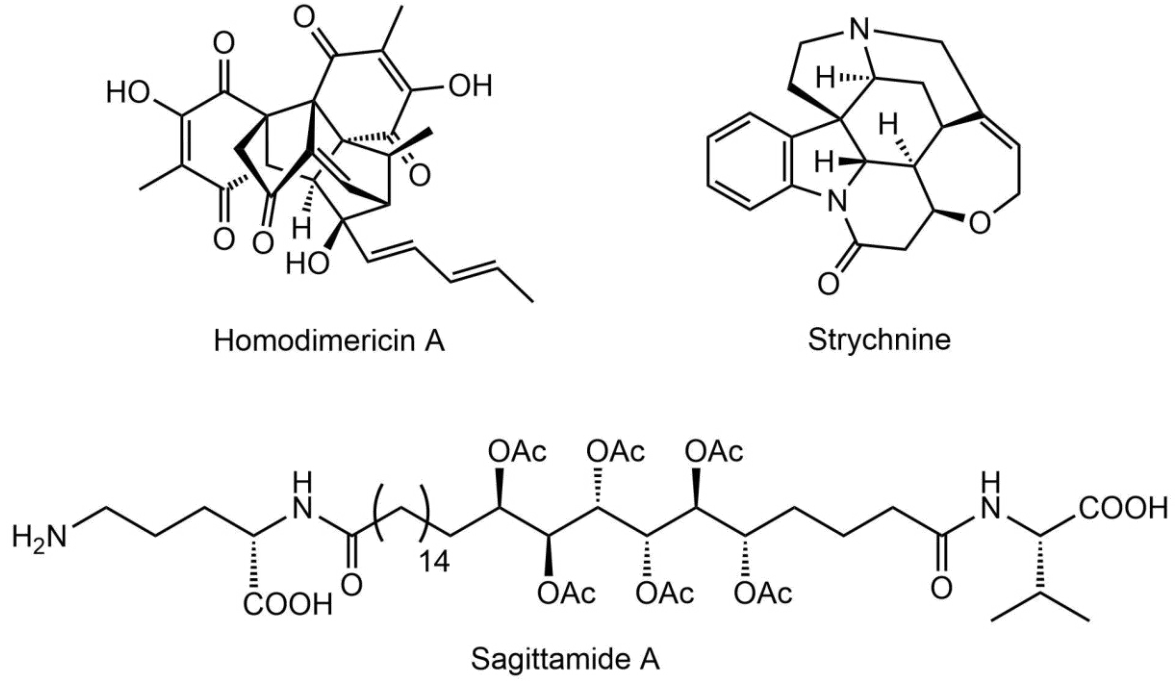

Figure 2.3. Examples of structures that have been explored by anisotropic NMR methods. Homodimericin A[26][27], Strychnine[28–30], and Sagittamide A[4].

Methods of gaining additional structural information from NMR spectroscopy take advantage of anisotropic interactions, which become observable if the compound is partially oriented relative to the magnetic field. Partial orientation, also known as weak alignment, is typically induced by an alignment media, which will be discussed below in further detail. In conventional isotropic NMR spectroscopy, the molecules tumble randomly in solution, which average interactions dependent on the field orientation. When a compound exhibits partial orientation in the magnetic field, these normally "invisible" effects become observable, namely the dipolar coupling, quadrupolar coupling, and chemical shift anisotropy.[31] Where *J*-coupling constants and NOE derived distances are based on local internuclear interactions, the anisotropy based methods provide global structural information as they are dependent on the external magnetic field.

The hydrogen isotope deuterium, ^{2}H, has a nuclear spin quantum number of $I = 1$, and therefore possess an electric quadrupole moment that interacts with the electric field gradient at the nucleus. This interaction is seen as a coupling in ^{2}H spectra when an anisotropic environment is created. The size of the coupling for the deuterated solvent peak, commonly referred to as the deuterium splitting, is commonly used as a measure of the degree of alignment.[32]

The anisotropic trilogy

RDC

The dipolar coupling is a direct interaction between nuclei, which depends on the relative angle to the external magnetic field.[33] By partially aligning molecules, a fraction of the coupling is observable in NMR spectra, hence the name residual dipolar coupling (RDC). The RDCs are observed as additions to the *J*-coupling constant and extracted by comparison of data under isotropic and anisotropic conditions. The method is most commonly applied for one bond ^{1}H-^{13}C correlations, where it provides angular information regarding orientation of the H-C bond relative to other H-C bonds in the molecule. Questions regarding stereochemistry and conformational behavior of complex structures may be answered due to the global structural information provided by RDCs.[34][35]

RCSA

The partial alignment can cause incomplete averaging of the chemical shielding tensor, which is seen as a change in the observed chemical shift of the individual nuclei compared to their isotropic value; the difference is known as the residual chemical shift anisotropy (RCSA).[36] The method is applied for ^{13}C data with acquisition of simple 1D ^{13}C NMR spectra under isotropic and aligned conditions. During data analysis, the RCSA has to be distinguished from any solvent effects due to changes of the chemical environment from the alignment media.[37] RCSA can provide unique structural information on quaternary carbons in contrast to RDCs, however due to their larger anisotropy the observation of RCSAs are generally most pronounced for sp^2 hybridized carbons.[32][38]

RQC

The quadrupolar coupling exhibited by deuterium can be a source of structural information and not solely be used to measure the degree of alignment.[38] Deuterium residual quadrupolar couplings (^{2}H-RQC) can be extracted and converted into structural information in a similar manner to the residual dipolar couplings, however the RQCs can be obtained at a higher accuracy due to their inherent larger size.[39] The low natural abundance of deuterium does challenge the sensitivity, but is also an advantage as the extraction of ^{2}H-RQCs does not suffer from interference from ^{2}H-^{2}H couplings. Earliest use of ^{2}H-RQCs required deuterium labelling, but modern high field spectrometers can acquire spectra at natural abundance using ^{2}H cryoprobes.[39]

2.2.1 Residual dipolar coupling

Nematic liquid crystals solutions were observed by Saupe in the 1960's to partly orient solutes, facilitating extraction of anisotropic parameters.[40][41] However, the induced degree of order of the solutions was so high that the observed dipolar coupling constants were in the kHz range, making interpretation of spectra extremely difficult.

Alignment was observed for biomacromolecules with magnetic susceptibility that aligned in the magnetic field in water.[42][43] The method was expanded to more biomolecules by the introduction of micelles, forming a LC structure in aqueous solution, which were tunable to induce a weaker alignment.[44] With weak alignment, the size of the dipolar coupling is ideally in the range of the scalar *J*-coupling constant, resulting in NMR spectra that are easier to analyze. Thus, the weakly aligned spectra only show a fraction of the effect, hence the name residual dipolar coupling (RDC).

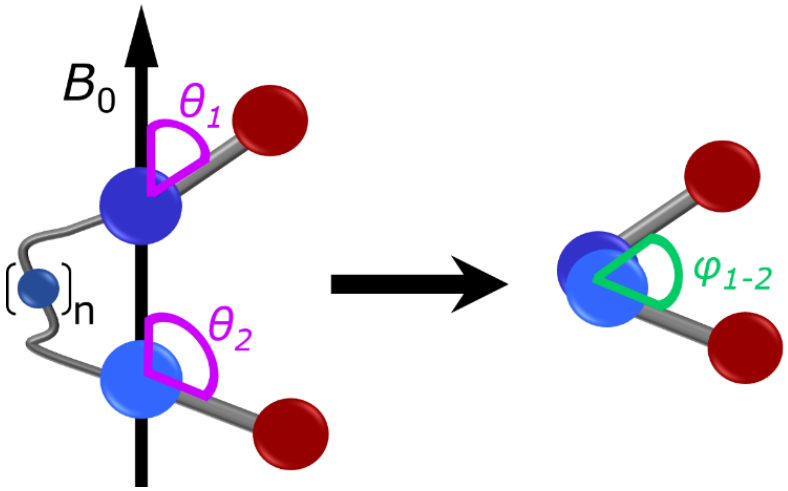

Figure 2.4.

Illustration of the angular structural information gained from RDCs.

The dipolar coupling, *D*, operates through space via magnetic dipole-dipole interactions from the magnetic fields generated by the nuclear spins, and is directly influenced by the orientation, θ, of the internuclear vector relative to the external magnetic field, B_0, according to the equation below.[45][46][47]

$$D_{IS} = -\frac{3\hbar\gamma_I\gamma_S\mu_0}{8\pi^2}\left\langle\frac{1}{r_{IS}^3}(\cos^2\theta_{IS}-1)\right\rangle$$

$\hbar$ is the reduced Planck constant, μ_0 the vacuum permeability constant, γ the gyromagnetic ratios for the nuclei *I* and *S*, r_{IS} their internuclear distance, and θ_{IS} the angle between the internuclear vector and the direction of the magnetic field as illustrated in Figure 2.4. Under isotropic conditions, the angular dependence is an average (indicated by the bracket in the equation above) over all orientations due to random tumbling and no net dipolar coupling is observed. In a weakly anisotropic environment, the molecule will on average display a slightly preferred orientation relative to the magnetic field and the RDC may become observable in the spectra as an addition to the *J*-coupling constant.[33]

$$T = J + D \implies D = T - J$$

Here *T* is the total coupling observed and the RDC (*D*) is found as the difference between coupling constants extracted from isotropic and anisotropic spectra.[48] The *J*-coupling constant

can be assumed independent of the anisotropic environment.[47] The notation $T = J + 2D$ can also be found in literature, and while it influences the size of the reported RDCs, it does not change the structural conclusions as it is the RDC orientation, which is of importance in the evaluation of data.[33]

The orientation of the molecule is described using an alignment tensor **A**; a 3x3 symmetric and traceless matrix.[46] To determine **A**, 5 linearly independent RDCs are needed, when more is used, structural information can be obtained.[33] From **A**, theoretical RDCs can be calculated and compared to experimental values. Using a singular value decomposition (SVD) procedure, the best correlation to theoretical values are found for a given 3D structure and the best alignment tensor constructed. The fit between the experimental values and the back-calculated RDCs is expressed in terms of the quality (Q) factor.[48]

$$Q = \sqrt{\frac{\sum (D^{exp} - D^{calc})^2}{\sum D^{exp}}}$$

With a good quality fit, the Q factor will approach zero. Often a value below 0.2 indicate a good fit between the experimental data and the predicted structures, which should truthfully represent the conformational space. Here it should be underlined that the calculations only evaluate against the proposed structures; it is up to the analytical chemist to ensure that the right structure(s) are among those assessed and that the conformational space has been properly evaluated.

2.2.2 Alignment media

Two classes of alignment media for small organic compounds were developed in the 2000's; new liquid crystal (LC) solutions and the novel research of stretched polymers (SPs). For biomolecules in water other types of alignment media such as micelles[44], lamellar LC[49] and phages[50] have been introduced.

Key stepping-stones towards the greater applicability of alignment media in structural studies of small molecules are 1) compatibility with organic solvents, 2) quality of the acquired spectra, 3) ease of synthesis of the alignment media and subsequent NMR sample preparation, and 4) tunable degree of alignment.

Most of the LC alignment media in use are based on polymer strands forming a helical structure in solution after reaching a critical concentration. The main drawback of most LC alignment media is that they induce a strong alignment, which may be a challenge if $D >> J$, due to decrease of spectral quality. So far, there has only been limited success in scaling the degree of alignment as a minimum critical concentration is needed for LC formation.[51] Sample preparation is relatively easy, although achieving the right homogeneity within the LC solution seems to be aided by experience.

Table 2.1. Various LC type alignment media with utilized solvent(s). Inspired by Li *et al*.[34]
[a]All solvents are fully deuterated. [b]Shown in this work (Chapter 4).

LC media	Solvent[a]	Chiral	Reference(s)
PBLG/PBDG	$CDCl_3$, CD_2Cl_2, DMF, THF, Dioxane	Yes	[8][36–38][51][54]
PCBLL/PCBDL	$CDCl_3$	Yes	[55]
PELG/PEDG	$CDCl_3$, CD_2Cl_2	Yes	[55][56]
Polyguanidines	$CDCl_3$	Yes	[57]
Polyisocyanides	$CDCl_3$, CD_2Cl_2, THF	Yes	[58][59]
Polyacetylenes	$CDCl_3$	Yes	[60–62]
PPLA/PPDA	$CDCl_3$	Yes	[63]
Cellulose	DMSO	No	[64]
Graphene (GO)	D_2O, DMSO, D_2O-DMSO, D_2O-CD_3CN, D_2O-Acetone, D_2O-EtOD, D_2O- CD_3OD, D_2O-DMF	No[b]	[7][9][20]

Alignment of small organic compounds via SPs or strain induced alignment in a gel (SAG) builds on observations on ordering of molecules within swollen crosslinked polymers and alignment of biomacromolecules in aqueous gels.[65–67] The degree of alignment may be scaled by varying the amount of crosslinker used in the synthesis, or by stretching or compressing the swollen gel which requires special equipment and may make sample preparation timeconsuming.[68–70]

The alignment may also be introduced within the gel during a swelling period, as the polymer can be synthesized as a rod that only allows swelling in either a radial or horizontal direction within an NMR tube.[69] A drawback of SP media is the long swelling time that ranges from hours to several weeks. In some cases the gel may be reused and the solute recovered.[69]

Graphene oxide LC solutions stand apart from other alignment media as samples can be prepared in minutes with dilution from a stabile stock solution. The degree of alignment can be directly adjusted by varying the graphene oxide concentration, enabling tuning to obtain fitting alignment conditions.[7] In addition, the GO solutions have low viscosity, making sample preparation easy for anyone with a minimum of experience with NMR sample preparation. Another benefit of graphene oxide is the absence of background signals, which are otherwise common for other types of alignment media. Chemical functionalization has shown that the solubility of graphene oxide can be increased in organic solvents, allowing for acquisition of RDCs in pure DMSO.[9] This indicates untapped potential for expanding the applicability of GO based alignment media to a broader range of compound classes and possibly the determination of absolute configuration.

Table 2.2. SP/SAG based alignment media with utilized solvent(s). Inspired by Li *et al.*[34]
[a]All solvents are fully deuterated.

Gel media	Solvent[a]	Chiral	Reference(s)
PDMS	$CDCl_3$	No	[71]
Polysterene (PS)	$CDCl_3$	No	[72]
Polyacrylamide (PH)	DMSO DMF D_2O	No	[73]
Poly(vinyl acetate) (PVac)	DMSO, CD_3OD, CD_3CN, $CDCl_3$	No	[68]
Polyacrylonitrile (PAN)	DMSO, DMF	No	[74]
PMMA	$CDCl_3$, CD_2Cl_2, C_6D_6, CD_3CN, Acetone, EtOAc	No	[69][75]
PBLG gel	$CDCl_3$, CD_2Cl_2, THF, C_6D_6, Dioxane	Yes	[76]
Poly(ethylene oxide) (PEO)	D_2O, CD_3CN, CD_3OD, DMSO, Acetone, THF, $CDCl_3$, CD_2Cl_2, C_6D_6, Dioxane, *n*-Hexane	No	[77]
Poly-HEMA	DMSO	No	[78]
Poly-DEGMEMA	CD_3OD	No	[79]

2.3 Computational methods

3D molecular structures are needed to evaluate the experimental results of NMR analysis. Fortunately, computational chemistry has developed to a point where 3D structures can be modelled with great accuracy. In this project, force field methods were used to generate multiple conformers of compounds, which in combination represents the dynamic structural behavior of the given compounds in solution. A large set of conformers was generated for evaluation against NOE data in the 3D structural analysis of the lassopeptide triculamine described in Chapter 8.

The structures were optimized by density functional theory (DFT), when higher accuracy was needed for calculations of chemical shifts, *J*-coupling constant and evaluation of experimental RDCs for analysis of small organic molecules.

Multiple computational methods have been described in literature; this brief introduction focus on the approaches and parameters used in this project, centered around the practical aspects and implications on the results.

2.3.1 Force field methods

One computational approach to model structures is by focusing on the nuclei and using their positions as variables in classical mechanic equations. The chemical bonds are treated like springs, i.e. having different lengths and "stiffness". When electrons are not considered explicitly, solving the electronic Schrödinger equation can be avoided, thus greatly simplifying the calculations and thereby the computational cost, that being computational power or time. In force field (FF) methods, also known as molecular mechanics, the overall energy of the system is modelled as a sum like the following equation, using the position of the nuclei to calculate the individual contributions.[80]

$$E_{FF} = E_{str} + E_{bend} + E_{tors} + E_{vdw} + E_{el} + E_{cross}$$

The E_{str} and E_{bend} terms cover the effect of stretching and bending bonds, typically expressed as deviations from a natural bond length and angle, respectively. The expressions can be expanded with increasingly more elaborate functions, generally showing higher accuracy, but at the cost of being more computationally demanding. The rotational energy around each bond is given in E_{tors} as a Fourier series with the rotational barriers expressed through constants. E_{vdw} and E_{el} are the non-bonded interactions from van der Waal forces and electric charges. The E_{cross} term, when included, accounts for the cross-effects between the other terms, e.g. bond elongation due to angle compressions. All contributions can be expressed with different functions and extensions, leading to a wide range of force fields with varying applicability for different compound classes. Likewise, the contributions contain a number of parameters and constants, which differ for each element and functional group, and should be taken into account when choosing force field, e.g. not all heavier atoms are covered for all force fields.

Force field methods are used here to sample the most stable structure conformation(s). The conformational sampling is carried out by a Monte Carlo method, where the nuclei coordinates are randomly varied and the total energy calculated in the search for relative energy minima representing stable conformations. For subsequent comparison with experimental data, it is important that the entire conformational space is sampled, meaning all relevant conformations are found. This is sought fulfilled by a surplus of steps and examining that the resulting conformers are found multiple times.

2.3.2 Density functional theory

Higher accuracy can be achieved if the computational calculations take the electrons explicitly into account, though at a higher computational cost. Density functional theory (DFT) aspires to determine the energy of a system by modelling the electron density.[80] This is realized through a set of functionals, which use functions describing the molecular orbitals to model the overall energy of the system. The molecular orbitals are comprised of linear combinations of atomic orbitals called basis functions, making up a basis set. These most often consists of Gaussian type orbitals (GTOs). The Pople basis set was used in this thesis and uses a notation of e.g. 6-31+G(d,p), meaning that the core orbitals are described by 6 GTOs, the inner valence orbitals by 3 GTOs and the outer valence orbitals by 1 GTO. The split of the valence orbitals allows for more flexibility in the description of the total molecular orbitals, leading to higher accuracy. On top of these GTOs can be added diffuse functions that allow for increased flexibility in the description of the electron density far from the nucleus and is noted by (+) for diffuse functions on heavier atoms and (++) for also adding diffuse functions to hydrogens. Polarization functions can be added as a vacant orbital of higher order than what is occupied by the electrons to allow for more asymmetry in the description of the electron density as a consequence of bonding to other atoms, noted as (d,p) meaning addition of a d-orbital to heavy atoms and a p-orbital to hydrogens.

DFT functionals use basis sets to model the electron density of the system and from that calculate the energy. A wide variety of functionals exists due to different approaches and approximations in their development. The matter of choosing the right DFT functional and basis set for a given problem is not always straightforward (at least for a non-computational chemist), but literature may provide inspiration on methods that have worked well for similar compounds, otherwise a screening of different methods may be advised. Computational efficiency may also be a factor as computationally demanding methods could lead to higher accuracy, but at a very high cost, where a less accurate method may give sufficient results to the problem at hand at a fraction of the computational time.[81] In this thesis, the functionals MPW1PW91[82] and the Becke Three Hybrid Functional (B3LYP)[83][84] have been used, the latter being very popular among organic chemists. Initial structures optimized by force field methods were then optimized to a DFT level of theory when needed for comparison with experimental data.

3 Graphene oxide background

Interest in GO has increased significantly since the isolation and characterization of graphene in 2004. Many discoveries concerning GO are motivated by its similarity to graphene, though the history of GO stretches far further back. The name "graphene oxide" has only been the convention in recent literature; earlier descriptions have e.g. referred to the material as graphite oxide or graphitic acid.[85] GO is thus an old material, whose potential has recently been fully realized.

GO related chemistry is a large, interesting, diverse, and still evolving field with many potential applications, thereby prompting delimitations to what could be addressed. The references given are meant to underline key discoveries and scientists involved in the exploration of GO and provide the interested reader with starting points for further studies. The aim is to provide a foundation of knowledge needed for the discussion of the experimental results in subsequent chapters.

3.1.1 History and synthesis

The history of GO can be traced back to the 19th century and investigations into graphite and the various forms of carbon.[16][17][84]–[86] Brodie was the first to discover and describe the oxidation of graphite by what was to be known as Brodie's method of reacting graphite in fuming nitric acid with potassium chlorate.[3][4] The two other main types of oxidation strategies are Staudenmaiers[89] using potassium chlorate in a mixture of concentrated nitric and sulfuric acids, and Hummers[90] based on potassium permanganate in concentrated sulfuric acid. Many variations of the oxidation procedure and subsequent purification steps have been described.[85] Of special interest here is modifications to the Hummers approach, which has been used in this project.[9][10]

During the 20th century, great effort was put into development of different GO structural models. This started with the application of X-ray diffraction by Hofmann in the 1930s.[93–95] Many other models were suggested, e.g. by the groups of Thiele[96], Ruess[97], Scholz and Boehm[98]. It was proposed that GO contained hydroxyl[96] or epoxy groups[95]; today there is general agreement upon the oxygen content of GO being largely made up by a combination of both hydroxyl and epoxide groups. This was confirmed by solid state magic angle spinning (MAS) NMR in the 1990s, which revealed chemical shifts at app. 60, 70, and 130 ppm, corresponding to epoxy, hydroxyl, and double bonded carbons, respectively.[17][18] This type of analysis led to the widely popularized Lerf-Klinowski model.[101–103] The model also proposed areas of preserved aromaticity between the oxidized domains with a random placement of epoxy and hydroxyl groups. Previously, the acidic and ion exchange properties of GO had been described[19][88][104], and the generally accepted theory was that carboxylic acids decorated the edges of the GO flakes and holes due to defects within the sheets.

Limited focus had been on the actual reaction mechanism for the conversion of graphite to GO and the exact oxidizing specie in solution remains unclear. A detailed study identified different stages in the conversion during the Hummers method, starting with the intercalation of sulfuric

acid into the graphite structure.[105] Upon addition of $KMnO_4$, the oxidation progress from edge to center of the flakes as long as there is oxidant available. The reaction appears to be diffusion controlled and the reaction time is therefore dependent on the graphite flake size to achieve full oxidation.[105] Other studies found direct effects of reaction time, temperature, and amount of oxidizing agent on the GO sheet size.[106][107] It has been described that the sulfuric acid can react with the formed epoxides and form covalently bonded sulfates.[108][109] Residual sulfur that is always found in GO prepared by Hummers method should therefore be considered part of the structure and not an impurity. The oxidized graphite is hereafter exfoliated by the addition of water into single layered GO in solution.[85][105]

The composition, properties and structure of GO have been debated ever since its discovery. Part of the discussion centered on establishing a sum formula or C/O ratio via combustion analysis, where widely different results have been reported. The composition of GO is very dependent on the graphite source, oxidizing reagents and the method used, and even then batch to batch variations are expected. So if every investigation has produced different types of GO, naturally different conclusions will be drawn, leading to e.g. different structural models. The earlier models often included a very ordered structure with periodic repetitions of functional groups; this changed and in the current descriptions of the GO structure the functional groups are randomly distributed in regions with irregular sizes.[102][110]

3.2 Characterization of graphene oxide

Like graphene, GO is based on a hexagonal carbon lattice, however the hybridization has been disrupted by the introduction of oxygenated functional groups. The detailed structure of GO has been studied by a wealth of different techniques; an overview can be seen in Table 3.1. Selected techniques and the information they provide on the GO structure and properties will be described in detail in the following.

Table 3.1. Examples of techniques used to study the structure of GO.

Technique	Ref.	Technique	Ref.
X-ray diffraction (XRD)	[94][111]	^{13}C Solid state NMR (ssNMR)	[99][103][112]
X-ray photoelectron spectroscopy (XPS)	[85][113]	Raman spectroscopy	[114][115]
Infrared (IR) spectroscopy	[116–119]	Transmission electron microscopy (TEM)	[120]
Atomic force microscopy (AFM)	[121][122]	High-resolution TEM (HRTEM)	[110][123][124]
AFM-IR	[125]	Scanning electron microscopy (SEM)	[126]
Thermogravimetric analysis (TGA)	[127]	Scanning tunneling microscopy (STM)	[122]
TGA-MS	[109]		

3.2.1 Infrared spectroscopy

Absorption of infrared light can cause vibrations of covalent bonds. The electromagnetic field of the radiation will interact with changing electric dipoles increasing the amplitude of vibrational or bending motions. Often the illustration of an oscillating spring connecting two masses is used to describe a covalent bond, where absorption of energy causes the spring to oscillate faster. The motion of a spring is dependent on a force constant and the masses it is connecting, and only energy matching this frequency will cause the spring to stretch or compress. The absorption at specific frequencies correlates to different types of bond vibrations and may be used to identify bonds and functional groups. However, the technique is generally not considered quantitative, as the relative intensity observed in the IR spectrum does not correlate to the number of bonds behind the absorption. As the interaction between the electromagnetic radiation and the covalent bonds is dependent on a changing electric dipole moment, highly symmetric bonds will not absorb infrared frequencies.

Research on the structure of GO have utilized IR spectroscopy and assignments of a number of frequency bands have been described. The overall most defining band is present at app. 1720 cm^{-1} assigned to the stretch of the C=O bond from carbonyls such as ketones and carboxylic acids. Thorough drying of GO and deuterium exchange experiments have proven that the broad band at 2500-3700 cm^{-1} is largely due to O-H stretch from adsorbed H_2O, overlapped with minor hydroxyl and carboxylic acids bands.[116][117]

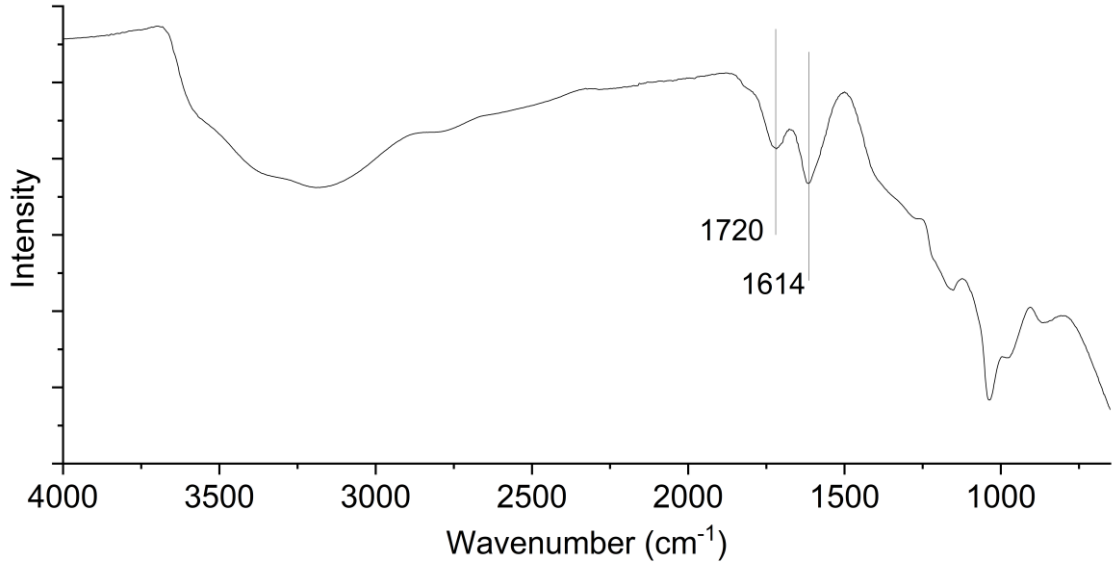

Figure 3.1. IR spectrum of GO with significant bands noted.

The IR band at app. 1614 cm^{-1} is often assigned to C=C stretch, however deuterium exchange has a strong effect on this peak and it is consequently connected to bending within H_2O adsorbed on the GO surface.[116][117] Aromatic C=C bonds may contribute with overlapping deformation bands, one is possible seen as a shoulder just under 1600 cm^{-1}. A number of IR bands in the fingerprint region of 600-1500 cm^{-1} have been assigned to various other bonds in the GO structure e.g. C-O from hydroxyls and epoxides. However, these assignments have to be evaluated with great caution, as their frequencies are very sensitive to specific structures and may overlap with other vibration bands. Even bands from simple organic molecules in this region are often only assigned tentatively.

3.2.2 Solid state ^{13}C NMR spectroscopy

GO in solution shows no NMR signals due to the large size of the GO sheets and very slow tumbling from the restricted motion by the formation of a LC structure. Instead, solid-state NMR (ssNMR) can be applied in the study of graphene-based materials. In contrast to solution NMR, ssNMR spectra are acquired on solid samples using magic-angle-spinning (MAS) to counteract the dipole-dipole interactions. ^{13}C MAS spectra provided important structural information about GO and led to the most commonly referred to structural model of GO, the Lerf-Klinowski model (*vida infra*).[20][21][101]

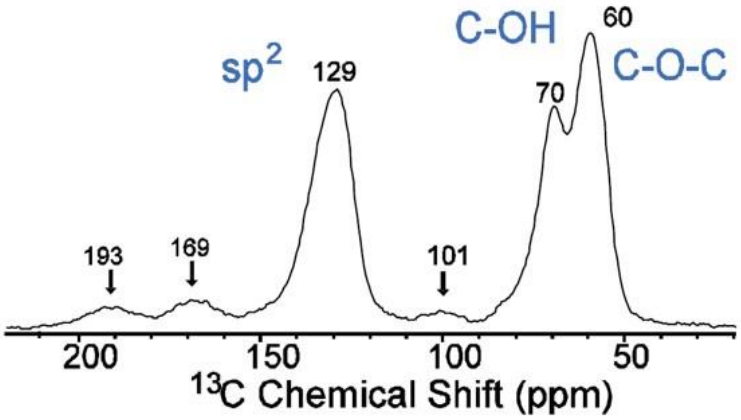

Figure 3.2. 1D ^{13}C MAS spectrum of GO from a ^{13}C labelled sample. The chemical shift of relevant peaks are noted and the assignment of the most abundant groups added. Reproduced from [112] with permission from the American Association for the Advancement of Science.

^{13}C MAS spectra of GO show three major peaks at app. 60, 70 and 129 ppm for carbons in epoxide, hydroxyl, and C=C in aromatic regions, respectively. Minor peaks have been observed at 101, 169, 193 ppm.[112] These can be tentatively assigned to carbon in diols/hemiacetals, carboxylic acids and ketones, respectively. The low signal-to-noise (*S/N*) ratio in ^{13}C MAS spectra of GO can hinder accurate observation and quantification of low intensity peaks. In solution NMR, the relatively narrow peaks allow detailed assignment of individual signals, something often not possible with the broader peaks of MAS spectra. Deconvolution of spectra can be necessary to determine accurate chemical shifts and potentially locate any peaks concealed by overlap.

NMR spectroscopy can be applied quantitatively, as the integral of the individual peaks relates directly to the relative amount of nuclei in a given chemical environment. By simulating the 1D ^{13}C MAS spectrum, the relative amount of different functional groups may be found. From ^{13}C MAS spectra it can be concluded that GO predominantly consists of hydroxyl and epoxide groups with some conservation of the original sp^2-hybridization. Other functional groups are only present in limited amounts.

3.2.3 Atomic force microscopy

The surface and dimensions of GO can be probed at high resolution using atomic force microscopy (AFM). The sample is placed on an atomically flat surface, which is probed by a sharp tip placed on a cantilever.[128] In tapping mode, the cantilever is set to oscillate near its resonance frequency. When the tip is brought close to the sample surface, the force of interaction between the tip and sample will make the cantilever deflect. To gain high resolution, the deflection of the cantilever is measured via a laser beam and a photodiode detector as illustrated in Figure 3.3. A topography image is constructed by mapping the cantilever deflection, when probing the sample surface. Modern AFMs allows vertical resolution down to the scale of 0.1 nm.

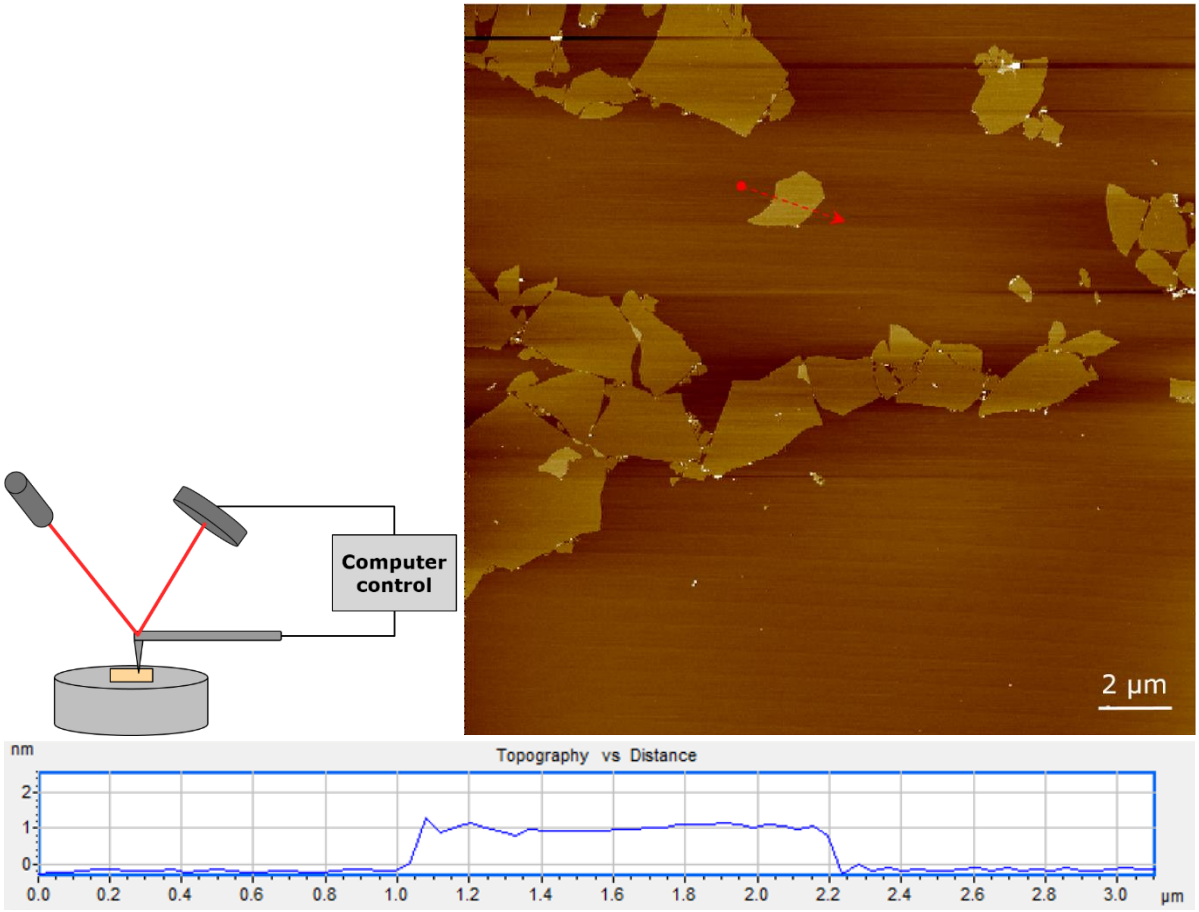

Figure 3.3. Left: Illustration of the principle behind AFM. Right: AFM image of GO on mica substrate. Bottom: Sheet height along the red arrow in the AFM spectrum.

The single layer GO sheets have a thickness of app. 1 nm when measured by AFM, while the diameter can be in the range of nanometers to micrometers depending on the method of synthesis and handling.[121] In comparison, graphene is typically reported with a thickness of 0.6-0.7 nm. The width of the cantilever tip determine the horizontal resolution and for AFM the tip width is generally a few tens of nanometers wide. Thus, AFM is ideal for verifying the single layer nature of GO and asses the sheet diameter distribution, but the technique may be limited in its ability to provide details about changes on the GO surface as these may be obscured by the inherent horizontal resolution.

3.3 Structure of graphene oxide

Over time many different structural models of GO have been proposed, often incorporating concepts from earlier models and adjusting to fit new data or new interpretations. The debate has still not fully settled with at least two new models that are very different being published in the last 10 years with ensuing discussions.[126][129–132]

The Lerf-Klinowski model as illustrated in Figure 3.4 was proposed in the late 1990s and are perhaps the most referenced GO structure model.[102][103] The GO structure is described to consist of a single layer carbon basal plane decorated with hydroxyl and epoxy groups on both sides of the plane with areas where the original sp^2 hybridization is still intact. The edges were assumed to be decorated by carboxyl groups due to the observed acidity and ion exchange properties of GO solutions.[103][104]

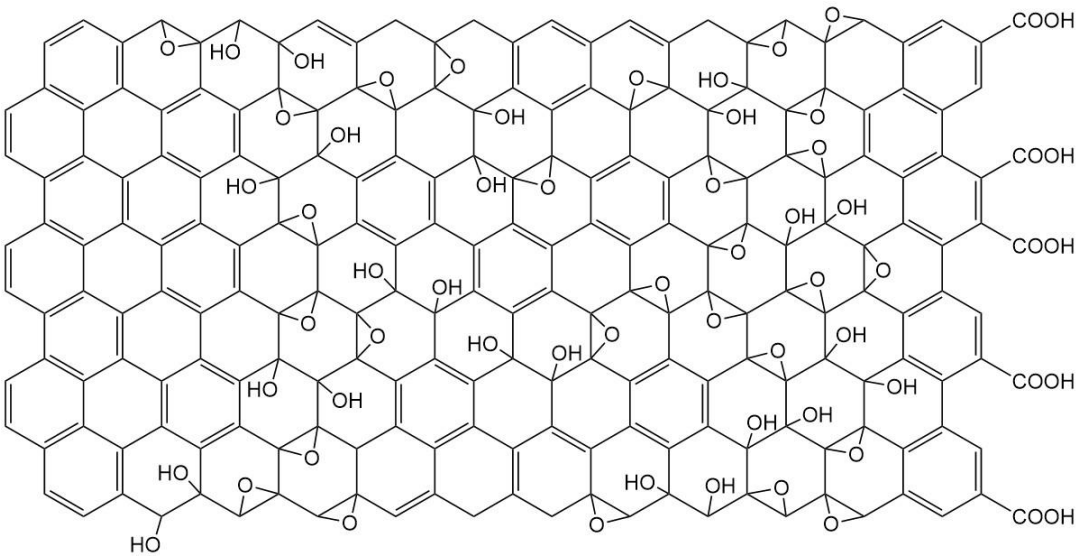

Figure 3.4. The Lerf-Klinowski structural model of GO. Inspired by [103].

The Lerf-Klinowski model of GO contains principles that can be generally agreed upon, while it has been proven not detailed enough to explain all experimental observations. High-resolution TEM (HRTEM) studies showed the GO surface at atomic resolution as seen in Figure 3.5, proving that the GO basal plane consists of random oxidized and aromatic domains of nm sizes.[110][123] The HRTEM images are in line with the Lerf-Klinowski model, though they reveal that the sizes of the oxidized and aromatic domains were bigger than described and holes in the sheets are integrated in the structure. Both aromatic domains and holes within the sheet are too small to be distinguished by AFM, which only sees the average height of the sheets.

During the oxidation process, defects and holes are introduced together with loss of carbon in the form of CO and CO_2.[108] The introduction of defects and holes are an additional obstacle towards obtaining high quality graphene from reduction of GO as complete sp^2 hybridization cannot be restored.

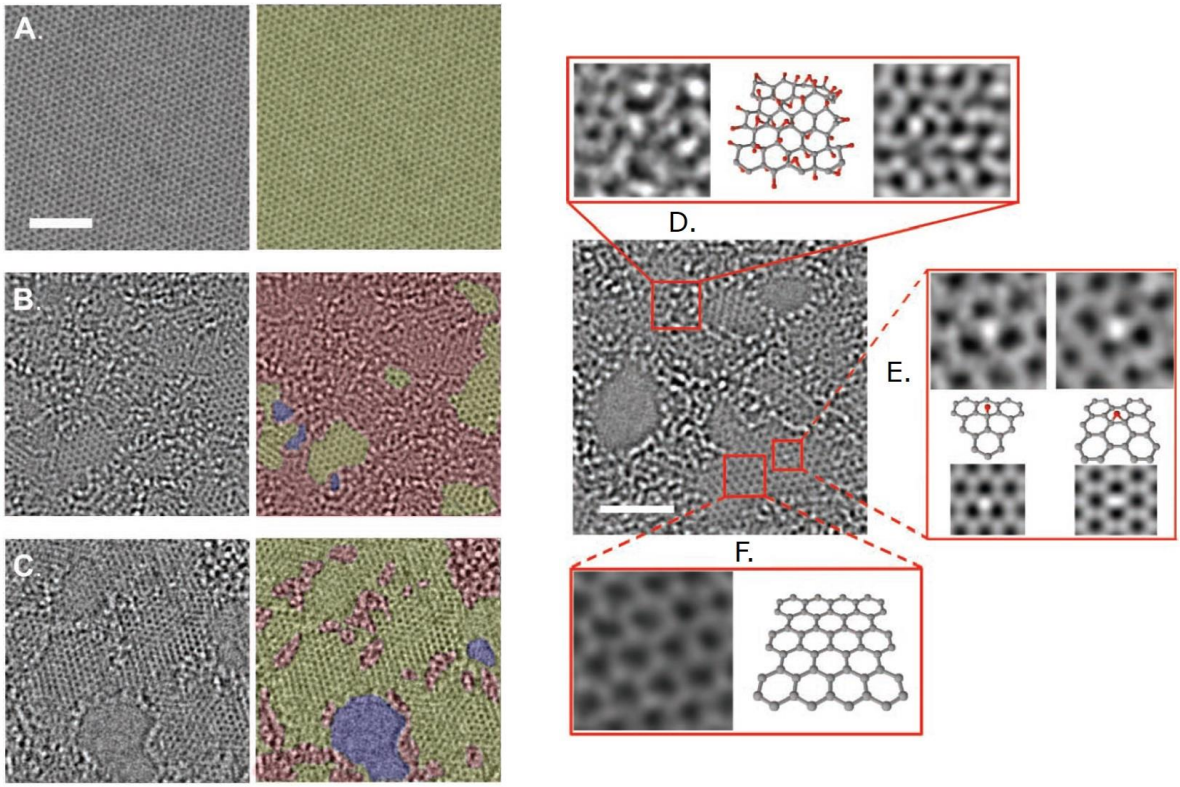

Figure 3.5. HRTEM image of (A) graphene, (B) GO, and (C) rGO. The same images are shown with color coding; aromatic domains in yellow-green, oxidized domains in red, and holes in blue. To the right is seen a HRTEM image with expansion of different regions and proposed structures with corresponding simulated TEM images of (D) a highly oxidized region, (E) a single oxygen, which moved across an aromatic domain due to the TEM electron beam, but was stationary at a hydroxyl and epoxide position for a few frames, (F) an aromatic domain. The scale bar denotes 2 nm for all images. Reproduced from [110] with permission from Wiley-VCH.

The edges of GO flakes (and holes) have widely been assumed to primarily be decorated with carboxylic acids, but other work has questioned the abundance.[116][126] Instead there are arguments for the presence of a more diverse range of functionalities present at the edges of GO e.g. ketones, enols, gem-diols and hemiacetals in addition to carboxylic acids.[85][126][116]

In many studies and related discussions regarding functionalization of GO, it has been treated as a uniform, mostly inert, backbone material with only a limited range of chemical reactivity being considered. A competing view of GO has started to form, where GO is seen as a broader term for oxidized graphene materials, where the exact composition is strongly dependent on graphite source, synthesis method, purification and storage conditions. Furthermore, the structure of GO is discussed as a dynamic structure that responds to its surroundings and evolves over time.[85][126] Using more nuanced terms when discussing GO materials could allow for more systematic variations and the importance of individual GO synthesis steps to be explored deeper, resulting in an understanding and availability of GO as a range of materials.[133–135]

A deeper understanding of the GO structure and properties could furthermore provide greater control of GO derivatization and tuning of the degree of functionalization. Discussions regarding different aspects of the GO structure will be revisited in subsequent chapters on GO functionalization.

3.4 Dispersibility and liquid crystal formation

Ever since its discovery, GO has been known to be dispersible in water in stark contrast to graphene. In the process of exploring the properties of GO, its ability to form a liquid crystal (LC) in aqueous solution was reported in 2011.[136][137] This discovery was in line with Onsager's theory due to the high aspect ratio of GO.[138] GO forms a nematic, lyoptropic LC, meaning the GO sheets show orientational order in one dimension after a critical concentration is reached.[139] The sheets are parallel in the basis plane, but does not stack uniformly on top of each other (columnar) or form sideways layers (smectic).[140]

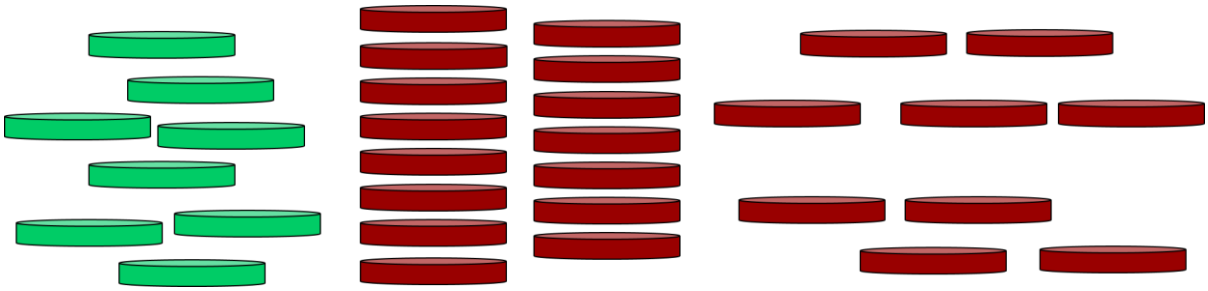

Figure 3.6. Illustrations of nematic (left), columnar (middle), and smectic (right) liquid crystal structures for plate-like particles.

The GO LC structure is stabilized by hydrogen bonding and electrostatic repulsion between the negatively charged sheets.[141][142] Consequently, an aqueous solution is an ideal medium for GO dispersion. However, the stability is sensitive towards pH and salts, which can be monitored via the zeta potential.[143–145] If the pH is lowered, the sheets no longer repel each other and the LC structure is lost. Cations have a similar effect of screening the negative charges on the GO surface, however the screening effect is influenced by the choice of cation.[144]

The liquid crystallinity of GO has also been reported in solvents such as DMF, DMSO, ethanol, and *N*-methyl-2-pyrrolidone.[146][147] The dispersibility of GO in a broad range of additional organic solvents has also been investigated.[148–151] GO solutions are generally stable in polar organic solvents with ability to form hydrogen bonds, though the stability is influenced by the GO concentration.

In confined volumes, GO has been observed by polarizing optical microscopy to obtain face-on orientation to a glass interface.[147][152] Reorientation of differently oriented domains within a thin, annealed GO sample relative to an applied magnetic field was reported by Kim *et al*. to merge into one domain, though the process took several hours.[136] The applied magnetic field strength by Kim *et al*. was app. 0.25 T, noteworthy lower than the typical field strengths of NMR spectrometers. The orientation of the GO LC, and thus the alignment vector of interacting compounds relative to a magnetic field, has not been described in relation to NMR analysis.

4 GO synthesis, behavior, and NMR properties

This chapter covers and expands on the discoveries published in the article "Practical considerations for working with graphene oxide as alignment media for RDC measurements"[20] with discussions of additional observations on GO behavior in solution. The chapter is meant to serve as a foundation for the following discussions on GO functionalization experiments and alignment properties. A routine workflow is illustrated through a case study of a menthol sample to present and discuss relevant factors in sample preparation, acquisition of NMR spectra, data extraction, computational modelling, back-calculation of residual dipolar couplings (RDCs), and evaluation of the results. For further description of experimental procedures, the reader is referred to the published article and the available supplementary information provided in appendix.

4.1 Menthol: sample preparation, modelling and alignment

Throughout this project, the organic compound (-)-menthol has been used to survey the alignment properties of GO solutions for NMR analysis. Menthol was chosen due to its availability, solubility, and chemical as well as conformational stability. Other compounds have been used to address specific issues, verify observations and conclusions.

Menthol can be fully assigned by multiplicity analysis and the use of 2D homo- and heteronuclear NMR experiments, including individual assignment of all methylene protons. Standard solvent composition for GO alignment was a 1:1 D_2O:DMSO-*d*6 mixture, the reasoning will be discussed in the following. This solvent mixture caused broader linewidths than for spectra acquired in $CDCl_3$, hindering accurate measurement of small *J*-coupling constants, hence the many noted multiplets in Table 4.1. Comparison of 1D ^1H NMR spectra of menthol in different solutions can be found in appendix.

Sample preparation for aligned samples began with extraction of the required amount of GO from a stock solution followed by exchange and dilution with deuterated solvent. Throughout this project, centrifugation has been used to exchange the solvent of GO solutions and later for purification after reactions. The process could be repeated numerous times as needed. Often 20-30 min high speed centrifugation were needed for full sedimentation depending on GO concentration and solvent. Centrifugation of GO in water was relatively easy, while sedimentation in a highly viscous solvent such as DMSO was challenging.

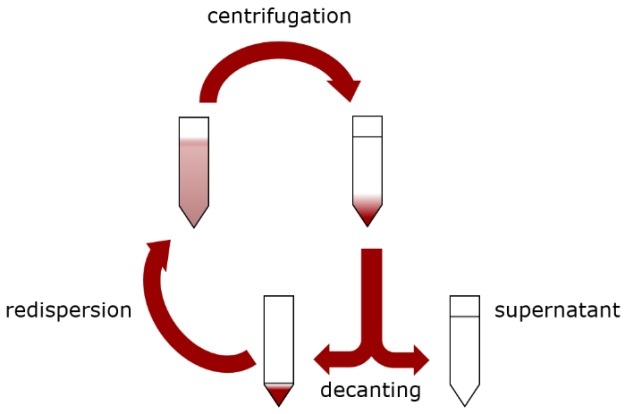

Figure 4.1. Illustration of the centrifugation and redispersion process of GO and the removal of supernatant by decantation. The process starts with centrifugation of GO sample(s), causing the GO to sediment. Decantation of the clear supernatant is then followed by redispersion of GO in solvent often needing vigorous shaking.

Table 4.1. Assignment of 4 mM (-)-menthol in 1:1 D_2O:DMSO-*d*6. For methylene groups X_a and X_b refer to equatorial and axial protons, respectively. Referenced to 2.50 ppm (^1H) and 39.5 (^{13}C) at 600 MHz.

#	δ_H [ppm] (int, mult., *J* [Hz])	δ_C [ppm]
1	3.20 (1H, td, 11.1, 4.4)	71.8
2a	1.77 (1H, d, 14.1)	45.5
2b	0.79 (1H, m)	
3	1.26 (1H, m)	32.5
4a	1.52 (1H, d, 14.1)	35.4
4b	0.68 (1H, m)	
5a	1.46 (1H, m)	23.9
5b	0.82 (1H, m)	
6	0.95 (1H, m)	50.5
7	1.98 (1H, sept, d, 7.3, 2.2)	26.4
8	0.77 (3H, d, 7.2)	22.2
9	0.63 (3H, d, 7.3)	16.9
10	0.77 (3H, d, 7.2)	23.2

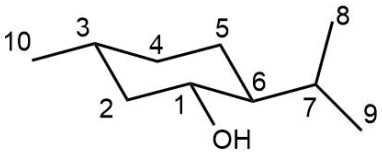

Figure 4.2.
Structure of menthol with the assignment used throughout the text.

GO in the concentrations used here (up to 10 mg/mL) does not change the viscosity of solutions notably, therefore addition of solute and NMR sample preparation is simple. Unless otherwise stated all NMR experiments throughout this project have been acquired in 5 mm NMR tubes at 298 K. The GO causes significantly broader peaks compared to isotropic spectra, but does not add any background signals to the spectra as seen in Figure 4.3.

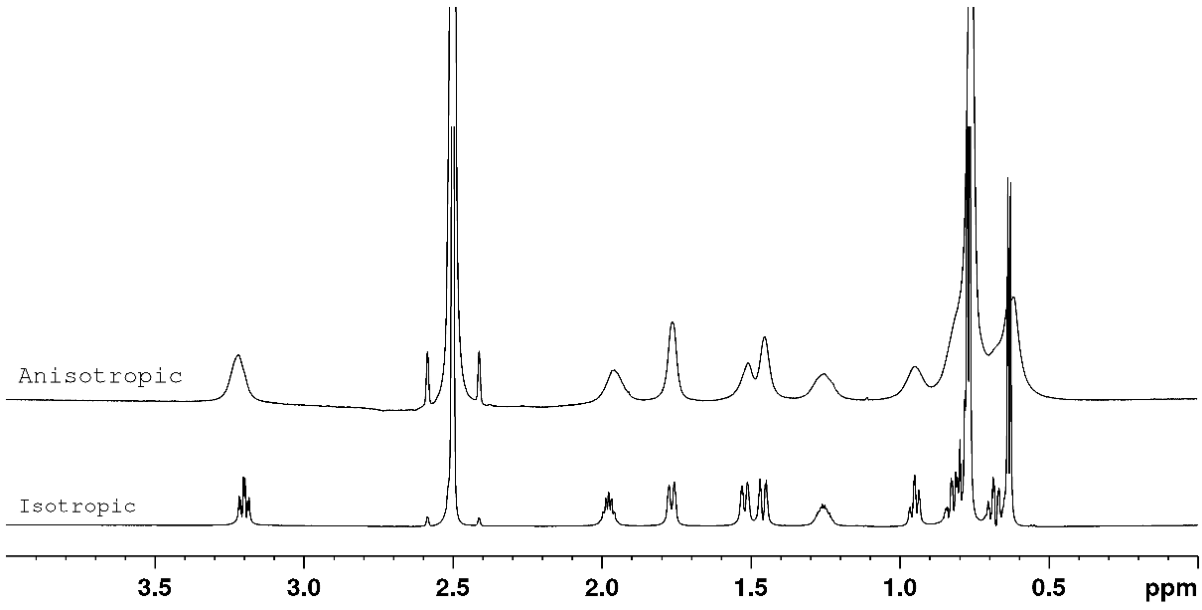

Figure 4.3. 1D ^1H NMR spectrum of menthol in 1:1 D_2O:DMSO-*d*6 compared to a corresponding sample with 1.6 mg/mL commercial GO illustrating the line broadening of signals upon addition of GO. Reproduced from [20] with permission from John Wiley & Sons.

RDCs were extracted via 2D CLIP-HSQC experiments, where the ^{1}H-^{13}C correlation peaks split with the size of their corresponding one-bond coupling constant in the direct (F2) dimension as illustrated in Figure 4.4. The same experiment was acquired for an isotropic menthol sample (i.e. without addition of GO) under otherwise same sample and experimental conditions. The RDCs were then obtained as the difference between the anisotropic and isotropic spectra as $^{1}D_{CH} = {}^{1}T_{CH} - {}^{1}J_{CH}$ for each resonance in the spectra. An example of measured RDCs is given in Table 4.2 and it can be noted that all the largest values correspond to axial protons in the stable chair form seen in Figure 4.5. The general uncertainty in measurement of RDCs is estimated to be ± 1 Hz.

A major drawback of extracting ${}^{1}J_{CH}$ / ${}^{1}T_{CH}$ in the F2 dimension is the interference from J_{HH}, which can cause broader linewidths and multiplets, hindering accurate measurements or increase the measurement uncertainty. The measurement of ${}^{1}J_{CH}$ / ${}^{1}T_{CH}$ in the indirect (F1) dimension is commonly used, though it can be challenged by methylene protons appearing as a sum of ${}^{1}J_{CHa} + {}^{1}J_{CHb}$.[153][154]

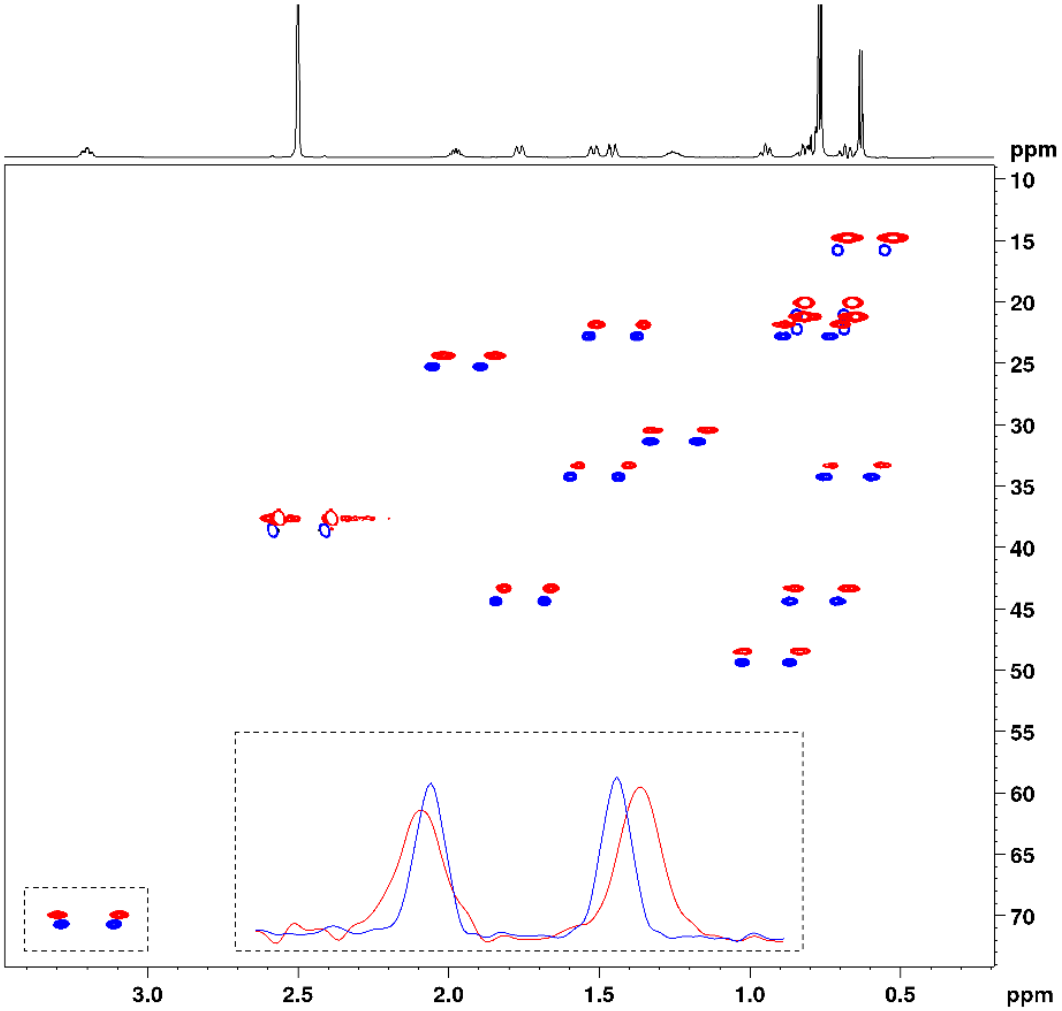

Figure 4.4. CLIP-HSQC spectrum of menthol (blue) and with 1.6 mg/mL commercial GO added (red) in 1:1 D_2O:DMSO-*d*6 at 800 MHz. 1D slices of the boxed signals are shown in the inset. J_{CH} and T_{CH} are measured between peak maxima. The red spectrum has been shifted slightly for clarity. Reproduced from [20] with permission from John Wiley & Sons.

Table 4.2. Size of experimental (D_{CH}) and back-calculated (D_{calc}) RDCs [Hz] for 6 mM menthol in 1:1 D_2O:DMSO-*d*6 with (T_{CH}) and without (J_{CH}) the presence of 1.6 mg/mL commercial GO solution. The missing values are due to distorted peak shape in the 1D traces hindering extraction of T_{CH}.

#	T_{CH}	J_{CH}	D_{CH}	D_{calc}
1	163.98	138.95	25.03	25.70
2a	123.57	128.51	-4.94	-3.09
2b	144.02	124.7	19.32	22.07
3	149.26	125.46	23.80	23.23
4a	129.56	127.94	1.62	1.86
4b		123.16		27.51
5a	125.65	127.86	-2.21	-3.74
5b	147.38	122.36	25.02	22.73
6	148.04	123.01	25.03	24.77
7	136.76	126.96	9.80	9.86
8	125.28	124.55	0.73	-
9	122.68	124.48	-1.80	-
10	135.39	125.24	10.15	6.89

3D structures of menthol were needed for back-calculation of RDCs to find the best fit to the experimental values. Computational modelling using force field methods resulted in a set of 8 conformers representing the conformational space displayed by menthol in solution. Conformers related to a chair-flip were not included as the chair form shown in Figure 4.5 was expected to be the most stable by far in the case of menthol, which was confirmed by examination of the J_{HH}-coupling constants. Each conformer was subsequently optimized by DFT methods before the structural ensemble was used for back-calculations of RDCs by SVD.[48] All methylene protons could be individually assigned based on analysis of *J*-coupling constants. Even without this information, the methylene protons could be assigned with a great level of confidence as the axial protons displayed similar RDC values due to their parallel orientation.[155][156] In cases where methylene resonances overlap, an average coupling constant can be extracted and used in the fitting of experimental data by calculating the theoretical average of the individual RDCs.[157] Methyl groups show one RDC as an average of the individual C-H vectors due to the free rotation around the C-CH_3 bond. In the fitting procedure this is handled by computing a virtual C-H vector pointing in the direction of the C-CH_3 rotation axis.[48] The RDCs for the methyl groups of the isopropyl group in menthol were not included in the calculations as they could not be individually assigned.

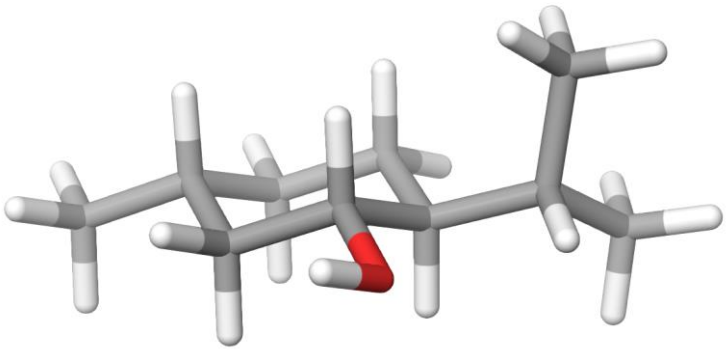

Figure 4.5. One of the DFT optimized menthol conformers used for back-calculation of RDCs.

The RDCs shown in Table 4.2 resulted in a Q factor of 0.099, the low value indicating good agreement between the input structures and the measured RDCs. In the following discussions of GO's alignment properties, the Q factor will be used as a practical indicator of the degree of alignment achieved in the various solutions. However, as the Q factor is only an indicator of the agreement between input structure(s) and RDCs, and not a direct measurement of the alignment, other factors such as the deuterium splitting or the size of the RDCs obtained for a given sample will also be included for a more nuanced discussion of alignment properties.

4.2 Factors affecting GO alignment

As discussed previously, GO sheet size and composition are dependent on several effects, which also influence their alignment properties in solution. Multiple factors are likewise relevant when examining GO solutions as alignment media for NMR structural analysis. Some factors have been explored in the following, where all RDCs and Q factors discussed are for menthol and acquired following the same methodology as was just described.

4.2.1 GO source

GO stock solution was initially synthesized in-house using a modified Hummers synthesis. Later GO was bought from a commercial supplier and this became the main GO source used in subsequent experiments. When referring to samples made from either of these aqueous stock solutions throughout this text, sGO will refer to GO synthesized in-house, while cGO will refer to commercially bought GO. The sGO was noted to produce a high amount of sedimentation, assumed to be residual multilayer fragments, though AFM measurements showed the single-layer nature of the sheets.[20] AFM images additionally revealed general GO sheet sizes in the range of 1-5 μm.

Sedimentation

Even stable GO solutions will over time show dark brown sediment, the degree of which seems to depend on solvent, pH, and GO properties like sheet size, composition, and amount of multilayer fragments.[158][159] Aqueous solutions of GO have been described to slowly degrade the material through a series of rearrangements of the oxygen functionalities on the sheets, resulting in expansion of the aromatic domains within GO[126], increasing the van der Waals attraction between the sheets and thus cause sedimentation. The term will here be used for the inherent GO trait to sediment over time, while other terms will be used to describe the response of GO to different chemical and mechanical manipulations.

The amount of sedimentation relative to dispersed material appeared to scale with the GO concentration and is therefore assumed not to be due to limited dispersibility. The sedimentation did not have an effect on the degree of alignment as seen by the constant deuterium splitting in Figure 4.6. The commercial GO produced samples with significantly less sedimentation and therefore required less material to obtain sufficient alignment.

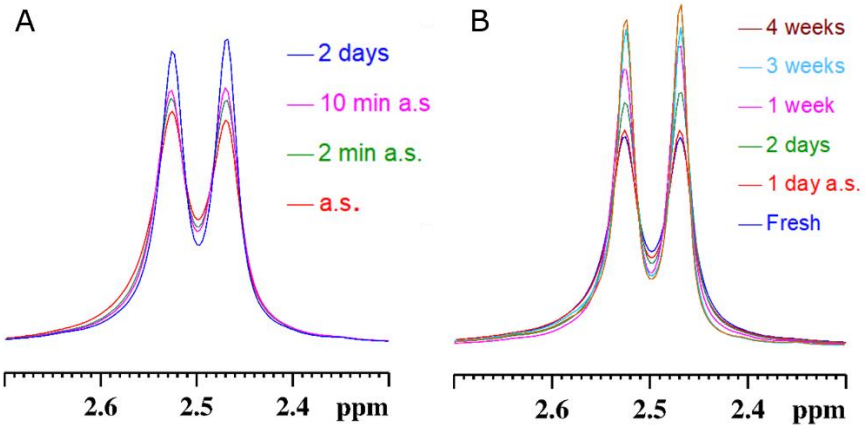

Figure 4.6. Overlay of 1D ^{2}H NMR spectra of a GO sample following its preparation, showing the deuterium splitting of the DMSO-*d*6 peak of 5.3 Hz over short and long time intervals. A) Immediate effect after shaking the sample (a.s., after shaking). B) Long-term effects of sedimentation. 8.23 mg/mL sGO in 1:1 D_2O:DMSO-*d*6 at 600 MHz, spectra acquired using the deuterium lock channel.

4.2.2 Time dependent stability

Abundant sedimentation may be seen under some experimental conditions, leading to concerns of sample stability. Figure 4.6 explores the short and long-term effects via the deuterium splitting, where the sedimentation appears to influence the peak shape, but not the degree of alignment. The peak sharpening trend was also observed in other types of NMR spectra acquired, with a general trend of better spectral quality seen a few days after sample preparation for samples of higher GO concentration. The direct alignment stability for dissolved compounds long-term was explored by repeated CLIP-HSQC experiments. As the long-term sedimentation of GO may be due to rearrangements of the oxygen groups, light sensitivity was also a factor to include.

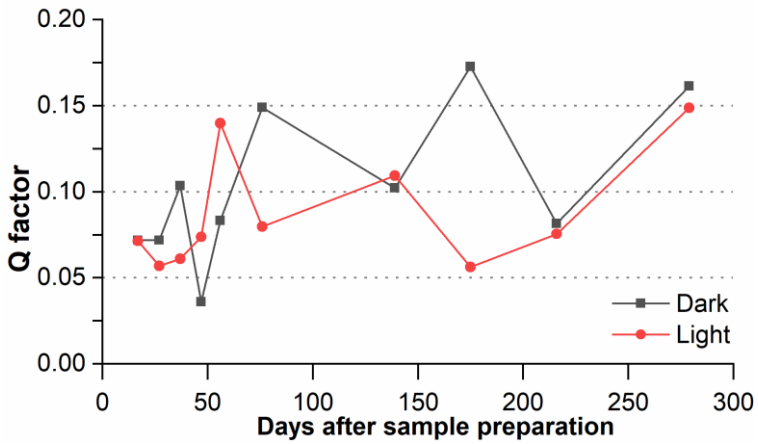

Figure 4.7. Q factors expressing the stability of two GO samples over time. One was exposed to natural light during storage (light) while the other was shielded (dark). Identical sample preparation of 4.1 mg/mL sGO in 1:1 D_2O:DMSO-*d*6 with 6 mM menthol. Reproduced from [20] with permission from John Wiley & Sons.

As expressed by the Q factors in Figure 4.7, the samples proved to be stable for more than 9 months when stored at room temperature. The RDCs for all protons are seen in Table 4.3 with an average value and average standard deviation for each proton. For both samples, the average of the standard deviations was 1 Hz.

The samples produced comparable average Q factors, proving that light sensitive is not a concern for sample stability under these conditions.

Dark: 0.103 ± 0.044

Light: 0.087 ± 0.034

If only data from the first 50 days are included, the average Q factors are 0.071 and 0.066 for the dark and light samples, respectively. The time span provides ample time to acquire any necessary NMR experiments. Typical experiment time for CLIP-HSQC experiments used here was app. 2 hours, but prolonged up to 15 hours when needed without using non-uniform sampling (NUS). Sample stability issues influencing data acquisition will depend on analyte stability and potential interactions that degrade the GO material.

Table 4.3: RDCs [Hz] over time and the associated Q factors. Gray and white cells refer to the "dark" and "light" sample from Figure 4.7, respectively. Sample preparation identical with 4.1 mg/mL sGO, 1:1 D_2O:DMSO-*d*6, 6 mM menthol. StDev=Standard deviation. Reproduced from [20] with permission from John Wiley & Sons.

Days	17	27	37	47	56	76	139	175	216	279	Average	StDev
1	8.78	6.62	7.74	8.24	7.98	8.96	8.03	7.95	9.50	10.83	8.46	1.14
2a	-0.91	-1.26	-0.64	-0.97	-1.79	-1.41	-1.56	-3.04	-1.74	-0.59	-1.39	0.72
2b	10.00	10.49	12.54	10.55	10.12	11.69	12.69	10.57	10.32	15.53	11.45	1.73
3	9.14	9.32	9.78	8.76	9.94	7.78	10.09	9.73	9.81	15.19	9.95	1.97
4a	1.69	1.37	1.55	0.97	1.80	1.21	1.51	0.37	-0.73	-0.92	0.88	0.99
4b	7.75	7.08	7.79	7.79	8.88	7.15	7.09	8.58	10.03	11.31	8.35	1.40
5a	-0.59	-0.83	-0.54	-0.27	-0.55	-0.33	-0.94	-0.96	0.62	-1.22	-0.56	0.51
5b	9.30	12.00	11.78	9.92	11.70	12.39	11.7	11.63	11.63	13.29	11.53	1.14
6	7.12	8.06	7.39	8.99	9.59	5.80	7.00	5.65	9.63	6.85	7.61	1.43
7	2.28	2.70	3.06	2.77	3.67	3.09	2.27	2.27	3.83	-0.37	2.56	1.17
8	0.78	0.86	0.82	0.77	0.49	0.80	0.65	0.72	0.68	0.63	0.72	0.11
9	-1.90	-1.69	-1.43	-1.81	-1.77	-1.72	-2.05	-1.98	-1.07	-2.18	-1.76	0.32
10	2.48	2.79	3.05	2.11	1.76	2.51	2.93	2.69	2.95	2.66	2.59	0.40
Q	0.072	0.072	0.103	0.036	0.083	0.149	0.102	0.173	0.082	0.161	0.103 ± 0.044	
1	8.85	10.38	8.71	9.69	10.64	9.22	10.61	10.75	10.85	10.64	10.03	0.84
2a	-1.95	-1.17	-1.64	-1.08	-1.69	-1.50	-1.64	-2.84	-3.20	-3.15	-1.99	0.79
2b	10.71	10.62	12.20	12.81	11.38	13.03	13.02	12.81	12.86	15.88	12.53	1.50
3	9.62	8.46	11.87	11.06	12.12	12.42	14.18	12.56	13.22	15.34	12.09	2.03
4a	1.48	1.90	1.60	1.72	1.50	1.86	1.18	1.61	0.85	-0.79	1.29	0.80
4b	7.69	8.60	8.43	9.08	9.69	7.38	9.63	10.07	8.62	12.76	9.20	1.52
5a	0.42	-0.69	-0.93	-0.43	-1.09	-1.17	-2.10	-0.88	-0.69	-2.43	-1.00	0.81
5b	10.99	12.30	13.17	13.20	14.28	11.65	14.25	11.77	11.94	14.91	12.85	1.32
6	9.08	9.06	9.44	9.07	7.78	8.15	9.71	11.11	12.08	9.39	9.49	1.28
7	2.45	3.37	2.28	2.12	2.74	2.13	3.48	0.99	0.92	3.70	2.42	0.96
8	0.64	0.70	0.26	-1.79	0.36	0.81	0.69	0.71	0.71	0.66	0.38	0.78
9	-1.68	-1.72	-2.28	0.35	-1.92	-1.08	-2.23	-1.97	-2.19	-2.21	-1.69	0.80
10	2.42	2.73	2.97	2.92	2.78	2.92	2.85	2.84	2.86	2.90	2.82	0.16
Q	0.071	0.057	0.061	0.074	0.140	0.080	0.109	0.056	0.075	0.149	0.087 ± 0.034	

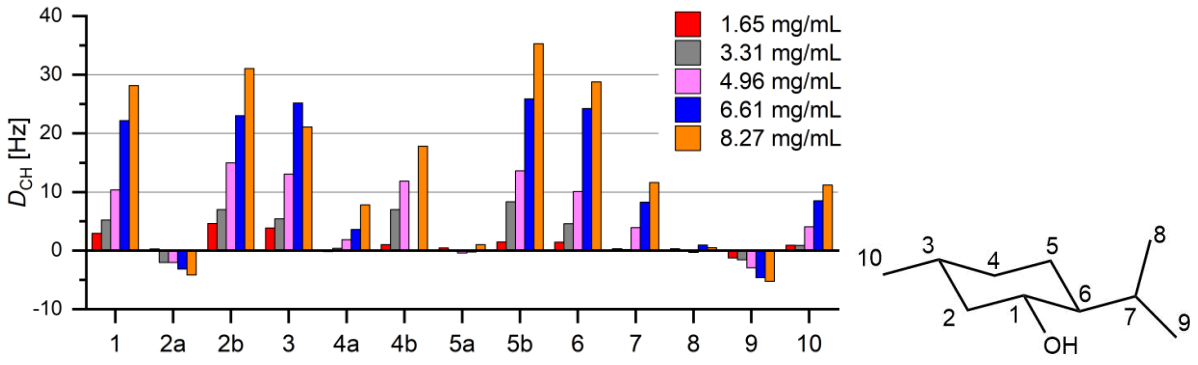

Figure 4.8. Size of measured RDCs dependent on GO concentration for the individual $^1D_{CH}$ of menthol.

4.2.3 Concentration

The color of GO solutions from yellow to dark brown is dependent on concentration and the same dependence is true for the degree of alignment.[160] This dependence is directly seen on the relative size of the RDCs for menthol as shown in Figure 4.8, where the effect is roughly linear with the largest effect seen for axial protons.

The concentration dependence also affect the calculated Q factor, but the effect does not scale linearly with GO concentration, see Figure 4.9. At low GO concentrations the RDCs almost disappear as seen in Figure 4.8 and the relative measurement uncertainty has a major effect resulting in higher Q factors. Maximum RDCs of 10-20 Hz generally resulted in good Q factors. With increased GO concentrations and observation of larger RDCs, peaks broadened and more often peak distortions hindering measurement occurred, which is reflected in the slight increase in Q factor in Figure 4.9.

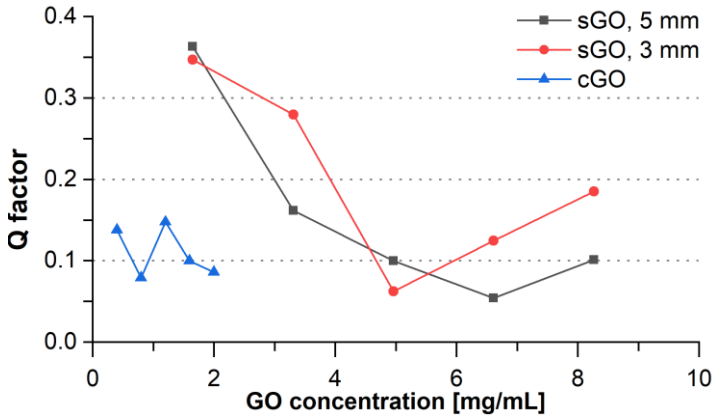

Figure 4.9. Influence of GO concentration on the measured RDCs expressed through the Q factor for samples with different sources of GO and NMR tubes. All samples in 1:1 D_2O:DMSO-*d*6. Reproduced with minor edits from [20] with permission from John Wiley & Sons.

With the low viscosity of GO solutions, preparation of samples in 3 mm NMR tubes was simple and provided similar results to conventional 5 mm samples. GO was applied for analysis of 2 mM menthol in a 3 mm sample, thus requiring minimal amount of solute. RDCs were extracted from spectra with an experimental NMR time of 2 days 10h (not applying NUS) and subsequent calculations resulting in an excellent Q factor of 0.071. Thus GO is applicable as alignment media also for limited amount of solute.

In line with cGO showing far less sedimentation, much less material was needed to achieve sufficient alignment. With the alignment effect of GO depending on multiple factors, reported GO concentrations necessary for alignment will undoubtedly vary. For cGO, the Q factors in Figure 4.9 do not show any trends, although the same effect on spectral quality was seen when varying the concentration and as reflected in the size of the measured RDCs shown in Table 4.4.

Table 4.4. Size of measured RDCs [Hz] relative to the amount of cGO in solution with 6 mM menthol in 1:1 D_2O:DMSO-*d*6. Missing values are due to distorted peaks in the 1D traces. Reproduced from [20] with permission from John Wiley & Sons.

#	2.0 mg/mL	1.6 mg/mL	1.2 mg/mL	0.8 mg/mL	0.4 mg/mL
1	24.76	25.03	16.14	11.04	4.02
2a	-5.73	-4.94	-4.04	-2.40	-0.35
2b	23.90	19.32	17.33	11.52	3.13
3		23.80	13.22	13.63	2.84
4a		1.62	3.08	3.96	3.18
4b			20.46	10.07	6.48
5a	-2.83	-2.21	-1.08	-1.39	-0.82
5b	32.23	25.02	20.27	14.21	2.67
6	28.45	25.03	13.62	11.33	3.90
7	5.95	9.80	5.05	3.72	1.49
8	1.25	0.73	0.79	0.11	0.05
9	-2.61	-1.80	-1.65	-1.53	-0.95
10	10.85	10.15	7.45	5.06	1.38
Q	0.086	0.099	0.147	0.079	0.137

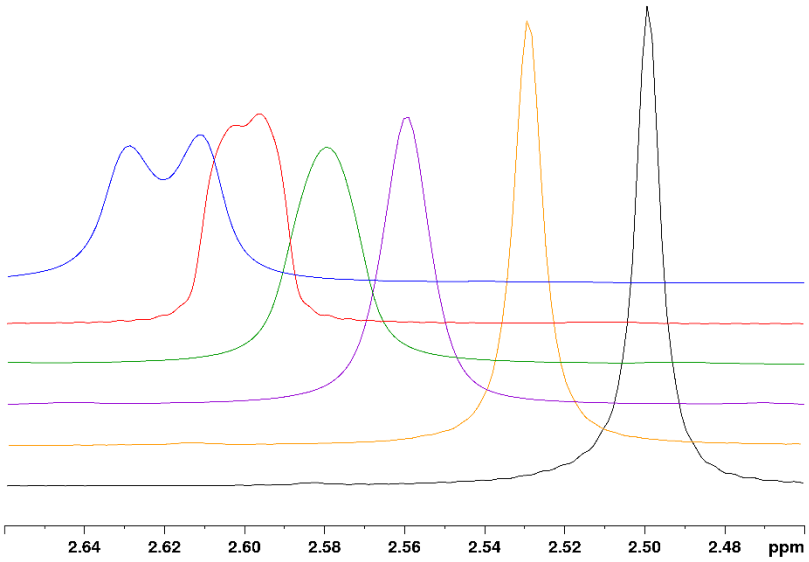

Figure 4.10. Overlay of 1D ^{2}H NMR spectra showing the DMSO-*d*6 peak for the varying concentrations of cGO from Table 4.4 compared to an isotropic sample (in black). Largest deuterium splitting seen here is 2.2 Hz. The spectra have been offset from the isotropic peak referenced at 2.50 ppm for clarity.

As mentioned in Chapter 2, the deuterium splitting is commonly used to assess the alignment degree for different alignment media. However, as seen in Figure 4.10, a broadening of the deuterium peak without clear split can indicate sufficient alignment for GO samples. For this reason, deuterium splitting have not been used routinely to discuss alignment properties throughout this project, though ^{2}H NMR spectra were acquired for all samples. When deuterium splitting was observed, it was related to the organic solvent peak and hardly ever for the D_2O peak.

4.2.4 Solvent

The dispersibility and ability of GO to form LCs were discussed in Chapter 3 as being highly dependent on solvent, with water as the preferred media. Variation of solvent composition was therefore expected to have an effect on the alignment properties of GO. The size of the RDCs proved to scale with the water content in solvent mixtures with various organic solvents as seen in Figure 4.11. Higher water content was not pursued due to the limited aqueous solubility of menthol.

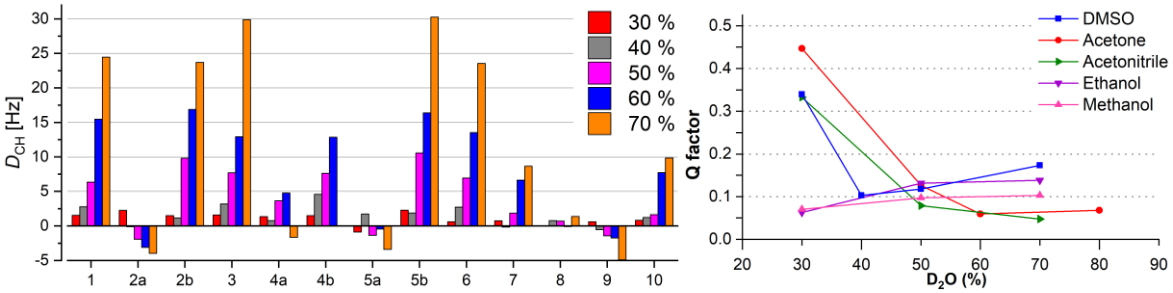

Figure 4.11. Left: Solvent effect on the measured RDCs for menthol in cGO D_2O:DMSO-*d*6 mixtures relative to the D_2O content. Right: Correlation between Q factor and relative amount of D_2O in solvent mixtures with selected deuterated polar organic solvents using. Reproduced from [20] with permission from John Wiley & Sons.

Although GO LCs have been reported in solvent such as DMF and DMSO[146][147], alignment of menthol was not observed in organic solvents without including a significant amount of water, as seen by the high Q factors at low water content in Figure 4.11. The Q factors of ethanol and methanol are exceptions to this trend, though the size of RCDs extracted at 30 % D_2O likewise had decreased drastically for both solvents with maximum RDC of 3.22 and 5.68 Hz for ethanol and methanol, respectively. Similar to the observations at increased GO concentrations, increased water content in solvent mixtures resulted in larger RDCs, but also broader or distorted peaks and consequently slightly higher Q factors due to uncertainty of $^1T_{CH}$ / $^1J_{CH}$ measurements with broader linewidths. A 50 % water content mixed with DMSO-*d*6 became the standard in subsequent experiments as it provided an optimum between fitting size of RDCs and sharp peaks. In keeping the solvent composition constant, the GO concentration becomes a main factor of comparison in the later discussions.

Varying the organic component of the solvent mixture did not appear to alter the alignment direction as seen by the similarity of measured RDCs. Calculations of the generalized angle[46] between alignment tensors for different solvent mixtures displayed small variations, which correlates with the observations of relative D_2O content being the deciding factor for the strength of GO alignment.[20]

Definition: Solubility or dispersibility?
Even though GO is at times described to be *soluble* in different solvents, given the size and nature of GO, the solutions may more accurately be called colloidal suspensions with GO sheets being *dispersed* in a given solvent. The differentiation serves another purpose here, as the ability of GO to induce alignment of other compounds is the focus, and discussions therefore includes considerations of the solubility of these compounds. Thus, this text aims for consistency in debating the *dispersibility* of GO and *solubility* of the analyzed compounds.

4.2.5 Resdispersion of dried GO

Lyophilization was used to determine concentration of GO or functionalized GO stock solutions (as a standard performed in triplicates). The lyophilized metallic-brown, porous material seen in Figure 4.12, was used directly for IR measurements by attenuated reflectance IR spectroscopy.

Figure 4.12. Left: Lyophilized GO. Right: Redispersion of lyophilized GO in 1:1 D_2O:DMSO-*d*6 compared to GO dried as a film.

GO dried by lyophilization was redispersible in both D_2O and D_2O:DMSO-*d*6 mixtures. Depending on the material and concentration, full redispersion often took hours and the process could be aided by short sonication. GO dried as a dark brown film under insufficient vacuum and would then not redisperse in solution even with extended sonication as seen in Figure 4.12.

Table 4.5. RDCs [Hz] of 16 mM menthol in 1:1 D_2O:DMSO-*d*6 aligned by redispersed cGO compared to conventional sample prepared by centrifugation. The missing values are due to distorted peak shapes in the 1D traces hindering extraction of T_{CH}.

#	2 mg/mL redispersed cGO	2.0 mg/mL cGO
1	21.51	24.76
2a	-4.99	-5.73
2b	26.18	23.90
3	16.98	
4a	8.96	
4b	15.34	
5a	-2.44	-2.83
5b	30.52	32.23
6	29.93	28.45
7	11.25	5.95
8	0.62	1.25
9	-3.58	-2.61
10	10.27	10.85
Q	0.088	0.086

Along with the redispersion, GO regains it LC structure and ability to function as alignment media. For a redispersed sample, the extracted RDCs of menthol seen in Table 4.5 were consistent with values acquired from a corresponding conventionally prepared sample. Lyophilization and redispersion of GO is another potential route to sample preparation with good control of solvent composition and concentration.

4.3 Other properties affecting GO

4.3.1 Temperature

Experimental time for acquisition of anisotropic spectra data may span hours (or days), increasing the requirements for GO stability at raised temperatures. The stability and conservation of GO sheet structure become an even larger concern when working with GO functionalization, as will be discussed in the following chapters. Lei *et al*. reported that the deuterium splitting of GO, and thus presumably its alignment properties, are stable at temperature intervals of 5-80°C.[160] However, deuterium spectra will typically be acquired quickly and therefore an experimental setup that tested the preservation of GO alignment properties after longer times at elevated temperatures were designed.

Aqueous cGO solution (50 mL, 0.4 mg/mL) was heated and 3 mL samples extracted sequentially after the time intervals at the different temperatures listed in Table 4.6. The brown GO solution darkened in color during the heating, but stayed fully dispersed during the entire period. The extracted GO samples were exchanged to 1:1 D_2O:DMSO-*d*6 solvent with addition of menthol, followed by acquisition of CLIP-HSQC data at 298 K. The GO concentration of each sample was 2.4 mg/mL based on the initial stock solution. The cGO concentration was above the tested concentrations described previously and the degree of alignment expressed via RDC_{max} increased correspondingly while lowering spectral quality.

Table 4.6. GO alignment stability over different temperatures expressed subsequently via Q factors for menthol. RDC_{max} is the largest RDC measured for each sample.

Sample	Temperature [°C]	Time [h]	RDC_{max} [Hz]	Q factor
1	40	1.5	41.84	0.123
2	40	2.5	37.99	0.110
3	50	2	42.43	0.128
4	60	2	42.29	0.187
5	70	2	43.82	0.090
6	80	2	41.59	0.077

Temperatures up to 80°C do not destroy the GO LC formation as seen by the acquired RDCs and corresponding Q factors in Table 4.6. The solution changed color to almost black during the first time interval at 40°C, indicating structural changes leading to expansion of the sp^2 hybridized domains. Often any changes leading to enhanced aromaticity are described as reductions of GO in literature, however no reduction agent has been added. The effect may be described as a series of rearrangements of the oxygen functional groups on the GO surface causing overall deoxygenation (decrease of oxygen functionalities and increase of C=C domains) of GO.[126]

4.3.2 Salts and acids

The stability and LC structure of GO solutions are in part due to the electrostatic repulsion between the negatively charged sheets. Therefore, if cations screen the charges, attractive van der Waals interactions between sheets dominate, which interrupt the LC formation and lead to aggregation.[145]

Aggregation
In contrast to sedimentation, which is used to describe a long-term effect (hours or days), aggregation is used to describe an immediate reaction (seconds) from a homogenous GO solution to visible GO aggregates in response to changes. These aggregates would initially be dispersed, but may have precipitated over time. Aggregation of GO was seen due to e.g. pH changes, addition of salts, or interactions with reagents, forming different types of aggregates ranging from small, just visible particles to large, flocculent agglomerates.

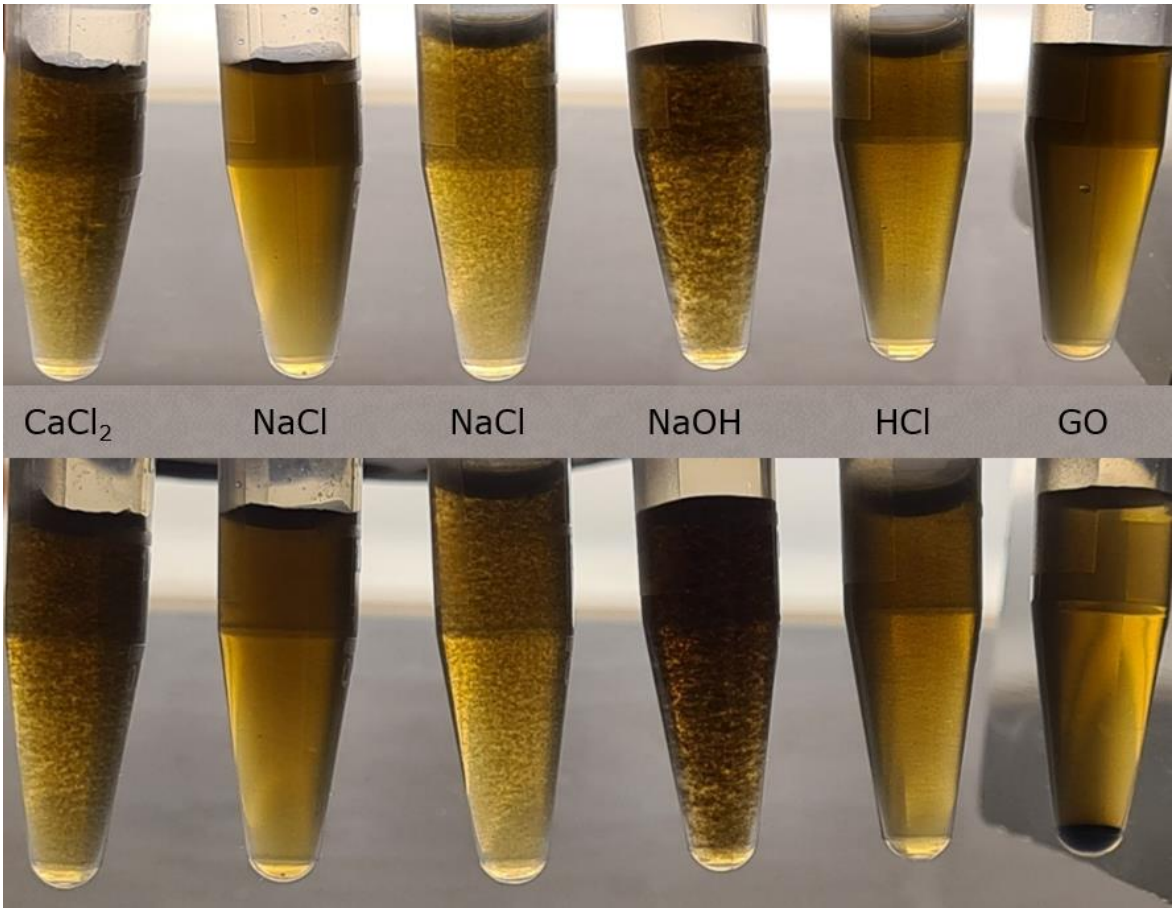

Figure 4.13. Effect of ion strength and pH on 0.4 mg/mL cGO solutions. From left to right: 0.020 M $CaCl_2$, 0.020 NaCl, 0.17 M NaCl, 0.14 M NaOH, 0.020 M HCl, and a sGO reference. Top picture immediately following addition, bottom picture same solutions after 1 day.

Ca^{2+} destabilized GO at a far lower concentration than Na^{+} ions as seen by the aggregation in Figure 4.13. This may be explained as the divalent calcium ions interacting more strongly with GO and screening the negative charges.[144] GO has been studied for its sorption capacity towards various cations.[161] Due to the effect of salts, Milli-Q water was used for all GO solutions and reactions.

The destabilization effect of salts should be kept in mind if GO is to be used as alignment media in buffered solution or for compounds analyzed as salts. Surfactants can stabilize the GO LC in solutions of higher ion strength and wider pH range, but have not been tested for alignment purposes.[162]

Upon addition of HCl to pH 1-2, small aggregates were seen (only just noticeable in Figure 4.13), which were very different from the flocculent aggregates formed upon addition of NaCl, $CaCl_2$ or NaOH. The presence of acid or salts prevent sedimentation, even at concentrations that does not induce visible aggregation. This may be explained by a dynamic presence of oxygen functionalities that respond to conditions of the solution.[126][163] The effects of base like the color change in Figure 4.13 will be discussed in detail in Chapter 6.

4.3.3 Two phase systems

In the above, GO has been discussed in aqueous solutions or in solvents miscible with water. In two phase systems, GO forms Pickering emulsions, where droplets are stabilized at the interface due to the amphiphilic nature of GO.[164] The preference of GO for either phase can be tuned by varying the pH of the aqueous phase as seen in Figure 4.14. With increased pH, the acidic groups on GO are deprotonated, making GO more hydrophilic. At low pH the functionalities on GO are fully protonated, which increase the sheet hydrophobicity.

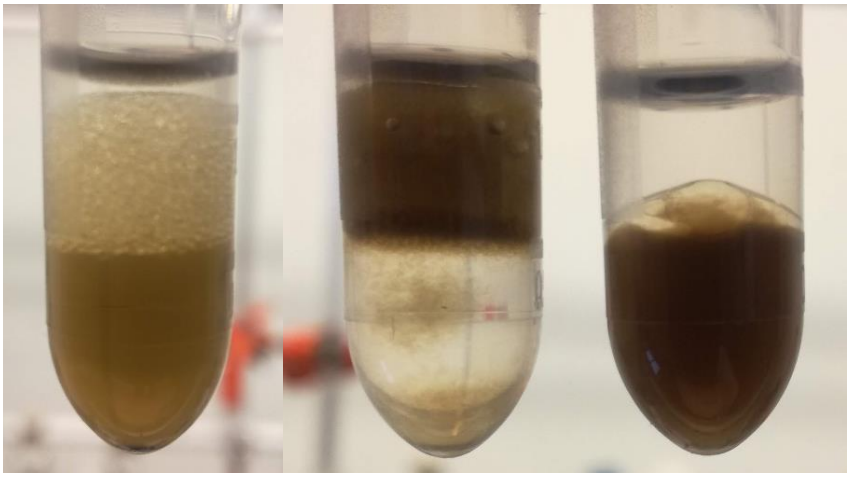

Figure 4.14. Left: GO in water/ethyl acetate mixture. Middle: addition of HCl until acidic pH causes the GO to move to ethyl acetate phase. Right: addition of NaOH until basic pH causes the GO to stay in the water phase.

Separation of GO from analytes or surplus reagents could feasibly be achieved by extraction and manipulation of pH, depending on compound properties. Alterations of the GO structure as a side effect of pH changes would be a factor to consider.

4.3.4 Ultrasonication

The use of sonication is often encountered both in the synthesis of GO and GO functionalization. In GO synthesis it is used to aid or initiate the exfoliation from the multi-sheet graphite oxide to single layer GO. Sonication is a factor in controlling the size of the produced GO sheets as it also causes the sheets to fragment and not just exfoliate.[165–168] In GO functionalization, sonication may be used to re-exfoliate GO derivatives after reaction[169] or with the explicit goal of reducing the GO sheet size.[9][159][170] In this study the use of sonication has been limited, and besides for GO synthesis, it has been used sparingly in redispersion efforts. The sonication time has often been kept short to limit the fragmentation of GO sheets, as large changes in sheet size would otherwise be another major factor influencing sample preparation and alignment properties.

4.4 GO alignment of other test compounds

4.4.1 Alignment and recovery of Me-α-Glc

An obvious class of water-soluble compounds with defining stereochemistry is carbohydrates. The induced alignment by GO solutions were tested with the monosaccharide methyl-α-D-glucopyranoside (Me-α-Glc) in D_2O. The NMR spectra showed the same type of broadened peaks as seen for menthol, with extraction of RDCs resulting in a Q factor of 0.177. After NMR acquisition, the solvent of the GO sample was repeatedly exchanged with fresh D_2O by centrifugation until ^{1}H-NMR spectra of the supernatant showed no peaks from Me-α-Glc. As the collected supernatants contained traces of GO, they were purified by filtration on a 0.2 μm Omnipore filter before the liquid was evaporated. NMR analysis confirmed that Me-α-Glc had been recovered with only minor impurities as seen in Figure 4.15.

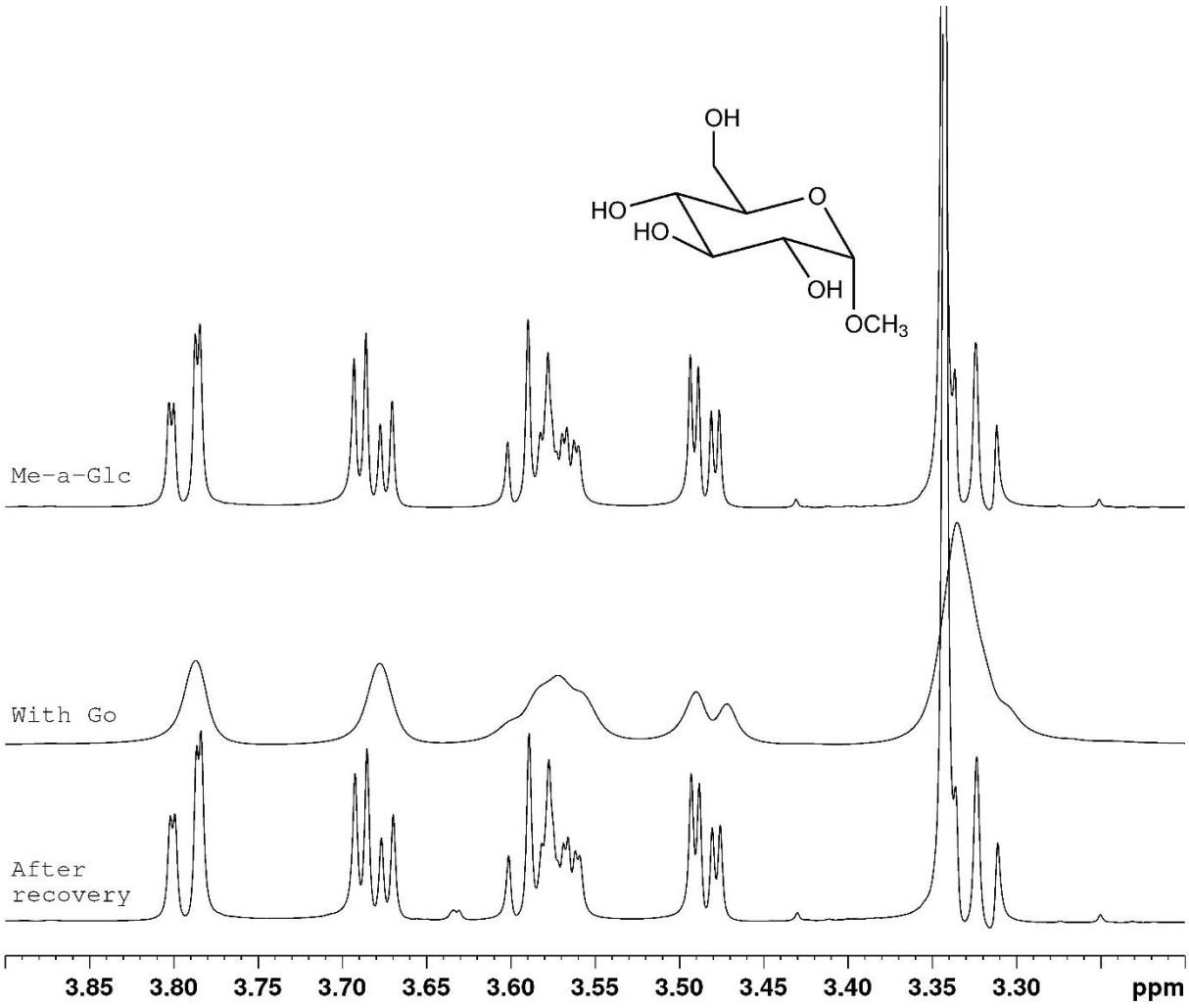

Figure 4.15. Overlay of ^{1}H NMR spectra of Me-α-Glc in D_2O with 4 mg/mL concentrated cGO and after recovery of Me-α-Glc compared to the pure compound. A peak at 4.73 ppm is excluded as it overlaps with water.

4.4.2 No enantiodiscrimination of pinanediol

The structure of GO is not inherently chiral, but Xu and Gao reported that it formed chiral liquid crystals.[171] GO was tested for enantiodiscriminative abilities by measuring the alignment of each enantiomer of pinanediol with comparison to a racemic mixture. However, GO showed no distinct discrimination as the RDCs in Figure 4.16 are comparable for both enantiomers and a racemic mixture of pinanediol (within measurement uncertainties). Thus, extra effort is needed for GO to assign absolute structures of compounds.

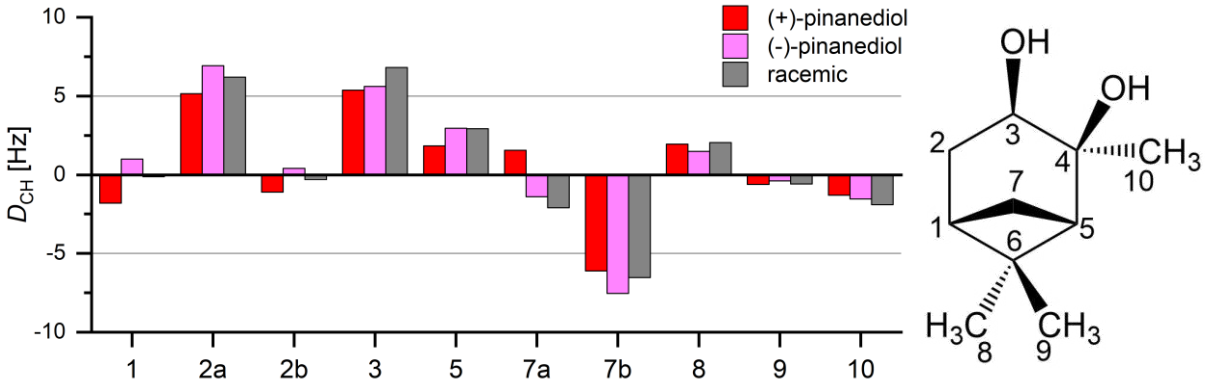

Figure 4.16. Extracted RDCs for each enantiomer and a racemic mixture of 4 mM pinanediol in D_2O:DMSO-*d*6 with 8.27 mg/mL sGO.

In addition, the dependence on GO concentration was also investigated for pinanediol and the results seen in Table 4.7. The degree of alignment displays similar dependence on GO concentration for pinanediol as previously shown for menthol. However, for pinanediol higher degree of alignment is needed before the RDCs obtain sizes significantly above measurement uncertainties.

"The lowest Q factor of 0.043 was seen for the highest tested GO concentration of 8.27 mg/ml. At this concentration, the maximum observed RDC was 35.27 and 6.65 Hz for menthol and pinanediol, respectively. From this, it is clear that the degree of alignment of each compound is different. The aligning interaction between the solutes and GO is assumed to be mostly steric, and in this case, the more spherical shape of pinanediol is very different from the flatter conformation of menthol." – Pedersen *et al.*[20]

Table 4.7. Size of measured RDCs [Hz] and corresponding Q factors for 4 mM (+)-pinanediol, relative to sGO concentration in 1:1 D_2O:DMSO-*d*6. Reproduced from [20] with permission from John Wiley & Sons.

#	2.07 mg/mL	4.13 mg/mL	6.20 mg/mL	8.27 mg/mL
1	-0.27	-0.21	-0.78	-0.46
2a	0.75	0.65	2.99	5.98
2b	0.21	-0.26	-0.63	-0.66
3	-0.48	1.08	2.81	6.65
5	-0.35	0.19	0.72	2.21
7a	0.11	0.93	-0.31	-2.41
7b	-0.24	-1.30	-3.37	-6.23
8	-0.09	0.59	1.44	1.93
9	-0.38	-0.28	-0.45	-0.74
10	-0.04	-0.52	-1.00	-1.52
Q	0.886	0.201	0.151	0.043

4.5 Conclusion

The stability of GO samples was documented by repeated measurements for samples over a time period of several months, monitored by measurements of RDCs and calculations of Q factors using menthol as model compound. The degree of alignment in GO solutions was seen to increase with the GO concentration, expressed by the size of measured RDCs and observations of the effect on the DMSO-*d*6 peak in ^{2}H NMR spectra. The effects of varying the solvent composition of GO solutions were examined for multiple aqueous mixtures with polar organic solvents. All solvent mixtures displayed increased degree of alignment with increased water content.

Various aspects related to sample preparation of GO solutions were explored and the results included the effect of elevated temperatures, lyophilization with subsequent redispersion, GO solution stability upon pH changes and addition of salts. It was shown that the monosaccharide Me-α-Glc could be recovered after acquisition of anisotropic spectra in GO solution, making the use of GO for analysis a non-destructive method. A major feature of the acquisition of anisotropic NMR information is the possibility of enantiodiscrimination. GO is not inherently chiral and therefore cannot be applied to distinguish between enantiomers, which was shown by comparison of RDCs extracted for each enantiomer and a racemic mixture of pinanediol.

4.6 Experimental

Information regarding instrumentation and acquisition of NMR spectra are found in appendix.

Materials and chemicals

Powdered graphite from Sigma Aldrich (particle size <20μm).
Commercial GO stock solution 0.4 w% and concentrated 2.5 w% from Graphenea.[172] Unless otherwise stated, cGO refers to the 0.4 w% solution.
All other chemicals were from Sigma Aldrich and used as received.

Synthesis of GO

GO was prepared by a modified Hummers' synthesis following a methodology developed in the group of Jingding Zhang. Powdered graphite was oxidized in two steps with subsequent sonication and dialysis to obtain a GO stock solution dispersed in water.

Pre-oxidized graphite

$K_2S_2O_8$ (2.5 g, 9.2 mmol) and P_2O_5 (2.5 g, 17.6 mmol) were dissolved in 15 mL H_2SO_4. 5.0 g graphite was added, which resulted in a viscous solution. The solution was stirred for 3 hours at 80°C. When the solution had cooled to room temperature, 120 mL water (Milli-Q, 0.05 μS/cm) was slowly added. The solution was filtered and the collected pre-oxidized graphite was washed with Milli-Q water until the filtrate had neutral pH. The solid was dried overnight at 50°C.

Graphene oxide

The pre-oxidized graphite was ground into a fine powder and 1.0 g was dispersed in 23 mL H_2SO_4 in an ice bath. $KMnO_4$ (3.0 g, 19 mmol) was added very slowly (over 30 min) while monitoring that the temperature of the solution stayed below 20°C. The mixture was heated to 35°C for 2 hours, during which the solution changed color from green-black to dark brown. Milli-Q water (50 mL) was added slowly and the solution stirred for 15 min at 35°C before additional 140 mL Milli-Q water was added. Excess $KMnO_4$ was reduced by addition of sufficient H_2O_2, estimated by noting a color change to green-brown and the development of gas upon addition ceasing. The room temperature solution was vacuum filtered on two Omnipore filter papers (hydrophilic, 0.2 μm pore size, 47 mm diameter) under continuous stirring and washed with 250 mL 1 M HCl. The entire filtration process took 3-4 hours. The solid was dispersed in app. 200 mL Milli-Q and sonicated for 2 hours in ice-water. The solution was centrifuged at 500 rpm (28 rcf) for 5 min and the sedimented solid discarded. The supernatant was then centrifuged at 12'000 rpm (15938 rcf) for 30 min. The new supernatant contained small graphene oxide sheets (<1 μm diameter) and was collected separately. Graphene oxide (GO) solution was obtained by redispersion of the solid in app. 100 mL Milli-Q water. The GO solutions were then purified of residual ions by dialysis using a cellulose membrane (MWCO 12000-14000). The Milli-Q water outside the membrane was changed 1-2 times a day for 8 days.

Simulations

Maestro suite version 11.6.013(2018-2) by Schrödinger with the program MacroModel was used to generate structures by force field calculations. A conformational search was performed using the force field MMFFs (water solvent), PRCG minimization, mixed torsional/low-mode sampling, 10’000 steps and an energy cutoff of 21 kJ/mol.

DFT calculations were performed using Gaussian version 09 revision B01 for optimizing the output structures from the conformational search with B3LYP/6-31G(d). Subsequent calculations of NMR shielding tensors used MPW1PW91/6-311+G(d,p) with GIAO. All DFT calculations used the PCM-SCRF model for implicit solvent water.

MSpin version 2.3.4-776, 2019, by MestReLab Research S. L. was used for RDC back-calculation using SVD and single tensor computation with averaging used for distinguishable methyl groups.

5 GO functionalization part 1: Amidation

With the diverse chemical structure of GO, a multitude of modifications could be envisioned and nearly as many has been tried.[173–176] Zong *et al.* described how GO grafted with polymer brushes could align compounds in DMSO, proving that modifying GO can enhance its utility as alignment media.[9][10] The grafting was achieved using free radical polymerization from the monomer trifluoroethyl methacrylate[9], however the procedure did not quantify the extent of grafting. A synthesis strategy based on radical polymerization was not pursued here in favor of strategies that theoretically allowed for greater control of the degree of functionalization and tuning of product properties.

A common strategy for GO functionalization aims to utilize the carboxylic acid groups at the edges of GO flakes and holes within the sheets. Likewise, this was the first synthesis strategy pursued for this project with initial experiments inspired by previous results in the group of Jingdong Zhang.[169] Here the amino acid cysteine was coupled to the GO carboxylic acids using the coupling reagents 1-ethyl-3-(3-dimethylaminopropyl)carbodiimide (EDC) and *N*-hydroxysuccinimide (NHS) well known from peptide synthesis.[177][178] A generalized reaction mechanism for the amide bond formation is shown in Figure 5.1.

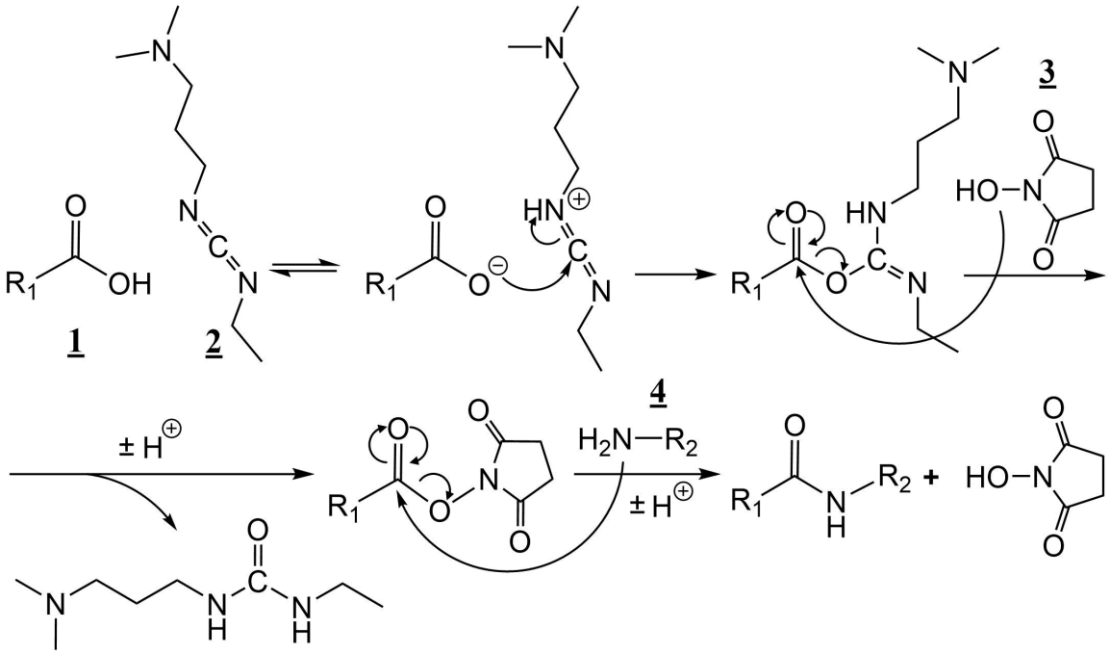

Figure 5.1. Mechanism of amide formation between carboxylic acid (1) and amine (4). The carbodiimide (2) is attacked by the deprotonated acid forming a reactive intermediate, which is exchanged with a coupling activator (3) forming an activated ester. Upon addition of amine, an amide bond can form instead and the activator is released. R_1 = GO, R_2 = amine.

The amide coupling is pH sensitive, thus the reaction is frequently carried out in buffered solutions.[177][179] This reaction is in some instances run in organic solvent under dry conditions to avoid hydrolysis of the carbodiimide or the intermediates.[180] In some cases, a coupling activator is omitted and the reactive intermediate reacts directly with the added amine. Amide formation on GO has also been reported using other synthetic routes, e.g. via an acid chloride intermediate.[181]

Amidation on GO has been reported with amines from a wide size distribution ranging from amino acids to proteins and polymers.[169][179][181–184] This promised a broad scope of potential GO derivatives, enabling fine-tuning of functionalized GO alignment properties. Important parameters would be: improved dispersibility and LC formation in organic solvent, compatibility and stability towards chemical conditions and compound classes, and potential enabling of enantiodiscrimination when used as alignment media in NMR analysis. The latter was of special interest and would be pursued by introducing amines containing one or more stereocenters, creating a chiral sample environment when GO partially aligns in a magnetic field.

5.1 GO-Tyr

Inspired by earlier work in the group of Jingdong Zhang on GO functionalized with cysteine[169], tyrosine was chosen for the initial reactions. *L*-Tyrosine is cheap, non-toxic, inherently chiral, and was preferred over cysteine due to the ease of characterization through recognizable double intensity doublets in the range of 6-8 ppm in ^{1}H-NMR spectra. The product of functionalization, GO-Tyr, is illustrated in Figure 5.2.

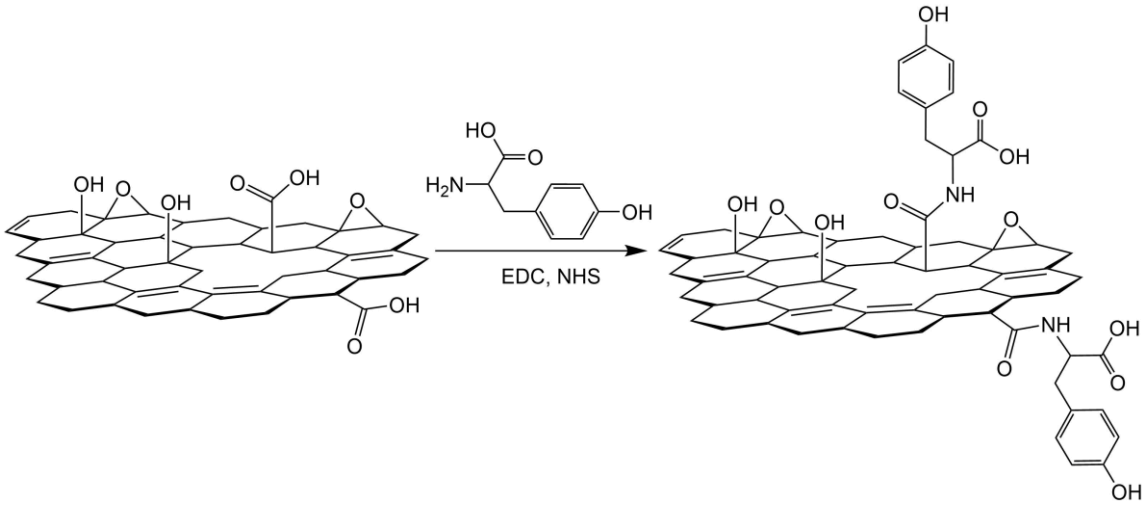

Figure 5.2. Synthesis of GO-Tyr utilizing the presence of carboxylic acids. The other functional groups on GO were assumed not to participate in any reaction.

5.1.1 Results and discussion

The functionalization of GO with tyrosine was initially tested using EDC and NHS, followed by coupling with tyrosine at 80°C. The reaction was first tried in water and later phosphate-buffered saline (PBS). In either case, the produced GO-Tyr was not dispersible in water or 2:3 mixtures of H_2O:DMSO-*d*6. Due to heavy aggregation noted during synthesis and the indispersibility of the products from reaction in aqueous solution, functionalization was tried in DMF at room temperature.[185][186] Alternative coupling reagents such as *N*,*N*'-diisopropylcarbodiimide (DIC) and ethyl (hydroxyimino)cyanoacetate (Oxyma) were tried in parallel.[177][187][188] In all experiments, the product was a black, indispersible material. It should be noted that both cysteine and tyrosine have been reported to reduce GO.[189][190]

Challenged by the low solubility of tyrosine[191], many purification procedures were tried. It was found that a 0.1 M NaOH solution raised the solubility of tyrosine drastically and

subsequent purification with sodium hydroxide removed remaining excess tyrosine, verified by ^{1}H NMR analysis. It was assumed that any covalently bound tyrosine would not be affected by sodium hydroxide at this concentration at room temperature.

In both this and the original study[169], unprotected amino acids were used, meaning polymerization of the amino acids may occur, forming free peptides that might be extremely difficult to separate from the GO in the purification process. Polymerization could also promote aggregation by cross-linking GO sheets. If polymerization was to be avoided, protection of the carboxylic acid within the amino acid is necessary using e.g. tButyl esters[192] or changing activation strategy to e.g. an acid chloride intermediate[181][185].

An additional reason for the indispersibility of the formed GO-Tyr could be due to the aromaticity of tyrosine acting as an interaction partner between neighboring GO sheets through π-π stacking, promoting aggregation and precipitation. Non-covalent interaction between Tyr and GO has been described.[193][194]

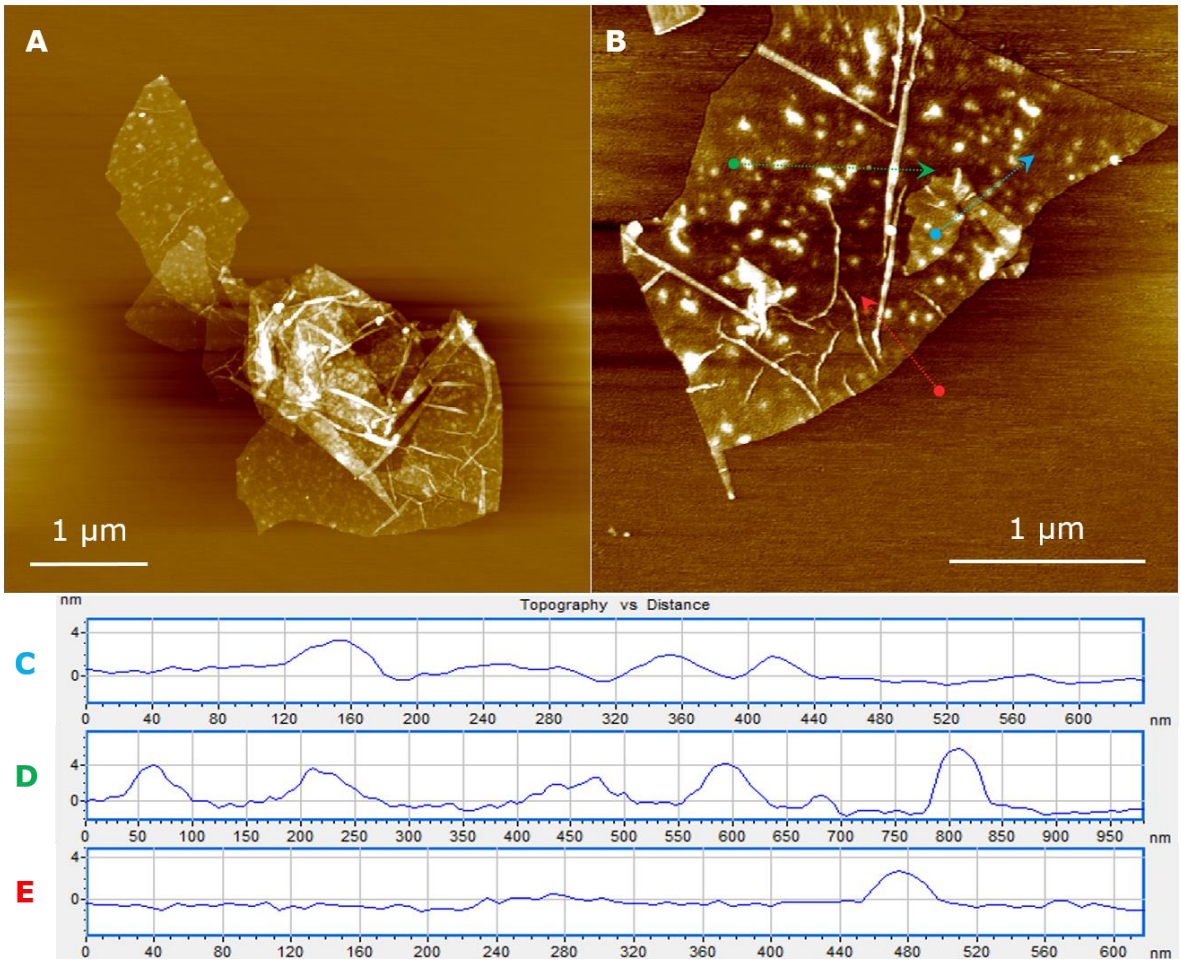

Figure 5.3. Example AFM images of GO-Tyr (made in DMF) on mica substrate. Note the different scales; A 5x5 µm, B 3x3 µm. C, D, and E: Contour height along the colored arrows marked in B.

AFM images as exemplified in Figure 5.3A displayed the aggregated nature of GO-Tyr in stark contrast to the smooth single layered sheets of GO as seen in Figure 3.3. The GO-Tyr material was found as aggregates often reaching heights of 20-30 nm. The detailed AFM image in Figure 5.3B revealed wrinkles and islands with heights up to 4 nm and 50-100 nm wide on the GO-Tyr surface, which appeared different from small debris also visible on the sheet surface. These islands had appeared as a result of the GO-Tyr synthesis, but this AFM analysis was unable to distinguish between adsorbed and covalently bonded tyrosine or other compounds present during synthesis.

All variations of GO-Tyr synthesis resulted in black, indispersible materials, independent of reagents and solvent used. Thus, the produced materials were of no interest as alignment media and further analysis and characterization efforts were not pursued.

5.2 GO-PEG

To avoid concerns of polymerization and π-π stacking, two simple amine polyethylene glycol (PEG) chains were chosen for the amidation. Functionalization with PEG (PEGylation) has commonly been used to alter the solubility of compounds due to its compatibility with water and multiple polar organic solvents.[177][195][196] NH_2PEG_3tBu was chosen as the tert-butyl group is seen as a high-intensity singlet in ^{1}H-NMR making its presence simple to monitor. Even if covalently bonded, PEG could be tumbling quickly in solution due to the large degree of freedom of the chain compared to the relatively stationary GO sheets. Consequently, the tert-butyl group could conceivably be visible in NMR spectra, opening possibilities of confirming the bonding to GO and provide quantitative measurements on the reaction yield via NMR. In addition, the $NH_2PEG_3NH_2$ would provide a "handle" for further chemical functionalization.

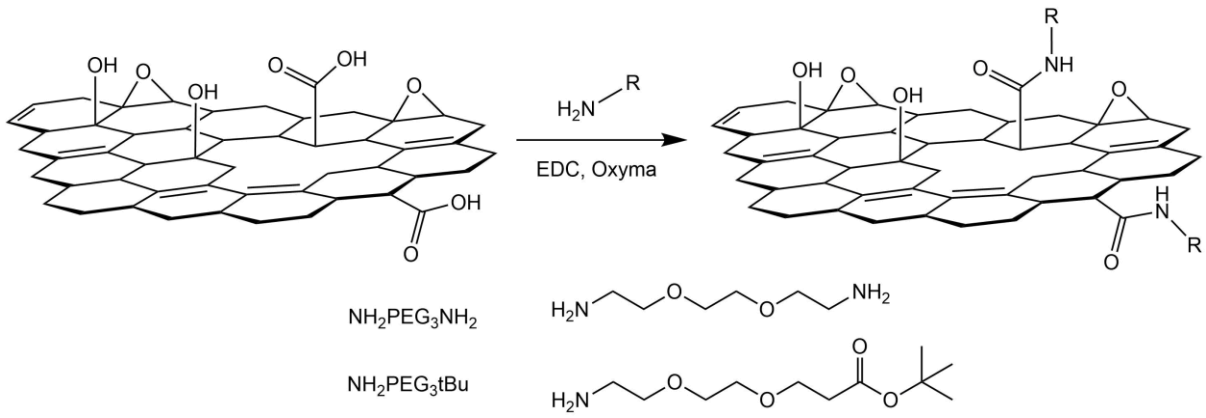

Figure 5.4. Reaction with either of the two pegylated compounds following the amidation strategy, forming GO-PEG_3NH_2 and GO-PEG_3tBu, respectively.

5.2.1 Results and discussion

Coupling reactions with PEG compounds were carried out in aqueous solution using EDC/Oxyma as coupling reagents at app. 1:1 eq., though tested at higher concentration for GO-PEG_3tBu than GO-PEG_3NH_2. Strong aggregation was seen upon addition of the coupling reagents accompanied by a darkened color change.

During purification of GO-PEG_3NH_2, it was observed that removal of excess amine required more effort than previously seen for other amines. It was theorized that unbound $NH_2PEG_3NH_2$ adsorbed strongly to the GO surface due to its two amine groups and the compound then slowly released from the material during purification.[197] As the protonated amines could interact with the negatively charged sheets, changing pH could influence this interaction. Raising the pH could deprotonate the amines while lowering the pH could protonate the negatively charged sheets, in both cases hindering the potential charge-charge interaction. A 2.5 mM sodium hydroxide solution proved beneficial for the purification effort as monitored by ^{1}H NMR, though the purification process often still required more centrifugation cycles than for other amines tested.

The synthesized materials, GO-PEG_3NH_2 and GO-PEG_3tBu, were dispersible in solution for acquisition of high quality NMR spectra for aligned menthol with Q factors of 0.120 and 0.086, respectively. The size of the acquired RDCs as seen in Table 5.1 were lower than values observed for solutions of non-modified cGO at corresponding concentrations. The diminished alignment strength could be due to partial deoxygenation effects providing less electrostatic repulsion, which is essential for GO colloidal stability in aqueous solution. Zong *et al.* described lower alignment strength of polymer functionalized GO due to higher critical concentration of LC formation as a result of the lower effective aspect ratio.[9]

Table 5.1. RDCs [Hz] and Q factors for menthol with pegylated GO in 1:1 D_2O:DMSO-*d*6 compared to values from corresponding concentrations of cGO.

#	GO-PEG_3NH_2 1.1 mg/mL	GO-PEG_3tBu 1.7 mg/mL	cGO 0.8 mg/mL	cGO 1.2 mg/mL	cGO 1.6 mg/mL
1	10.76	5.26	11.04	16.14	25.03
2a	-2.91	-1.35	-2.40	-4.04	-4.94
2b	12.43	6.94	11.52	17.33	19.32
3	9.89	3.17	13.63	13.22	23.80
4a	5.56	2.8	3.96	3.08	1.62
4b	10.99	7.99	10.07	20.46	
5a	-2.42	0.27	-1.39	-1.08	-2.21
5b	16.1	7.93	14.21	20.27	25.02
6	10.72	5.32	11.33	13.62	25.03
7	8.04	5.26	3.72	5.05	9.80
8	-0.05	-1.23	0.11	0.79	0.73
9	-2.67	-2.57	-1.53	-1.65	-1.80
10	5.38	1.19	5.06	7.45	10.15
Q	0.120	0.086	0.079	0.147	0.099

With the produced GO-PEG retaining the ability to function as alignment media, the characterization of the materials became the focus. The analytical efforts centered on the verification of covalent bond formation between the compounds and GO. Subsequently, methods to quantify the extent of functionalization would be pursued.

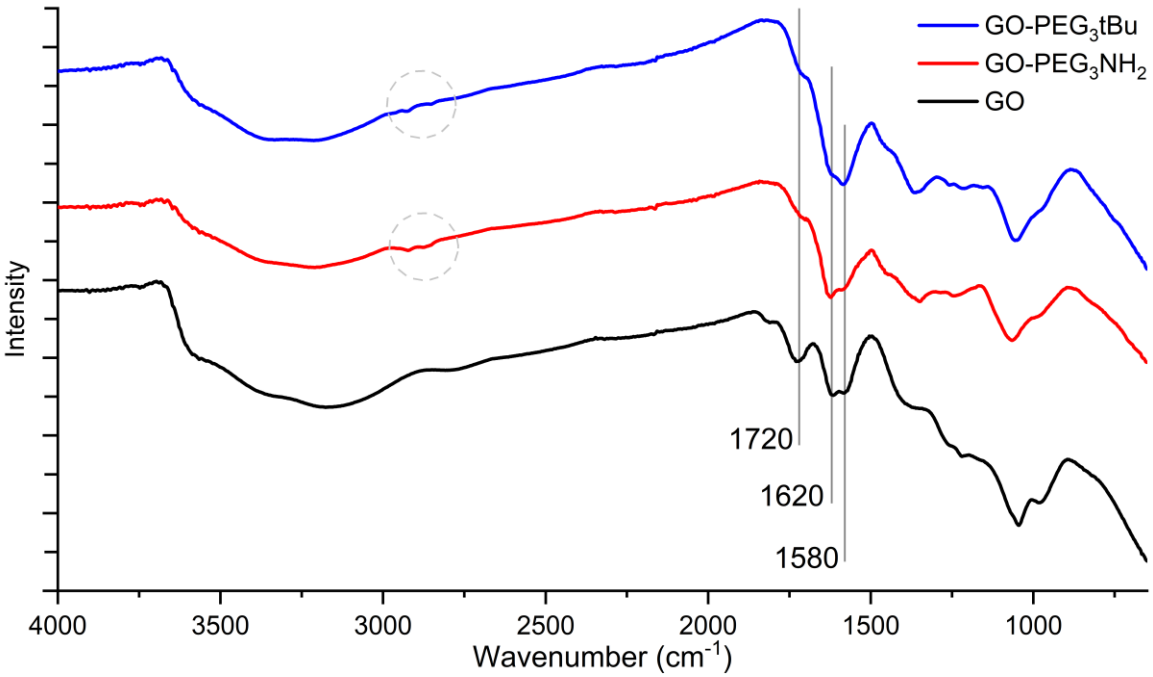

Figure 5.5. IR spectra of GO-PEG$_3$tBu and GO-PEG$_3$NH$_2$ compared to sGO.

The IR spectra in Figure 5.5 established that both GO-PEG$_3$NH$_2$ and GO-PEG$_3$tBu were different from GO, but only hinted at the nature of the reaction products. The broad band at 3600-2500 cm^{-1} due to O-H stretch from adsorbed water overlapped with hydroxyl and carboxylic acids groups. Small bands just below 3000 cm^{-1} due to C-H stretch from sp^3 carbons indicated presence of PEG, but did not discriminate between adsorbed or covalently bonded reagents. The band at 1720 cm^{-1}, assigned to carboxylic acid C=O stretch, was seen as a shoulder of the neighboring band. Literature values report amide C=O stretch at app. 1685 cm^{-1}.[24] The 1620 cm^{-1} band varied slightly in intensity when comparing IR spectra, but as this band was mainly due to adsorbed water[116], no direct structural conclusions could be drawn. The 1580 cm^{-1} peak could be due to deformation of C=C bonds from aromatic domains of GO.

The formation of an amide bond to GO is very difficult to definitively verify using IR spectroscopy as the significant bands involved overlap with bands already present in GO or the reagents. A primary amine may show a N-H deformation band at 1650-1590 cm^{-1}, which may overlap with C=O stretch and N-H deformation from amides in addition to the 1620 and 1580 cm^{-1} bands from GO.[24] Thus it is extremely difficult to distinguish between covalent amide functionalized GO and modified GO due to reaction conditions that may even contain adsorbed reagents.

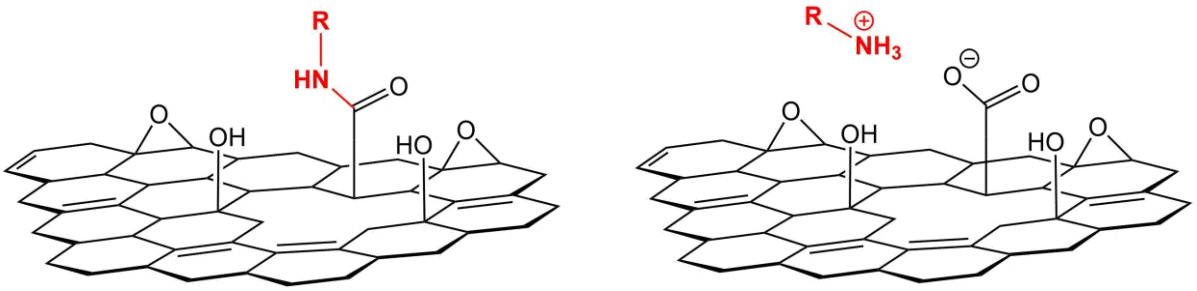

Figure 5.6. Drawing of two possible scenarios upon addition of an amine to GO. The left shows the successful amide coupling. The right is the amine interacting with GO non-covalently, e.g. by hydrogen bonding or π-π stacking for aromatic amines. At neutral pH the amine is protonated, enabling ionic interactions with the negatively charged sheets.

Critical questions regarding the verification of covalent bond formation as illustrated in Figure 5.6 was rarely answered or even addressed during a comprehensive literature search (*vida infra*). It appeared not to be of immediate concern in many applications as the focus often centered on the synthesis of new materials with desirable overall properties, e.g. conductivity. A similar discussion was raised regarding covalent functionalization of carbon nanotubes with proteins by Gao and Kyratzis.[198]

In regard to the use of IR spectroscopy for characterization of functionalized GO presented in literature, Basu *et al.* listed the appearance of a sharp 1607 cm^{-1} IR band as a sign of an amide link between GO and a folic acid-PEG conjugate, but in the discussion omitting that a comparable peak was present in the starting reagent.[199] The spectra provided by Basu *et al.* undoubtedly prove the presence of folic acid-PEG conjugate in the new GO material, but does not unambiguously show that a covalent bond has been formed. This is not the only instance where spectra of the modified GO are very similar to spectra of the added reagent.[182][183] In other cases the authors do not supply spectra of the reagents, providing no means of distinguishing new bands due to covalent bond formation from bands solely due to the presence of adsorbed reagent.[170][181][200][201] Changes caused by side reactions such as deoxygenation effects may also interfere with the analysis of experimental data.

The arguments and concerns presented when discussing IR data can be transferred to discussions of other typically employed techniques within the field with a few debated in some detail, *vida infra*.

5.3 Discussion of experimental aspects and techniques

Certain aspects of the experimental methodology for GO amidation are discussed in the following to highlight their importance. This is accompanied by examples of discussions on the structural information gained from regularly encountered characterization techniques in literature. A central question is the distinction between adsorbed and covalently bonded compounds as illustrated in Figure 5.6. During the literature search, a tendency to interpret any changes of the spectra compared to GO as sign of covalent functionalization was noted.

5.3.1 Purification

The question of whether new compounds are covalently bound or adsorbed on the GO surface is deeply connected to how the GO material is purified for excess reagent after reaction. Purification methods such as rinsing, centrifugation, filtration, and dialysis are most often encountered in literature. However, the verification of sample purity is rarely addressed. The centrifugation method used for this project allows monitoring of the stepwise purification process as will be discussed in greater detail in Chapter 6. Only adsorbed reagents are assumed removed during this process. If amide bonds are formed, they should be stable under the mild washing conditions used. The number of sufficient purification cycles were significantly increased compared to what was expected (up to 20 cycles in some cases).

During these studies, ^{1}H NMR spectroscopy was used to monitor the purification cycles as the signal intensity correlates to amount of compound present in the washing solvent. Another potential technique for verification of the purification could be mass spectrometry (MS). Liu *et al*. described repeated washing with ethanol and toluene, utilizing thin layer chromatography and UV-Vis spectroscopy to verify that reagents were no longer present in the wash.[184]

Thorough purification do not eliminate the possibility of any adsorbed reagent, but does exclude the existence of loosely adsorbed reagents, even if characterization efforts are unable to unequivocally confirm covalent functionalization. The verification method of material purity may set the threshold for the subsequent analysis.

5.3.2 Solid state ^{13}C NMR spectroscopy

As discussed in Chapter 3, ^{13}C MAS NMR spectra of GO show three major peaks at app. 60, 70 and 130 ppm for epoxide, hydroxyl, and aromatic groups with minor peaks occasionally observed at 101, 169, 193 ppm.[112] These can be tentatively assigned to the carbons in diols/lactols, carboxylic acids and ketone functional groups. An amide carbon will typically be seen in the spectrum in the same range as carboxylic acids[24] and due to the line broadening in ^{13}C MAS spectra of GO, they are difficult to distinguish. Sousa *et al*. functionalized GO with pegylated folic acid and in the subsequent ^{13}C MAS spectra of the product, a new peak at 172.8 ppm was seen and assigned to both the newly formed amide coupling and the amide already present in folic acid.[182] The validity of this argument may be questioned as proof of covalent amide coupling to GO.

Liu *et al*. argued functionalization of GO with an oligo(alkylthiophene) based on the appearance of new peaks at 13-44 ppm.[184] These peaks were due to the alkyl substituents on the thiophenes, which were not involved in the amide bond formation and the same peaks would be expected in case of adsorbed reagent. The oligothiophene could possible act as a surfactant[162] or be bonded non-covalently.[202]

Changes in the intensities of the major peaks show that the chemical structure of GO itself is modified too as a side reaction to most coupling reactions.[182][184] Frequently, spectral analysis reveal decreased content of epoxy and/or hydroxyl groups, seen as a result of GO deoxygenation or reduction to some degree accompanying functionalization. For some applications, the side effect of GO reduction is beneficial as the goal is the synthesis of a modified functionalized graphene material produced via GO.[169] However, when analyzing experimental data, discussions of possible covalent functionalization by amidation would ideally be kept separate from evaluation of the degree of reduction.

5.3.3 X-ray photoelectron spectroscopy

Irradiating a sample with X-rays leads to release of electrons and forms the foundation for X-ray photoelectron spectroscopy (XPS).[203] The kinetic energy of the emitted electrons is measured, which is correlated to the electronic binding energy. The technique can identify elements present in a sample as well as provide information regarding the local bonding environment. XPS spectra are typically presented as the number of detected electrons at different binding energies. Succeeding irradiation by X-rays, electrons have to escape the material to be detected. Therefore, XPS is a surface analysis technique reaching nanometer depths into materials.[203] Typically, a survey spectra will reveal all elements in a sample, while elemental spectra at higher resolution allow deconvolution into different components as seen in Figure 5.7.

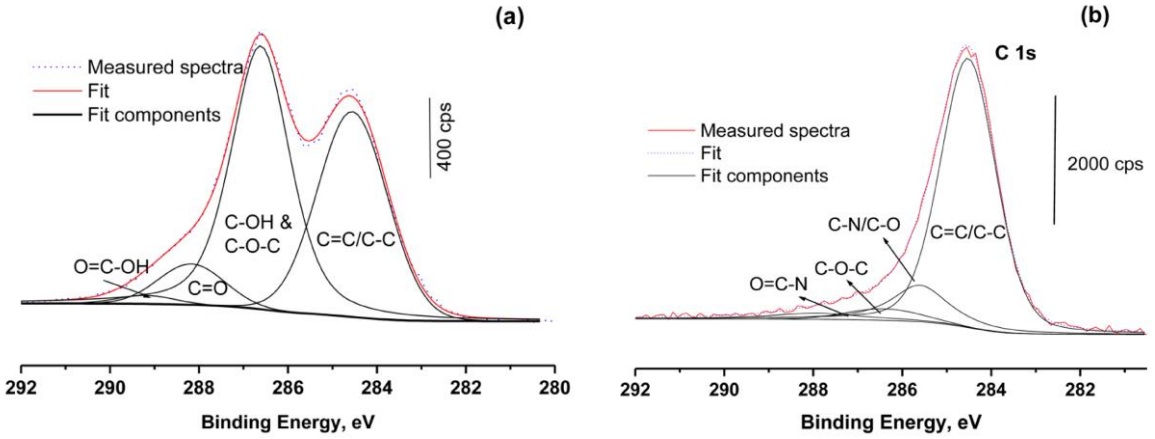

Figure 5.7. Example of high-resolution C 1s XPS spectra of (a) GO and (b) rGO sheets functionalized with octadecylamine by amide linkage. Reprinted (adapted) with permission from [181]. Copyright 2021 American Chemical Society.

C 1s core-level XPS spectra of GO is often described to consist of three components; C-C/C=C, C-O, and C=O[85], though some deconvolute the spectrum with several sub-components of these.[204] The relative ratio between these peaks can be used as a measure of the degree of oxidation. The contribution from C=O is by some divided into ketone and carboxylic acid contributions.[181][205]

Bai *et al*. argued that the appearance of a new C-N peak in the XPS spectra was a sign of functionalization.[201] However, the added amine contained C-N bonds in itself, thus adsorbed amine would provide the same peaks. Mungse and Khatri distinguished C-N from O=C-N contribution as shown in Figure 5.7, but then in their discussion attributed the amide bond to the same component as the carbonyl, which was also present in the original GO.[181] Reflection on this argument may question its validity as confirmation of amide coupling.

XPS can provide detailed, quantitative, structural information for characterization of GO and its functionalized products and is therefore among the most powerful techniques for analysis of GO materials. However, careful, critical approach has to be taken in the deconvolution of XPS spectra as it is otherwise possible to fit almost anything, essentially letting you choose your interpretation of the data.[85]

5.3.4 Raman spectroscopy

Analogous to IR spectroscopy, Raman spectroscopy is based on the interaction of electromagnetic radiation with chemical bonds. However, here only the effect on the polarizable electron density is seen and Raman spectroscopy is therefore of use when studying non-polar or easy polarizable bonds. Thus, Raman spectra will contain information about the C=C bonds and overall conjugation within graphene-based materials, while not being disturbed by traces of the very polar adsorbed water. The major peaks in Raman spectra of graphene are the G and 2D peaks at app. 1580 cm^{-1} and 2700 cm^{-1}, respectively.[114] Oxidation or otherwise introduction of defects to the hexagonal sp^2 hybridization of graphene leads to the appearance of a D band at app. 1340 cm^{-1}.[127] The effect of changes made to graphene is typically surveyed by comparing the intensities of the G and D bands (I_D/I_G ratio), but also the specific frequency of the peaks and the full width at half-maximum have been used in spectral analysis.[206]

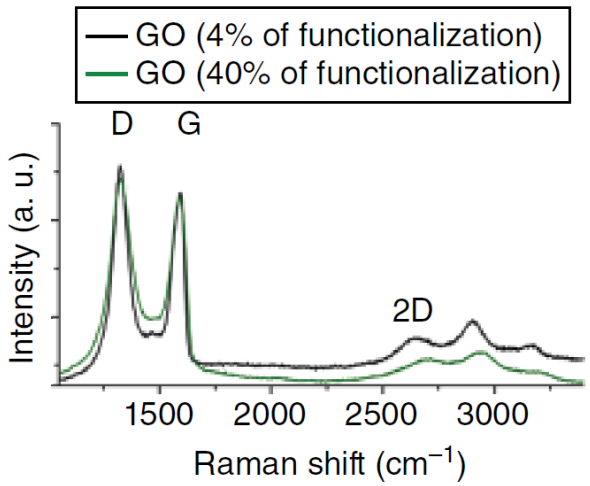

Figure 5.8. Raman spectra of GO with different degrees of oxidation (40 % is representative of conventional GO). The percentages refer to the amount of sp^3 hybridized carbons. Reproduced from [207] with permission from John Wiley & Sons.

Raman spectroscopy is typically used for two purposes in work related to GO; 1) for confirmation that GO has been formed by oxidation of graphite, 2) for assessment of the subsequent reduction to rGO.

However, when using Raman spectroscopy to assess the degree of functionalization of GO, the technique faces obstacles.[208] Firstly, Raman spectroscopy has difficulty distinguishing GO materials where the degree of oxidation is up to 50 %, as variations in the degree of functionalization do not cause great changes to the spectra as illustrated in Figure 5.8.[85][115] Raman spectroscopy can more accurately characterize reduced GO with a significantly lower amount of defects. Secondly, the appearance of the D band, which most analysis of GO is based on, is the results of any defects in the graphene structure. This can be due to missing C atoms, non-6-membered rings, or functionalized atoms, which are sp^3 hybridized instead of a part of the sp^2 conjugation. The nature of the cause of the defect is not readily apparent in the spectrum. The formation of an amide bond, as is the focus of this text, is therefore not directly evidenced in Raman spectra.

5.3.5 Design of experiments

Experience from organic chemistry should be kept in mind when designing and discussing experiments of GO functionalization via organic chemical reactions.[186] The scarcity of optimization efforts regarding e.g. concentration of reagents, reaction time and temperature hints that current practices have left more to be explored. Common literature examples rarely include reflections on reactions conditions to optimize the degree of functionalization. This exemplifies the need for characterization techniques and methods that can quantify the GO modifications and with certainty distinguish covalently bonded functionalization.

A general method to probe the effect and efficiency of coupling reactions could be to set up a number of parallel control experiments varying e.g. amounts of reagents and time. The most obvious control for the formation of an amide bond is the omission of coupling reagent(s) facilitating the bond formation. Without a coupling reagent, amide bonds are unlikely to form, but amines may still adsorb to the GO surface. Comparison of the resulting materials could give good indications of whether amide bonds are formed, or at least which techniques that are unable to distinguish between covalently bonded and adsorbed materials. Control experiments could also serve to explore whether the reagents separately have an effect on the GO structure. Reagents of the studies referenced here have been mentioned to have deoxygenative properties[184] or can e.g. act as a base, the effects of which will be discussed in detail in Chapter 6.

Bourlinos *et al*. argued that reaction between GO and amines happens predominantly through attack on the GO epoxides in a S_N2-like ring opening reaction forming secondary amines, which complicates analysis even further.[209] Others have argued similar reactions.[205][210][211] Comparison between products of reaction with and without the addition of coupling reagents by Vacchi *et al*. highlighting their similarity, is a strong argument against the formation of amide bonds.[212] The discussion of distinguishing functionalization via covalent amine bonds from adsorbed reagents would largely be based on the same arguments as was just stated for the amide bond formation.

5.4 Conclusion

Functionalization of GO by amide coupling was tested for different amines under various reaction conditions. GO products could be utilized as alignment media, though they displayed lower alignment strength. The materials were characterized by AFM and IR spectroscopy, however the analysis could not distinguish between amide functionalization and side effects of the reaction. A comprehensive literature search did not provide better alternatives of characterization method.

The literature provide numerous studies that describe modification of GO by covalent functionalization, creating new materials with diverse properties. However, when critically reviewing the experimental data used for characterization of amide functionalized GO, the data falls short of unambiguously verifying newly formed covalent bonds. Furthermore, the evaluation of the experimental data often omits considerations of adsorbed reagents or the effects of side reactions, in a rush to introduce the overall properties of the newly made materials. Efforts towards quantifying the degree of functionalization are rarely encountered. The effort towards functionalizing GO by amide couplings was halted due to (our) inability to confirm the covalent bond formation or quantitatively evaluate the results.

The considerations presented here do not intent to degrade or question the discoveries of the studies referenced here or to diminish the hope and potential of GO as a material. The intention is to shed a light on the need for a critical discussion of the characterization efforts most often encountered. For many applications, the exact binding between GO and added compounds is not of critical concern as the overall material properties are the focus. Examples of non-covalent functionalization of GO are abundant with plenty exciting potential applications.[175]

5.5 Experimental

Information regarding instrumentation and acquisition of NMR spectra are found in appendix. Simulations and back-calculations of RDCs were carried out following the procedure described in Chapter 4.

sGO refers to GO synthesized according to the procedure described in Chapter 4. sGO refers to 0.4 w% GO stock solution from Graphenea.[172] NH_2PEG_3tBu was from Biochempeg.[213] All other chemicals were from Sigma Aldrich and used as received.

GO-Tyr in water/PBS

The following procedure was inspired by the methodology previously used in the group of Jingdong Zhang.[169] To a 0.2 mg/mL sGO solution in 100 mL Milli-Q water, 99.3 mg (0.52 mmol) EDC was slowly added and the solution was stirred at RT for 15 min followed by 45 min sonication. The sonication was performed in ice water to prevent a temperature increase. 58.6 mg (0.51 mmol) NHS was added and the solution stirred for 10 min followed by 45 min sonication. Upon addition of coupling reagents, the GO aggregated strongly. 97.7 (0.54 mmol) mg tyrosine was added and the mixture heated to 80°C for 7h. During this period, the GO aggregates changed color from lighter brown to dark brown/black.
Same procedure was repeated in PBS buffer. The products were purified by 5 repeated cycles of centrifugation in water. ^{1}H NMR showed the presence of free tyrosine in GO-Tyr solution.

GO-Tyr in DMF

Aqueous sGO stock solution was exchanged to DMF solvent by repeated centrifugation prior to reaction. Variations to the GO-Tyr synthesis was tried and described below. All resulting materials appeared alike both visibly and in behavior, and are discussed as one in the text as GO-Tyr.

Table 5.2. Variations in GO-Tyr synthesis performed in DMF.

Reaction*	**1**	**2**	**3**
Conditions inspired by	[180][201]	[180][201]	[182]
sGO [mg]	119	119	119
Total volume [mL]	39.5	39.5	53.5
Carbodiimide	276 mg (EDC) 1.44 mmol	281.5 mg (DIC) 2.23 mmol	264 mg (EDC) 1.38 mmol
Activator	205 mg (Oxyma) 1.44 mmol	202 mg (Oxyma) 1.42 mmol	201 mg (NHS) 1.75 mmol
Tyrosine	244.7 mg 1.35 mmol	242.8 mg 1.34 mmol	247 mg 1.36 mmol

*Due to concerns about light sensitivity, all reaction mixtures were wrapped in tin foil.

Reaction 1&2: Oxyma was added to the GO solution in DMF. The carbodiimide was dissolved in a small volume of DMF and added slowly to the GO solution. After 40 min at RT, tyrosine was added and the mixture stirred for 5 days. Purified by cycles of centrifugation in water, DMSO, and 0.1 M NaOH.

Reaction 3: NHS was added to the GO solution in DMF. EDC was dissolved in a small volume of DMF and added slowly to the GO solution. The reaction mixture was stirred for 21 h. Excess coupling reagents were removed from the reaction mixture by 3 cycles of centrifugation. The activated GO was redispersed in 25 mL DMF. Tyrosine was added and the reaction mixture stirred for another 25 h. Purified by repeated rounds of centrifugation in water, DMSO, and 0.1 M NaOH.

GO-PEG_3NH_2

To 50 mL 1 mg/mL cGO solution was added 262 mg (1.4 mmol) EDC and 220.4 mg (1.6 mmol) Oxyma, and the mixture stirred at RT for 4.5h before addition of 200 µL (1.4 mmol) $NH_2PEG_3NH_2$ (1,8-Diamino-3,6-dioxaoctane) and stirring for additional 85h at RT. The GO solution aggregated at addition of EDC and Oxyma with heavier aggregation seen after addition of $NH_2PEG_3NH_2$. After the reaction, the GO solution appeared homogenous. Purification was initially done by 3 centrifugation cycles in water. The pH was increased by addition of 20 µL 1 M NaOH or HCl at every centrifugation cycle to $1/6^{th}$ of the divided reaction mixture dispersed in 8 mL water (total 13 cycles). The purified GO-PEG_3NH_2 was brought back to neutral pH by 3 centrifugation cycles with water.

GO-PEG_3tBu

To 12 mL 1 mg/mL cGO solution was added 2.4 g (12.5 mmol) EDC, 1.94 g (13.7 mmol) Oxyma, and 36 mg (0.15 mmol) NH_2PEG_3tBu (tert-Butyl 3-(2-(2-aminoethoxy)ethoxy) propanoate). The reaction was kept at RT for 20h. Purification first in water, then alkaline solution as described above.

Purification

All purification efforts were monitored by 1D ^{1}H NMR spectra of the supernatants from centrifugation with 10% D_2O. Typical centrifugation cycles used 12’000 rpm (15938 rcf) for 30 min, decantation of the supernatant, and redispersion in equal amounts of solvent.

AFM

Very diluted GO-Tyr solutions were drop casted on freshly cleaved mica substrate. Samples dried overnight at RT and AFM images were measured the following day using an Agilent Technologies 5500 AFM in tapping mode.

6 GO functionalization part II: Carboxylation

Parallel to the functionalization attempts of GO via the amidation strategy, chemical procedures to increase the extent of carboxylic acid functionalization were investigated. As mentioned previously, the presence of carboxylic acids in GO is limited, thus increasing their abundance could increase the degree of functionalization in a subsequent amide-coupling reaction. One approach is carboxylation via substitution on cloroacetic acid by GO after activation of the abundant hydroxyl and epoxy groups with sodium hydroxide.[159] Figure 6.1 illustrates the reaction and the resulting product GO-COOH. Due to concerns about changes to the GO from the basic conditions, a control reaction omitting the addition of chloroacetic acid was performed in parallel, the product of this reaction being referred to as GO-base.

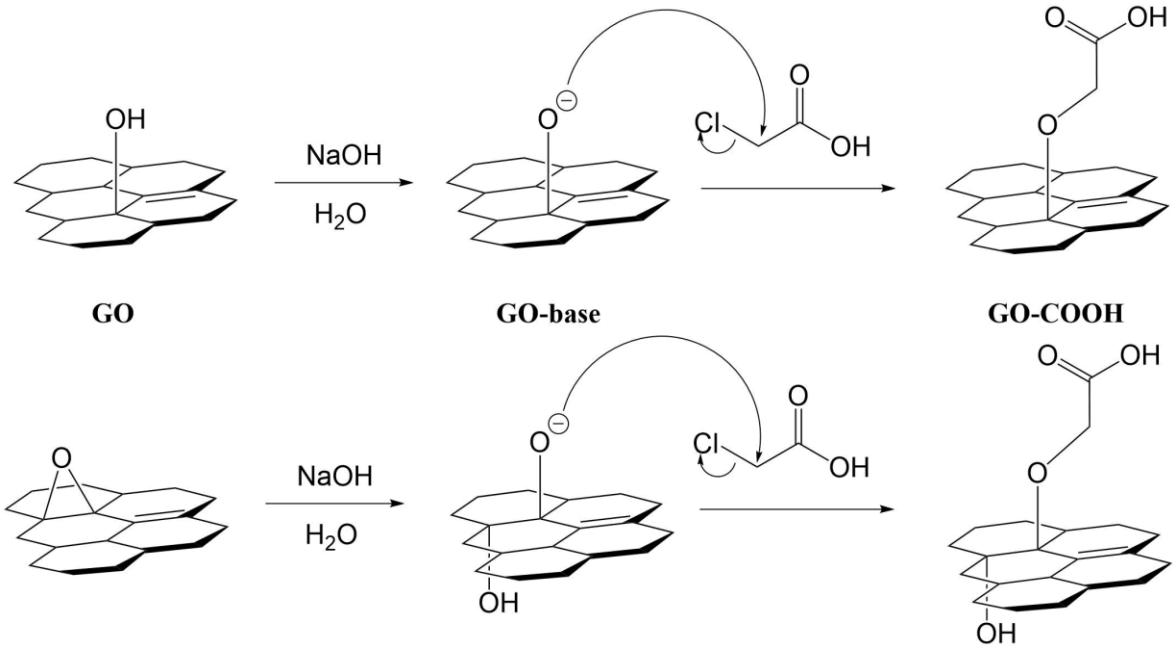

Figure 6.1. Mechanism of possible S_N2 reactions between GO and chloroacetic acid. The carboxylation is assumed to be initiated by deprotonation of hydroxy groups and nucleophilic ring-opening of epoxides by hydroxide.

6.1 Results

The solutions of GO-COOH and GO-base had both changed from the golden brown color of GO to dark brown or black solutions, indicating that the synthesis also increased the sp^2 hybridized domains. Strong aggregation of GO upon addition of base was observed during reaction, though not discussed in the publications that served as inspiration for this functionalization strategy.[159][170][201] The aggregation was reversible and homogenous solutions were obtained during purification upon removal of sodium hydroxide and neutralization of pH. The purification process was monitored by ^{1}H NMR. For chloroacetic acid, the chemical shift of the methylene group at app. 3.9 ppm was dependent on pH, but the peak was otherwise easy to monitor in the spectra. The integral of the methylene peak gradually decreased until it was no longer visible in the spectra after 6 centrifugation cycles. The spectra also showed that app. 15 % of chloroacetic acid had reacted with sodium hydroxide forming glycolic acid. The decrease of a factor of 10 in intensity seen in Figure 6.2 may depend on the solubility of chloroacetic acid in water and any non-covalent interactions to the GO surface. After verifying that all excess reagent had been removed, the new GO material could be examined in further detail.

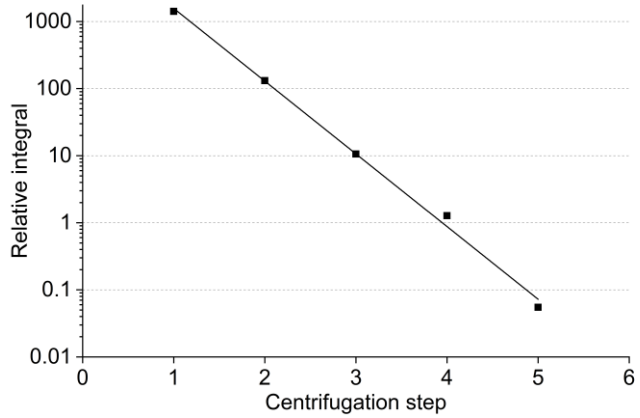

Figure 6.2.

Amount of chloroacetic acid present in the supernatant after stepwise purification. Quantified by ^{1}H-NMR relative to an external standard. Note the logarithmic scale.

Table 6.1. Extracted RDCs [Hz] for 20 mM menthol in 1:1 D_2O:DMSO-*d*6 in app. 1.3 mg/mL GO-COOH and GO-base compared to 1.2 mg/mL cGO.

#	GO	GO-COOH	GO-base
1	16.14	17.86	15.86
2a	-4.04	-3.34	-4.37
2b	17.33	18.88	18.52
3	13.22	22.36	17.88
4a	3.08	4.56	4.34
4b	20.46	12.41	11.33
5a	-1.08	-3.51	-3.31
5b	20.27	21.57	19.97
6	13.62	22.99	17.47
7	5.05	6.96	5.33
8	0.79	0.99	0.82
9	-1.65	-3.41	-2.28
10	7.45	5.56	5.79
Q	0.147	0.119	0.058

Both GO-COOH and GO-base were fully dispersible in aqueous solution. Alignment of menthol resulted in Q factors of 0.119 and 0.058 for GO-COOH and GO-base, respectively. The size of the extracted RDCs seen in Table 6.1 are comparable to RDCs at corresponding GO concentrations.

Lyophilized GO-COOH was analyzed by IR spectroscopy and compared to cGO and the control sample, GO-base. As seen in Figure 6.3, GO-COOH is clearly altered compared to GO. Most notably, the IR band from C=O stretch at 1723 cm^{-1} appear to be decreased, seen as a shoulder of the increased 1617 and 1585 cm^{-1} bands from OH bend in adsorbed water and C=C stretch, respectively.[116] The increase of the 1585 cm^{-1} band is consistent with the noted color change, indicating expansion of the C=C conjugation. The spectra are in agreement with examples seen in literature.[159][201]

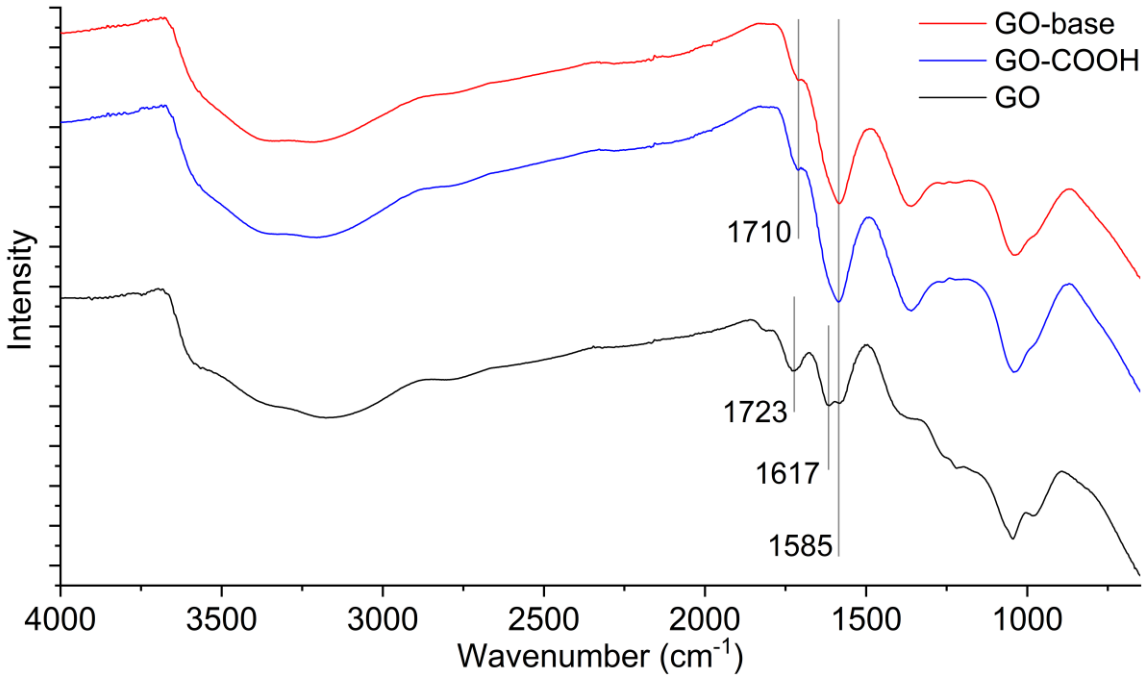

Figure 6.3. Overlaid IR spectra of lyophilized GO, GO-COOH, and the control sample GO-base.

The spectra of GO-COOH and the control sample are overwhelmingly identical in Figure 6.3, which indicate that the envisioned reaction with chloroacetic acid only occurs to a very limited extent. Instead it appears that the alteration of GO seen here, and the actual cause of the observed changes, is the addition of base. The effect of base on GO has been discussed in the literature and the reported IR spectra are very similar.[214][126]

The materials were also studied by ^{13}C MAS ssNMR and the resulting spectra are seen in Figure 6.4. The GO spectrum is characterized by the major peaks at 130, 69, and 59 ppm due to aromatic, hydroxyl, and epoxide groups, respectively, in agreement with literature.[112] The deconvoluted spectrum shows that epoxides are the dominant functional group with 41 %. The combined presence of hydroxyl and epoxy groups far exceed that of C=C carbon, which is in agreement with a C/O ratio of 2:1 generally reported for GO. The minor peaks sometimes reported elsewhere and described in Chapter 3 are indistinguishable here due to strong spinning sidebands.

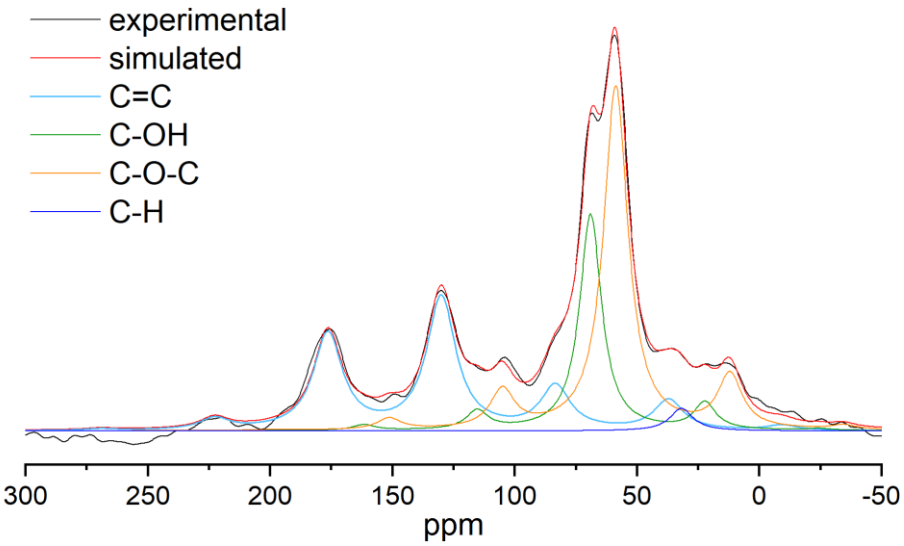

GO

	ppm	%
C=C	130	35
C-OH	69	22
C-O-C	59	41
C-H	32	2

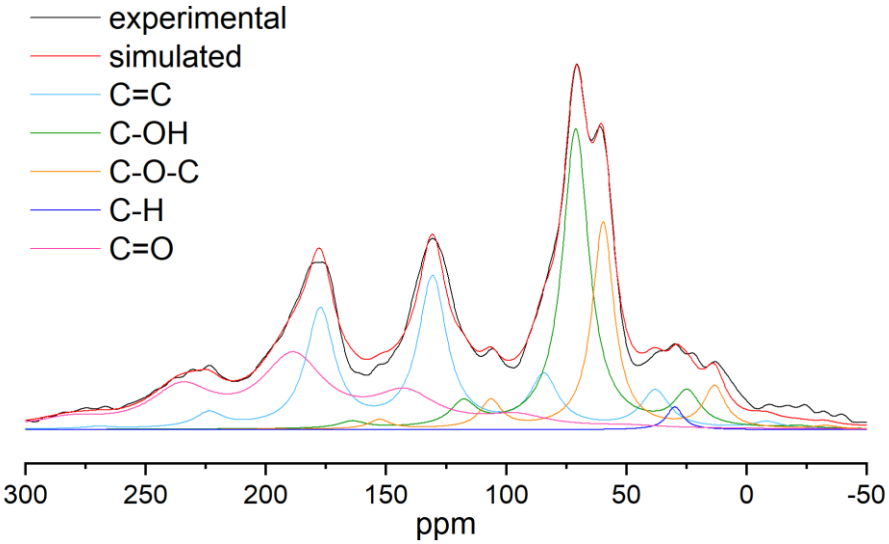

GO-COOH

	ppm	%
C=C	131	29
C-OH	71	26
C-O-C	60	17
C=O	189	27
C-H	30	1

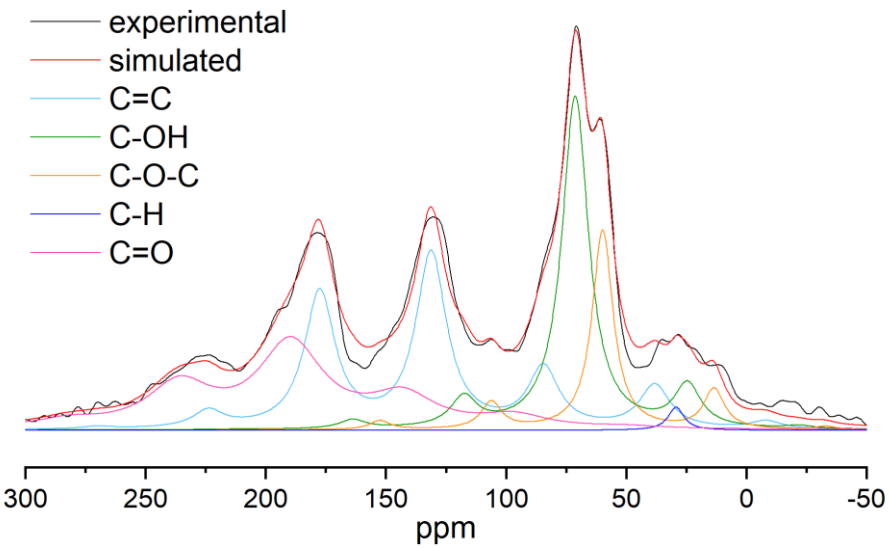

GO-base

	ppm	%
C=C	131	32
C-OH	71	26
C-O-C	60	14
C=O	190	27
C-H	30	1

Figure 6.4. Experimental and simulated 1D ^{13}C MAS spectra of GO, GO-COOH and GO-base. The spectra show strong spinning side bands obscuring the potential presence of minor peaks.

The simulated spectrum of GO-COOH reveals a reduced epoxide peak at 60 ppm ascribed to opening of epoxides due to attack by hydroxide. A new, broad peak is seen at 189 ppm, which is a notably higher chemical shift than for the carbonyl carbon in chloroacetic acid. From 1D ^{13}C NMR spectra, the carbons of chloroacetic acid in solution were assigned at 41.3 and 171.8 ppm for the methylene and carbonyl carbon, respectively.

Only looking at the results for GO-COOH, one might ascribe the new signal at 189 ppm to an increase in carboxylic acid content due to successful carboxylation. However, the spectra of GO-COOH and GO-base in Figure 6.4 have strong similarities, revealing that the major changes when compared to the GO spectrum are due to the addition of base. Both spectra show a drastically decreased epoxy content, while the hydroxyl content has slightly increased. Covalent carboxylic acid functionalization of GO are not evident in the spectrum of GO-COOH.

6.2 Effect of base on the GO structure

Changes in the GO structure in basic solution have been investigated in earlier studies, but different explanations have been proposed e.g. being the foundation for the two-component structural model with ensuing discussion.[126]–[129][160][214] The studies did agree that treatment with base results in a modified GO product with a decreased oxygen content, though usually not to the same degree as the methods most often used for GO reduction (app. C/O ratio: GO ≈ 2, rGO > 10[17][127]). The reaction with base has sometimes been referred to as a reduction and terms like "base reduced GO" can be found in literature, though not adhering to common definitions of reduction. The effect of base has been explained to cause a series of rearrangements leading to deoxygenation as part of the dynamic structural model of GO by Dimiev *et al*.[126]

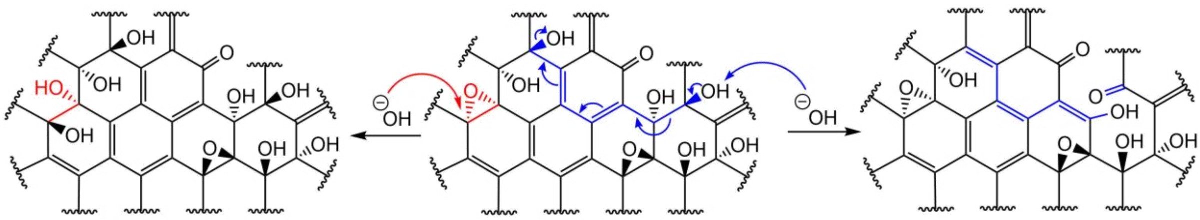

Figure 6.5. The effect of base on the GO structure, exemplified as epoxide opening and C-C bond breaking leading to formation of enols and ketones according to the dynamic structure model. Inspired by [126].

The reactions shown in Figure 6.5 also account for the observed color change as the sp^2 hybridization is expanded. The new peak at 189 and 190 ppm of 27 % in Figure 6.4 from GO-COOH and GO-base, respectively, is due to formation of ketones, though some C=C content is assumed to contribute to the peak intensity. The combined integrals for the C=C and C=O peaks of 56 % and 59 % for GO-COOH and GO-base, respectively, are more descriptive of the increased aromaticity of the base-treated products compared to the 35 % C=C content in GO. The combined content of C-O-C and C-OH likewise decreased from 63 % in GO to 42 % and 40 % in GO-COOH and GO-base, respectively, as a results of the deoxygenation caused by the basic conditions.

Dimiev *et al*. further described how strongly alkaline conditions lead to decarboxylation.[126] The loss of carbon in the form of CO_2 causes permanent degradation of the GO sheet, while the epoxy ring opening has been described as a reversible reaction.[163]

During reaction with the amines and coupling reagents discussed in Chapter 5, a darker color change indicating deoxygenation was routinely observed. Thus, when interpreting characterization data for carboxylated or amide functionalized GO, the extent of side reactions between added reagents and other functionalities on GO should be included in the analysis. The analytic challenge involves distinguishing between proof of successful coupling and changes due to side reactions. Raised temperatures also caused a color change as discussed in Chapter 4 indicating similar deoxygenation on the GO surface. The reaction speed of the rearrangements leading to deoxygenation is slow in neutral aqueous solution, but increases at elevated temperatures and in the presence of base.

6.3 Discussion

The analysis of GO-COOH and GO-base highlight the need for critical evaluation of experimental data used for characterization of GO products. The comparison of IR and NMR spectra shown here question whether the carboxylation occur, or at the very least show that these techniques cannot be used to distinguish between signs of functionalization and side effects due to the reaction conditions. When consulting literature, arguments similar to what was found in the discussion of the amidation regarding ambiguous characterization of GO reaction products was encountered.

The verification of GO carboxylation is often superficially discussed in the literature cited throughout this chapter; some studies only address GO-COOH very briefly as an intermediate product for further functionalization.[215] Sun *et al.* showed an IR spectrum in support of the successful reaction and mentioned increased water solubility, but no experimental evidence was presented in support of this.[159] Turcheniuk *et al*. additionally presented XPS and SEM data to document the synthesis of GO-COOH.[170] SEM images displayed micrometer sized aggregates reminiscent of base treated GO.[131] The C1s core-level XPS spectra revealed decreased presence of C-O bonds and an increase in C/O ratio, which is expected solely from the deoxygenation in basic solution. A novel, low intensity, very broad band at higher energy was by Turcheniuk *et al*. ascribed to “carbon species of higher oxidation states such as carboxylic acid”.[170] The appearance of an extra XPS signal may, as pointed out by the authors, be evaluated as evidence of the successful carboxylation, but it does raise possible questions that are not addressed in the publication:

i. Could this signal be caused by the deoxygenation due to base alone?

ii. How can one discriminate between covalently bound carboxymethoxy groups and residual chloroacetic acid adsorbed on the surface?

Parallel to the examination of the carboxylation reaction carried out here, Guo *et al.* published a deeper study of the efficiency of the carboxylation reaction compared to epoxide ring-opening by an amine and concluded that carboxylation is an inefficient approach to GO functionalization.[205] Alternatively, synthesis of graphene acid (G-COOH) starting from fluorographene via cyanographene could potentially sidestep the major issues discussed here, since it appears to have a more uniform structure.[180] Further, nitric acid has also been described to promote oxidation to carboxylic acid at the edges of GO.[181][216]

6.4 Conclusion

Carboxylation of GO using chloroacetic acid and sodium hydroxide was tested as a synthesis strategy towards further GO functionalization in the pursuit of increasing the applicability of GO based alignment media for NMR structural analysis of compounds. The product, GO-COOH was dispersible in aqueous solution and anisotropic NMR measurements resulted in RDCs that corresponded to values obtained for GO solutions.

Analysis by IR and NMR spectroscopy concluded that the product GO-COOH was different from GO, but comparison with a base treated GO control sample revealed that the observed changes were due to the reaction with base. The synthesized materials contained decreased amounts of surface epoxy groups, while the degree of sp^2 hybridization had increased.

Based on the discussed results in the present and previous chapter, the carboxylation and amidation strategies were abandoned in favor of reactions that promised better options for characterization of products.

6.5 Experimental

Information regarding instrumentation and acquisition of solution NMR spectra are found in appendix. Structure simulations and back-calculations of RDCs were carried out following the procedure described in Chapter 4.

sGO refers to 0.4 w% GO stock solution from Graphenea.[172] Other chemicals were from Sigma Aldrich and used as received.

Synthesis

Synthesis of GO-COOH used reaction condition inspired by literature.[170][201] 25 mL cGO was diluted to 250 mL with Milli-Q water to 0.4 mg/mL GO concentration. (6.988 g (175 mmol) NaOH and 5.008 g (53 mmol) chloroacetic acid were added and the solution stirred at room temperature for 24h. Upon addition of NaOH, the GO aggregated and soon started to darken in color. A second (control) reaction was done in parallel under the same conditions, where no chloroacetic acid was added and 3.550 g (89 mmol) NaOH (lesser amount as no acid was added). The resulting material of this reaction is called GO-base.

The material was purified by repeated rounds of centrifugation and redispersion in Milli-Q water. During the purification process, the GO stopped the aggregation and looked homogenously dispersed again. Purification was confirmed by testing pH and by ^{1}H NMR verifying that no amount of reagent was present in the supernatant after centrifugation. The decanted supernatant from each step of centrifugation was tested by ^{1}H-NMR with 10 % D_2O. External standard of maleic acid (0.1 M) was used for quantification. The product was then lyophilized, resulting in a dark gray/black porous material.

Solid state NMR acquisition and simulation

^{13}C ssNMR spectra acquired at a 150 MHz spectrometer (^{13}C frequency) at magic angle spinning (MAS) rotation speed of 7000 Hz using 90° excitation pulse of 3.85 μs, high-power (100 kHz) ^{1}H SPINAL64 decoupling and a relaxation delay of 60 s. Chemical shift relative to TMS (d=0.0 ppm) using adamantane (d=38.48 ppm) as secondary reference. Line broadening of 200 Hz was applied during processing of spectra.

Deconvolution of ssNMR spectra in TopSpin version 3.6.1 by Bruker using the Solids Line Shape Analysis tool (sola). Simulation of spectra used the CSA model with a Haeberlen fit.

Table 6.2. Relevant parameters from simulation of the GO 1D ^{13}C MAS spectra. The simulated spectrum had a 95.9% overlap with the experimental data.

	C=C	C-OH	C-O-C	C-H
Intensity	1911973.9	3052402.1	4849777.6	318848.7
δ(iso)	130.063	69.005	58.684	32.046
δ(CSA)	-114.33	56.37	61.78	0
η(CSA)	0.101	0.085	0.346	0.116
LB*	2175.0953	1639.4245	1813.0294	1741.9088
Integral	276285988	175761487	325461540.9	15675658.7
%	34.8	22.2	41.0	2.0

*Line broadening parameter

Table 6.3. Relevant parameters from simulation of the GO-COOH 1D ^{13}C MAS spectra. The simulated spectrum had a 96.8% overlap with the experimental data.

	C=C	C-OH	C-O-C	C-H	C=O
Intensity	2169661.2	4228489.8	2924069.4	324106.4	1092434.6
δ(iso)	130.98	71.376	59.946	30.025	188.723
δ(CSA)	-117.69	54.45	68.92	0.0	-101.39
η(CSA)	0.105	0.099	0.264	0.125	0.814
LB*	2166.8249	2000.2195	1642.2473	1263.1199	4820.43
Integral	327678249	292294450	188973377	11644166	309361092
%	28.99932	25.86788	16.72403	1.030502	27.3782669

Table 6.4. Relevant parameters from simulation of the GO-base 1D ^{13}C MAS spectra. The simulated spectrum had a 96.4% overlap with the experimental data.

	C=C	C-OH	C-O-C	C-H	C=O
Intensity	1915210.1	3547933.3	2129532.7	245911.7	992866
δ(iso)	131.197	71.252	60.022	29.688	189.675
δ(CSA)	-117.26	57.03	68.73	0	-98.83
η(CSA)	0.113	0.107	0.296	0.101	0.657
LB*	2329.1426	2015.2422	1581.2048	1209.446	4911.6038
Integral	307452064	251974426	132617018	8402198	265412378.5
%	31.832012	26.0881417	13.730487	0.869921	27.47943851

7 GO functionalization part III: Click chemistry

Following the discussion regarding effectivity and verification of GO functionalization by amidation reactions, alternative reaction strategies were approached. Inspired by the carboxylation, utilization of the most abundant functional groups was considered advantageous.

The ring opening of epoxides by a nucleophilic attack was used for the introduction of azides on the GO sheets. The synthesized GO-N_3 was further functionalized by Cu(I) catalyzed azide-alkyne cycloaddition (CuAAC), popularly known as click chemistry.[217][218]

The presence of azide could be followed by its distinct IR band, which is far removed from any bands in the spectrum from GO. Click conjugations are known for providing high control of reactivity, having high yields, and being tolerant of most functional groups.[219]

7.1 GO-N_3

Nucleophiles such as the azide ion can react with epoxides in a ring-opening S_N2-like reaction resulting in an alcohol and the formation of a C-N covalent bond as illustrated in Figure 7.1. As the reaction happens directly on carbons within the GO sheets, bulky nucleophiles may be prevented from reacting due to steric hindrance by the sheet itself. Additionally, the high presence of oxygen may deter some nucleophilic attacks. The azide ion is presumably a good nucleophile in this reaction due to its small size and linear shape. It has also been proposed that azide mainly replaces any organosulfate groups leftover from the oxidation, which, if present, would happen in a similar S_N2 reaction.[109][220]

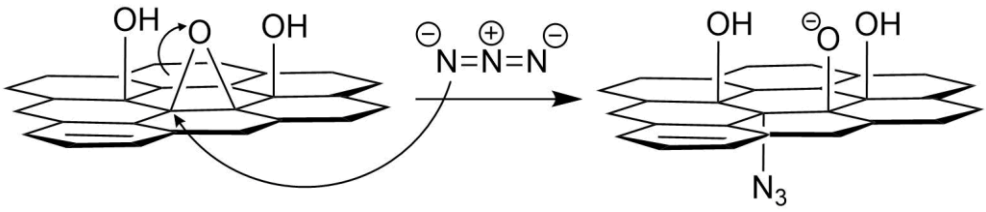

Figure 7.1. Reaction mechanism expected for the reaction of the azide anion with epoxide groups on GO.

Though azide functionality presents advantageous opportunities for synthesis of organic compounds, azide chemistry is seldom used due to the inherent risk of explosion. A guideline for organic azides states that the sum of carbon and oxygen atoms should exceed that of nitrogen by a factor of 3 for a compound to be considered non-explosive.[221] With the carbon-based backbone, the synthesized GO-N_3 was considered safe to handle.

7.1.1 Synthesis

Aside from the azide functionality being a key reagent in the click chemistry reaction that would follow, the introduction of azides presents a new aspect in the characterization of the produced GO-N_3. The covalently bonded azide has a unique IR band at app. 2120 cm^{-1}, which is free from overlap with any peaks already present in GO. Excess sodium azide is seen as an IR band at 2065 cm^{-1}, easily distinguishable from the bonded azide band, see Figure 7.2.[220][222]

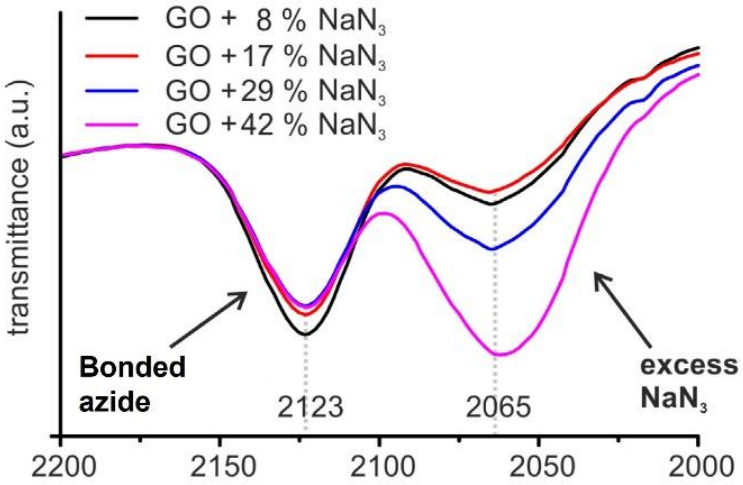

Figure 7.2. IR bands from bonded and non-bonded azide after reaction on GO. Reproduced from [220] with minor edits with permission from RCS Pub.

The reaction between GO and sodium azide has been reported in both organic and aqueous solvents and mixtures thereof, see Table 7.1. The reaction in aqueous solvent only proceeded during freeze drying and the ensuing rise in concentration.[220] No such issues have been reported for the reaction in organic solvents.[223] Due to the risk involved in handling solid or concentrated amounts of sodium azide, the reaction was carried out in DMF.

Table 7.1. Examples of reaction conditions for the synthesis of GO-N_3.

Concentration		Ratio	Reaction time	Temp.	Solvent	Ref.
GO [mg/mL]	NaN_3 [M]	N_3/GO [mg/mg]		[°C]		
20	0.385	1.25	1 week	reflux (inert)	1:1 H_2O:AcCN	[224]
1	0.012	0.8	1h	10° then freezedrying	H_2O	[220]
1	0.015	1.0	48 h	40	DMF	[223]
0.5	0.077	10	48 h	40	DMF	[225]

The overview seen in Table 7.1 aims to highlight the large difference in reaction conditions reported in literature. To the best of the author's knowledge, a full systematic study on the effect of different reaction conditions on the synthesis yield has not been conducted. Here yield relates both to the amount of azide covalently bonded to the GO and to the amount of GO-N_3 obtained.

For this project, reaction conditions similar to those reported by Huang *et al.* were used.[223] This was partly due to inspiration from organic chemistry.[226] Mild heating was chosen to speed up the reaction with minimum change and deoxygenation of GO.

7.1.2 Results and discussion

The synthesized GO-N_3 was a dark brown material, which remained fully dispersed in both water and DMF. A darker color change indicated some degree of deoxygenation during reaction, which likely is a result of the elevated temperature. The purification of excess sodium azide consisted of 7 cycles of centrifugation, but was not verified, as the azide salt contained no proton peaks, which would be detectable in ^{1}H-NMR.

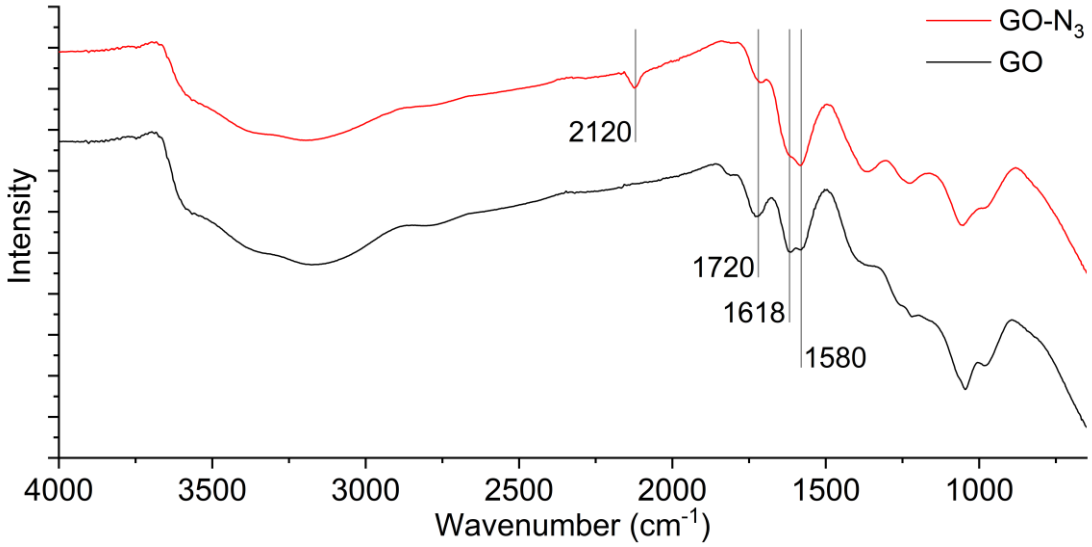

Figure 7.3. IR spectrum of GO (bottom) and the synthesized GO-N_3 (top) with significant peaks labelled.

The IR spectrum of the lyophilized GO-N_3 is shown in Figure 7.3, with the band of the GO bound azide stretch seen at 2120 cm^{-1}. The C=O stretch at 1720 cm^{-1} appear unchanged, while the 1580 cm^{-1} C=C stretch has increased slightly, indicating expansion of the aromatic domains in agreement with the darker color change. There is no sign of excess unbound sodium azide at 2065 cm^{-1}. Based on the IR spectrum it is concluded that azide has been covalently bonded to GO, with little to no adsorbed excess reagent. However, IR spectroscopy can here not be used as a quantitative measure for the degree of functionalization.

Analysis of the GO-N_3 ^{13}C MAS NMR spectrum seen in Figure 7.4 showed major peaks at 131, 71, and 60 ppm, which are assigned to C=C, C-OH, and C-O-C groups, respectively.[112] Simulation of the 1D ^{13}C MAS spectrum revealed a decreased intensity of C-O-C, which is consistent with the epoxide ring opening by azide. The new, broad peak at 189 ppm was ascribed to C=O as a result of deoxygenation occurring as a side effect of the elevated temperature during reaction. The color change noted during reaction are in agreement with the extended sp^2 hybridization as measured as the combined C=C/C=O content of 50 % compared to 35% in GO.

The dispersible GO-N_3 retained its ability to function as alignment media, providing high quality NMR spectra. Figure 7.5 shows the correlation between the solvent composition and the calculated Q factors for the extracted RDCs. Compared to the alignment behavior of GO as described in Chapter 4, GO-N_3 exhibits higher degree of alignment at lower D_2O content as seen by both the Q factors and the size of the extracted RDCs at the same GO concentration. The higher tolerance towards organic solvent reflects the lower hydrophilicity due to deoxygenation.

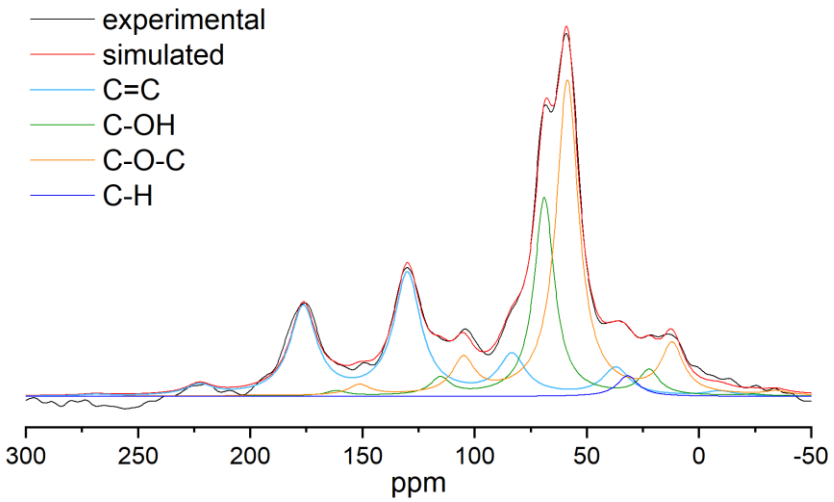

GO

	ppm	%
C=C	130	35
C-OH	69	22
C-O-C	59	41
C-H	32	2

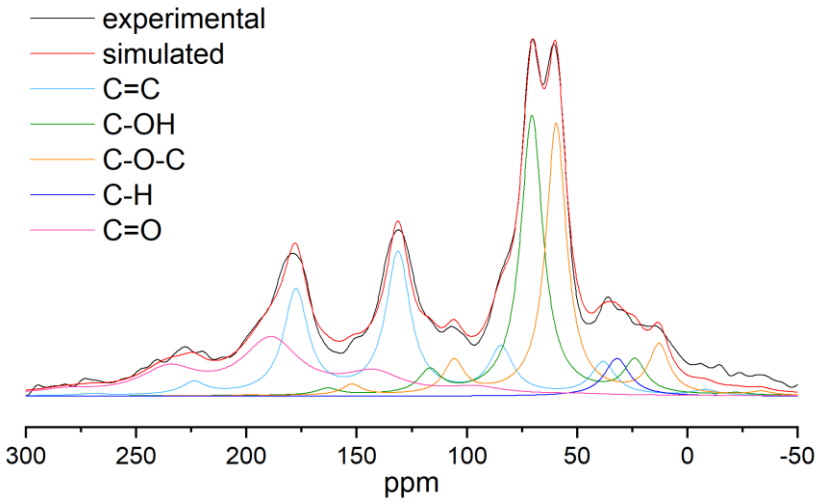

GO-N_3

	ppm	%
C=C	131	27
C-OH	71	23
C-O-C	60	24
C-H	33	2
C=O	189	23

Figure 7.4. Experimental and simulated 1D ^{13}C MAS NMR spectra of GO-N_3 compared to GO. The spectra show strong spinning side bands.

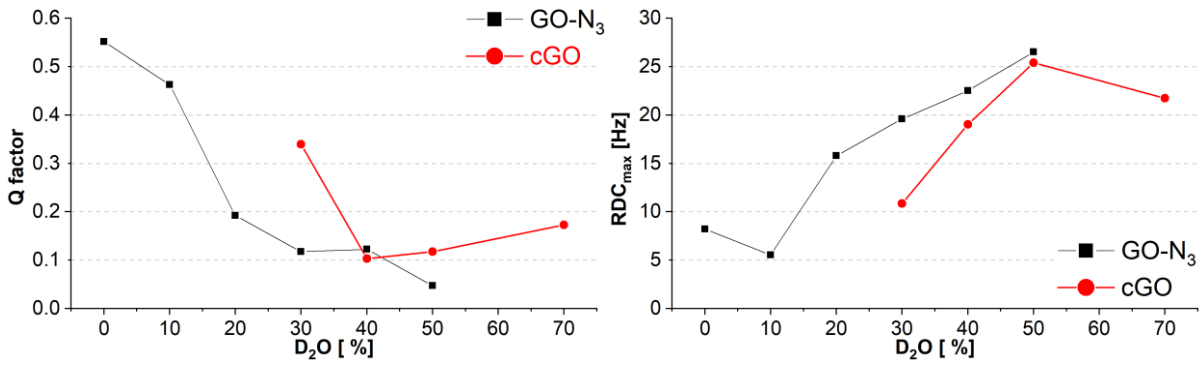

Figure 7.5. The alignment strength of 1.6 mg/mL GO-N_3 and sGO relative to solvent composition of D_2O:DMSO-*d*6 expressed by the Q factor and maximum size of RDCs measured for menthol.

7.2 Click chemistry on GO-N_3

The term "Click Chemistry" covers reactions that are stereospecific, high-yielding, give easily removable byproducts and proceeds under simple reaction conditions.[227] The copper(I) catalyzed azide-alkyne cycloaddition (CuAAC) is for many synonymous with click chemistry.[217][218] Among the favorable reaction qualities are: 1) it can be carried out in water, 2) it can take place at room temperature, 3) it tolerates a wide pH range, 4) it is insensitive to a broad range of functional groups.[228] This makes it an attractive reaction for GO functionalization as GO contains a mix of functional groups and the mild reaction conditions does not promote large degrees of GO reduction.

The CuAAC reaction is a nonconcerted Huisgen 1,3-dipolar cycloaddition catalyzed by two Cu(I) ions forming a 1,2,3-triazole as seen in Figure 7.6.[229] The reaction is regioselective towards the 1,4-disubstituted triazole, while the uncatalyzed reaction results in a mixture of the 1,4- and 1,5-products.

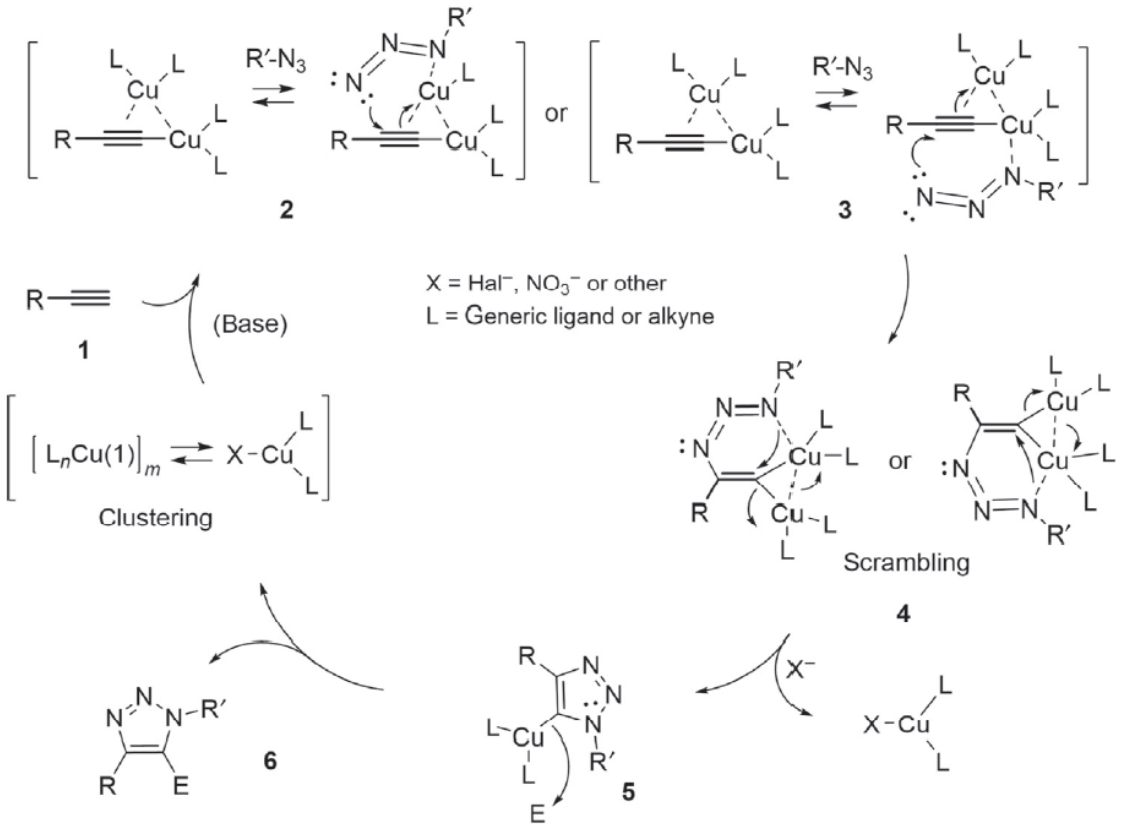

Figure 7.6. Proposed mechanism of the CuAAC click reaction between an azide and alkyne going through a dinuclear copper intermediate. Reproduced from [230] with permission from Elsevier.

7.2.1 Synthesis strategy

The click reaction on GO-N_3 has, similarly to the synthesis of GO-N_3 itself, been reported with varying reaction conditions, i.e. solvents, temperature, reaction time, and concentration of reagents. Likewise, a wide range of alkynes from an interval of small organic compounds like 4-ethylaniline[231], alkyne-modified monosaccharides[232], and alkyl chains[224], over polymers[223][233][234] to biomolecules[225] have been used.

A small alkyne, 4-(tertbutyldimethylsilyloxy)-1-butyne (Si-alk), was used to probe the click reaction as its presence could be easily monitored by ^{1}H NMR due to the upfield shifted methyl groups. The reaction products were evaluated by IR spectroscopy, where elimination of the azide stretch at 2120 cm^{-1} was seen as signifying the completion of the click coupling reaction. IR bands from triazole itself were not used to monitor reaction as the characteristic bands are found in the interval 1645-1023 cm^{-1}, which overlap with background bands from GO.[232][234][235]

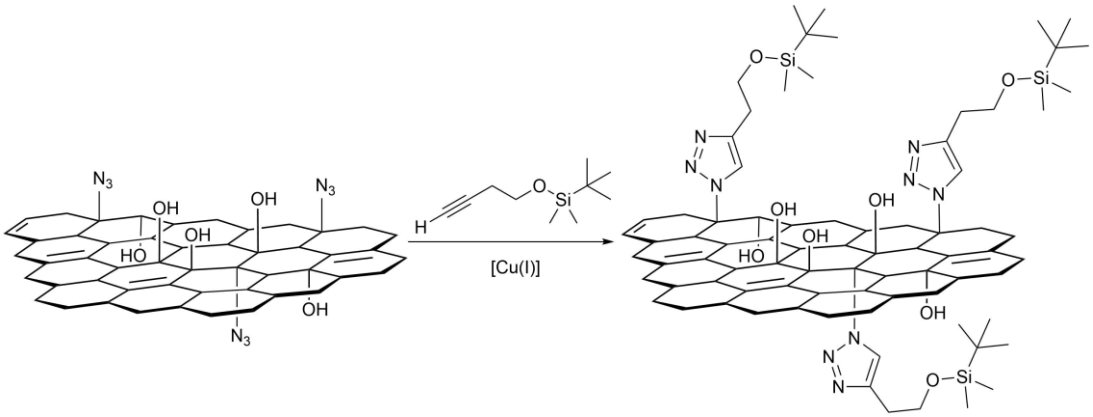

Figure 7.7. CuAAC click reaction between GO-N_3 and Si-alk. Various Cu(I) sources have been tested.

Three different strategies were tested regarding the source of Cu(I):

1) $CuSO_4$/ascorbic acid

Copper was provided as Cu^{2+} and reduced in situ by a reduction agent. This strategy is perhaps the most commonly utilized source of Cu(I).[218][219] Most literature uses sodium ascorbate, but here the acid was used, inspired by Mei *et al*.[222] Avoiding the addition of base was considered beneficial for suppression of deoxygenative sidereactions. As a reducing agent, ascorbic acid has been reported to reduce GO, though not as strongly as other more common reducing agents.[236][237][17]

2) Solid Cu

Addition of copper in the form of copper turnings is believed to generate Cu(I) by comproportionation of Cu(II)/Cu(0).[228] The limited amount of generated copper ions was of interest due to the sensitivity of GO towards cations. The copper turnings were additionally easy to remove during purification.

3) Cu(I)OTf

The direct addition of a Cu(I) salt avoided the addition of a reducing agent and provided direct control of the Cu(I) concentration. However, Cu(I) is easily oxidized to the unreactive Cu(II), and thus requires inert conditions during the reaction.[218] Various Cu(I) sources have been utilized in literature[219]; upon recommendation copper(I) triflate (Cu(I)OTf) was tested here.[238]

7.2.2 Results and discussion

An initial reaction using $CuSO_4$/ascorbic acid as the source of Cu(I) was carried out in a H_2O:DMF mixture at RT, inspired by Namvari *et al*.[232] IR analysis of the product, GO-click$_1$, revealed a continued presence of azide with an IR band at 2120 cm^{-1} as seen in Figure 7.8, indicating incomplete click reaction. The strong band at 1640 cm^{-1} is ascribed to adsorbed water.[116] The reaction was subsequently repeated at 50°C with increased concentration of reagents, producing GO-click$_2$. The product was indispersible in all tested solvents due to reduction of GO-N_3 by ascorbic acid as seen by an IR band at 1580 cm^{-1} due to increased intensity of C=C stretch.

Reactions using solid copper as the source of Cu(I) were similarly tested in a H_2O:DMF mixture at both RT and 50°C with increased concentration of reagents, producing GO-click$_3$ and GO-click$_4$, respectively. Both products revealed unchanged azide groups as seen in Figure 7.8 with the IR band at 2120 cm^{-1}. The reaction with solid copper was then tried under inert conditions, producing GO-click$_5$ with the same result.

Lastly, the use of Cu(I)OTf was tried with GO-N_3 dispersed in acetonitrile (ACN). For the catalytic reaction, Cu(I) is assumed to form copper clusters, which then forms a complex with the alkyne and azide during formation of the triazole as illustrated in Figure 7.6. ACN is a good copper ligand during the transition state as it stabilizes the cluster, while allowing reorganization of the complex for the reaction.[238] GO-N_3 did not form a homogenous dispersion in ACN, so rapid stirring was used to ensure constant mixing of the solution. The reaction was carried out under inert (N_2) conditions as Cu(I) is very sensitive towards oxidation. Deprotonation of the alkyne has to occur for the formation of the dinuclear Cu(I)-alkyne complex to take place, therefore *N*,*N*-diisopropylethylamine (DIPEA) was added in excess relative to Si-alk. The Cu(I)OTf was added for a concentration of app. 100 μM, as concentrations in this range have provided the best performance.[230] GO-click$_6$ was dispersible in aqueous solution, and at a concentration of 0.89 mg/mL in 1:1 D_2O:DMSO-*d*6 GO-click$_6$ aligned menthol, resulting in a Q factor of 0.063 (RDC_{max} 14.83 Hz).

IR analysis of GO-click$_6$ showed an azide band at 2120 cm^{-1} of slightly reduced intensity compared to GO-N_3, which could be interpreted as partial click coupling. However, reduced intensity of the azide band could be due to loss of azide by other mechanisms. Control experiments may have revealed whether the reaction conditions influenced the azide stability. This type of control experiments would be essential for verification of a successful click coupling, especially if IR spectroscopy was the main characterization method. This work is still ongoing with focus on finding suitable reaction conditions and scope of alkynes for successful coupling to produce GO materials with favorable properties for NMR analysis.

The Cu(I) could have been oxidized by reactive species on the GO surface e.g. peroxides or radicals leftover from the synthesis.[239] A potential method to avoid loss of catalytic Cu(I) could to flush GO with Cu(I) species prior to reaction to clear the surface of highly reactive oxidative groups.[238] This theory was not tested due to time limitations. The GO stock solutions used for reactions was more than a year old and the amount of highly reactive species should have attenuated with time.[239]

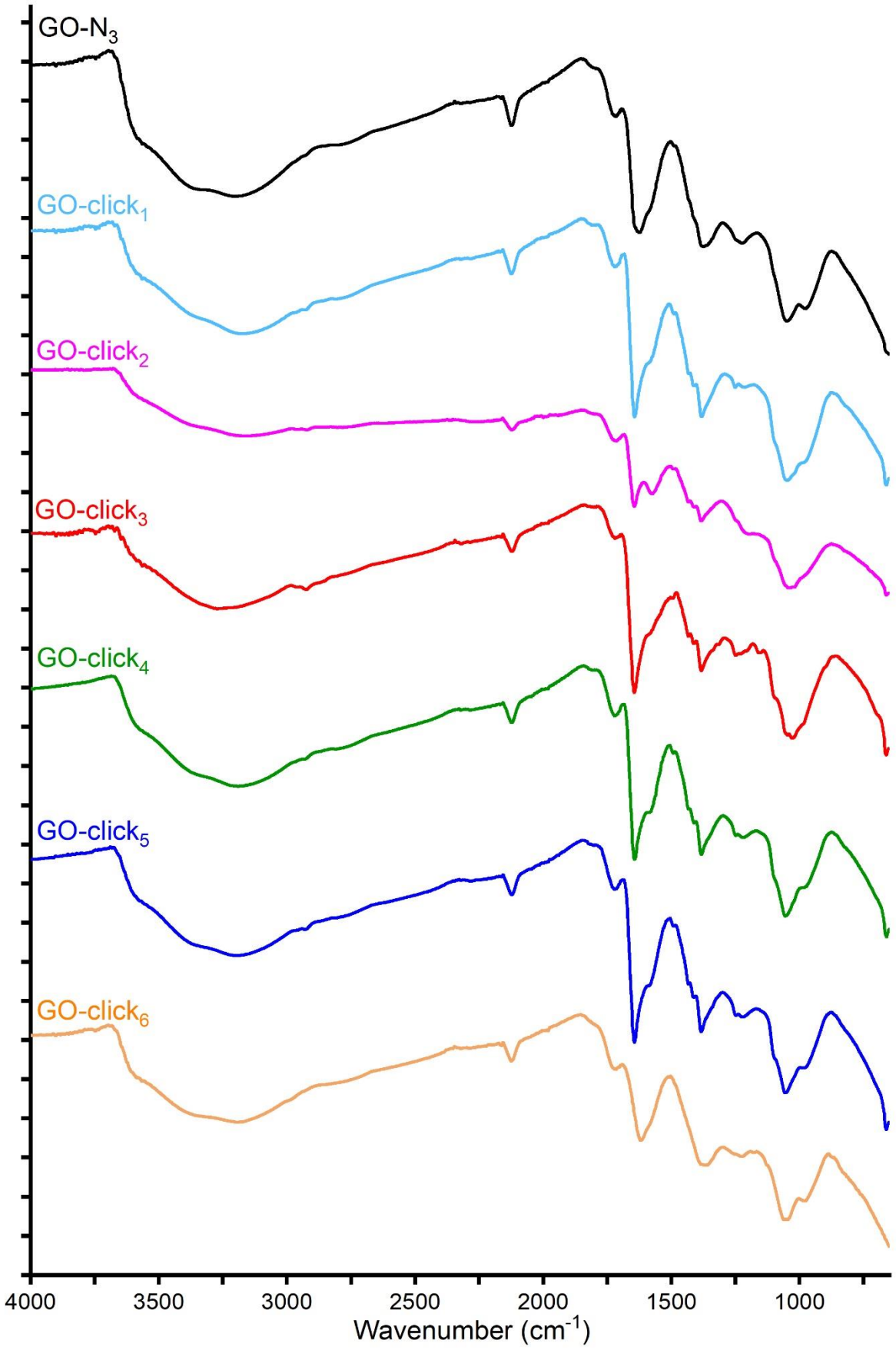

Figure 7.8. IR spectra of GO click products.

7.3 Conclusion

GO was functionalized using sodium azide, producing the material GO-N_3. The presence of covalently bonded azide was confirmed by IR spectroscopy analysis and the spectrum showed no bands due to residual sodium azide. The functionalization occurred via S_N2-like ring opening of the GO epoxides, which correlated with decreased amount of epoxides seen in ^{13}C MAS NMR spectra. Simulation of the 1D ^{13}C MAS spectra revealed a new peak at 189 ppm, which may be a result of deoxygenation during the synthesis.

The product GO-N_3 retained the ability to function as alignment media for NMR structural analysis and displayed increased alignment strength in solvent mixtures with decreased amount of D_2O compared to the alignment behavior of GO. This was explained by the increased hydrophobicity of GO-N_3 due to deoxygenation.

CuAAC click chemistry was tested for further functionalization of GO-N_3. Various sources of catalytic Cu(I) were tried with different reaction conditions. IR analysis of the products revealed continued presence of azide, indicating incomplete reaction. Continued efforts towards GO functionalization will focus on the use of Cu(I) salt as the catalyst for click coupling of alkynes.

7.4 Experimental:

Information regarding instrumentation and acquisition of solution NMR spectra are found in appendix. Structure simulations and back-calculations of RDCs were carried out following the procedure described in Chapter 4. sGO refers to 0.4 w% GO stock solution from Graphenea.[172] Other chemicals were from Sigma Aldrich and used as received.

GO-N_3

100 mg cGO was dispersed in 100 ML DMF in a round-bottomed. After addition of 108.7 mg (1.67 mmol) NaN_3, the solution was heated to 40°C for 48h. The synthesized GO-N_3 was purified of excess NaN_3 by repeated centrifugation in DMF followed by H_2O. The change of solvent was believed to aid the purification process due to solubility of NaN_3.

^{13}C ssNMR spectra acquired at a 150 MHz spectrometer (^{13}C frequency) at magic angle spinning (MAS) rotation speed of 7000 Hz using 90° excitation pulse of 3.85 μs, high-power (100 kHz) ^{1}H SPINAL64 decoupling and a relaxation delay of 60 s. Chemical shift relative to TMS (d=0.0 ppm) using adamantane (d=38.48 ppm) as secondary reference. Line broadening of 200 Hz was applied during processing of spectra.

Deconvolution of ssNMR spectra in TopSpin version 3.6.1 by Bruker using the Solids Line Shape Analysis tool (sola). Simulation of spectra used the CSA model with a Haeberlen fit.

Table 7.2. Relevant parameters from simulation of GO ^{13}C MAS spectra. The simulated spectrum had a 95.9% overlap with the experimental data.

	C=C	C-OH	C-O-C	C-H
Intensity	1911973.9	3052402.1	4849777.6	318848.7
δ(iso)	130.063	69.005	58.684	32.046
δ(CSA)	-114.33	56.37	61.78	0
η(CSA)	0.101	0.085	0.346	0.116
LB*	2175.0953	1639.4245	1813.0294	1741.9088
Integral	276285988	175761487	325461540.9	15675658.7
%	34.8	22.2	41.0	2.0

*Line broadening parameter

Table 7.3. Relevant parameters from simulation of GO-N_3 ^{13}C MAS spectra. The simulated spectrum had a 96.3% overlap with the experimental data.

	C=C	C-OH	C-O-C	C-H	C=O
Intensity	2090802.8	4222482.3	3990694.4	504400.2	992372.4
δ(iso)	131.44	71.041	60.098	32.564	188.873
δ(CSA)	-112.38	49.72	63.71	0	-99.89
η(CSA)	0.006	-0.092	0.519	0	0.651
LB*	2281.9181	1851.4502	1743.0599	1800.693	4754.7186
Integral	1227748747	1045552723	1062589866	102484507	1044927539
%	27.4	23.3	23.7	2.3	23.3

GO click

Following reaction, all GO products were exchanged from organic to aqueous solvent. The products were dispersible in aqueous solution unless otherwise stated.

GO-click$_1$
14.5 mg GO-N3 was dispersed in 10 mL 7:3 H_2O:DMF mixture. 150 µL Si-alk (0.73 mmol), 5.5 mg ascorbic acid (0.031 mmol) and 0.0040 mmol $CuSO_4$ from a stock solution was added. The mixture was stirred at rt for 48h. GO-click$_1$ was purified by centrifugation in DMF and removal of excess Si-alk (4-(tertbutyldimethylsilyloxy)-1-butyne) was verified by ^{1}H NMR.

GO-click$_2$
11.5 mg GO-N_3 was dispersed in 9 mL 2:1 H_2O:DMF mixture. 300 µL Si-alk (1.45 mmol), 12.3 mg ascorbic acid (0.070 mmol), and 0.010 mmol $CuSO_4$ from a stock solution was added. The mixture was stirred at 50°C for 48h. GO-click$_2$ was purified by centrifugation in DMF and removal of excess Si-alk was verified by ^{1}H NMR. The product was indispersible in D_2O, DMSO-*d*6, ethyl acetate, $CDCl_3$, and pyridine-*d*5.

GO-click$_3$
10.4 mg GO-N_3 was dispersed in a 5 mL 7:3 H_2O:DMF mixture. 50 µL Si-alk (0.25 mmol) and 19 mg solid Cu turnings were added. The mixture was stirred at rt for 48h. The solid Cu was then removed with a tweezer. GO-click$_3$ was purified by centrifugation in DMF and removal of excess Si-alk was verified by ^{1}H NMR.

GO-click$_4$
14.5 mg GO-N_3 was dispersed in a 10 mL 7:3 H_2O:DMF mixture. 150 µL Si-alk (0.73 mmol) and 23.2 mg solid Cu turnings were added. The mixture was stirred at 50°C for 48h. The solid Cu was then removed with a tweezer. GO-click$_4$ was purified by centrifugation in DMF and removal of excess Si-alk was verified by ^{1}H NMR.

GO-click$_5$
14.5 mg GO-N_3 was dispersed in a 10 mL 7:3 H_2O:DMF mixture, which were purged with N_2 for 20 min. 150 µL Si-alk (0.73 mmol) and 22.7 mg solid Cu turnings were added before the flask was sealed and the mixture stirred at rt under inert conditions for 48h. Inert atmosphere was created by alternately purging and refilling the flask with N_2 (3x) by standard Schlenk techniques. The solid Cu was then removed with a tweezer. GO-click$_5$ was purified by centrifugation in DMF and removal of excess Si-alk was verified by ^{1}H NMR.

GO-click$_6$
61 mg GO-N_3 was dispersed in 30 mL acetonitrile (ACN). The dispersion was not stabile with visible aggregates. The GO-N_3 solution were diluted to 100 mL with dry ACN, which were purged with N_2 for 20 min. 45 µL DIPEA was added (0.26 mmol). 4 mg $Cu(I)SO_3CF_3$*4ACN (0.011 mmol, 106 µM) was measured and quickly transferred to the flask. Inert atmosphere was created by alternately purging and refilling the flask with N_2 (3x) by standard Schlenk techniques. 35 µL Si-alk (0.17 mmol) dissolved in 1 mL ACN was dropwise added through a septum over 45 min. The mixture was stirred at rt for 48h. GO-click$_6$ was purified by centrifugation in ACN and removal of excess Si-alk was verified by ^{1}H NMR.

8 Structure elucidation of Triculamin – a lasso peptide

NMR spectroscopy can provide information for structure elucidation of a multitude of different types of compounds. In this chapter, NMR analysis was applied in the structure elucidation of the peptide triculamin, revealing a fascinating 3D structural ensemble. The NMR analysis was predominantly based on the use of NOE data, which supplied internuclear distances for use in computational modelling.

The project was a collaboration with the group of Associate Professor Thomas Tørring at Aarhus University, who were responsible for isolation of triculamin from the bacteria *Steptomyces triculaminicus*.[240] All NMR data was acquired at the 950 MHz NMR spectrometer at Aarhus University by Dennis W. Juhl prior to our involvement in the project. A draft for publication with description of the full procedure can be found in appendix.

With the threat of multidrug resistant *Mycobacterium tuberculosis* (MDR-TB), the need for new drugs to treat infections is ever present.[241] Lasso peptides have been reported with diverse bioactivities, among these activity against MDR-TB.[242] Triculamin was discovered in 1967 and reported to have potent anti-mycobacterial activity.[243] Degradation studies had previously established an amino acid content of at least 17 amino acids and fragments of the sequence.[244] The compound alboverticillin is described to have a similar structure and properties, but the structure of alboverticillin is yet unknown.[245] Genome sequencing of *S. triculaminicus* revealed the following peptide sequence, containing the 17 amino acids previously established.[240]

SKKSKPGDGIRGKGVRG

The strain was cultured in 10 L liquid medium for 8 days and triculamin extracted from the medium after separation from the biomass. Isolation of triculamin was achieved by reverse-phase HPLC purification.[240] High-resolution mass spectrometry (HRMS) data provided a molecular weight of 1709.0074, in accordance with the molecular weight of the amino acid sequence above with loss of one H_2O.[240] The mass, stability and bioinformatic analysis indicated triculamin belonged to the group of lasso peptides.[240][244]

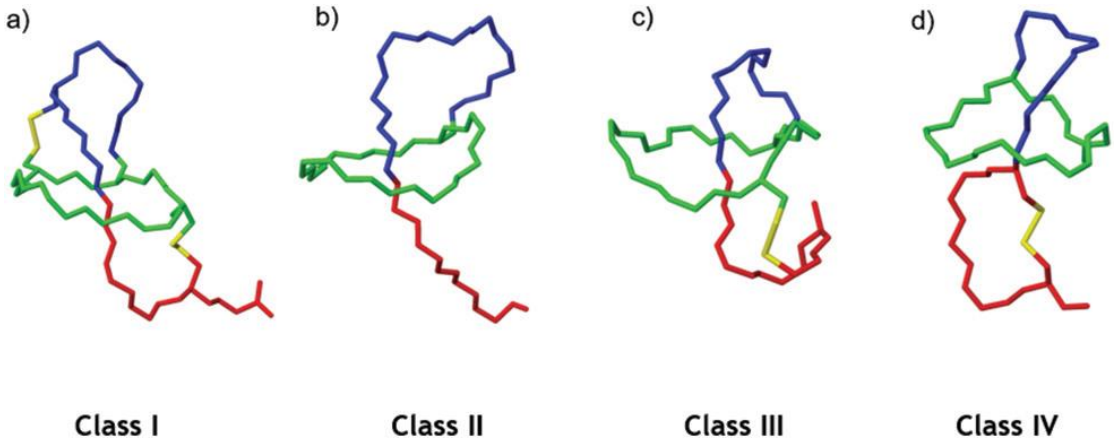

Figure 8.1. Backbone of four classes of lasso peptides. The macrolactam ring is shown in green, the loop of the C-terminus in blue and the tail in red with disulfide bonds in yellow when present. Reproduced from [246] with permission from Royal Society of Chemistry.

Lasso peptides belong to a class of ribosomally synthesized and posttranslationally modified peptides (RiPPs) and are characterized by the N-terminus forming a macrolactam ring with an Asp or Glu side chain, which the C-terminus intersects. Due to the folded structure of lasso peptides, they are very stable against degradation, while displaying great selectivity and potency, making them attractive candidates in drug discovery.[246] The absence of cysteine in the peptide sequence indicated a Class II lasso peptide structure similar to the example in Figure 8.1. Even with the absence of a disulfide bond, Class II lasso peptides are stabile due to bulky amino acids acting like plugs stabilizing the folded structure.

8.1 Assignment

The NMR assignment were carried out independently of the Aarhus group, but were in agreement when compared. An independent assignment was deemed beneficial to obtain an in-depth understanding of the spectra and structure for the subsequent 3D structure generation. ^{1}H, ^{13}C and ^{15}N chemical shifts were assigned using a combination of 1D ^{1}H, ^{1}H-^{13}C HSQC, ^{1}H-^{13}C HSQC-TOCSY, HMBC, and ^{1}H-^{15}N HSQC spectra, see Table 8.1. The HSQC-TOCSY spectrum was used to establish the amino acid side chain spin systems, while the ^{1}H-^{13}C HSQC spectrum resolved overlap in the proton dimension. The repetition of amino acids, especially within the macrolactam ring with 2 serines and 3 lysines, did present a challenge in the assignment process. HMBC and 2D NOESY spectra aided the confirmation of the sequential assignment of the backbone, which were in agreement with the peptide sequence found via analysis of the genome sequence.

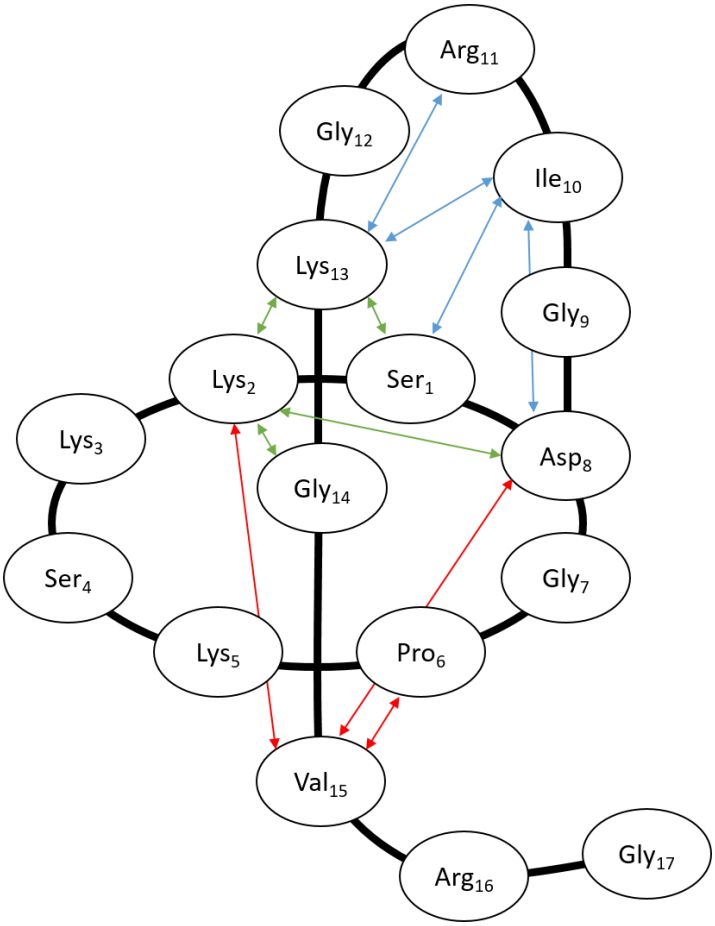

Figure 8.2. Schematic representation of the folded lassopeptide with key observed NOE correlations indicated by arrows.

The macrolactam ring is formed by the Ser_1 N-terminus and the Asp_8 side chain, which was confirmed by HMBC correlations from Ser_1H_α and Ser_1NH to Asp_8C_γ. This was additionally supported by NOE correlations between Asp_8H_β and Ser_1NH. The macrolactam ring closure is in agreement with reported structures of lasso peptides in literature.[246][247] Several NOE correlations from the macrolactam ring to the loop and tail protons supported the initial assumption that triculamin is a lasso peptide. Key NOE correlations are indicated in Figure 8.2.

Additional relevant NOE correlations may have been observed if not for the overlap and interference with the broad water resonance at 4.7 ppm. Furthermore, overlap of signals also decreased the number of usable NOEs, e.g. correlations to Ser_1NH and Lys_5NH was only included in the subsequent analysis after careful consideration as their signals overlap and they share the same chemical environment.

Table 8.1. NMR Assignment of triculamin [ppm]. For protons, the multiplicity, integral, and *J*-coupling constant(s) [Hz] are added where applicable. Missing values indicate unassignable resonances with the spectra available. *Signal affected by water suppression.

AA		NH	N	H_α	H_β	H_γ	H_δ	He	C=O	C_α	C_β	C_γ	C_δ	C_ε	Other
1	Ser	8.05 (m, 1H)	112.8	4.33* (dt, 10.3, 2.6)	3.96 (dd, 1H, 11.7, 3.1) 3.48 (dd, 1H, 11.7, 2.0)	-	-	-	171.8	54.9	62.3	-	-	-	-
2	Lys	9.28 (d, 1H, 8.0)	127.1	4.52* (m)	1.73 (m, 1H) 1.56 (m, 1H)	1.29 (m, 1H) 1.18 (m, 1H)	1.46 (m, 1H)	2.84 (m, 2H)		53.2	28.7	22.5	26.5	39.6	-
3	Lys	7.99 (broad)	122.8	4.52* (m)	1.76 (m, 1H) 1.70 (m, 1H)	1.34 (m, 1H) 1.28 (m, 1H)	1.56 (m, 1H)	2.88 (m, 2H)		55.1	32.5	22.6	26.4	39.5	-
4	Ser	8.40 (m, 1H)	113.7	4.23 (m, 1H)	3.89 (m, 1H) 3.60 (m, 1H)	-	-	-	170.0	55.5	61.0	-	-	-	-
5	Lys	8.04 (m, 1H)	120.7	4.18 (m, 1H)	1.68 (m, 1H) 1.57 (m, 1H)	1.28 (m)		2.86 (m, 2H)		51.9	30.2	21.7		39.5	-
6	Pro	-		4.51* (m)	2.40 (m, 1H) 2.19 (m, 1H)	1.84 (m, 1H) 1.69 (m, 1H)	3.41 (m, 2H)	-	172.5	59.4	32.7	22.1	48.3	-	-
7	Gly	8.56 (d, 1H, 5.1)	106.3	4.52* (m) 3.86 (m)	-	-	-	-	171.4	43.7	-	-	-	-	-
8	Asp	7.71 (d, 1H, 9.9)	119.8	4.8*	3.29 (m, 1H) 2.03 (m, 1H)	-	-	-	173.1	47.8	37.2	170.8	-	-	-
9	Gly	8.41 (m, 1H)	109.1	4.26 (m, 1H) 3.44 (m, 1H)	-	-	-	-	171.0	42.1	-	-	-	-	-
10	Ile	7.30 (d, 1H, 10.2)	121.5	4.21 (m, 1H)	1.73 (m, 1H)	0.82 (d, 3H, 7.2)	1.21 (m, 1H) 1.04 (m, 1H)	0.65 (t, 3H, 7.8)	173.4	56.2	34.9	14.6	24.1	8.6	-
11	Arg	8.65 (s, 1H)	129.6	3.90 (m, 1H)	1.73 (m, 1H) 1.67 (m, 1H)	1.61 (m, 1H) 1.47 (m, 1H)	3.12 (m)	7.10 (t, 1H, 5.9)	174.4	56.1	26.9	24.1	40.7	156.8	N 114.4
12	Gly	8.76 (t, 1H, 6.5)	113.5	4.08 (m, 1H) 3.64 (m, 1H)	-	-	-	-	171.3	42.6	-	-	-	-	-
13	Lys	8.11 (d, 1H, 9.8)	120.5	4.54* (m)	1.96 (m, 1H) 1.80 (m, 1H)	1.14 (m, 1H) 1.10 (m, 1H)	1.51 (m, 1H) 1.39	2.89 (m, 1H) 2.82 (m, 1H)	173.6	52.4	25.7	22.6	31.2	39.8	-
14	Gly	6.60 (d, 1H, 9.5)	105.8	4.75* 3.44 (m, 1H)	-	-	-	-	172.0	43.0	-	-	-	-	-
15	Val			4.12 (m, 1H)	2.23 (m, 1H)	0.79 (d, 3H, 7.3)	0.76 (d, 3H, 7.5)	-	174.6	59.9	29.9	18.9	16.0	-	-
16	Arg	8.35 (d, 1H, 8.4)	120.8	4.43* (m)	1.77 (m, 1H) 1.62 (m, 1H)	1.54 (m)	3.13 (m)	7.13 (t, 1H, 5.6)	173.0	52.8	28.7	25.0	40.4	156.9	N 114.6
17	Gly	8.40 (m, 1H)	112.5	3.88 (m, 1H) 3.76 (dd, 1H, 17.8, 6.0)	-	-	-	-	174.7	42.4	-	-	-	-	-

8.2 Introduction to NOEs

The nuclear Overhauser effect (NOE) is an internuclear dipolar cross-relaxation mechanism that acts through space.[248][249] This sets the NOE apart from other types of structural information conventionally extracted from NMR spectra and used in the elucidation process, as most NMR experiments show nuclear correlations via bonds. In the 2D NOESY NMR experiment, the signal intensity is dependent on individual NOE correlations as expressed in the equations below.[250]

$$\eta_{IS} = \sigma_{IS}\tau_m$$

$$\sigma_{IS} = \left(\frac{\mu_0}{4\pi}\right)^2 \frac{\hbar^2 {\gamma_I}^2 {\gamma_S}^2}{10}\left(\frac{6\tau_c}{1+4\omega^2{\tau_c}^2} - \tau_c\right){r_{IS}}^{-6}$$

Here η_{IS} is the intensity of the NOE signal between the nuclei *I* and *S*, τ_m the mixing time, and σ_{IS} the cross-relaxation rate constant, which can be expressed as depending on the internuclear distance r_{IS}. γ is the gyromagnetic ratio of the nuclei, ω the frequency in rad/s, and τ_c the rotational correlation time.[249]

The cross-relaxation occurs during the mixing time, where correlations between nuclei are developed, which can be controlled as an explicit experimental parameter. The dependence on ${r_{IS}}^{-6}$ means that NOE correlations are observed locally for $r_{IS} < 5$ Å. According to the equations above long mixing times linearly result in higher intensity signals and consequently better *S/N* ratio), however limitations apply. During the mixing time, magnetization is transferred from one nuclei to another, resulting in the correlation seen in the NMR spectra. However, once sufficient magnetization has been built up at this neighboring nucleus, it can diffuse to other nuclei in its vicinity as illustrated in Figure 8.3. This effect, known as spin diffusion, affects the observed intensity, η_{IS}, which then no longer correlates to the correct internuclear distance r_{IS}.[249]

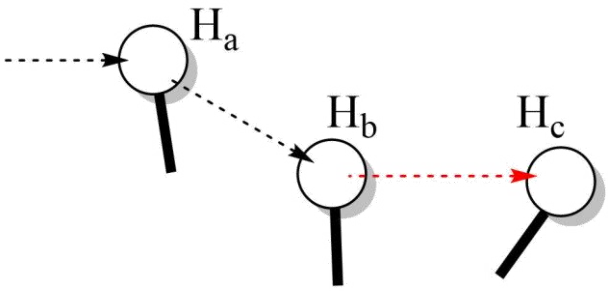

Figure 8.3. Illustration of the concept of spin diffusion. Magnetization from H_a is transferred to H_b during the mixing time. When enough magnetization has been built up at H_b, it can diffuse to H_c as illustrated by the red arrow. The result is an observed lower intensity signal between H_a and H_b, while a "fake" correlation is seen between H_a and H_c.

The extent of spin diffusion can be assessed by acquiring NOESY spectra at different mixing times. A buildup curve is constructed by plotting the mixing time against the integrated signal intensity for each observed NOE correlation; deviations from a linear correlation indicate spin diffusion. Based on this analysis, an assessment of an appropriate mixing time can be made

that allow for the highest signal intensities without significant spin diffusion. The NMR data acquired for triculamin contained NOESY spectra with mixing times of 60, 120, and 200 ms, arguably too few to construct proper buildup curves. The method was still applied and from the 221 NOE correlations observed and quantified from the spectra, 118 was accepted and used for subsequent structure analysis at 120 ms mixing time. The remainder was discarded due to signs of spin diffusion or signal overlap.

Using the isolated spin pair approximation (ISPA)(also known as the initial rate approximation), the NOE intensities can be converted to internuclear distances.[251][252] The approximation assumes the rotational correlation time τ_c is equal for all protons and that cross-relaxing spin pairs behave as isolated spins. By further assuming that everything, but the distance r_{IS}, is constant for all proton pairs in the expression of the cross-relaxation rate constant, the following equation describes the relationship between two separate NOE intensities (η_1, η_2) and their correlated internuclear distances (r_1, r_2) at a defined mixing time.

$$r_1 = r_2 \left(\frac{\eta_1}{\eta_2}\right)^{-1/6}$$

By assuming a value for one internuclear distance (r_2), all other distances can be calculated from their relative NOE intensities.[251][252] Here, 1.78 Å was used as the distance between the germinal protons of Asp_8; as diastereotopic protons their internuclear distance is static and their resonances were free from overlap in the spectra.[251] The distance 2.48 Å for *ortho* aromatic protons have also been described as a possible reference distance.[250] In addition, the peak amplitude normalization for improved cross-relaxation (PANIC) approach was used, which normalize the cross-peak intensities by their diagonal peaks.[250][253][254] This methodology extends the linear range of the NOE buildup curve by taking into account the auto-relaxation of the nuclei. The practical approach to analysis of 2D NOESY data followed here was developed by Casper Hoeck.[250] The same approach was used in the Master's Thesis "Structural Studies of Autoinducing Peptides" by the author.[255] The PANIC approach has recently been included in the Stereofitter plugin for the NMR analysis software Mnova.[256]

8.3 Finding the conformational fit

An initial 3D structure of triculamin was generated in the modelling suite Maestro. Force field methods were used to generate multiple conformers to simulate the behavior of triculamin in solution. Rather than one highly optimized structure, a set of conformers is argued to better represent triculamin in solution as it has a large degree of flexibility. The conformational search was restricted by a total of 19 internuclear distance constraints derived from the NOE intensities. Unconstrained simulations presented too many structures, which did not correlate with the experimental data. The used constraints were considered key to the backbone and lasso structure. The result was a collection of 1498 conformations, displaying a variety of possible structural flexibility. Optimizing this number of structures by DFT methods were not feasible. It was assumed that the large amount of generated structures covered the conformational space inhabited by the compound. To narrow down which structures best fit the complete set of NOE correlations extracted from the NMR data, a Matlab[257] script developed previously in the

group by Casper Hoeck was used.[250] The script accepts structural information in the form of *J*-coupling constant, NOE correlations, and RDCs, and iteratively adds structures that on average fit the data best from a pool of possible structures. Here the program input was the analyzed NOE correlations and the 1498 output structures of the conformational search. Diastereotopic protons can either be averaged if they overlap in the spectra or the program can find the individual assignment that fit the data best. During the fitting procedure, the script will re-evaluate the chosen reference distance to possible account for measurement uncertainties or interference from zero-quantum coherence cross peaks. The output was a set of 11 conformers with an average deviation of 0.6 Å to the experimental data. Each output structure carry different weight in the overall average fit. This is given as a percentage and expresses how often the structure was chosen in the iterative process.

The overlay seen in Figure 8.4 display the conformational stability of the macrolactam and dynamic nature of the loop and tail regions due to the added flexibility. Gly_{14} intersects the ring, while the bulkier Lys_{13} and Val_{15} appear to sterically block movement from above and below the ring. Lys_{13}, Gly_{14}, and Val_{15} also showed multiple NOE correlations to macrolactam protons.

Of 118 included NOE correlations, 58 were associated with amino acids forming the macrolactam ring and the three intersecting amino acids, Lys_{13}, Gly_{14}, and Val_{15}. 54 NOE correlations related to the loop region, while only 6 were from the short tail region. The included NOE correlations were thus evenly distributed between the macrolactam ring and the loop, and evaluation of the deviations between experimental data and fitted structured results in average deviations of 0.65 Å and 0.54 Å for the macrolactam ring and the loop, respectively. The similar values indicate the fitting procedure has provided the best ensemble of structures to fit the entire experimental NMR data available and not favored only one region. The average deviation for the tail was 0.85 Å, which is a reflection of the flexibility of this region.

In parallel, alternative structures were evaluated against the experimental data. The initial assignment process was ambiguous regarding from which direction the C-terminus intersected the macrolactam ring. Structures with opposite (left-handed) folding of the loop was generated following the same modelling procedure as described. These types of structures routinely presented higher average deviations when evaluated against the experimental NOE derived internuclear distances. The (right-handed) folding presented in Figure 8.4 is in agreement with other reported lassopeptides.[247]

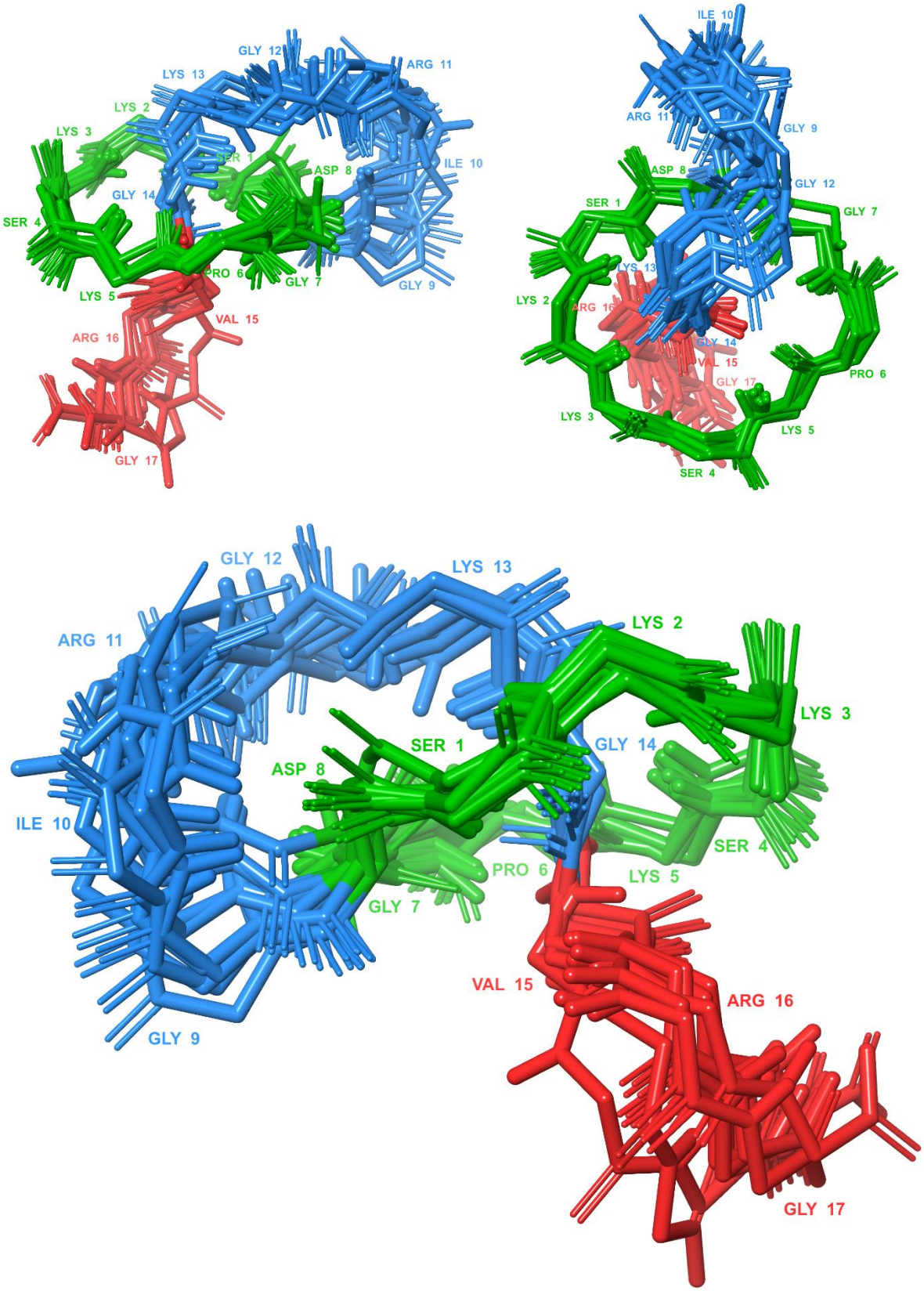

Figure 8.4. Overlay of the 11 conformers representing the 3D structure of triculamin from different angles. Sidechains are not included for clarity. Color legend: green = macrolactam ring, blue = loop, red = tail.

8.4 Conclusion

A 3D structural ensemble of triculamin was explored by restrained molecular modelling using experimentally derived NOE restraints obtained from analysis of NMR spectra. Structure elucidation agreed with the peptide sequence suggested by genome sequencing and confirmed the presence of a macrolactam ring formed by the N-terminal serine to an aspartic acid side chain. Observation of multiple NOE correlations from the C-terminal to the macrolactam ring were consistent with a suggested lasso peptide 3D structure based on bioinformatics analysis. Manual integration of 2D NOESY spectra yielded 118 internuclear distances, which were evaluated against a large collection of conformers generated by computational modelling. An iterative fitting procedure provided a set of 11 conformers, which combined provided the best fit to the experimental data. The combined set of conformers showed conformational stability of the macrolactam ring and the intersecting amino acids, while the loop and tail regions displayed greater flexibility.

This approach will provide a set of conformers that express the dynamic nature of compounds in solution. One single, highly optimized structure will not be the best method to express the 3D structure of flexible compounds with multiple structural conformations. By generating a large set of conformers without heavily constricting the structure, a large degree of dynamic motion is allowed. The iterative fitting process averages the calculated properties for the added selected structures to find a possible best fit for the experimental NOE intensities, which are observed as an average of the conformations present in the sample during data acquisition and thus give insights into the structural space occupied by the compound.

Lasso peptides represent an attractive new type of potential therapeutic compounds due to their combined advantageous properties of larger biomolecules e.g. selectivity and potency with the stability of small molecules. The folded structure of lasso peptides like triculamin is responsible for the enhanced stability, and detailed understanding of their structure is of great benefit for future generation of potent antibiotics.

8.5 Experimental

Incubation, isolation, purification, and acquisition of NMR spectra were carried out by the group of Thomas Tørring and Dennis Wilkens Juhl at Aarhus University (Denmark), see included draft for publication in appendix for further details on the experimental procedure. 10-12 mg freeze-dried triculamin was dissolved in 0.5 mL H_2O:D_2O 90:10 solution. NMR spectra acquired at 298 K on a Bruker 950 MHz Avance III+ spectrometer equipped with a cryogenically cooled triple resonance probe.

NMR processing and NOESY data integration in Topspin 3.6.1 (2018) by Bruker. Experimental details and processing parameters are described as used on Bruker spectrometers.

1D ^{1}H:
Water suppression using pulse program (pp): zgesgp, SI (Fourier transform size): 32k, spectral width (SW): 16 ppm, number of scans (ns): 16, dummy scans (ds): 2, relaxation delay (d1): 1s.

^{1}H-^{13}C HSQC:
Pp: hsqcetgpsp.3, SI: 1k, number of increments (ni): 256, ns: 8, ds: 32, d1: 1.5 s, SW: 16 ppm (F2) x 80 ppm (F1). Spectra zero filled to 2k x 512.

HSQC-TOCSY:
Pp: hsqcdietgpsisp.2, SI: 2k, ni: 256, ns: 64, ds: 32, d1: 2 s, SW: 16 x 80 ppm. Zero filling: 4k x 1k.

HMBC:
Pp: hmbcetgpnd.dwj, SI: 2k, ni: 1k, ns: 170, ds: 16, d1: 1.5 s, SW: 13 x 300 ppm. Zero filling: 4k x 2k.

^{1}H-^{15}N HSQC:
Pp: hsqcetfpf3gpsi2, SI: 2k, ni: 256, ns: 16, ds: 8, d1: 1.5 s, SW: 16 x 32 ppm. Zero filling: 4k x 512.

2D NOESY:
Pp: noeyesgpph, SI: 2k, ni: 1k, ns: 8, ds: 16, d1: 1.5 s, SW: 14 x 14 ppm. Zero filling: 4k x 2k.

Simulations
The modelling suite Maestro version 2018-2 from Schrödinger, LLC, was used to model the initial structure. Program MacroModel version 12.0 from Schrödinger, LLC, was used to perform a conformational search using the force field OPLS05 and water as solvent. The program would use mixed torsional/low mode sampling to alter the conformation by random Monte Carlo simulations before minimizing the new structure. If the newly simulated structure was notably different from previous structures and within an energy minimum, it was saved. To explore the conformational space, the conformational search used an energy cutoff of 50 kJ/mol and 100’000 steps.

Table 8.2. Relative weight of the output structures.

Str.	1	2	3	4	5	6	7	8	9	10	11
Weight [%]	23.1	11.7	11.7	10.8	10.8	10.4	9.2	7.1	3.3	1.8	0.1

9 Overall conclusion and outlook

This thesis contains several studies and techniques that for all carry an aspect of NMR spectroscopy to gain structural information. A common theme has also been the use of multiple analytical methods, which when combined offer new opportunities for characterization of compounds and materials.

NMR structural analysis was applied for the lasso peptide triculamin and in combination with computational modelling, a structural ensemble representing its 3D structure in solution was found. The assignment process of triculamin confirmed the presence of a macrolactam ring at the N-terminus. Computational modelling was used to generate a large collection of conformers, which were evaluated against internuclear distances derived from NOE correlations. The result was a set of 11 conformers that in combination represent the 3D structure of triculamine in solution, displaying flexibility of the folded tail and greater conformational stability of the macrolactam ring. Triculamin displays potent anti-mycobacterial activity making it a potential therapeutic. Lasso peptides are remarkably stable towards thermal and enzymatic treatments due to their folded structure. The encoding gene cluster tolerates variations in the peptide sequence for modifications toward therapeutic applications, thus making lasso peptides a scaffold for future exploration.[242]

The use of NOE correlations provided valuable information on the 3D structure of triculamin. In contrast, the analysis of more complex natural compounds may be challenged or hindered by the lack of structural information from NMR data, as is the case for proton-deficient compounds, where observations of both NOE correlations and *J*-coupling constants might be scarce. Here NMR spectra acquired for compounds under anisotropic conditions can supply additional structural information, which can aid in the assignment of stereocenters, reflect intramolecular dynamic motion or reveal positioning of different regions of modular structures.

GO is a novel alignment media for acquisition of NMR spectra under anisotropic conditions. Chapter 4 concerned the alignment properties of GO solutions with discussions of various practical parameters associated with sample preparation to deepen the understanding on the possibilities and limitations for application of GO. Advantages of the use of GO as alignment media include simple sample preparation, acquisition of high quality anisotropic NMR spectra, and easy recovery of the studied compounds. Among the limitations can be mentioned the loss of alignment in organic solvents and the inability to distinguish between enantiomers for unfunctionalized GO.

To expand the utility of GO as alignment media, multiple methods of functionalization was tried. Chapter 5 and 6 described the efforts towards GO functionalization by amide coupling and carboxylation. Various reagents and reaction conditions were tested, and modified GO materials were obtained that displayed alignment properties. Characterization of the synthesized GO materials was unable to definitively verify covalent functionalization by use of AFM, IR and ^{13}C MAS NMR spectroscopy. The characterization efforts were challenged by the fact that characteristics signifying covalent bond formation are obscured by signals originating from the GO backbone. Furthermore, the importance of distinguishing the effects of side reactions was shown. There is still many unanswered questions regarding the structure

and innate reactivity of GO, which complicate the analysis of synthesis products. A comprehensive literature search did not provide better methods of characterization. A comparison by Vacchi *et al*. in 2016 concluded that coupling of amines to GO happens by epoxide ring opening and not amidation.[212] This result may yet inspire wide debate on GO amidation and influence the design of future experiments.

Click chemistry offered an orthogonal functionalization strategy after the successful introduction of azides on the GO sheets was achieved. The CuAAC click reaction, though so far unsuccessful, remain a functionalization strategy with great potential. The orthogonal reactivity is an advantage with the multitude of functional groups present on GO and offer a wide distribution of functionalization products. Continued efforts towards GO functionalization using a click approach are currently being pursued, also evaluating optimal reaction conditions and scope for the use of alkynes as the first future steps to drive this reaction.

As described above, GO has been explored as alignment media for NMR spectra under anisotropic conditions with many practical observations for future endeavors and potential as results. However, the goal of synthesizing a novel, chiral, functionalized GO alignment media for structural analysis of organic compounds was only partly achieved. The many pending questions regarding the nature of GO proved to be a large obstacle for the design of effective synthesis methods. Different functionalization strategies were pursued, but all were challenged by the lack of techniques for accurate, quantitative characterization of the functionalized products. Consequently, future GO functionalization efforts will be accompanied by a search for techniques that can provide unambiguous verification of covalent bond formation with a special focus on quantifying the degree of functionalization. However, the knowledge gained in the process show the potential for the planned application and more opportunities to resolve the bottlenecks in analysis.

A part of the challenge is that GO related research in modern science is a new field and thus conventions regarding synthesis, characterization, and scope of the field have not fully formed yet. As pointed out in 2020 by Wang *et al*., the doping of graphene with practically anything has been reported to enhance its electrocatalytic effect[258], however there is a risk that without a deeper understanding of the mechanisms and reactivity behind, time, effort, and resources will be wasted on unnecessary studies.

A complete understanding of the structure of GO and the development of optimized functionalization methods might only be fully realized by an interdisciplinary effort by researchers of nano-, organic-, and analytical chemistry.

The use of isotope labelling has provided key information about the structure of GO.[112][116] The analysis of ^{13}C labelled GO by ssNMR provided insight of the GO structure, and the methodology could be expanded to investigate GO functionalization products, potentially contributing with detailed, quantifiable information about covalent binding on the surface.[112] ^{13}C labelled GO was obtained by oxidation of ^{13}C labelled graphene produced by chemical vapor deposition using a labelled starting material.[112] Synthesis of graphene in the amounts needed for extended analysis is laborious by chemical vapor deposition and is thus not easily

applicable for large scale applications. Dynamic nuclear polarization (DNP) NMR could be used for analysis of functionalized products with ^{13}C labelled reagents, providing information on the presence and chemical environment of the reagent after reaction.

Combination of technologies may offer great advantages. TGA-MS allow a more nuanced understanding of GO decomposition products and when combined with isotope labelling, characterization of functionalized GO can be discussed in greater detail.[109][115][220][259] AFM-IR enables IR spectroscopy at AFM resolution, which provides more detailed mapping of the GO surface.[125] With the effort to develop smaller AFM tips, structural information at enhanced lateral resolution may be obtained.

The continued pursuit of structural information at atomic resolution are beneficial for the characterization efforts of GO materials. High-resolution TEM images at atomic resolution provided essential information for the understanding of GO structure, however the intense electron beam used in TEM can degrade the sample during measurements, making analysis of functionalized products challenging.[110][124]

The development of TEM has resulted in the emergence of single-particle electron cryo-microscopy (cryo-EM), which can resolve 3D structures at true atomic resolution, though so far only applied to proteins.[260][261] GO has been applied as an affinity grid for cryo-EM, but studies have not focused on the structure of GO itself.[262] Due to the diverse chemical functionality randomly distributed on GO, resolving its structure represents a different type of challenge.

As argued above, the scope of GO related research is still at the forefront of the field and has potential in several scientific disciplines, where control of GO functionalization may impact both current applications in NMR analysis, catalysis, biosensors, energy materials, biomedicine, and also new ones.

10 References

[1] D. J. Newman, G. M. Cragg, *J. Nat. Prod.* **2020**, *83*, 770–803.

[2] A. G. Atanasov, S. B. Zotchev, V. M. Dirsch, I. E. Orhan, M. Banach, J. M. Rollinger, D. Barreca, W. Weckwerth, R. Bauer, E. A. Bayer, M. Majeed, A. Bishayee, V. Bochkov, G. K. Bonn, N. Braidy, F. Bucar, A. Cifuentes, G. D'Onofrio, M. Bodkin, M. Diederich, A. T. Dinkova-Kostova, T. Efferth, K. El Bairi, N. Arkells, T. P. Fan, B. L. Fiebich, M. Freissmuth, M. I. Georgiev, S. Gibbons, K. M. Godfrey, C. W. Gruber, J. Heer, L. A. Huber, E. Ibanez, A. Kijjoa, A. K. Kiss, A. Lu, F. A. Macias, M. J. S. Miller, A. Mocan, R. Müller, F. Nicoletti, G. Perry, V. Pittalà, L. Rastrelli, M. Ristow, G. L. Russo, A. S. Silva, D. Schuster, H. Sheridan, K. Skalicka-Woźniak, L. Skaltsounis, E. Sobarzo-Sánchez, D. S. Bredt, H. Stuppner, A. Sureda, N. T. Tzvetkov, R. A. Vacca, B. B. Aggarwal, M. Battino, F. Giampieri, M. Wink, J. L. Wolfender, J. Xiao, A. W. K. Yeung, G. Lizard, M. A. Popp, M. Heinrich, I. Berindan-Neagoe, M. Stadler, M. Daglia, R. Verpoorte, C. T. Supuran, *Nat. Rev. Drug Discov.* **2021**, *20*, 200–216.

[3] M. E. García, S. Pagola, A. Navarro-Vázquez, D. D. Phillips, C. Gayathri, H. Krakauer, P. W. Stephens, V. E. Nicotra, R. R. Gil, *Angew. Chemie - Int. Ed.* **2009**, *48*, 5670–5674.

[4] A. Schuetz, J. Junker, A. Leonov, O. F. Lange, T. F. Molinski, C. Griesinger, *J. Am. Chem. Soc.* **2007**, *129*, 15114–15115.

[5] Y. Liu, J. Saurí, E. Mevers, M. W. Peczuh, H. Hiemstra, J. Clardy, G. E. Martin, R. T. Williamson, *Science* **2017**, *356*, eaam5349.

[6] A. Z. Monroe, W. H. Gordon, J. S. Wood, G. E. Martin, J. B. Morgan, R. T. Williamson, *Chem. Commun.* **2021**, *57*, 5658–5661.

[7] X. Lei, Z. Xu, H. Sun, S. Wang, C. Griesinger, L. Peng, C. Gao, R. X. Tan, *J. Am. Chem. Soc.* **2014**, *136*, 11280–11283.

[8] D. R. Dreyer, S. Park, C. W. Bielawski, R. S. Ruoff, *Chem. Soc. Rev.* **2010**, *39*, 228–240.

[9] W. Zong, G. W. Li, J. M. Cao, X. Lei, M. L. Hu, H. Sun, C. Griesinger, R. X. Tan, *Angew. Chemie - Int. Ed.* **2016**, *55*, 3690–3693.

[10] J. A. A. França, A. Navarro-Vázquez, X. Lei, H. Sun, C. Griesinger, F. Hallwass, *Magn. Reson. Chem.* **2017**, *55*, 297–303.

[11] The Royal Swedish Academy of Sciences, "Graphene – the perfect atomic lattice," can be found under https://www.nobelprize.org/prizes/physics/2010/press-release/, **2010**.

[12] I. V. G. and A. A. F. K. S. Novoselov, A. K. Geim, S. V. Morozov, D. Jiang, Y. Zhang, S. V. Dubonos, *Science* **2004**, *306*, 666–669.

[13] K. S. Novoselov, D. Jiang, F. Schedin, T. J. Booth, V. V. Khotkevich, S. V. Morozov, A. K. Geim, *Proc. Natl. Acad. Sci. U. S. A.* **2005**, *102*, 10451–10453.

[14] "Graphene-flagship," can be found under https://graphene-flagship.eu/

[15] K. S. Kim, Y. Zhao, H. Jang, S. Y. Lee, J. M. Kim, K. S. Kim, J. H. Ahn, P. Kim, J. Y. Choi, B. H. Hong, *Nature* **2009**, *457*, 706–710.

[16] Y. Hernandez, V. Nicolosi, M. Lotya, F. M. Blighe, Z. Sun, S. De, I. T. McGovern, B. Holland, M. Byrne, Y. K. Gun'ko, J. J. Boland, P. Niraj, G. Duesberg, S. Krishnamurthy, R. Goodhue, J. Hutchison, V. Scardaci, A. C. Ferrari, J. N. Coleman, *Nat. Nanotechnol.* **2008**, *3*, 563–568.

[17] C. K. Chua, M. Pumera, *Chem. Soc. Rev.* **2014**, *43*, 291–312.

[18] B.C. Brodie, *Ann. Chim. Phys.* **1855**, *45*, 351–352.

[19] B.C. Brodie, *Philos. Trans. R. Soc. London* **1859**, *149*, 249–259.

[20] K. D. Pedersen, J. Zhang, C. H. Gotfredsen, *Magn. Reson. Chem.* **2021**, *59*, 738–745.

[21] J. Giberson, J. Scicluna, N. Legge, J. Longstaffe, in *Annu. Reports NMR Spectrosc.*, Elsevier Ltd., **2021**, pp. 153–246.

[22] J. Keeler, *Understanding NMR Spectroscopy*, Wiley, **2010**.

[23] T. D. W. Claridge, *High-Resolution NMR Techniques in Organic Chemistry*, Elsevier, **2016**.

[24] E. Pretsch, P. Bühlmann, M. Badertscher, *Structure Determination of Organic Compounds: Tables of Spectral Data*, Springer, **2009**.

[25] J. Saurí, W. Bermel, A. V Buevich, E. C. Sherer, L. A. Joyce, M. H. M. Sharaf, P. L. Schiff, T. Parella, R. T. Williamson, G. E. Martin, *Angew. Chem. Int. Ed.* **2015**, *54*, 10160–10164.

[26] E. Mevers, J. Saurí, Y. Liu, A. Moser, T. R. Ramadhar, M. Varlan, R. Thomas Williamson, G. E. Martin, J. Clardy, *J. Am. Chem. Soc.* **2016**, *138*, 12324–12327.

[27] S. Immel, M. Köck, M. Reggelin, *Chirality* **2019**, *31*, 384–400.

[28] C. M. Thiele, S. Berger, *Org. Lett.* **2003**, *5*, 705–708.

[29] C. M. Thiele, *Angew. Chemie - Int. Ed.* **2005**, *44*, 2787–2790.

[30] G. Kummerlöwe, S. L. Grage, C. M. Thiele, I. Kuprov, A. S. Ulrich, B. Luy, *J. Magn. Reson.* **2011**, *209*, 19–30.

[31] P. Lesot, C. Aroulanda, P. Berdagué, A. Meddour, D. Merlet, J. Farjon, N. Giraud, O. Lafon, *Prog. Nucl. Magn. Reson. Spectrosc.* **2020**, *116*, 85–154.

[32] Y. Liu, A. Navarro-Vázquez, R. R. Gil, C. Griesinger, G. E. Martin, R. T. Williamson, *Nat. Protoc.* **2019**, *14*, 217–247.

[33] C. M. Thiele, *European J. Org. Chem.* **2008**, 5673–5685.

[34] G.-W. Li, H. Liu, F. Qui, X. Wang, X. Lei, *Nat. Products Bioprospect.* **2018**, *8*, 279–295.

[35] V. Schmidts, *Magn. Reson. Chem.* **2017**, *55*, 54–60.

[36] F. Hallwass, M. Schmidt, H. Sun, A. Mazur, G. Kummerlöwe, B. Luy, A. Navarro-Vázquez, C. Griesinger, U. M. Reinscheid, *Angew. Chemie - Int. Ed.* **2011**, *50*, 9487–9490.

[37] N. Nath, M. Schmidt, R. R. Gil, R. T. Williamson, G. E. Martin, A. Navarro-Vázquez, C. Griesinger, Y. Liu, *J. Am.*

Chem. Soc. **2016**, *138*, 9548–9556.
[38] M. Sarfati, P. Lesot, D. Merlet, J. Courtieu, *Chem. Commun.* **2000**, 2069–2081.
[39] P. Lesot, R. R. Gil, P. Berdagué, A. Navarro-Vázquez, *J. Nat. Prod.* **2020**, *83*, 3141–3148.
[40] A. Saupe, G. Englert, *Phys. Rev. Lett.* **1963**, *11*, 462–464.
[41] A. Saupe, *Angew. Chemie Int. Ed.* **1968**, *7*, 97–112.
[42] H. C. Kung, K. Y. Wang, I. Goljer, P. H. Bolton, *J. Magn. Reson. Ser. B* **1995**, *109*, 323–325.
[43] J. R. Tolman, J. M. Flanagan, M. A. Kennedy, J. H. Prestegard, *Proc. Natl. Acad. Sci. U. S. A.* **1995**, *92*, 9279–9283.
[44] N. Tjandra, A. Bax, *Science* **1997**, *278*, 1111–1114.
[45] G. Kummerlöwe, B. Luy, *Trends Anal. Chem.* **2009**, *28*, 483–493.
[46] F. Kramer, M. V. Deshmukh, H. Kessler, S. J. Glaser, *Concepts Magn. Reson. Part A Bridg. Educ. Res.* **2004**, *21*, 10–21.
[47] M. H. Levitt, *Spin Dynamics: Basics of Nuclear Magnetic Resonance*, 2nd Ed., John Wiley & Sons Ltd, **2008**.
[48] A. Navarro-Vázquez, *Magn. Reson. Chem.* **2012**, *50*, S73–S79.
[49] M. Rückert, G. Otting, *J. Am. Chem. Soc.* **2000**, *122*, 7793–7797.
[50] M. R. Hansen, L. Mueller, A. Pardi, *Nat. Struct. Biol.* **1998**, *5*, 1065–1074.
[51] A. Marx, C. Thiele, *Chem. - A Eur. J.* **2009**, *15*, 254–260.
[52] I. Canet, J. Courtieu, A. Meddour, J. M. Pechine, A. Loewenstein, *J. Am. Chem. Soc.* **1995**, *117*, 6520–6526.
[53] A. Meddour, P. Berdague, A. Hedli, J. Courtieu, P. Lesot, *J. Am. Chem. Soc.* **1997**, *119*, 4502–4508.
[54] A. Marx, V. Schmidts, C. M. Thiele, *Magn. Reson. Chem.* **2009**, *47*, 734–740.
[55] C. Aroulanda, M. Sarfati, J. Courtieu, P. Lesot, *Enantiomer* **2001**, *6*, 281–287.
[56] C. M. Thiele, *J. Org. Chem.* **2004**, *69*, 7403–7413.
[57] L. Arnold, A. Marx, C. M. Thiele, M. Reggelin, *Chem. - A Eur. J.* **2010**, *16*, 10342–10346.
[58] M. Dama, S. Berger, *Org. Lett.* **2012**, *14*, 241–243.
[59] M. Reller, S. Wesp, M. R. M. Koos, M. Reggelin, B. Luy, *Chem. - A Eur. J.* **2017**, *23*, 13351–1335.
[60] A. Krupp, M. Reggelin, *Magn. Reson. Chem.* **2012**, *50*, S45–S52.
[61] N. C. Meyer, A. Krupp, V. Schmidts, C. M. Thiele, M. Reggelin, *Angew. Chemie - Int. Ed.* **2012**, *51*, 8334–8338.
[62] A. Krupp, M. Noll, M. Reggelin, *Magn. Reson. Chem.* **2021**, *59*, 577–586.
[63] M. Schwab, D. Herold, C. M. Thiele, *Chem. - A Eur. J.* **2017**, *23*, 14576–14584.
[64] Z. K. Ma, X. Y. Han, H. Liu, J. C. Ji, S. Y. Qin, X. D. Li, X. Lei, *New J. Chem.* **2020**, *44*, 4262–4265.
[65] B. Deloche, E. T. Samulski, *Macromolecules* **1981**, *14*, 575–581.
[66] H. J. Sass, G. Musco, S. J. Stahl, P. T. Wingfield, S. Grzesiek, *J. Biomol. NMR* **2000**, *18*, 303–309.
[67] R. Tycko, F. J. Blanco, Y. Ishii, *J. Am. Chem. Soc.* **2000**, *122*, 9340–9341.
[68] J. C. Freudenberger, S. Knör, K. Kobzar, D. Heckmann, T. Paululat, H. Kessler, B. Luy, *Angew. Chemie - Int. Ed.* **2005**, *44*, 423–426.
[69] C. Gayathri, N. V. Tsarevsky, R. R. Gil, *Chem. - A Eur. J.* **2010**, *16*, 3622–3626.
[70] G. Kummerlöwe, E. F. McCord, S. F. Cheatham, S. Niss, R. W. Schnell, B. Luy, *Chem. - A Eur. J.* **2010**, *16*, 7087–7089.
[71] J. C. Freudenberger, P. Spiteller, R. Bauer, H. Kessler, B. Luy, *J. Am. Chem. Soc.* **2004**, *126*, 14690–14691.
[72] B. Luy, K. Kobzar, H. Kessler, *Angew. Chemie - Int. Ed.* **2004**, *43*, 1092–1094.
[73] P. Haberz, J. Farjon, C. Griesinger, *Angew. Chemie - Int. Ed.* **2005**, *44*, 427–429.
[74] G. Kummerlöwe, J. Auernheimer, A. Lendlein, B. Luy, *J. Am. Chem. Soc.* **2007**, *129*, 6080–6081.
[75] R. R. Gil, C. Gayathri, N. V. Tsarevsky, K. Matyjaszewski, *J. Org. Chem.* **2008**, *73*, 840–848.
[76] T. Montag, C. M. Thiele, *Chem. - A Eur. J.* **2013**, *19*, 2271–2274.
[77] C. Merle, G. Kummerlöwe, J. C. Freudenberger, F. Halbach, W. Stöwer, C. L. V. Gostomski, J. Höpfner, T. Beskers, M. Wilhelm, B. Luy, *Angew. Chemie - Int. Ed.* **2013**, *52*, 10309–10312.
[78] L. F. Gil-Silva, R. Santamaría-Fernández, A. Navarro-Vázquez, R. R. Gil, *Chem. Eur. J.* **2016**, *22*, 472–476.
[79] M. E. García, S. R. Woodruff, E. Hellemann, N. V. Tsarevsky, R. R. Gil, *Magn. Reson. Chem.* **2017**, *55*, 206–209.
[80] F. Jensen, *Introduction to Computational Chemistry*, 3rd Ed., John Wiley & Sons Ltd, **2017**.
[81] T. Bally, P. R. Rablen, *J. Org. Chem.* **2011**, 4818–4830.
[82] C. Adamo, V. Barone, *J. Phys. Chem.* **1998**, *108*, 664.
[83] A. D. Becke, *J. Chem. Phys.* **1993**, *98*, 5648.
[84] P. J. Stephens, F. J. Devlin, D. F. Chabalowski, M. J. Frisch, *J. Phys. Chem.* **1994**, *98*, 11623–11627.
[85] A. M. Dimiev, S. Eigler, Eds. , *Graphene Oxide: Fundamentals and Applications*, Wiley, **2017**.
[86] C. Schafthäutl, *J. für Prakt. Chemie* **1840**, *21*, 129–157.
[87] C. Schafthäutl, *J. für Prakt. Chemie* **1859**, *76*, 257–310.
[88] F. Gottschalk, *J. für Prakt. Chemie* **1865**, *95*, 321–350.
[89] L. Staudenmaier, *Berichte Der Dtsch. Chem. Gesellschaft* **1898**, *31*, 1481–1487.
[90] W. S. Hummers, R. E. Offeman, *J. Am. Chem. Soc.* **1958**, *80*, 1339–1339.
[91] N. I. Kovtyukhova, P. J. Ollivier, B. R. Martin, T. E. Mallouk, S. A. Chizhik, E. V. Buzaneva, A. D. Gorchinskiy, *Chem. Mater.* **1999**, *11*, 771–778.
[92] D. C. Marcano, D. V. Kosynkin, J. M. Berlin, A. Sinitskii, Z. Sun, A. Slesarev, L. B. Alemany, W. Lu, J. M. Tour, *ACS Nano* **2010**, *4*, 4806–4814.
[93] U. Hofmann, *Berichte Der Dtsch. Chem. Gesellschaft* **1928**, *61*, 435–441.
[94] U. Hofmann, A. Frenzel, *Berichte Der Dtsch. Chem. Gesellschaft* **1930**, *63*, 1248–1262.
[95] U. Hofmann, A. Frenzel, E. Csalán, *Justus Liebigs Ann. Chem.* **1934**, *510*, 1–41.
[96] H. Thiele, *Zeitschrift für Anorg. und Allg. Chemie* **1930**, *190*, 145–160.
[97] G. Ruess, *Monatshefte für Chemie und Verwandte Teile Anderer Wissenschaften* **1947**, *76*, 381–417.

[98] W. Scholz, H. P. Boehm, *Zeitschrift Fur Anorg. Und Allg. Chemie* **1969**, *369*, 327–340.
[99] M. Mermoux, Y. Chabre, *Synth. Met.* **1989**, *34*, 157–162.
[100] M. Mermoux, Y. Chabre, A. Rousseau, *Carbon N. Y.* **1991**, *29*, 469–474.
[101] H. He, T. Riedl, A. Lerf, J. Klinowski, *J. Phys. Chem.* **1996**, *100*, 19954–19958.
[102] H. He, J. Klinowski, M. Forster, A. Lerf, *Chem. Phys. Lett.* **1998**, *287*, 53–56.
[103] A. Lerf, H. He, M. Forster, J. Klinowski, *J. Phys. Chem. B* **1998**, *102*, 4477–4482.
[104] H. Thiele, *Kolloid-zeitschrift* **1937**, *80*, 1–20.
[105] A. M. Dimiev, J. M. Tour, *ACS Nano* **2014**, *8*, 3060–3068.
[106] G. Shao, Y. Lu, F. Wu, C. Yang, F. Zeng, Q. Wu, *J. Mater. Sci.* **2012**, *47*, 4400–4409.
[107] L. Zhang, J. Liang, Y. Huang, Y. Ma, Y. Wang, Y. Chen, *Carbon N. Y.* **2009**, *47*, 3365–3368.
[108] A. Dimiev, D. V. Kosynkin, L. B. Alemany, P. Chaguine, J. M. Tour, *J. Am. Chem. Soc.* **2012**, *134*, 2815–2822.
[109] S. Eigler, C. Dotzer, F. Hof, W. Bauer, A. Hirsch, *Chem. - A Eur. J.* **2013**, *19*, 9490–9496.
[110] K. Erickson, R. Erni, Z. Lee, N. Alem, W. Gannett, A. Zettl, *Adv. Mater.* **2010**, *22*, 4467–4472.
[111] T. Nakajima, A. Mabuchi, R. Hagiwara, *Carbon N. Y.* **1988**, *26*, 357–361.
[112] W. Cai, R. D. Piner, F. J. Stadermann, S. Park, M. A. Shaibat, Y. Ishii, D. Yang, A. Velamakanni, J. A. Sung, M. Stoller, J. An, D. Chen, R. S. Ruoff, *Science* **2008**, *321*, 1815–1817.
[113] S. Stankovich, R. D. Piner, X. Chen, N. Wu, S. T. Nguyen, R. S. Ruoff, *J. Mater. Chem.* **2006**, *16*, 155–158.
[114] A. C. Ferrari, J. C. Meyer, V. Scardaci, C. Casiraghi, M. Lazzeri, F. Mauri, S. Piscanec, D. Jiang, K. S. Novoselov, S. Roth, A. K. Geim, *Phys. Rev. Lett.* **2006**, *97*, 1–4.
[115] S. Eigler, C. Dotzer, A. Hirsch, *Carbon N. Y.* **2012**, *50*, 3666–3673.
[116] T. Szabó, O. Berkesi, I. Dékány, *Carbon N. Y.* **2005**, *43*, 3186–3189.
[117] D. Hadži, A. Novak, *Trans. Faraday Soc.* **1955**, *51*, 1614–1620.
[118] A. Clauss, R. Plass, H. P. Boehm, U. Hofmann, *Zeitschrift Fur Anorg. Und Allg. Chemie* **1957**, *291*, 205–220.
[119] T. Szabó, O. Berkesi, P. Forgó, K. Josepovits, Y. Sanakis, D. Petridis, I. Dékány, *Chem. Mater.* **2006**, *18*, 2740–2749.
[120] H. P. Boehm, A. Clauss, G. O. Fischer, U. Hofmann, *Zeitschrift für Anorg. und Allg. Chemie* **1962**, *316*, 119–127.
[121] S. Stankovich, D. A. Dikin, G. H. B. Dommett, K. M. Kohlhaas, E. J. Zimney, E. A. Stach, R. D. Piner, S. B. T. Nguyen, R. S. Ruoff, *Nature* **2006**, *442*, 282–286.
[122] D. Pandey, R. Reifenberger, R. Piner, *Surf. Sci.* **2008**, *602*, 1607–1613.
[123] C. Gómez-Navarro, J. C. Meyer, R. S. Sundaram, A. Chuvilin, S. Kurasch, M. Burghard, K. Kern, U. Kaiser, *Nano Lett.* **2010**, *10*, 1144–1148.
[124] S. H. Dave, C. Gong, A. W. Robertson, J. H. Warner, J. C. Grossman, *ACS Nano* **2016**, *10*, 7515–7522.
[125] Z. Liu, K. Nørgaard, M. H. Overgaard, M. Ceccato, D. M. A. Mackenzie, N. Stenger, S. L. S. Stipp, T. Hassenkam, *Carbon N. Y.* **2018**, *127*, 141–148.
[126] A. M. Dimiev, L. B. Alemany, J. M. Tour, *ACS Nano* **2013**, *7*, 576–588.
[127] S. Stankovich, D. A. Dikin, R. D. Piner, K. A. Kohlhaas, A. Kleinhammes, Y. Jia, Y. Wu, S. B. T. Nguyen, R. S. Ruoff, *Carbon N. Y.* **2007**, *45*, 1558–1565.
[128] G. Binnig, C. F. Quate, *Phys. Rev. Lett.* **1986**, *56*, 930–934.
[129] J. P. Rourke, P. A. Pandey, J. J. Moore, M. Bates, I. A. Kinloch, R. J. Young, N. R. Wilson, *Angew. Chemie - Int. Ed.* **2011**, *50*, 3173–3177.
[130] H. R. Thomas, S. P. Day, W. E. Woodruff, C. Vallés, R. J. Young, I. A. Kinloch, G. W. Morley, J. V. Hanna, N. R. Wilson, J. P. Rourke, *Chem. Mater.* **2013**, *25*, 3580–3588.
[131] A. M. Dimiev, T. A. Polson, *Carbon N. Y.* **2015**, *93*, 544–554.
[132] J. P. Rourke, N. R. Wilson, *Carbon N. Y.* **2016**, *96*, 339–341.
[133] J. Chen, Y. Zhang, M. Zhang, B. Yao, Y. Li, L. Huang, C. Li, G. Shi, *Chem. Sci.* **2016**, *7*, 1874–1881.
[134] S. Eigler, M. Enzelberger-Heim, S. Grimm, P. Hofmann, W. Kroener, A. Geworski, C. Dotzer, M. Röckert, J. Xiao, C. Papp, O. Lytken, H. P. Steinrück, P. Müller, A. Hirsch, *Adv. Mater.* **2013**, *25*, 3583–3587.
[135] I. Rodriguez-Pastor, G. Ramos-Fernandez, H. Varela-Rizo, M. Terrones, I. Martin-Gullon, *Carbon N. Y.* **2015**, *84*, 299–309.
[136] J. E. Kim, T. H. Han, S. H. Lee, J. Y. Kim, C. W. Ahn, J. M. Yun, S. O. Kim, *Angew. Chemie - Int. Ed.* **2011**, *50*, 3043–3047.
[137] Z. Xu, C. Gao, *ACS Nano* **2011**, *5*, 2908–2915.
[138] L. Onsager, *Ann. N. Y. Acad. Sci.* **1949**, *51*, 627–659.
[139] A. P. Draude, I. Dierking, *Crystals* **2019**, *9*, 455.
[140] F. M. Van Der Kooij, H. N. W. Lekkerkerker, *Philos. Trans. R. Soc. A Math. Phys. Eng. Sci.* **2001**, *359*, 985–995.
[141] W. Du, H. Wu, H. Chen, G. Xu, C. Li, *Carbon N. Y.* **2020**, *158*, 568–579.
[142] B. Konkena, S. Vasudevan, *J. Phys. Chem. Lett.* **2012**, *3*, 867–872.
[143] D. Li, M. B. Müller, S. Gilje, R. B. Kaner, G. G. Wallace, *Nat. Nanotechnol.* **2008**, *3*, 101–105.
[144] H. Tang, Y. Zhao, X. Yang, D. Liu, P. Shao, Z. Zhu, S. Shan, F. Cui, B. Xing, *Environ. Sci. Technol.* **2017**, *51*, 9674–9682.
[145] M. M. Gudarzi, *Langmuir* **2016**, *32*, 5058–5068.
[146] M. M. Gudarzi, M. H. M. Moghadam, F. Sharif, *Carbon N. Y.* **2013**, *64*, 403–415.
[147] S. Al-Zangana, M. Iliut, M. Turner, A. Vijayaraghavan, I. Dierking, *2D Mater.* **2017**, *4*.
[148] J. I. Paredes, S. Villar-Rodil, A. Martínez-Alonso, J. M. D. Tascón, *Langmuir* **2008**, *24*, 10560–10564.
[149] R. Jalili, S. H. Aboutalebi, D. Esrafilzadeh, K. Konstantinov, S. E. Moulton, J. M. Razal, G. G. Wallace, *ACS Nano* **2013**, *7*, 3981–3990.
[150] D. Konios, M. M. Stylianakis, E. Stratakis, E. Kymakis, *J. Colloid Interface Sci.* **2014**, *430*, 108–112.
[151] S. Park, J. An, I. Jung, R. D. Piner, S. J. An, X. Li, A. Velamakanni, R. S. Ruoff, *Nano Lett.* **2009**, *9*, 1593–1597.

[152] F. Guo, F. Kim, T. H. Han, V. B. Shenoy, J. Huang, R. H. Hurt, *ACS Nano* **2011**, *5*, 8019–8025.
[153] L. Castañar, M. Garcia, E. Hellemann, P. Nolis, R. R. Gil, T. Parella, *J. Org. Chem.* **2016**, *81*, 11126–11131.
[154] N. Marcó, A. A. Souza, P. Nolis, R. R. Gil, T. Parella, *J. Magn. Reson.* **2017**, *276*, 37–42.
[155] J. Yan, A. D. Kline, H. Mo, M. J. Shapiro, E. R. Zartler, *J. Org. Chem.* **2003**, *68*, 1786–1795.
[156] C. Aroulanda, V. Boucard, F. Guibé, J. Courtieu, D. Merlet, *Chem. Eur. J.* **2003**, *9*, 4536–4539.
[157] J. D. Snider, E. Troche-Pesqueira, S. R. Woodruff, C. Gayathri, N. V. Tsarevsky, R. R. Gil, *Magn. Reson. Chem.* **2012**, *50*, S86–S91.
[158] X. Wang, H. Bai, G. Shi, *J. Am. Chem. Soc.* **2011**, *133*, 6338–6342.
[159] X. Sun, Z. Liu, K. Welsher, J. T. Robinson, A. Goodwin, S. Zaric, H. Dai, *Nano Res.* **2008**, *1*, 203–212.
[160] X. Lei, Z. Xu, H. Sun, S. Wang, C. Griesinger, L. Peng, C. Gao, R. X. Tan, *J. Am. Chem. Soc.* **2014**, *136*, 11280–11283.
[161] K. Klímová, M. Pumera, J. Luxa, O. Jankovský, D. Sedmidubský, S. Matějková, Z. Sofer, *J. Phys. Chem. C* **2016**, *120*, 24203–24212.
[162] X. Zhao, Z. Xu, Y. Xie, B. Zheng, L. Kou, C. Gao, *Langmuir* **2014**, *30*, 3715–3721.
[163] T. Taniguchi, S. Kurihara, H. Tateishi, K. Hatakeyama, M. Koinuma, H. Yokoi, M. Hara, H. Ishikawa, Y. Matsumoto, *Carbon N. Y.* **2015**, *84*, 560–566.
[164] J. Kim, L. J. Cote, J. Huang, *Acc. Chem. Res.* **2012**, *45*, 1356–1364.
[165] C. Y. Su, Y. Xu, W. Zhang, J. Zhao, X. Tang, C. H. Tsai, L. J. Li, *Chem. Mater.* **2009**, *21*, 5674–5680.
[166] S. Pan, I. A. Aksay, *ACS Nano* **2011**, *5*, 4073–4083.
[167] X. Qi, T. Zhou, S. Deng, G. Zong, X. Yao, Q. Fu, *J. Mater. Sci.* **2014**, *49*, 1785–1793.
[168] A. Esmaeili, M. H. Entezari, *J. Colloid Interface Sci.* **2014**, *432*, 19–25.
[169] N. Seselj, C. Engelbrekt, Y. Ding, H. A. Hjuler, J. Ulstrup, *Adv. Energy Mater.* **2018**, *1702609*, 1–12.
[170] K. Turcheniuk, C.-H. Hage, L. Heliot, S. Railian, V. Zaitsev, J. Spadavecchia, R. Boukherroub, S. Szunerits, *Nano Life* **2015**, *05*, 1540002.
[171] Z. Xu, C. Gao, *Nat. Commun.* **2011**, *2*, 1–9.
[172] *Graphenea*, San Sebastian, Spain.
[173] D. R. Dreyer, A. D. Todd, C. W. Bielawski, *Chem. Soc. Rev.* **2014**, *43*, 5288–5301.
[174] W. Yu, L. Sisi, Y. Haiyan, L. Jie, *RSC Adv.* **2020**, *10*, 15328–15345.
[175] V. Georgakilas, J. N. Tiwari, K. C. Kemp, J. A. Perman, A. B. Bourlinos, K. S. Kim, R. Zboril, *Chem. Rev.* **2016**, *116*, 5464–5519.
[176] L. Kan, Z. Xu, C. Gao, *Macromolecules* **2011**, *44*, 444–452.
[177] G. T. Hermanson, *Bioconjugate Techniques*, Elsevier Inc., **2008**.
[178] N. Nakajima, Y. Ikada, *Bioconjug. Chem.* **1995**, *6*, 123–130.
[179] F. Perreault, M. E. Tousley, M. Elimelech, *Environ. Sci. Technol. Lett.* **2013**, *1*, 71–76.
[180] A. Bakandritsos, M. Pykal, P. Boński, P. Jakubec, D. D. Chronopoulos, K. Poláková, V. Georgakilas, K. Čépe, O. Tomanec, V. Ranc, A. B. Bourlinos, R. Zbořil, M. Otyepka, *ACS Nano* **2017**, *11*, 2982–2991.
[181] H. P. Mungse, O. P. Khatri, *J. Phys. Chem. C* **2014**, *118*, 14394–14402.
[182] M. de Sousa, L. A. Visani de Luna, L. C. Fonseca, S. Giorgio, O. L. Alves, *ACS Appl. Nano Mater.* **2018**, *1*, 922–932.
[183] X. Yu, W. Liu, X. Deng, S. Yan, Z. Su, *Chem. Eng. J.* **2018**, *335*, 176–184.
[184] Y. Liu, J. Zhou, X. Zhang, Z. Liu, X. Wan, J. Tian, T. Wang, Y. Chen, *Carbon N. Y.* **2009**, *47*, 3113–3121.
[185] X. Wang, F. Zhang, J. Xia, Z. Wang, S. Bi, L. Xia, Y. Li, Y. Xia, *J. Electroanal. Chem.* **2015**, *738*, 203–208.
[186] A. Kasprzak, A. Zuchowska, M. Poplawska, *Beilstein J. Org. Chem.* **2018**, *14*, 2018–2026.
[187] N. Fattahi, M. Ayubi, A. Ramazani, *Tetrahedron* **2018**, *74*, 4351–4356.
[188] R. Subirós-Funosas, R. Prohens, R. Barbas, A. El-Faham, F. Albericio, *Chem. - A Eur. J.* **2009**, *15*, 9394–9403.
[189] D. Chen, L. Li, L. Guo, *Nanotechnology* **2011**, *22*.
[190] Q. Wang, M. Li, S. Szunerits, R. Boukherroub, *Electroanalysis* **2014**, *26*, 156–163.
[191] Q. He, Y. Cong, M. Zheng, A. Farajtabar, H. Zhao, *J. Chem. Thermodyn.* **2018**, *124*, 123–132.
[192] F. Albericio, A. Isidro-llobet, A. Mercedes, *Chem. Rev.* **2009**, *109*, 2455–2504.
[193] S. Pandit, M. De, *J. Phys. Chem. C* **2017**, *121*, 600–608.
[194] D. Stauffer, N. Dragneva, W. B. Floriano, R. C. Mawhinney, G. Fanchini, S. French, O. Rubel, *J. Chem. Phys.* **2014**, *141*.
[195] B. Ensing, A. Tiwari, M. Tros, J. Hunger, S. R. Domingos, C. Pérez, G. Smits, M. Bonn, D. Bonn, S. Woutersen, *Nat. Commun.* **2019**, *10*, 1–8.
[196] M. Meldal, in *Methods Enzymol.* (Ed.: G.B. Fields), Academic Press, **1997**, pp. 83–104.
[197] P. Chen, H. Li, S. Song, X. Weng, D. He, Y. Zhao, *Results Phys.* **2017**, *7*, 2281–2288.
[198] Y. Gao, I. Kyratzis, *Bioconjug. Chem.* **2008**, *19*, 1945–1950.
[199] A. Basu, P. Upadhyay, A. Ghosh, D. Chattopadhyay, A. Adhikary, *ACS Biomater. Sci. Eng.* **2019**, *5*, 373–389.
[200] X. Sun, Z. Liu, K. Welsher, J. T. Robinson, A. Goodwin, S. Zaric, H. Dai, *Nano Res.* **2008**, *1*, 203–212.
[201] Y. Bai, Y. Yuan, L. Miao, C. Lü, *J. Memb. Sci.* **2019**, *570–571*, 481–493.
[202] E. Y. Choi, T. H. Han, J. Hong, J. E. Kim, S. H. Lee, H. W. Kim, S. O. Kim, *J. Mater. Chem.* **2010**, *20*, 1907–1912.
[203] S. Tougaard, in *Encycl. Anal. Sci.* (Eds.: P. Worsfold, A. Townshend, C. Poole, M. Miro), 3rd Ed., Elsevier, **2013**, pp. 400–409.
[204] P. L. Chiu, D. D. T. Mastrogiovanni, D. Wei, C. Louis, M. Jeong, G. Yu, P. Saad, C. R. Flach, R. Mendelsohn, E. Garfunkel, H. He, *J. Am. Chem. Soc.* **2012**, *134*, 5850–5856.
[205] S. Guo, J. Raya, D. Ji, Y. Nishina, C. Ménard-Moyon, A. Bianco, *Nanoscale Adv.* **2020**, *2*, 4085–4092.
[206] S. Eigler, F. Hof, M. Enzelberger-Heim, S. Grimm, P. Müller, A. Hirsch, *J. Phys. Chem. C* **2014**, *118*, 7698–7704.

[207] S. Eigler, A. M. Dimiev, in *Graphene Oxide Fundam. Appl.*, John Wiley & Sons, Ltd, **2016**, pp. 85–120.
[208] J. M. Englert, P. Vecera, K. C. Knirsch, R. A. Schäfer, F. Hauke, A. Hirsch, *ACS Nano* **2013**, *7*, 5472–5482.
[209] A. B. Bourlinos, D. Gournis, D. Petridis, T. Szabó, A. Szeri, I. Dékány, *Langmuir* **2003**, *19*, 6050–6055.
[210] D. A. Jasim, C. Ménard-Moyon, D. Bégin, A. Bianco, K. Kostarelos, *Chem. Sci.* **2015**, *6*, 3952–3964.
[211] A. Liu, Y. Li, D. Shu, Y. Zhou, *Fullerenes Nanotub. Carbon Nanostructures* **2021**, *29*, 407–413.
[212] I. A. Vacchi, C. Spinato, J. Raya, A. Bianco, C. Ménard-Moyon, *Nanoscale* **2016**, *8*, 13714–13721.
[213] *Biochempeg Scientific Inc.*, Watertown, MA, USA.
[214] X. Fan, W. Peng, Y. Li, X. Li, S. Wang, G. Zhang, F. Zhang, *Adv. Mater.* **2008**, *20*, 4490–4493.
[215] W. Zhang, Z. Guo, D. Huang, Z. Liu, X. Guo, H. Zhong, *Biomaterials* **2011**, *32*, 8555–8561.
[216] Q. Li, F. Fan, Y. Wang, W. Feng, P. Ji, *Ind. Eng. Chem. Res.* **2013**, *52*, 6343–6348.
[217] C. W. Tornøe, C. Christensen, M. Meldal, *J. Org. Chem.* **2002**, *67*, 3057–3064.
[218] V. V. Rostovtsev, L. G. Green, V. V. Fokin, K. B. Sharpless, *Angew. Chemie - Int. Ed.* **2002**, *41*, 2596–2599.
[219] M. Meldal, C. W. Tomøe, *Chem. Rev.* **2008**, *108*, 2952–3015.
[220] S. Eigler, Y. Hu, Y. Ishii, A. Hirsch, *Nanoscale* **2013**, *5*, 12136–12139.
[221] S. Bräse, C. Gil, K. Knepper, V. Zimmermann, *Angew. Chemie - Int. Ed.* **2005**, *44*, 5188–5240.
[222] K. C. Mei, N. Rubio, P. M. Costa, H. Kafa, V. Abbate, F. Festy, S. S. Bansal, R. C. Hider, K. T. Al-Jamal, *Chem. Commun.* **2015**, *51*, 14981–14984.
[223] W. Huang, S. Wang, C. Guo, X. Yang, Y. Li, Y. Tu, *Polymer (Guildf).* **2014**, *55*, 4619–4626.
[224] R. Salvio, S. Krabbenborg, W. J. M. Naber, A. H. Velders, D. N. Reinhoudt, W. G. Van Der Wiel, *Chem. - A Eur. J.* **2009**, *15*, 8235–8240.
[225] T. Wei, T. Dong, H. Xing, Y. Liu, Z. Dai, *Anal. Chem.* **2017**, *89*, 12237–12243.
[226] D. Tanner, L. Tedenborg, A. Almario, I. Pettersson, I. Csöregh, N. M. Kelly, P. G. Andersson, T. Högberg, *Tetrahedron* **1997**, *53*, 4857–4868.
[227] H. C. Kolb, M. G. Finn, K. B. Sharpless, *Angew. Chemie - Int. Ed.* **2001**, *40*, 2004–2021.
[228] F. Himo, T. Lovell, R. Hilgraf, V. V. Rostovtsev, L. Noodleman, K. B. Sharpless, V. V. Fokin, *J. Am. Chem. Soc.* **2005**, *127*, 210–216.
[229] B. T. Worrel, J. A. Malik, V. V. Fokin, *Science* **2013**, *340*, 457–461.
[230] M. Meldal, F. Diness, *Trends Chem.* **2020**, *2*, 569–584.
[231] M. S. Ramasamy, S. S. Mahapatra, D. H. Yi, H. J. Yoo, J. W. Cho, *RSC Adv.* **2014**, *4*, 23936–23942.
[232] M. Namvari, H. Namazi, *Carbohydr. Res.* **2014**, *396*, 1–8.
[233] M. S. Ramasamy, S. S. Mahapatra, J. W. Cho, *Int. J. Nanotechnol.* **2016**, *13*, 318–329.
[234] J. Han, H. Lee, J. Kim, S. Kim, H. Kim, E. Kim, Y. E. Sung, K. Kim, J. C. Lee, *J. Memb. Sci.* **2020**, *612*, 118428.
[235] H. Li, Q. Zheng, C. Han, *Analyst* **2010**, *135*, 1360–1364.
[236] J. Zhang, H. Yang, G. Shen, P. Cheng, J. Zhang, S. Guo, *Chem. Commun.* **2010**, *46*, 1112–1114.
[237] J. Gao, F. Liu, Y. Liu, N. Ma, Z. Wang, X. Zhang, *Chem. Mater.* **2010**, *22*, 2213–2218.
[238] M. Meldal, *Personal Communication*, **2021**.
[239] L. Yang, R. Zhang, B. Liu, J. Wang, S. Wang, M. Y. Han, Z. Zhang, *Angew. Chemie - Int. Ed.* **2014**, *53*, 10109–10113.
[240] F. D. Andersen, K. D. Pedersen, D. W. Juhl, T. Mygind, P. Chopin, E. B. Svenningsen, T. B. Poulsen, M. B. Lund, A. Schramm, C. H. Gotfredsen, T. Tørring, *Triculamine: An Unusual Lassopeptide with Potent Anti-Mycobacterial Activity (Draft)*, **2021**.
[241] WHO, *Global Tuberculosis Report*, **2021**.
[242] C. Cheng, Z. C. Hua, *Front. Bioeng. Biotechnol.* **2020**, *8*, 571165.
[243] S. Suzuki, K.-I. Asahi, J. Nagatsu, Y. Kawashima, I. Suzuki, *J. Antibiot. (Tokyo).* **1967**, *20*, 126.
[244] K. Anzai, S. Suzuki, *Agric. Biol. Chem.* **1969**, *33*, 1737–1744.
[245] K. Maeda, S. Kondo, K. Ohi, H. Kondo, E. L. Wang, Y. Osato, H. Umezawa, *J. Antibiot. (Tokyo).* **1958**, *11*, 30–31.
[246] H. Martin-Gómez, J. Tulla-Puche, *Org. Biomol. Chem.* **2018**, *16*, 5065–5080.
[247] M. O. Maksimov, S. J. Pan, A. James Link, *Nat. Prod. Rep.* **2012**, *29*, 996–1006.
[248] I. Solomon, *Phys. Rev.* **1955**, *99*, 559–565.
[249] D. Neuhaus, M. Williamson, *The Nuclear Overhauser Effect in Structural and Conformational Analysis*, VCH Publishers, **1989**.
[250] C. Hoeck, *Solving a 3D Structural Puzzle*, Springer Thesis, **2016**.
[251] A. M. Gronenborn, G. M. Clore, *Prog. NMR Spectrosc.* **1985**, *17*, 1–32.
[252] B. Borgias, M. Gochin, D. Kerwood, T. James, *Prog. NMR Spectrosc.* **1990**, *22*, 83–100.
[253] S. Macura, B. T. Farmer, L. R. Brown, *J. Magn. Reson.* **1986**, *70*, 493–499.
[254] H. Hu, K. Krishnamurthy, *J. Magn. Reson.* **2006**, *182*, 173–177.
[255] K. D. Pedersen, Structural Studies of Autoinducing Peptides, Technical University of Denmark (DTU), **2017**.
[256] *Stereofitter*, Mestrelab Research, **2021**.
[257] *Matlab*, MathWorks Inc.
[258] L. Wang, Z. Sofer, M. Pumera, *ACS Nano* **2020**, *14*, 21–25.
[259] C. E. Halbig, P. Rietsch, S. Eigler, *Molecules* **2015**, *20*, 21050–21057.
[260] K. M. Yip, N. Fischer, E. Paknia, A. Chari, H. Stark, *Nature* **2020**, *587*, 157–161.
[261] T. Nakane, A. Kotecha, A. Sente, G. McMullan, S. Masiulis, P. M. G. E. Brown, I. T. Grigoras, L. Malinauskaite, T. Malinauskas, J. Miehling, T. Uchański, L. Yu, D. Karia, E. V. Pechnikova, E. de Jong, J. Keizer, M. Bischoff, J. McCormack, P. Tiemeijer, S. W. Hardwick, D. Y. Chirgadze, G. Murshudov, A. R. Aricescu, S. H. W. Scheres, *Nature* **2020**, *587*, 152–156.
[262] F. Wang, Y. Liu, Z. Yu, S. Li, S. Feng, Y. Cheng, D. A. Agard, **2020**, 1–5.

Appendix

Contents

A1 Instrumentation 1

A1.1 NMR 1

A1.2 Software 2

A1.3 Equipment 2

A2 Brief theoretical background of NMR 3

A2.1 Calculations of NMR observables by DFT 5

A3 Assignments 6

A3.1 Menthol 6

A3.2 Methyl-α-D-glucopyranoside (Me-α-Glc) 7

A3.3 (+)-Pinanediol 8

A3.4 NH_2PEG_3tBu 9

A3.5 $NH_2PEG_3NH_2$ 10

A3.6 Si-alk 11

A3.7 Me-alk 12

A3.8 DIPEA 13

A4 ^{13}C MAS spectra 14

A5 Triculamin 15

A6 RDC tables 16

A7 References 18

A8 Publications 19

A1 Instrumentation

A1.1 NMR

A1.1.1 Spectrometers

All spectra were acquired on the NMR spectrometers given below (*marks the most utilized instrument). Spectra were acquired in 5 mm NMR tubes at 298 K using standard pulse sequences unless otherwise stated.

- *Bruker AVANCE III 800 MHz system with a 5mm ^{1}H / (^{13}C, ^{15}N) TCI CryoProbe
- Bruker AVANCE III 800 MHz system with a 5mm TCI ^{1}H & ^{19}F/ (^{13}C, ^{15}N) CryoProbe
- Bruker AVANCE 600 MHz system utilizing either a 5mm SmartProbe BB(F)-H-D, HR-MAS probe or CP-MAS solid state probe.
- Bruker AVANCE 400 MHz system with a 5mm Prodigy CryoProbe
- Bruker AVANCE 400 MHz system, 5mm SmartProbe BB(F)-H-D

A1.1.2 Acquisition

Typical acquisition and processing parameters are given below as used on Bruker spectrometers. Spectra were as a standard zero-filled by a factor of 2.

1D ^{1}H

Pulse sequence/program (pp): zgesgp/zg30 (w/wo water suppression), number of scans (ns): 32, relaxation delay (d1): 1.5 s.
When used to monitor purification processes, the number of scans were varied between 32 and 1k depending on concentration of the monitored reagent.

1D ^{2}H

pp: zg2h using the lock channel, ns: 2, time domain (TD): 4k.

CLIP-HSQC[1]

pp: hsqcetgpipjcsp.2, TD: 2k, number of increments (ni): 512, ds: 32, d1: 1.5 s, SW: 14 ppm (F2) x 120 ppm (F1). Adjusted to $^{1}J_{CH}$ of 145 Hz. Number of scans varied between 4 and 64 scans depending on solute and GO concentration.

^{1}H-^{13}C HSQC[2–4]

Pp: hsqcedetgpsisp2.3, TD: 2k, number of increments (ni): 256, d1: 1.5 s, SW: 12 ppm (F2) x 165 ppm (F1).

HMBC[5,6]

pp: hmbcetgpl3nd, TD: 4k, ni: 256, ns: 4, ds: 16, d1: 1.5 s, SW: 16 x 220 ppm. J_{HMBC}=8 Hz.

DQF-COSY[7–10]

pp: cosygpmfphpp, TD: 2k, ni: 256, ns: 4, ds: 4.

A1.1.3 Solvent

Chemical shift of deuterated solvents used to calibrate spectra for assignments. The multiplicity of the solvent peak is given in parentheses.

Solvent	**δ_H [ppm]**	**δ_C [ppm]**
DMSO-*d*6	2.50 (5)	39.5 (7)
CDCl3	7.24 (1)	77.23(3)
D_2O	4.70 (1)	-
CD_3CN	1.94 (5)	1.39 (7)

A1.2 Software

A1.2.1 TopSpin

NMR spectra processed in TopSpin version 3.6.1 (2018) by Bruker BioSpin

A1.2.2 Maestro

The modelling suite Maestro version 2018-2 from Schrödinger, LLC, used to model the initial structure. Program MacroModel version 12.0 from Schrödinger, LLC, was used for force field calculations.

A1.2.3 Gaussian

DFT calculations were performed using Gaussian version 09 revision B01 for optimization of 3D structures and calculations of NMR observables.[11]

A1.2.4 MSpin

MSpin version 2.3.4-776, 2019, by MestReLab Research S. L. was used for RDC back-calculation using SVD and single tensor computation.[12]

A1.3 Equipment

A1.3.1 Sonicator

Branson Ultrasonics™ M Series Ultrasonic Cleaning Bath, M3800-E, 40 kHz.

A1.3.2 MilliQ water

Synergy® UV Water Purification System

A1.3.3 Centrifuge

Eppendorf centrifuge 5810R (rotor radius 9.9 rad) used for large volume solutions, most often used for GO synthesis and purification of functionalization products.

VWR Micro star 17R or Biofuge Pico Heraeus centrifuges used for small volumes (<1.5 mL) most often in preparation of GO NMR samples.

A1.3.4 Lyophilization

GO and functionalized GO products were freeze-dried using a ScanVac CoolSafe.

A1.3.5 IR spectroscopy

GO and functionalized GO products were analyzed by IR spectroscopy using a PerkinElmer Spectrum 100 FTIR, (ATR spectrometer) with the software Spectrum 10.02.00.0041.

A2 Brief theoretical background of NMR

Nuclear magnetic resonance (NMR) spectroscopy utilizes the nuclear property of spin, *I*.[13][14] When placed in a magnetic field, the otherwise degenerate spin states will have different energies and the nuclei will populate the different states according to Boltzmann's equation. The difference between the different energy spin states corresponds to electromagnetic radiation in the radio frequency (RF) domain. The stronger the magnetic field, B_0, the larger the energy gap and the bigger the difference in populations, meaning greater sensitivity. Nuclei are surrounded by moving electrons that generate a small local magnetic field, which counter the external field. This effect is referred to as shielding and each nucleus, having a slightly different environment due to the electron density surrounding it, will be shielded differently. With different degrees of shielding, the nuclei will experience dissimilar magnetic fields, corresponding to different energy frequencies. It is the electronic shielding, σ, which is used to separate the nuclei in the spectrum with the chemical shift, δ.

$$\frac{N_\alpha}{N_\beta} = e^{-\frac{\Delta E}{kT}} \quad \Delta E = \gamma \hbar B_0 (1-\sigma) = h\nu$$

N is the population of a given spin state, *k* is Boltzmann's constant, and *T* the temperature in Kelvin. The energy difference between the spin states, ΔE, depends on the gyromagnetic ratio γ of the nuclei, the reduced Planck constant $\hbar$, the strength of the external magnetic field B_0, and the degree of electronic shielding σ experienced by the given nuclei.

For nuclei to be NMR active, their nuclear spin quantum number must be $I \neq 0$. This is true for e.g. protons, ^{1}H, which have $I = ½$ (referred to as spin-half). Nuclei have spin states equal to $2I$; for ^{1}H these are denoted +½ and -½, referred most commonly to as α- and β-spin (or alternatively spin up and spin down), respectively.

When placed in a magnetic field, the difference in the populated spin states results in a net magnetization along the magnetic field, conventionally set as the z-axis. The nuclei will precess around the axis with a frequency dependent on the magnetic field strength and their own chemical shielding. This frequency is called the Larmor frequency. The net magnetization can be manipulated by RF pulses which when set to the Larmor frequency will resonate with the nuclei initiating precession around the magnetic field. Detecting the relaxation of the net magnetization back to its equilibrium state along the z-axis, the free induction decay (FID) is acquired. The FID is subsequently converted to a spectrum using Fourier transformation, something that can be done easily and rapidly using NMR software.

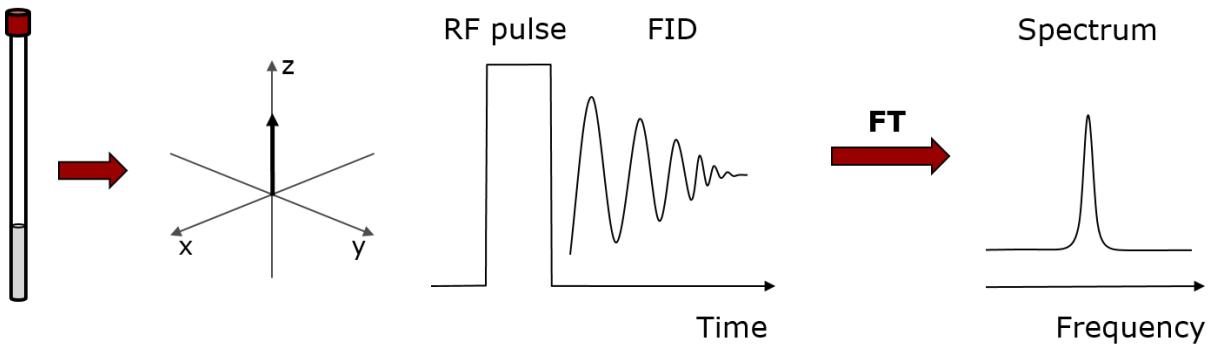

Figure 1. Illustration of the process from sample preparation to data acquisition resulting in an NMR spectrum.

NMR spectra are conventionally shown with the chemical shift on a parts-per-million (ppm) scale, where the compound tetramethylsilane (TMS) were chosen as the reference at 0 ppm. An advantage of using the ppm scale is the independence of magnetic field strength and therefore the results from different spectrometers can be directly compared. A key factor when comparing spectrometers e.g.in terms of sensitivity and resolution is the magnet strength. Magnetic fields are usually given in Tesla (T), however among NMR spectroscopist the tradition is to refer to the magnetic field strength by the proton Larmor frequency in the given magnetic field. An 800 MHz NMR spectrometer correspond to 18.8 T in magnetic field strength.

In conventional, solution samples, the molecules rotate and move freely around each other, their motion is generally described as random tumbling. RF pulses of μs to ms lengths are used to manipulate the magnetization away from the steady state. The system can relax back to equilibrium through various processes, some of which are used to extract information. The FID acquired after one set of RF pulses (called a scan) may contain insufficient signal strength to obtain reliable information. By collecting data from repeated scans, Fourier transformation of the total FID results in a spectrum for analysis with higher signal-to-noise (*S/N*) ratio. The duration of an NMR experiment is largely made up of the necessary delay between scans to re-establish the equilibrium magnetization, which can take seconds to minutes depending on nuclei.

Relaxation back to equilibrium occurs by different mechanisms, divided into longitudinal (T_1) and transverse (T_2) relaxation. Simplified, T_1 relaxation is the recovery of spin magnetization along the z-axis, while T_2 is the loss of net magnetization in the transverse (x-y) plane. Slow tumbling molecules have short T_2 timeframes with rapid loss of magnetization and thus lower intensity in the acquired spectra. The length of the necessary delay between scans is dependent on the T_1 relaxation with $5*T_1$ being the norm for full relaxation back to equilibrium.

A2.1 Calculations of NMR observables by DFT

The chemical shift is calculated as the NMR shielding tensor defined as the second order derivative of the energy with respect to the nuclear magnetic moment and the applied magnetic field, and evaluated at zero [15].

$$\sigma_I = \left.\frac{\partial^2 E}{\partial \mu_I \partial B_0}\right|_{\mu_I, B_0 = 0}$$

The observed chemical shift is reported relative to the reference compound TMS and similarly the calculation of the NMR shielding tensors depend on the choice of gauge origin [16]. Here this is circumvented by the gauge invariant atomic orbitals (GIAO) method, where each atomic orbital is dependent on the external magnetic field with a local gauge origin at the center of the atomic orbital[17]. The calculated GIAO shielding tensors are then converted by use of linear correlation to the observed chemical shifts [18]. This method can give accurate results with RMSD down to app. 0.1 ppm for δ_H and 1 ppm for δ_C.

The *J*-coupling constant between two nuclei can be expressed as the second derivative of the energy with respect to their magnetic moments [19]

$$J_{IS,xy} = \frac{\partial^2 E}{\partial \mu_{I,x} \partial \mu_{S,y}}$$

The scalar coupling is transmitted by the bonding electrons and the interaction is described as the sum of a number of terms covering different mechanism. For proton-proton coupling constants it has been found that calculating only the dominant Fermi contact term and scaling the results gave accurate values with a RMSD of less than 0.5 Hz [20]. For this method of calculating *J*-coupling constants augmenting the basis functions with additional compact 1s functions was needed as the Fermi contact was very sensitive to the description of the electrons near the nucleus [20]. The results are given in Hz and can thus be directly compared to the experimental data.

A3 Assignments

A3.1 Menthol

(-)-menthol in $CDCl_3$

#	$\delta^{1}H$ [ppm] (int., mult., J_{HH} [Hz])	$\delta^{13}C$ [ppm]
1	3.39 (1H, td, 10.5, 4.3)	71.8
OH	1.42 (m)	-
2	1.94 (1H, dtd, 12.1, 3.8, 2.0) 0.93 (1H, td, 12.1, 10.5)	45.3
3	1.40 (m)	31.9
4	1.64 (1H, dqd, 12.9, 3.4, 2.0) 0.83 (1H, qd, 13.0, 3.5)	34.8
5	1.59 (1H, dq, 13.3, 3.4) 0.95 (1H, qd, 13.0, 3.5)	23.4
6	1.09 (1H, dddd, 13.0, 10.5, 3.4, 2.8)	50.4
7	2.15 (1H, sept, d, 7.0, 2.8)	26.1
8	0.91 (3H, d, 7.0)	21.2
9	0.79 (3H, d, 6.9)	16.3
10	0.89 (3H, d, 6.6)	22.4

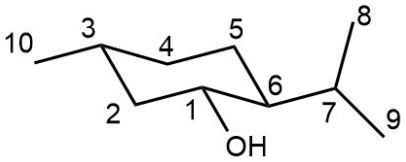

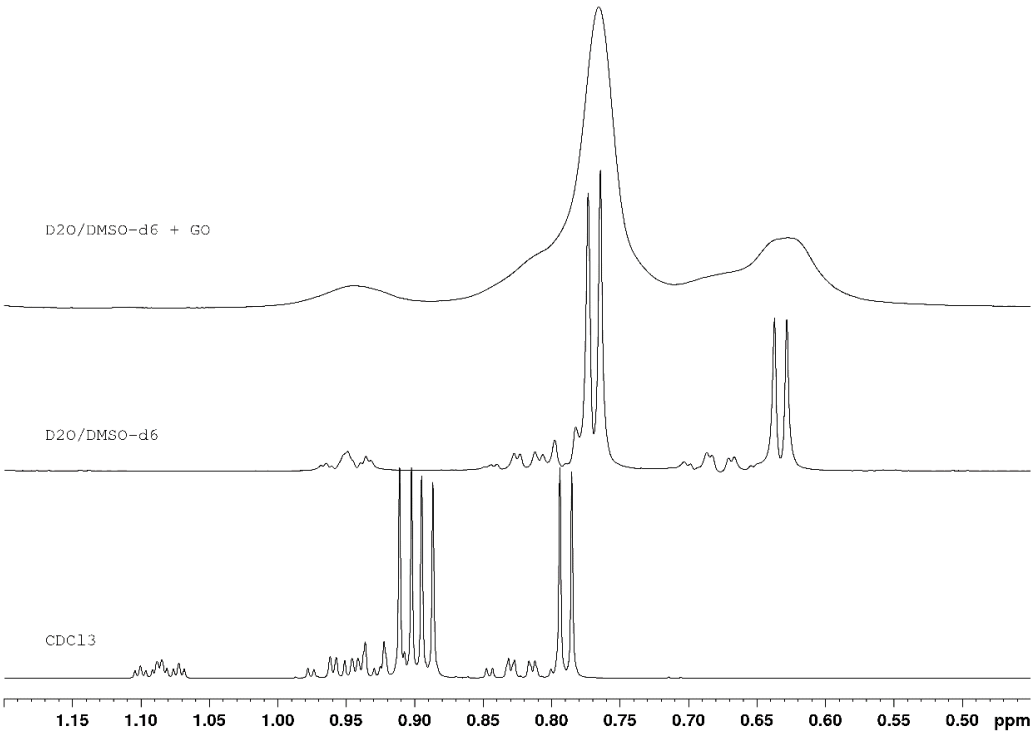

Figure 3.1. Overlay of 1D ^{1}H NMR spectra of menthol to show the line broadening due to varying solvent and addition of GO. Different solvents resulted in different chemical shifts, but showed little effect on the observed *J*-coupling constants.

A3.2 Methyl-α-D-glucopyranoside (Me-α-Glc)

32.7 mg in 500 µL D_2O

#	δ_H [ppm] (int, mult., *J* [Hz])	δ_C [ppm]	
1	4.73 (1H, d, 3.9)	99.3	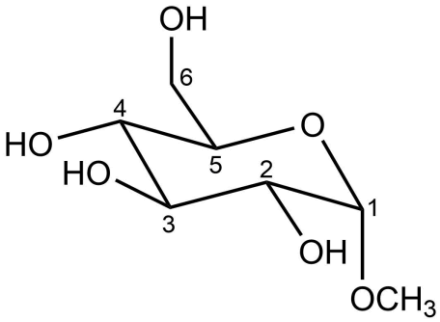
2	3.48 (1H, dd, 9.8, 3.8)	71.2	
3	3.59 (1H, t, 9.6)	73.1	
4	3.32 (1H, t, 9.3)	69.5	
5	3.56 (1H, ddd, 10.0, 5.6, 2.2)	71.6	
6	3.79 (1H, dd, 12.3, 2.3) 3.68 (1H, dd, 12.3, 5.6)	60.5	
Me	3.34 (3H, s)	55.0	

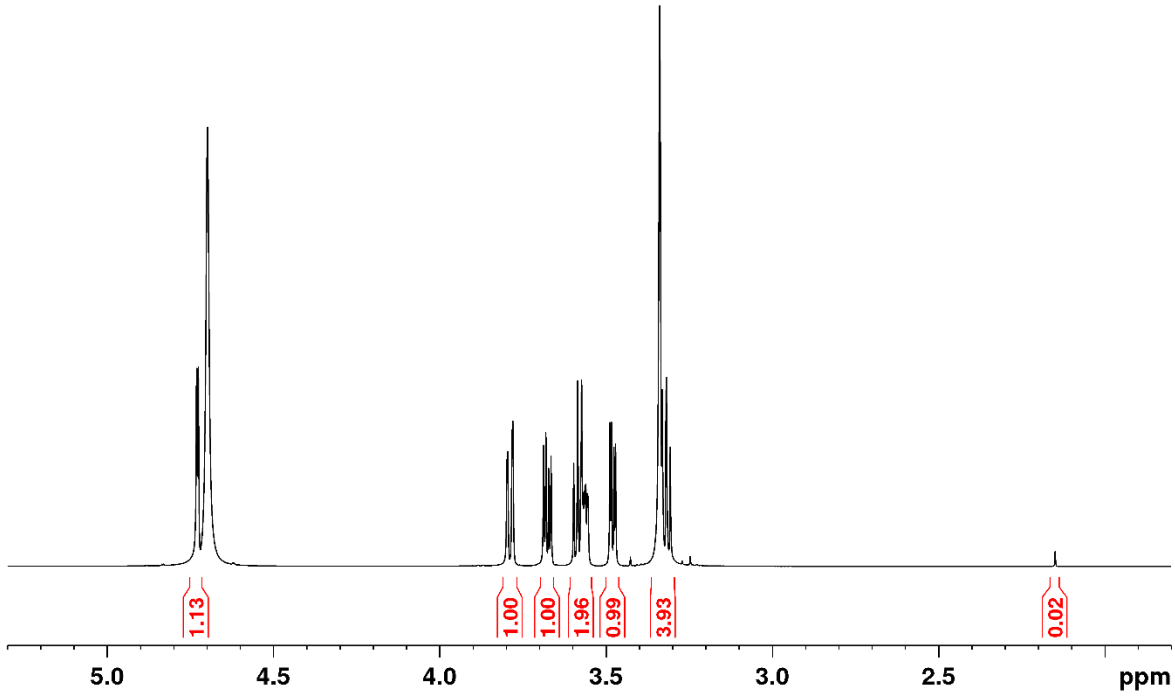

A3.3 (+)-Pinanediol

1.1 mg (+)-Pinanediol in 1 mL DMSO-*d*6

#	δ_H [ppm] (int, mult., *J* [Hz])	δ_C [ppm]
1	1.80 (1H, m) *(1H, tdd, 5.8, 3.6, 2.3)*	40.0
2	2.27 (1H, dddd, 13.7, 9.4, 3.6, 2.3) 1.50 (ddd, 13.7, 5.4, 2.3)	37.7
3	3.80 (1H, dt, 9.4, 5.8)	67.7
3 OH	4.95 (1H, d, 6.3)	-
4	-	72.2
4 OH	4.28 (1H, s)	-
5	1.83 (1H, t, 5.8)	53.7
6	-	38.1
7	2.03 (1H, dtd, 9.9, 5.8, 2.3) 1.36 (1H, d, 9.9)	27.9
8	0.89 (3H, s)	24.0
9	1.21 (3H, s)	27.9
10	1.13 (3H, s)	29.9

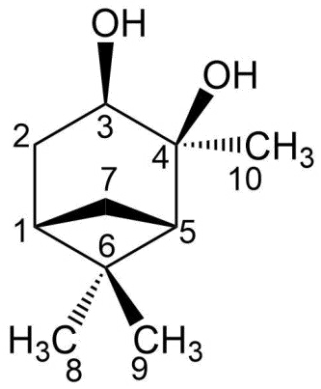

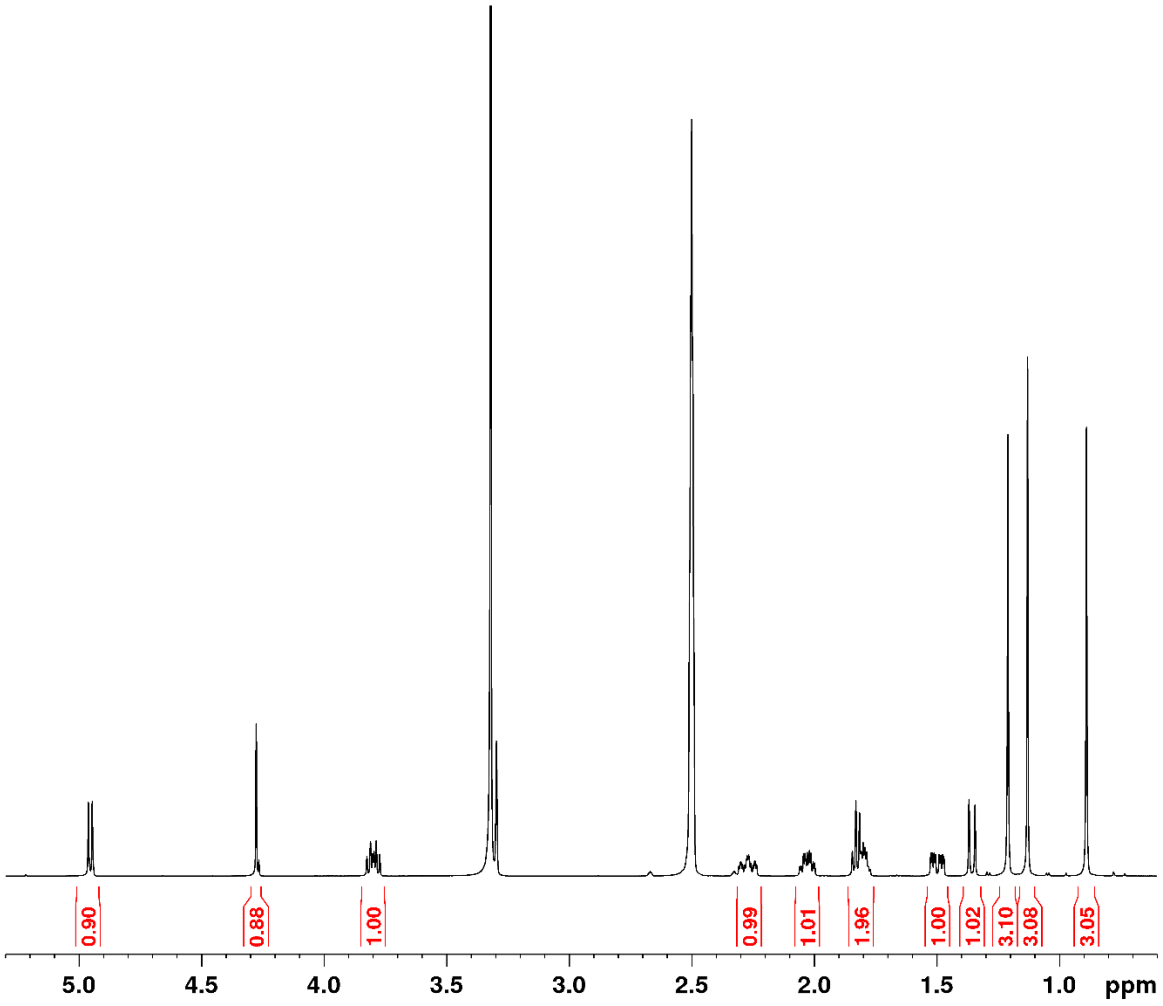

A3.4 NH_2PEG_3tBu

5 µL dissolved in 450 µL DMSO-*d*6

#	δ_H [ppm] (int, mult., *J* [Hz])	δ_C [ppm]
1	-	170.9
2	2.41 (2H, t, 6.3)	36.3
3	3.59 (2H, t, 6.2)	66.7
4	3.48 (2H, s*)	70.1
5	3.48 (2H, s*)	70.0
6	3.34 (2H, t, 5.8)	73.6
7	2.62 (2H, t, 5.8)	41.9
8	-	80.2
9	1.39 (9H, s)	28.2

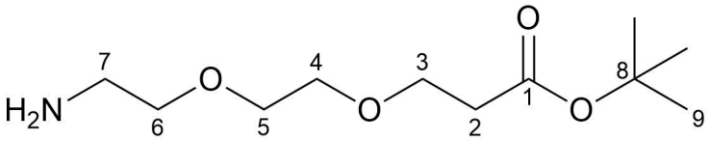

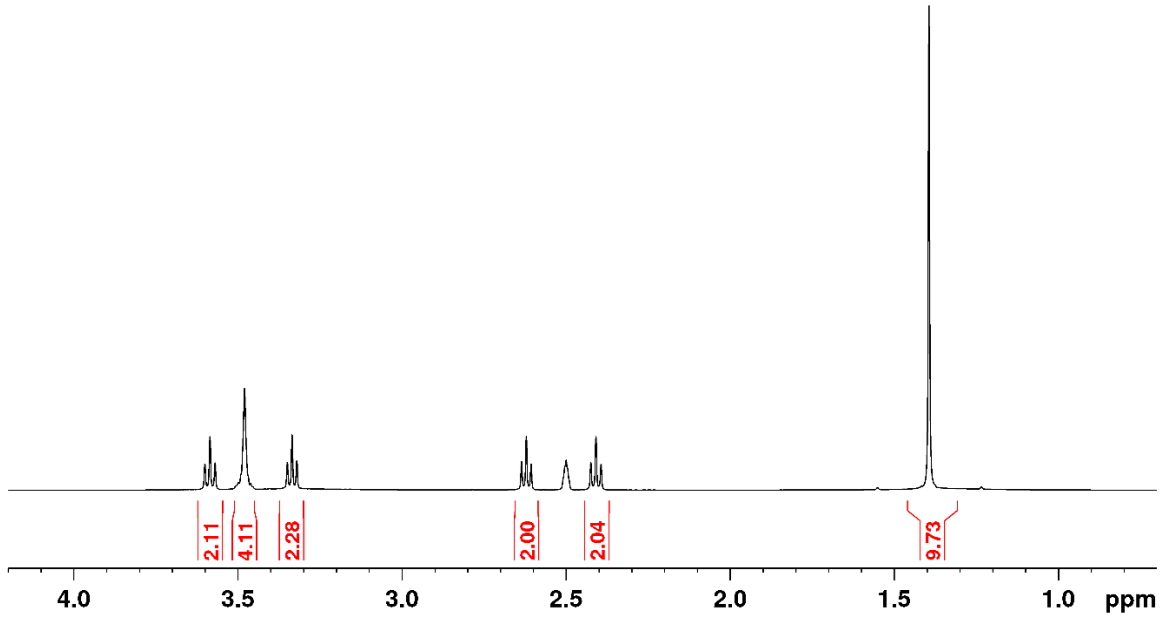

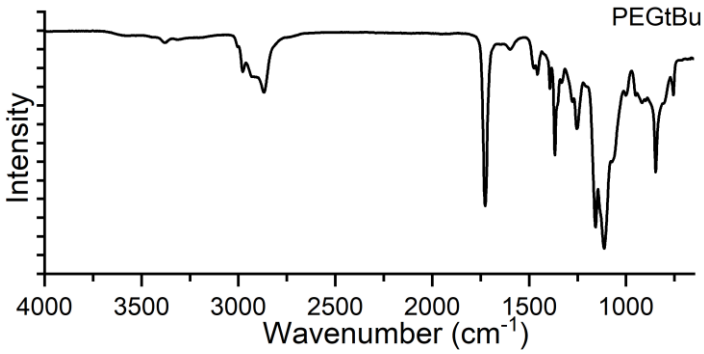

A3.5 $NH_2PEG_3NH_2$

1,8-Diamino-3,6-dioxaoctane

5 µL dissolved in 500 µL D_2O

#	δ_H [ppm] (int, mult., *J* [Hz])	δ_C [ppm]
1	2.70 (4H, t, 5.4)	39.8
2	3.49 (4H, t, 5.4)	72.2
3	3.61 (4H, s)	69.4

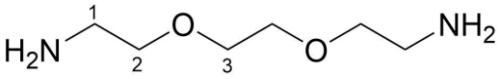

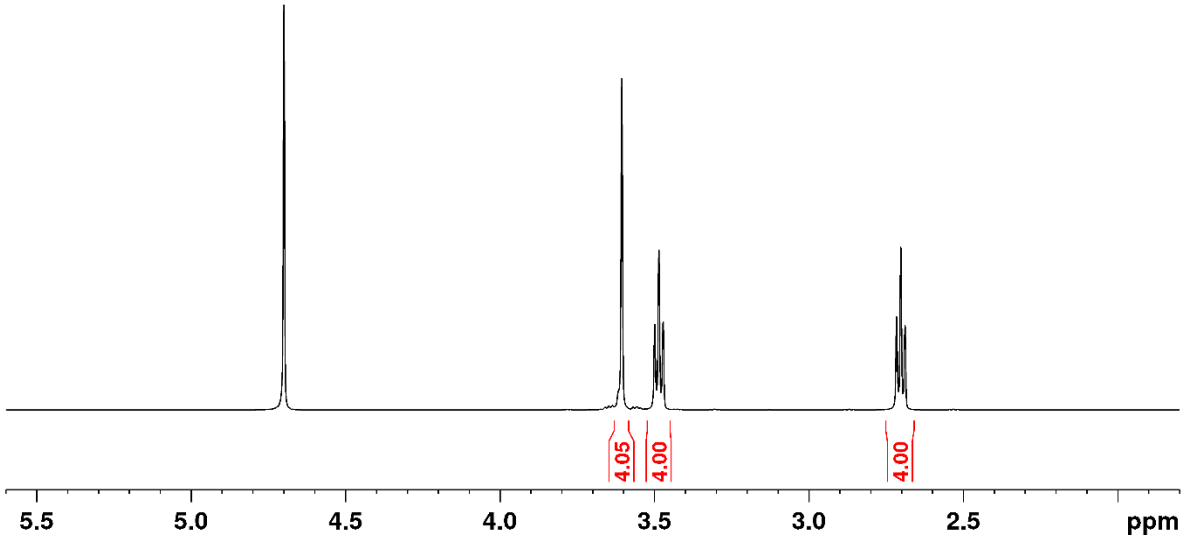

A3.6 Si-alk

4-(tertbutyldimethylsilyloxy)-1-butyne

2 µL in 500 µL DMSO-*d*6

#	δ_H [ppm] (int, mult., *J* [Hz])	δ_C [ppm]	
1	2.78 (1H, t, 2.58)	72.5	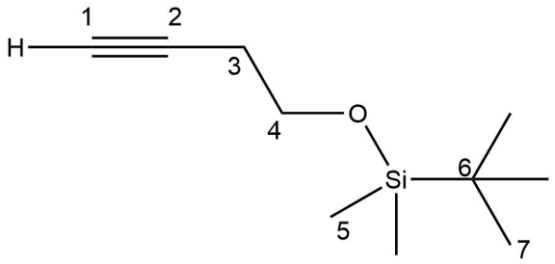
2	-	82.4	
3	2.32 (2H, td, 6.7, 2.6)	22.7	
4	3.66 (2H, t, 6.6)	61.7	
5	0.05 (6H, s)	-4.8	
6	-	18.5	
7	0.87 (9H, s)	26.3	

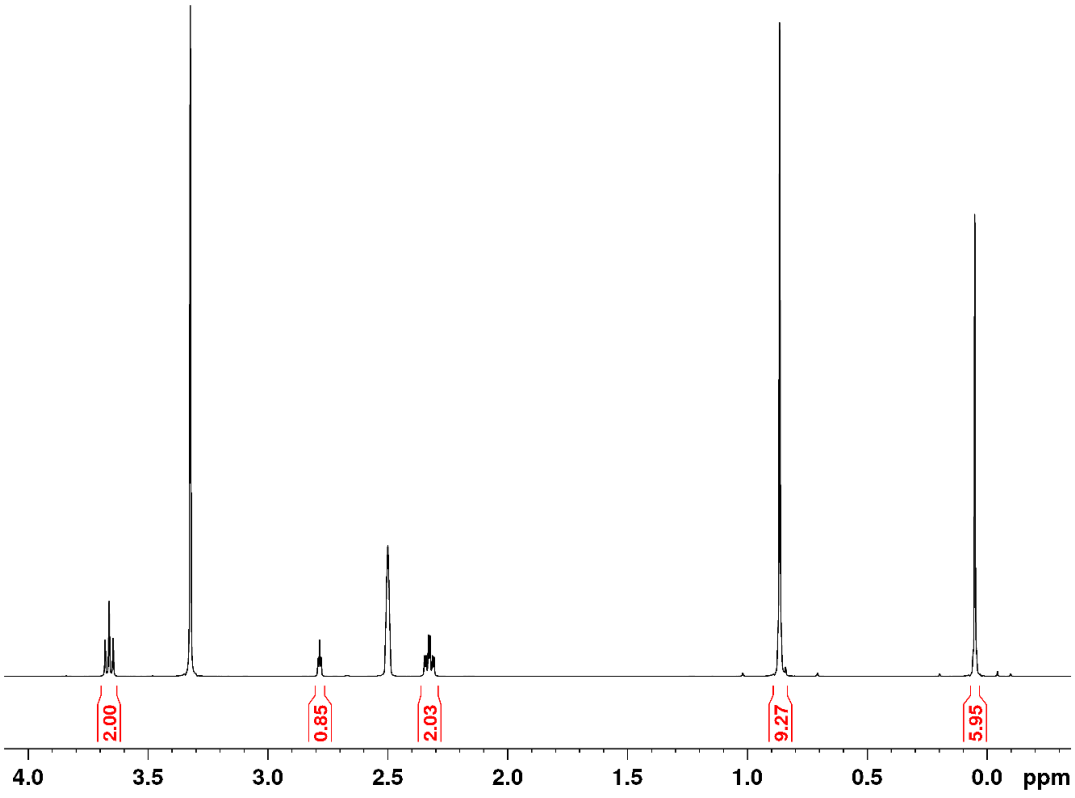

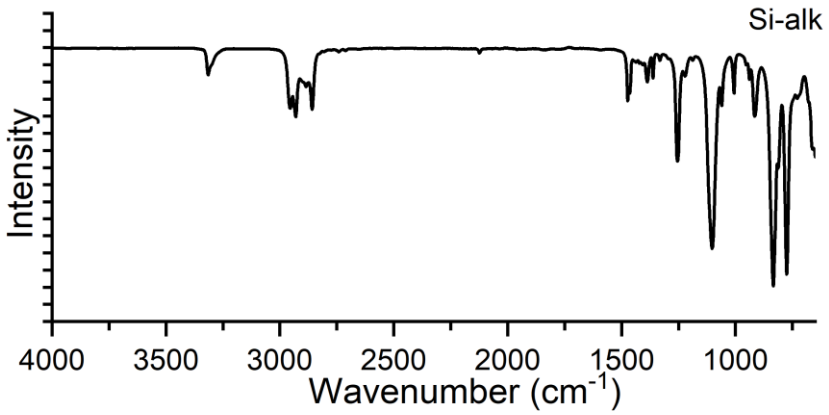

A3.7 Me-alk

5-methyl-1-hexyne

2 µL in 500 µL DMSO-*d*6

#	δ_H [ppm] (int, mult., *J* [Hz])	δ_C [ppm]	
1	2.72 (1H, t, 2.58)	71.5	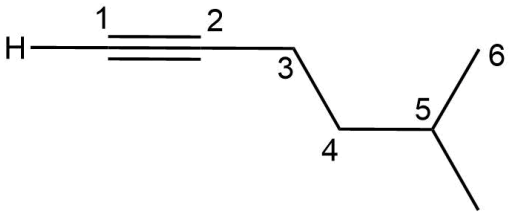
2	-	85.0	
3	2.15 (2H, td, 7.4, 2.6)	16.2	
4	1.33 (2H, q, 7.2)	37.4	
5	1.64 (1H, nonet, 6.7)	27.0	
6	0.86 (6H, d, 6.6)	22.4	

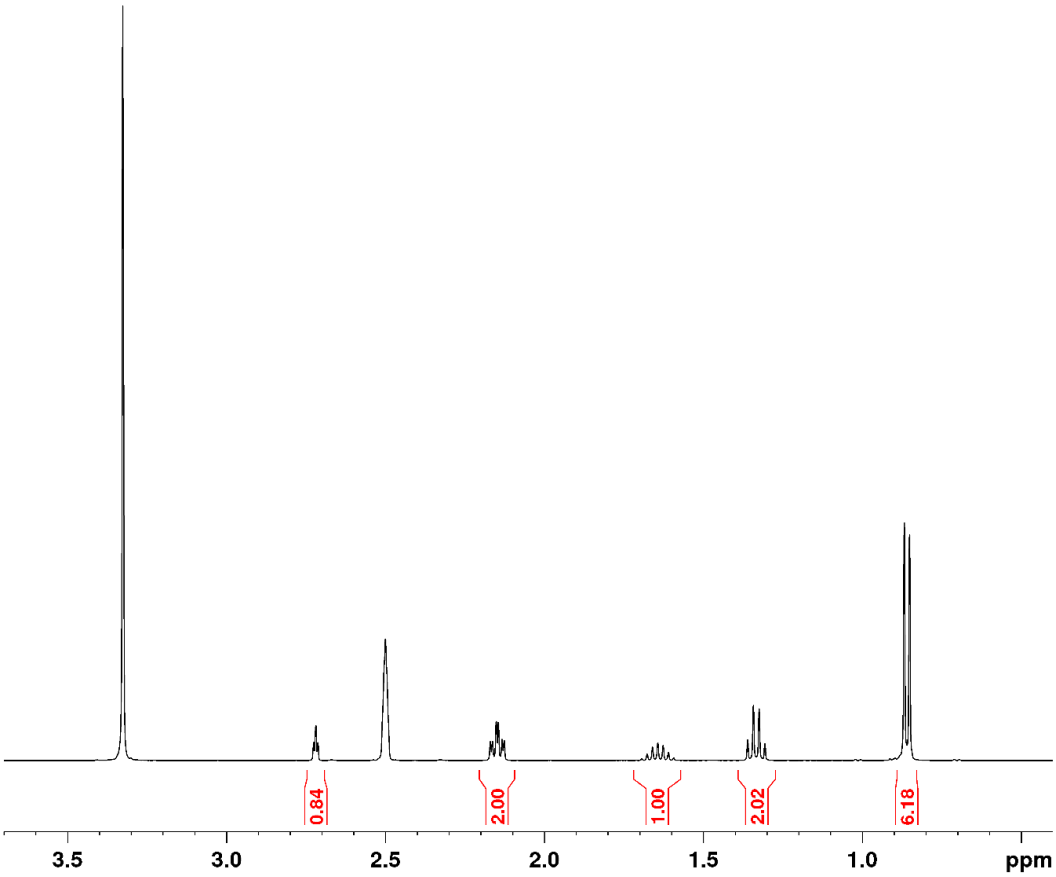

A3.8 DIPEA

Diisopropylethylamine

5 µL in 500 µL CD_3CN

#	δ_H [ppm] (int, mult., *J* [Hz])	δ_C [ppm]	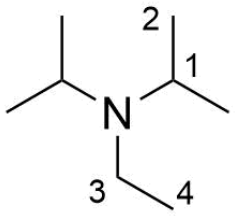
1	3.01 (2H, sept., 6.6)	48.9	
2	0.97 (12H, d, 6.6)	21.1	
3	2.47 (2H, q, 7.1)	39.3	
4	0.96 (3H, m)	17.4	

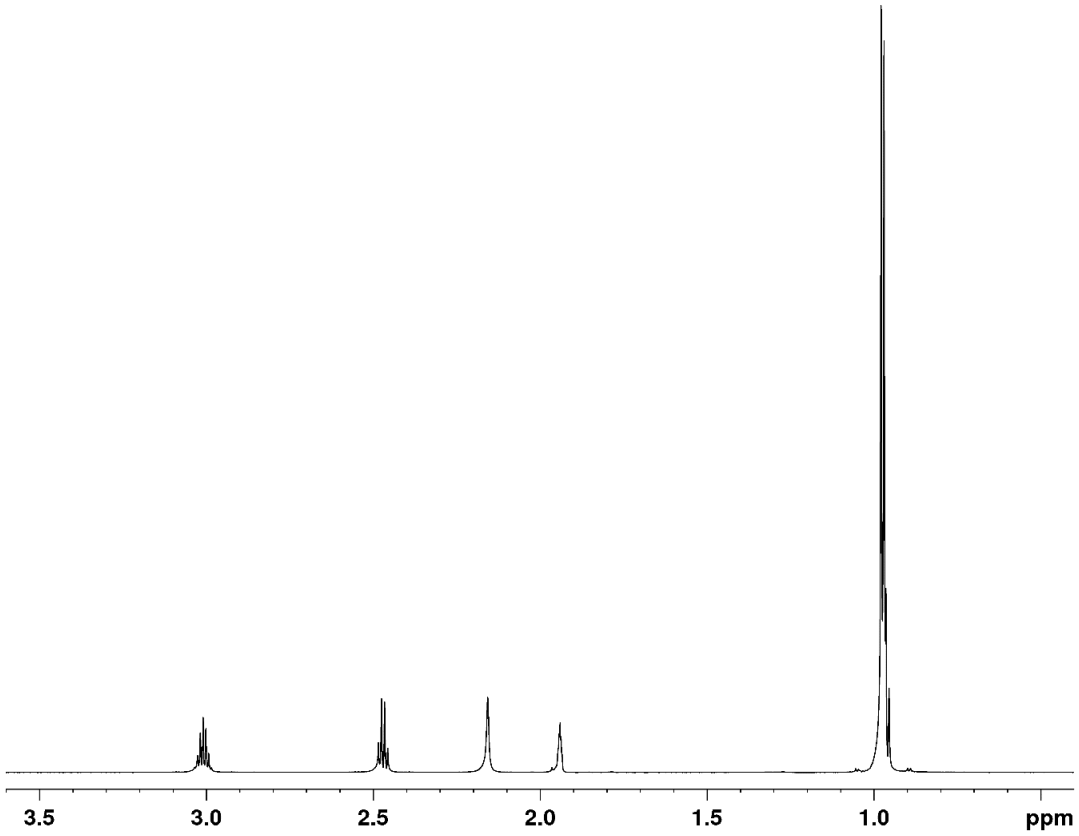

A4 ^{13}C MAS spectra

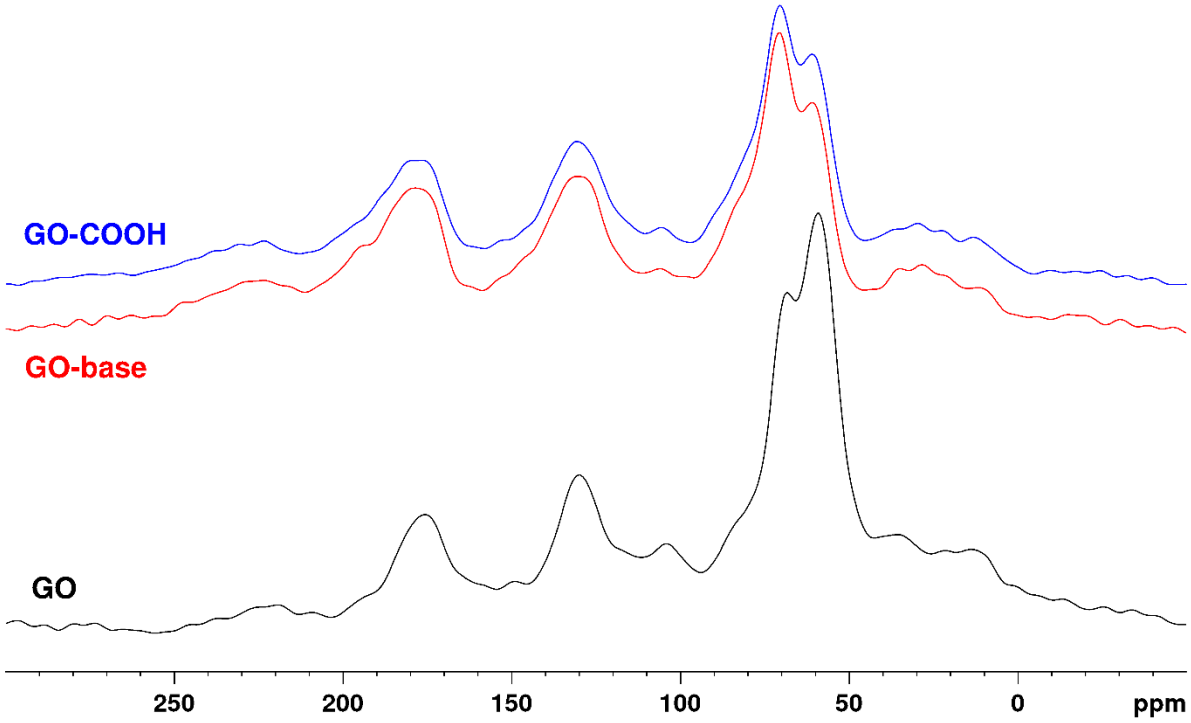

Overlay of 1D ^{13}C MAS NMR spectra of GO, GO-COOH, and GO-base. Their respective intensities have been normalized relative to the peak at 130 ppm.

A5 Triculamin

1D ^{1}H NMR spectrum of triculamine

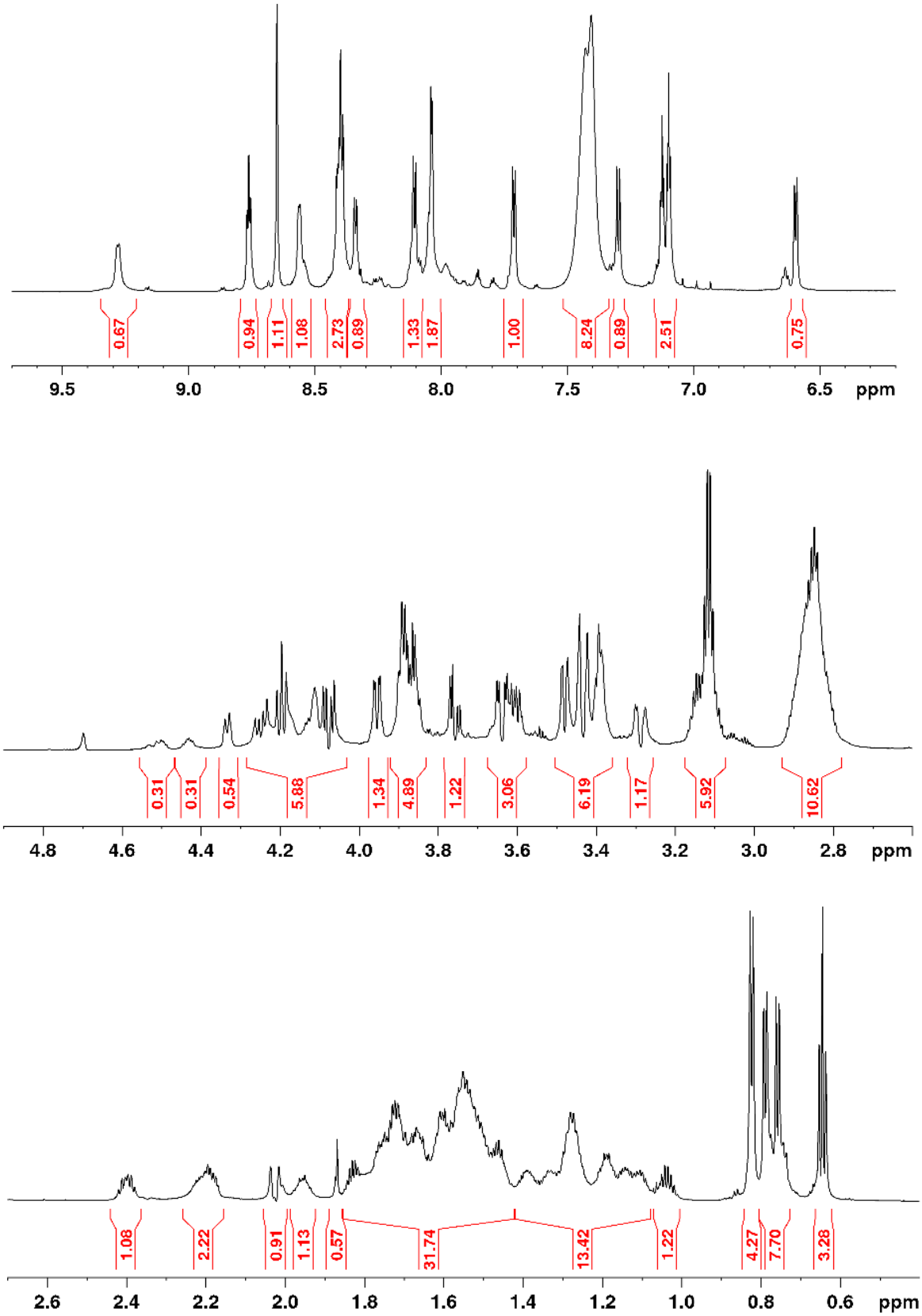

A6 RDC tables

Tables of measured RDCs not included in the text or the supplementary information of [21].

From Chapter 4

Table A6.1. Extracted RDCs [Hz] for the samples described in Table 4.6 of the text. GO alignment stability after time at elevated temperatures. 20 mM menthol in 1:1 D_2O:DMSO-*d*6 in app. 2.4 mg/mL cGO.

#	1	2	3	4	5	6
1	28.71	28.81	31.97	30.94	32.91	37.99
2a	-5.85	-5.85	-6.17	-4.76	-5.83	-8.29
2b	32.23	29.58	33.68	32	34.12	39.61
3	36.67	31.26	33.08	31.52	42.98	35.4
4a	1.42	-1.24	-4.43	-4.76		
4b				9.5		
5a	-2.03	-1.94	-2.48	-2.36	-3.24	-7.99
5b	41.84	37.99	42.43	42.29	42.91	41.59
6	30	30.34	34.62	33.39	43.82	28.22
7	13.14	14.08	14.36	14.78	12.02	16.21
8	0.76	0.78	0.65	0.75	1.03	1.29
9	-5.25	-4.89	-7.69	-6.51	-9.7	-3.87
10	13.99	12.78	16.22	14.94	15.3	18.53
Q	0.123	0.110	0.128	0.187	0.090	0.077

Table A6.2. RDCs [Hz] for each enantiomer and a racemic mixture of pinanediol. 4 mM pinanediol, 8.7 mg/mL sGO in 1:1 D_2O:DMSO-*d*6.

#	(+)	(-)	racemic
1	-1.81	1.00	-0.12
2a	5.15	6.92	6.2
2b	-1.11	0.41	-0.31
3	5.37	5.61	6.81
5	1.84	2.96	2.93
7a	1.56	-1.41	-2.11
7b	-6.12	-7.54	-6.53
8	1.95	1.49	2.05
9	-0.62	-0.40	-0.6
10	-1.31	-1.54	-1.91
Q	0.100	0.155	0.065

Table A6.3. Extracted RDCs [Hz] of 20 mM menthol for 1.6 mg/mL GO-N_3 relative to solvent composition of D_2O:DMSO-*d*6 described in Figure 7.5 in the text. Percentages refer to D_2O content.

#	0 %	10 %	20 %	30 %	40 %	50 %
1	2.85	4.35	7.79	12.23	14.14	18.83
2a	0.04	-1.40	-1.50	-2.20	-3.25	-3.13
2b	1.01	2.78	8.21	12.84	15.35	23.08
3	1.12	2.92	5.60	12.61	14.83	21.81
4a	2.83	0.22	4.01	3.67	6.03	9.27
4b	1.9	7.79	8.06	10.96	12.80	14.81
5a	8.09	5.54	0.13	-2.82	-2.87	-3.12
5b	8.19	5.53	15.82	19.59	22.52	26.51
6	3.84	5.49	8.11	14.13	18.99	20.07
7	0.29	-0.07	1.52	4.39	7.49	7.89
8	-0.01	0.00	0.08	0.66	1.42	0.95
9	-2.51	-2.55	-1.29	-1.91	-2.36	-4.41
10	0.07	0.01	1.11	3.44	6.37	8.81
Q	0.552	0.463	0.192	0.117	0.122	0.047

Table A6.4. Extracted RDCs [Hz] of 20 mM menthol for 0.89 mg/mL GO-$click_6$ in 1:1 D_2O:DMSO-*d*6.

#	GO-$click_6$
1	10.80
2a	-3.15
2b	13.14
3	13.10
4a	4.49
4b	9.88
5a	-1.97
5b	14.83
6	12.26
7	6.33
8	0.73
9	-2.35
10	5.62
Q	0.063

A7 References

[1] A. Enthart, J. C. Freudenberger, J. Furrer, H. Kessler, B. Luy, *J. Magn. Reson.* **2008**, *192*, 314–322.

[2] L. E. Kay, P. Keifer, T. Saarinen, *J. Am. Chem Soc.* **1992**, *114*, 10663–10665.

[3] A. G. Palmer III, J. Cavanagh, P. E. Wright, M. Rance, *J. Magn. Reson.* **1991**, *93*, 151–170.

[4] J. Schleucher, M. Schwendinger, M. Sattler, P. Schmidt, O. Schedletzky, S. J. Glaser, O. W. Sørensen, C. Griesinger, *J. Biomol. NMR* **1994**, *4*, 301–306.

[5] D. O. Cicero, G. Barbato, R. Bazzo, *J. Magn. Reson.* **2001**, *148*, 209–213.

[6] A. Bax, M. F. Summers, *J. Am. Chem. Soc.* **1986**, *108*, 2093–2094.

[7] W. P. Aue, E. Bartholdi, R. R. Ernst, *J. Chem. Phys.* **1976**, *64*, 2229–2246.

[8] U. Pianiini, O. W. Sorenscn, R. R. Ernst, **1982**, *0*, 6800–6801.

[9] R. E. Hurd, *J. Magn. Reson.* **1990**, *87*, 422–428.

[10] A. L. Davis, E. D. Laue, J. Keeler, D. Moskau, J. Lohman, *J. Magn. Reson.* **1991**, *94*, 637–644.

[11] M. J. Frisch, G. W. Trucks, H. B. Schlegel, G. E. Scuseria, M. A. Robb, J. R. Cheeseman, G. Scalmani, V. Barone, B. Mennucci, G. A. Petersson, H. Nakatsuji, M. Caricato, X. Li, H. P. Hratchian, A. F. Izmaylov, J. Bloino, G. Zheng, J. L. Sonnenberg, M. Hada, M. Ehara, K. Toyota, R. Fukuda, J. Hasegawa, M. Ishida, T. Nakajima, Y. Honda, O. Kitao, H. Nakai, T. Vreven, J. A. J. Montgomery, J. E. Peralta, F. Ogliaro, M. Bearpark, J. J. Heyd, E. Brothers, K. N. Kudin, V. N. Staroverov, T. Keith, R. Kobayashi, J. Normand, K. Raghavachari, A. Rendell, J. C. Burant, S. S. Iyengar, J. Tomasi, M. Cossi, N. Rega, J. M. Millam, M. Klene, J. E. Knox, J. B. Cross, V. Bakken, C. Adamo, J. Jaramillo, R. Gomperts, R. E. Stratmann, O. Yazyev, A. J. Austin, R. Cammi, C. Pomelli, J. W. Ochterski, R. L. Martin, K. Morokuma, V. G. Zakrzewski, G. A. Voth, P. Salvador, J. J. Dannenberg, S. Dapprich, A. D. Daniels, O. Farkas, J. B. Foresman, J. V. Ortiz, J. Cioslowski, D. J. Fox, **2010**.

[12] A. Navarro-Vázquez, *Magn. Reson. Chem.* **2012**, *50*, S73–S79.

[13] J. Keeler, *Understanding NMR Spectroscopy*, Wiley, **2010**.

[14] T. D. W. Claridge, *High-Resolution NMR Techniques in Organic Chemistry*, Elsevier, **2016**.

[15] S. R. Jensen, T. Flå, D. Jonsson, R. S. Monstad, K. Ruud, L. Frediani, *Phys. Chem. Chem. Phys.* **2016**, *18*, 21145–21161.

[16] J. C. Facelli, *Concepts Magn. Reson. Part A Bridg. Educ. Res.* **2004**, *20*, 42–69.

[17] R. Jain, T. Bally, P. R. Rablen, *J. Org. Chem.* **2009**, *74*, 4017–4023.

[18] M. W. Lodewyk, M. R. Siebert, D. J. Tantillo, *Chem. Rev.* **2012**, *112*, 1839–1862.

[19] I. Alkorta, J. Elguero, *Int. J. Mol. Sci.* **2003**, *4*, 64–92.

[20] T. Bally, P. R. Rablen, *J. Org. Chem.* **2011**, 4818–4830.

[21] K. D. Pedersen, J. Zhang, C. H. Gotfredsen, *Magn. Reson. Chem.* **2021**, *59*, 738–745.

A8 Publications

I **Pedersen, Katja D**; Zhang, Jingdong; Gotfredsen, Charlotte H. "Practical considerations for working with graphene oxide as alignment media for RDC measurements." *Magn Reson. Chem*. 2021; 1–8.

II F. D. Andersen; **Pedersen, Katja D**; Juhl, Dennis W; Mygind, Tobias; Chopin, Paul; Svenningsen, Esben B; Poulsen, Thomas B; Lund, Marie B; Schramm, Andreas; Gotfredsen, Charlotte H; Tørring, Thomas. "Triculamine: an unusual lassopeptide with potent anti-mycobacterial activity" (draft).

Received: 1 September 2020 | Revised: 20 February 2021 | Accepted: 23 February 2021

DOI: 10.1002/mrc.5143

WILEY

LETTER - APPLICATION NOTE

Practical considerations for working with graphene oxide as alignment media for RDC measurements

Katja D. Pedersen | **Jingdong Zhang** | **Charlotte H. Gotfredsen**

Department of Chemistry, Technical University of Denmark, Kongens Lyngby, Denmark

Correspondence
Charlotte H. Gotfredsen, Department of Chemistry, Technical University of Denmark, Kongens Lyngby, Denmark.
Email: chg@kemi.dtu.dk

1 | INTRODUCTION

Nuclear magnetic resonance (NMR) spectroscopy is one of the most powerful techniques for identification and structure determination of organic compounds. By using chemical shifts, spin–spin *J*-coupling constants, and nuclear Overhauser effect (NOE) data, spectroscopists have been able to elucidate the structure of countless compounds. However, major challenges and limitations may arise for structures with proton deficient regions and chiral centers. Determining relative and absolute stereochemistry becomes an even larger challenge for highly flexible compounds as conformational averaging occurs.

Anisotropic NMR-derived parameters are gaining attention in order to access additional structural information that may enable new solutions for small to medium size compounds with respect to the challenges mentioned above.[1,2] Global molecular information may aid in elucidation of hydrogen deficient structures, as it is not limited by proton–proton proximity requirements in contrast to *J*-coupling constants and NOE/rotating-frame Overhauser effect (ROE) experiments. Anisotropic data such as residual dipolar couplings (RDCs) can provide orthogonal angular structural information to aid in structure elucidation and especially towards resolving molecular diastereomers and specific assignment of prochiral methylene protons. RDCs have also been used to determine the structure of flexible compounds for which conventional analysis gave ambiguous results.[3,4]

An alignment media is conventionally used to create a weak alignment effect in the NMR sample prior to acquisition of NMR spectra. A myriad of alignment media has already been reported, falling into the categories (1) stretched polymer gels, for example, PS,[5] PH,[6] PMMA,[7] poly-HEMA[8]; or (2) liquid crystal (LC) phases, for example, PBLG/PBDG,[9–13] PELG/PEDG,[14] polyacetylenes,[15] polyguanidines.[16] In the last category, graphene oxide (GO) solutions were reported as an interesting new type of alignment media.[17] Among its favorable qualities highlighted were (1) no background signals were seen, (2) high-quality spectra were acquired enabling easy extraction of RDCs, and (3) the degree of alignment could be tuned by varying the concentration of GO.[17] With the proven possibility of modifying the GO sheets to be compatible with even more organic solvents, this alignment media has many exciting unexplored possibilities for becoming the alignment media of choice in future RDC studies.[18,19]

There is currently a high threshold towards the use of RDCs in routine analysis by non-specialists. Part of this is due to sample preparation being complicated or at least greatly dependent on/aided by experience. The use of GO as alignment media makes sample preparation easier and at a low cost for the material. The GO can be obtained from graphite via, for example, a modified Hummers method or directly from commercial suppliers.[20] In this paper, GO from both sources has been used to further explore the properties of GO as alignment media in order to lower the threshold of application for others interested in using RDCs in structure elucidation. Here, the sample stability, concentration dependence, solvent influence, solute sample amount needed, and the possibility of recovering the sample are discussed using the model compounds menthol, pinanediol, and methyl-α-D-glucopyranoside (Me-α-Glc).

2 | WORK FLOW AND SAMPLE PREPARATION

Standard preparation of samples was initiated by extracting the required amount of GO from a stock solution, followed by centrifugation with subsequent removal of the supernatant in exchange for deuterated solvent. Afterwards, GO was dispersed back into solution by vigorous shaking, and the solute of interest was added. Unless otherwise discussed in the text, samples were stored at room temperature, not shielded from light and not shaken before measurements. Menthol was chosen as the main compound for testing as it gave spectra without significant overlap, had a fitting solubility in a range of solvents, and is known to adapt primarily one conformation.

RDCs were found as $D_{CH} = {}^1T_{CH} - {}^1J_{CH}$, where ${}^1T_{CH}$ was measured from the aligned samples and ${}^1J_{CH}$ from corresponding isotropic samples via acquisition of CLIP-HSQC spectra.[21] Measurement uncertainty of the individual RDCs of minimum 0.5 (to ~0.7) Hz is estimated from comparison of independent, but identical isotropic samples. For GO samples, the measurement uncertainty could go up to 2 Hz.

The conformational space of the investigated compounds was generated computationally in parallel via a conformational search in the program Maestro.[22] A set of conformers were selected to cover the conformational space and subsequently energy-minimized by density functional theory (DFT). The minimized conformers were used for back-calculations of RDCs by singular value decomposition (SVD) using the program MSpin.[23] Within MSpin, the fit between the experimental and back-calculated RDCs is evaluated by an overall quality (Q) factor.[24] However, it has to be kept in mind that the Q factor only evaluates how well the input structures fit the experimental data and not whether the input structures are correct. The following exploration of GO as alignment media is largely evaluated through comparison of the resulting Q factors, but supported by evaluation of other parameters and experimental observations when needed. Elsewhere, the splitting of the deuterium signal is often used, though here, the absolute sizes of the obtained RDCs are also discussed in relation to measurement uncertainties together with the generalized degree of order (GDO) of alignment tensors and the generalized angle between alignment tensors.[25] The alignment of GO is mainly described in the following discussion via the effect on menthol, Figure 1, used throughout to highlight various influences on the acquired data.

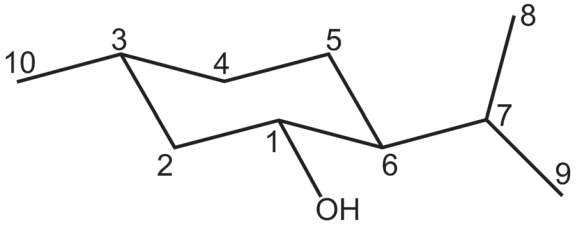

FIGURE 1 Structure of (−)-menthol with the used assignment

3 | GO SOLUTION STABILITY AND LIGHT SENSITIVITY

The RDCs did not change significantly over a time period of more than 9 months as shown in Figure 2. The GO samples are long-term stable, and only the stability of the solute is of concern. It has been proposed that GO might be sensitive to light. In order to address this concern, the stability of two identical samples was monitored. One was wrapped in tin foil, the other left out in the normal light of the laboratory. RDC data were acquired for both samples on the same dates. Table 1 shows concurrent data together with the back-calculated RDCs and resulting Q factors. The methyl groups of the isopropyl group were not included in the calculations as individual assignment was not possible. The same approach was used in all calculations. Additional details can be found in the supporting information.

The Q factors of both samples are shown in Figure 2 as a function of time. The light sample showed a lower average Q factor, but the dark sample had the overall lowest single Q value. However, as the data are comparable, it leads to the conclusion that light sensitivity is not of concern, though direct sunlight for extended time is not recommended.

4 | GO SEDIMENTATION

NMR samples prepared from GO stock solutions synthesized in our laboratory following a modified Hummers

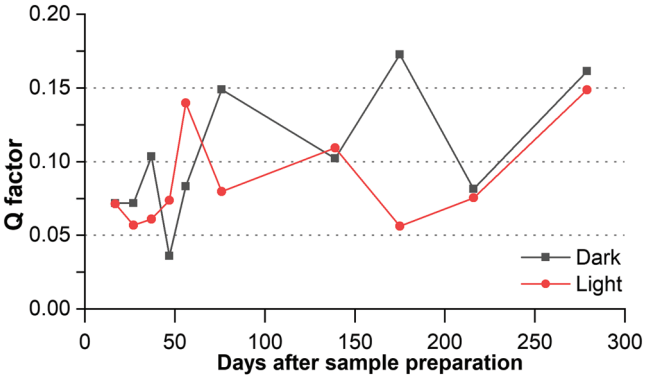

FIGURE 2 Q factors over time for the same samples expressing the stability of the samples. One was exposed to light (light) and the other not (dark). Average Q factor: Dark sample 0.103 ± 0.044, light sample 0.087 ± 0.034

TABLE 1 Acquired residual dipolar couplings (RDCs) for the light and dark samples (Exp.) compared with the back-calculated RDCs from MSpin (Calc.) of menthol

	Light		Dark	
#	Exp.	Calc.	Exp.	Calc.
1	8.85	8.64	8.78	8.85
2a	−1.95	−0.90	−0.91	−0.67
2b	10.71	10.93	10.00	9.21
3	9.62	9.65	9.14	9.25
4a	1.48	1.47	1.69	1.71
4b	7.69	7.51	7.75	8.02
5a	0.42	−0.64	−0.59	−0.82
5b	10.99	10.71	9.30	8.74
6	9.08	9.45	7.12	8.14
7	2.45	2.37	2.28	2.08
10	2.42	2.96	2.48	2.93
Q		**0.071**		**0.072**

Note: The assignment refers to Figure 1, a and b to equatorial and axial methylene protons, respectively.

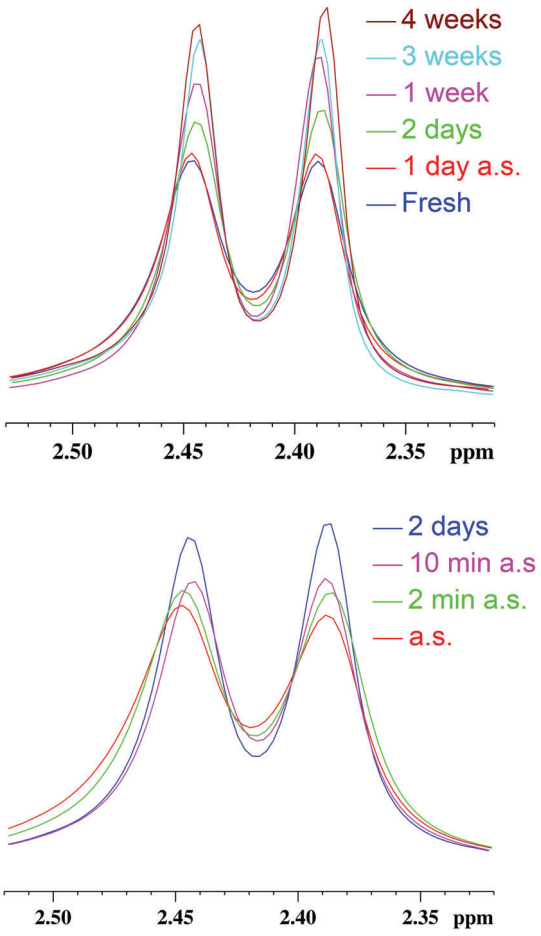

FIGURE 3 Overlay of 1D ^{2}H spectra with 8.23 mg/ml graphene oxide (GO) sample in 1:1 D_2O:dimethyl sulfoxide (DMSO)-*d*6 at 600 MHz following its preparation, showing the splitting of the DMSO-*d*6 peak of 5.3 Hz over short and longer time intervals. Top: long-term effects of sedimentation. Bottom: immediate effect after shaking the sample. a.s., after shaking

method showed sedimentation upon storage. The extent of sedimentation depended on the time they were left undisturbed, see Figure S2. This led us to address what effect this might have on the spectral quality, alignment properties, general stability, and reproducibility of the extracted NMR structural parameters. The degree of sedimentation is batch, sheet size, and sample preparation dependent. The effect of sedimentation on the alignment properties was first investigated by acquiring ^{2}H 1D spectra at various times after sample preparation.

The deuterium quadrupolar splitting of 5.3 Hz, shown in Figure 3, remained approximately the same over time; however, the peaks get sharper by a factor of 2 as the sample settles. It should also be noted that the shape of the peaks was very sensitive to the homogeneity of the magnetic field; shimming often had to be done manually for concentrated samples as automatic shimming generally proved insufficient (if possible at all). Spectra acquired for the freshly prepared sample and after 1 day are very similar, which is consistent with the sample being shaken just prior to the measurement, redispersing the sediment. As the deuterium quadrupolar splitting is constant over time, it is assumed that the degree of alignment remains the same and the liquid crystal structure is unaffected by the sedimentation. The sediment mainly contains residual multilayer fragments leftover from the synthesis. When evaluating samples prepared from commercial GO solutions, much less sedimentation was often observed. The commercial GO solutions are also assumed to have a very low presence of graphite fragments and a narrower distribution in sheet size.

The direct effect of shaking sediment into solution is also seen in Figure 3, where broader peaks are observed when sediment is re-dispersed into solution. The peaks are sharper after just minutes, indicating that here sedimentation starts immediately after sample preparation, but is obscured by the dark solution. The quadrupolar splitting remains constant during this process, showing the stability of the GO LC, indicating that the LC structure alignment is either instantaneous in the magnetic field or unaffected by the general handling and shaking of the sample.

In conclusion, it appears that the aligning effect of the GO is unaffected by the sedimentation. Instead, it can be argued that it is beneficial for better spectral quality to let the sample stand undisturbed 1–2 days after sample

preparation for concentrated GO samples to obtain a more homogenous solution after the larger fragments have settled, as a similar trend of better resolved peaks was also seen in CLIP-HSQC spectra. The effective concentration of GO LC in solution is however different than initially determined based on the GO stock solution due to the sedimentation, which may lead to different reports of fitting GO concentrations for alignment.

5 | SOLVENT DEPENDENCE

The study showed a clear influence of solvent composition on the degree (strength) of alignment of GO. This is in agreement with GO being more dispersible in polar solvents.[26] In Table 2, larger RDCs are seen with increasing amounts of D_2O. With less than 50% D_2O, the size of the RDCs decreases significantly. A high amount of hydrogen bonding must be needed to sustain the GO LC structure necessary for acquisition of RDCs. The decrease in RDC size correlates to higher Q factors as seen on Figure 4, showing an increase in uncertainty. For the RDCs of menthol, we observe the same dependence on water content for mixtures of D_2O with acetone, acetonitrile, dimethylformamide (DMF), methanol, and ethanol; see supporting information, pp. 8–10. For most of these solvents, the decrease in D_2O content similarly correlates to a higher Q factor. An exception is seen for methanol and ethanol, which are also the most polar of the solvents tested. However, it should be noted that for both methanol and ethanol, the sizes of the RDCs had decreased significantly to a point where measurement uncertainty could have greater influence on the results. The same dependence on D_2O content is also reflected in the GDO, see Figure S7. In this case, changing the solvent does not appear to influence the direction of the alignment, as the generalized angle between alignment tensors vary very little across the solvents used here; see Table S8.

For most of the tested solvent mixtures, a further increase in relative D_2O content results in a slightly higher Q factor. We generally also observed broader and occasionally distorted peaks with >50% D_2O content, and often more scans were needed to acquire spectra with

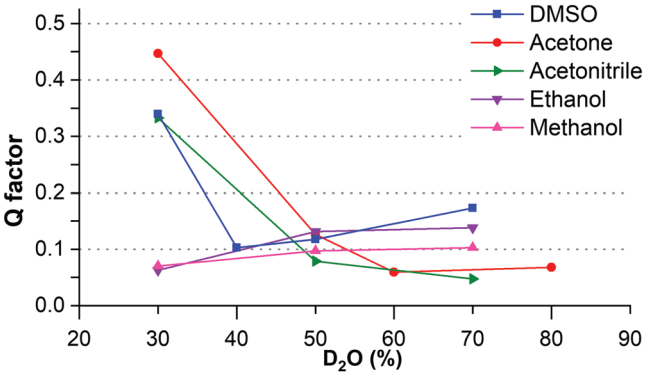

FIGURE 4 Solvent dependence on the measured residual dipolar couplings (RDCs). Shown as correlation between calculated Q factor and percentage amount of D_2O in the solvent mixture with varying polar deuterated organic solvents with commercial graphene oxide (GO)

#	30%		40%		50%		70%	
1	1.54	8.56	2.79	14.91	6.36	20.70	24.46	18.93
2a	2.25	−2.53	−0.12	−2.61	−1.93	−2.90	−3.96	−3.83
2b	1.49	10.73	1.15	13.65	9.81	25.39	23.70	18.58
3	1.58	10.83	3.18	11.96	7.69	14.98	29.87	14.03
4a	1.35	5.21	0.77	4.62	3.65	3.07	−1.65	7.94
4b	1.49	11.00	4.57	13.16	7.62	11.05		10.83
5a	−0.89	−2.24	1.72	−1.51	−1.36	−2.62	−3.40	−2.22
5b	2.28	13.40	1.88	19.03	10.57	24.89	30.26	21.50
6	0.60	8.66	2.73	14.69	6.94	19.31	23.55	21.74
7	0.75	3.78	−0.17	5.37	1.86	10.54	8.65	9.62
8	−0.05	−0.72	0.77	−0.22	0.69	0.10	1.36	−0.01
9	0.60	−0.26	−0.54	−2.68	−1.42	−4.34	−4.90	−0.19
10	0.82	2.69	1.22	6.51	1.64	8.30	9.85	12.36
Q	**0.478**	**0.340**	**0.218**	**0.103**	**0.102**	**0.118**	**0.106**	**0.173**

Note: White cells: 4.1 mg/ml graphene oxide (GO), gray cells: 1.6 mg/ml commercial GO. Percentages refer to D_2O ratio. Blank cell is due to distorted peaks.

TABLE 2 Comparison of acquired residual dipolar couplings (RDCs) in Hz for menthol dependent on D_2O: dimethyl sulfoxide (DMSO)-*d*6 solvent mixture

TABLE 3 Comparison of acquired residual dipolar couplings (RDCs) in Hz for menthol dependent on graphene oxide (GO) concentration

#	1.65 mg/ml	3.31 mg/ml	4.96 mg/ml	6.61 mg/ml	8.27 mg/ml	0.4 mg/ml	0.8 mg/ml	1.2 mg/ml	1.6 mg/ml	2.0 mg/ml
1	2.92	5.20	10.33	22.19	28.14	4.02	11.04	16.14	25.03	24.76
2a	0.27	−2.05	−2.05	−3.15	−4.18	−0.35	−2.40	−4.04	−4.94	−5.73
2b	4.62	6.97	14.99	23.02	31.04	3.13	11.52	17.33	19.32	23.90
3	3.83	5.40	13.04	25.17	21.11	2.84	13.63	13.22	23.80	
4a	−0.17	0.38	1.83	3.58	7.79	3.18	3.96	3.08	1.62	
4b	0.99	6.99	11.83		17.80	6.48	10.07	20.46		
5a	0.44	0.00	−0.44	−0.24	0.99	−0.82	−1.39	−1.08	−2.21	−2.83
5b	1.47	8.32	13.60	25.90	35.27	2.67	14.21	20.27	25.02	32.23
6	1.42	4.58	10.05	24.24	28.77	3.90	11.33	13.62	25.03	28.45
7	0.30	0.18	3.89	8.23	11.58	1.49	3.72	5.05	9.80	5.95
8	0.32	0.12	−0.31	0.94	0.48	0.05	0.11	0.79	0.73	1.25
9	−1.25	−1.59	−2.93	−4.62	−5.24	−0.95	−1.53	−1.65	−1.80	−2.61
10	0.91	0.85	4.04	8.47	11.17	1.38	5.06	7.45	10.15	10.85
Q	**0.363**	**0.162**	**0.099**	**0.054**	**0.101**	**0.137**	**0.079**	**0.147**	**0.099**	**0.086**

Note: White cells: GO, gray cells: Commercial GO. All samples in 1:1 D_2O:DMSO-*d6*. Blank cells are due to distorted peaks

acceptable signal-to-noise. In the case of menthol, a 1:1 mix seems to be the optimum between sharp peaks and fitting size of the RDCs. This is in agreement with Lei et al. who observed RDCs with excellent correlation in 1:1 mixtures with dimethyl sulfoxide (DMSO), acetone, and acetonitrile as well.[17]

Here lies a limit in the use of pure GO as alignment media as a number of organic compounds are insoluble when high water content is necessary. Modifying the GO is a promising path to overcome this limitation.[18,19] Modified GO might also facilitate changing the alignment direction and not just the strength of alignment.

6 | CONCENTRATION OF GO

We observed an immediate effect of the GO concentration on the degree of alignment, as seen by the varying sizes of the measured RDCs in Table 3, and this is mirrored in the GDO in Figure S9. The dependence of the RDCs on the GO concentration is linear for most protons in menthol, with the largest effects seen for the axial protons. The effect of varying the GO concentration is also observed on the calculated Q factors as seen in Figure 5. For GO made in our own laboratory, an optimal concentration is noted around 5 mg/ml. At lower concentration, the RDCs of menthol shown in Table 3 decreased to a level where the relative measurement uncertainty causes an increase in the Q factor. At higher GO concentrations, broader peaks were observed, and more often peaks were distorted, disabling accurate measurements and thereby resulting in higher Q factors. This trend in size and quality of the RDCs were also seen for samples made from commercial GO as shown in Table 3; however, here this trend was not directly translated to the Q factors, but show better correlation to the GDO as seen in Figure S9. For commercial GO, much less material was needed to achieve sufficient alignment, and only a minimum of sediment was observed.

Deuterium spectra for the commercial GO samples of Table 3 are shown in Figure 6. Only the most concentrated samples show a discernable deuterium splitting. Other spectra display a broadening of the signal to varying degrees. As all samples resulted in Q factors of less than 0.15, this proves that a broadening of the deuterium peak may be enough to indicate sufficient alignment for GO samples. The direct dependence of GO concentration on the RDCs supports previous observations by Lei et al. through observations of the deuterium quadrupolar splitting at different concentrations.[17]

Figure 5 also contain Q factors for menthol RDC data acquired in 3-mm NMR tubes. The GO sample solutions were the same for the 5- and 3-mm samples, RDC data shown in Table 3 and Table S10, respectively. The sample preparation of 3 mm samples was straightforward and required no extra considerations as the GO solutions have low viscosity.

A Q factor of 0.071 was seen for a 2-mM menthol sample in a 3-mm tube with an experimental time of 2 days 10 h with 256 scans and not using non-uniform sampling. This means only a minimal amount of solute is needed for analysis; thus, this method is applicable when limited amount of material is available, for example, when studying scarce natural products. No effect beyond the measurement uncertainty was seen when varying the amount of menthol in the range of 2–10 mM in isotropic samples, thereby excluding concerns regarding menthol–

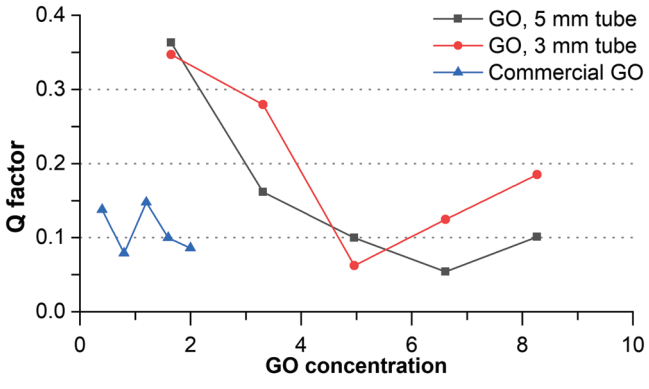

FIGURE 5 Graphene oxide (GO) concentration influence on the measured residual dipolar couplings (RDCs) for menthol, shown through the calculated Q factor for samples in different sized nuclear magnetic resonance (NMR) tubes and GO sources. All samples in 1:1 D_2O:dimethyl sulfoxide (DMSO)-*d6*

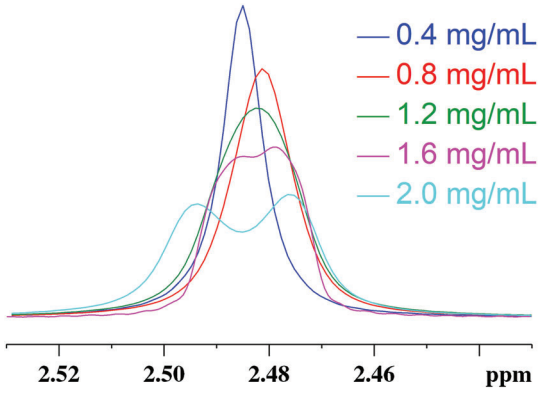

FIGURE 6 Overlay of 1D ^2H spectra showing the dimethyl sulfoxide (DMSO)-*d6* peak for the varying concentrations of commercial graphene oxide (GO) from Figure 5 and Table 3. The largest deuterium splitting seen here is 2.2 Hz. The DMSO-*d6* peak for the sample with the lowest GO concentration (blue) is still slightly wider than a sample without GO

menthol interactions and other solute concentration dependent effects.

A similar trend was seen when varying the concentration of GO for samples of (+)-pinanediol. At concentrations below 4 mg/ml GO the measured RDCs are too small to be meaningful and the obtained Q factor rose drastically; see Table S14. The lowest Q factor of 0.043 was seen for the highest tested GO concentration of 8.27 mg/ml. At this concentration, the maximum observed RDC was 35.27 and 6.65 Hz for menthol and pinanediol, respectively. From this, it is clear that the degree of alignment of each compound is different. The aligning interaction between the solutes and GO is assumed to be mostly steric, and in this case, the more spherical shape of pinanediol is very different from the flatter conformation of menthol.

7 | RE-DISSOLVING DRIED GO

Drying GO by lyophilization or vacuum centrifugation resulted in a dark gray spongy or porous material. The dried GO could be re-dissolved in both D_2O and a D_2O:DMSO-*d*6 1:1 mixture sometimes aided by sonication. Good quality CLIP-HSQC spectra were acquired, RCDs extracted, and back-calculation resulted in a Q factor of 0.088. This proves the successful regain of dispersibility, LC formation, and alignment properties, providing other potential routes of sample preparation. The resulting solutions often still had an amount of undissolved material. In some instances, the use of sonication resulted in a stronger alignment effect rendering the acquired spectra difficult to analyze and hindering extraction of exact RDCs. The use of sonication has been linked to fragmentation of the GO sheets, less sedimentation, and higher dispersibility.[18,27,28]

8 | RECOVERY OF SOLUTE

RDCs were also measured for methyl-α-D-glucopyranoside (Me-α-Glc) in a GO solution in D_2O and RDCs back-calculated with a Q factor of 0.177; see Table S16. The GO solution was subsequently repeatedly centrifuged and the clear supernatant exchanged with fresh D_2O until proton spectra showed no Me-α-Glc signals. The collected supernatants were then filtered through a 0.2-μm Omnipore filter to discard residual GO sheets, and the solution was evaporated to dryness. The mass of the remainder was higher than the initial amount of Me-α-Glc added, taken as an indication that very small GO fragments had passed the filter. Spectra of the remainder showed that Me-α-Glc had been recovered with only minor impurities visible in 1D ^{1}H spectra, see Figure S11. The isolation procedure may be improved, but recovery of the solute is indeed possible, making the choice of GO as alignment media more attractive in cases where the sample amount is precious as the use of GO can be non-destructive.

9 | PERSPECTIVES AND CONCLUSION

We hope that the results presented here have highlighted the extensive possibilities and choices provided by the use of GO solutions as alignment media in NMR spectroscopy. Further modifications of GO to allow greater alignment in organic solutions and provide enantiodiscrimination will be stepping stones towards GO being the general alignment media of choice. With regard to the ease of sample preparation from a stock solution of GO, we believe that this could lower the threshold for those looking to get into this area of research. To further facilitate this purpose, illustrative spectra, pictures of samples, examples of calculation scripts, and so forth have been included in the supporting information.

In summation, GO can be used as alignment media for organic compounds that are

- Polar and sufficiently soluble in at least 30% D_2O solvent mixtures
- Not poly-aromatic, as they will likely stack with the GO material causing it all to precipitate.

Whether or not GO has superior advantages over other alignment media with respect to obtaining RDCs for flexible molecules still has to be explored. This is part of an ongoing study focusing on the application of GO as alignment media for different compound classes.

The most important points to evaluate during sample preparation are as follows:

1. The solubility of the solute/compound to be studied
   Start with the highest percentage D_2O that still allows solubility of the compound. If broad and distorted peaks are observed together with large RDCs, increasing the amount of organic solvent may be beneficial. Here choose the deuterated organic solvent that the compound is most soluble in (which also has to be miscible with D_2O).
2. The optimal GO concentration
   The correlation between GO concentration and size of the RDCs is roughly linear. Therefore, one approach could be starting with a low concentration of GO and

gradually adding more GO until the measurable RDCs are large enough, for example, significantly beyond the measurement uncertainties, while at the same time, the induced broadening and distorting effects of GO do not hinder measurement.

ACKNOWLEDGEMENTS

We are grateful to DTU Chemistry for an academic excellence PhD scholarship for KDP. KDP would like to thank Jing Tang for the introduction to GO synthesis and AFM measurements. The NMR Center • DTU and the Villum Foundation are acknowledged for access to the 600- and 800-MHz spectrometers.

PEER REVIEW

The peer review history for this article is available at https://publons.com/publon/10.1002/mrc.5143.

ORCID

Katja D. Pedersen https://orcid.org/0000-0002-4193-2678

Charlotte H. Gotfredsen https://orcid.org/0000-0002-7386-119X

REFERENCES

[1] C. M. Thiele, *Eur. J. Org. Chem.* **2008**, 5673.
[2] Y. Liu, J. Saurí, E. Mevers, M. W. Peczuh, H. Hiemstra, J. Clardy, G. E. Martin, R. T. Williamson, *Science* **2017**, *356*, eaam5349.
[3] A. Schuetz, J. Junker, A. Leonov, O. F. Lange, T. F. Molinski, C. Griesinger, *J. Am. Chem. Soc.* **2007**, *129*(49), 15114.
[4] M. E. Di Pietro, P. Tzvetkova, T. Gloge, U. Sternberg, B. Luy, *Liq. Cryst.* **2020**, 1.
[5] B. Luy, K. Kobzar, H. Kessler, *Angew. Chem. Int. Ed.* **2004**, *43* (9), 1092.
[6] P. Haberz, J. Farjon, C. Griesinger, *Angew. Chem. Int. Ed.* **2005**, *44*(3), 427.
[7] R. R. Gil, C. Gayathri, N. V. Tsarevsky, K. Matyjaszewski, *J. Organomet. Chem.* **2008**, *73*(3), 840.
[8] L. F. Gil-Silva, R. Santamaría-Fernández, A. Navarro-Vázquez, R. R. Gil, *Chem. Eur. J.* **2016**, *22*(2), 472.
[9] I. Canet, J. Courtieu, A. Meddour, J. M. Pechine, A. Loewenstein, *J. Am. Chem. Soc.* **1995**, *117*(24), 6520.
[10] A. Meddour, P. Berdague, A. Hedli, J. Courtieu, P. Lesot, *J. Am. Chem. Soc.* **1997**, *119*(19), 4502.
[11] M. Sarfati, P. Lesot, D. Merlet, J. Courtieu, *Chem. Commun.* **2000**, (21), 2069.
[12] C. M. Thiele, S. Berger, *Org. Lett.* **2003**, *5*(5), 705.
[13] A. Marx, V. Schmidts, C. M. Thiele, *Magn. Reson. Chem.* **2009**, *47*(9), 734.
[14] C. M. Thiele, *J. Organomet. Chem.* **2004**, *69*(22), 7403.
[15] N. C. Meyer, A. Krupp, V. Schmidts, C. M. Thiele, M. Reggelin, *Angew. Chem. Int. Ed.* **2012**, *51*(33), 8334.
[16] L. Arnold, A. Marx, C. M. Thiele, M. Reggelin, *Chem. Eur. J.* **2010**, *16*(34), 10342.
[17] X. Lei, Z. Xu, H. Sun, S. Wang, C. Griesinger, L. Peng, C. Gao, R. X. Tan, *J. Am. Chem. Soc.* **2014**, *136*(32), 11280.
[18] W. Zong, G. W. Li, J. M. Cao, X. Lei, M. L. Hu, H. Sun, C. Griesinger, R. X. Tan, *Angew. Chem. Int. Ed.* **2016**, *55*(11), 3690.
[19] J. A. A. França, A. Navarro-Vázquez, X. Lei, H. Sun, C. Griesinger, F. Hallwass, *Magn. Reson. Chem.* **2017**, *55*(4), 297.
[20] W. S. Hummers, R. E. Offeman, *J. Am. Chem. Soc.* **1958**, *80*(6), 1339.
[21] A. Enthart, J. C. Freudenberger, J. Furrer, H. Kessler, B. Luy, *J. Magn. Reson.* **2008**, *192*(2), 314.
[22] "Maestro." Schrödinger, version 11.6.013 (2018–2).
[23] "MSpin." Version 2.3.4-776, MestReLab Research S. L., 2019.
[24] A. Navarro-Vázquez, *Magn. Reson. Chem.* **2012**, *50* (November), S73.
[25] F. Kramer, M. V. Deshmukh, H. Kessler, S. J. Glaser, *Concepts Magn. Reson. Part a Bridg. Educ. Res.* **2004**, *21*(1), 10.
[26] D. Konios, M. M. Stylianakis, E. Stratakis, E. Kymakis, *J. Colloid Interface Sci.* **2014**, *430*, 108.
[27] X. Sun, Z. Liu, K. Welsher, J. T. Robinson, A. Goodwin, S. Zaric, H. Dai, *Nano Res.* **2008**, *1*(3), 203.
[28] J. I. Paredes, S. Villar-Rodil, A. Martínez-Alonso, J. M. D. Tascón, *Langmuir* **2008**, *24*(19), 10560.

SUPPORTING INFORMATION

Additional supporting information may be found online in the Supporting Information section at the end of this article.

How to cite this article: Pedersen KD, Zhang J, Gotfredsen CH. Practical considerations for working with graphene oxide as alignment media for RDC measurements. *Magn Reson Chem*. 2021; 1–8. https://doi.org/10.1002/mrc.5143

Supporting information

Practical considerations for working with GO as alignment media for RDC measurements

Katja D. Pedersen, Jingdong Zhang, and Charlotte H. Gotfredsen

Department of Chemistry, Technical University of Denmark

Materials and chemicals

Powdered graphite from Sigma Aldrich (<20µm).

Commercial GO stock solution 0.4 w% and concentrated 2.5 w% from Graphenea S.A. (https://www.graphenea.com/). Unless otherwise stated, commercial GO refers to the 0.4 w% solution.

All other chemicals from Sigma Aldrich and used as received.

Instruments

Bruker AVANCE 800 MHz system, 5mm TCI CryoProbe.
Bruker AVANCE 600 MHz system, 5mm SmartProbe BB(F)-H-D.

M3800-E Branson Ultrasonics™ M Series Ultrasonic Cleaning Bath.

Eppendorf centrifuge 5810R (larger volumes for synthesis) and VWR Micro star 17R (for sample preparation).

Lyophilization (freeze-drying) by ScanVac Coolsafe.

Synthesis of GO

Graphene oxide was made through a modified Hummers' synthesis, where powdered graphite was oxidized in two steps, followed by sonication and dialysis to obtain graphene oxide dispersed in water.

Pre-oxidized graphite

2.5 g $K_2S_2O_8$ and 2.5 g P_2O_5 were dissolved in 15 mL H_2SO_4 and 5.0 g graphite was added to give a viscous solution, which reacted for 3 hours at 80°C with stirring in a flask fitted with a reflux condenser. When the solution had cooled to room temperature, 120 mL water MilliQ (0.05 µS/cm) was slowly added. The solution was filtered and the collected pre-oxidized graphite was washed with MilliQ water until the filtrate had neutral pH. The solid was dried overnight at 50°C.

Graphene oxide

The pre-oxidized graphite was ground and 1.0 g was added to 23 mL H_2SO_4 in an ice bath. Then 3.0 g ground $KMnO_4$ was added very slowly while monitoring that the temperature of the solution stayed below 20°C. The mixture was heated to 35°C for 2 hours under a reflux condenser, during which the solution changed color from green-black to dark brown. 50 mL MilliQ water was added slowly and the solution left for 15 min at 35°C before additional 140 mL MilliQ water was added. H_2O_2 was added drop-by-drop as long as bubbles appeared and the solution changed to green-brown. The room temperature solution was vacuum filtered on two Omnipore filter papers (hydrophilic, 0.2 µm pore size, 47 mm diameter) under continuous stirring and washed with 2x125 mL 1 M HCl. The entire filtration process took 3-4 hours. The solid was dispersed in app. 200 mL MilliQ and sonicated (40 kHz) for 2 hours in ice-water. The solution was first centrifuged at 500 rpm (28 rcf) for 5 min and the solid was discarded as it was presumed to be residual graphite. The supernatant was then centrifuged at 12'000 rpm (15938 rcf) for 30 min. The new supernatant contained small graphene oxide sheets (<1 µm diameter) and was collected separately. The solid was larger graphene oxide sheets, which was redispersed in app. 100 mL MilliQ water. The graphene oxide solutions were then purified by dialysis with a cellulose membrane (MWCO 12000-14000). The MilliQ water outside the membrane was changed 1-2 times a day for 8 days.

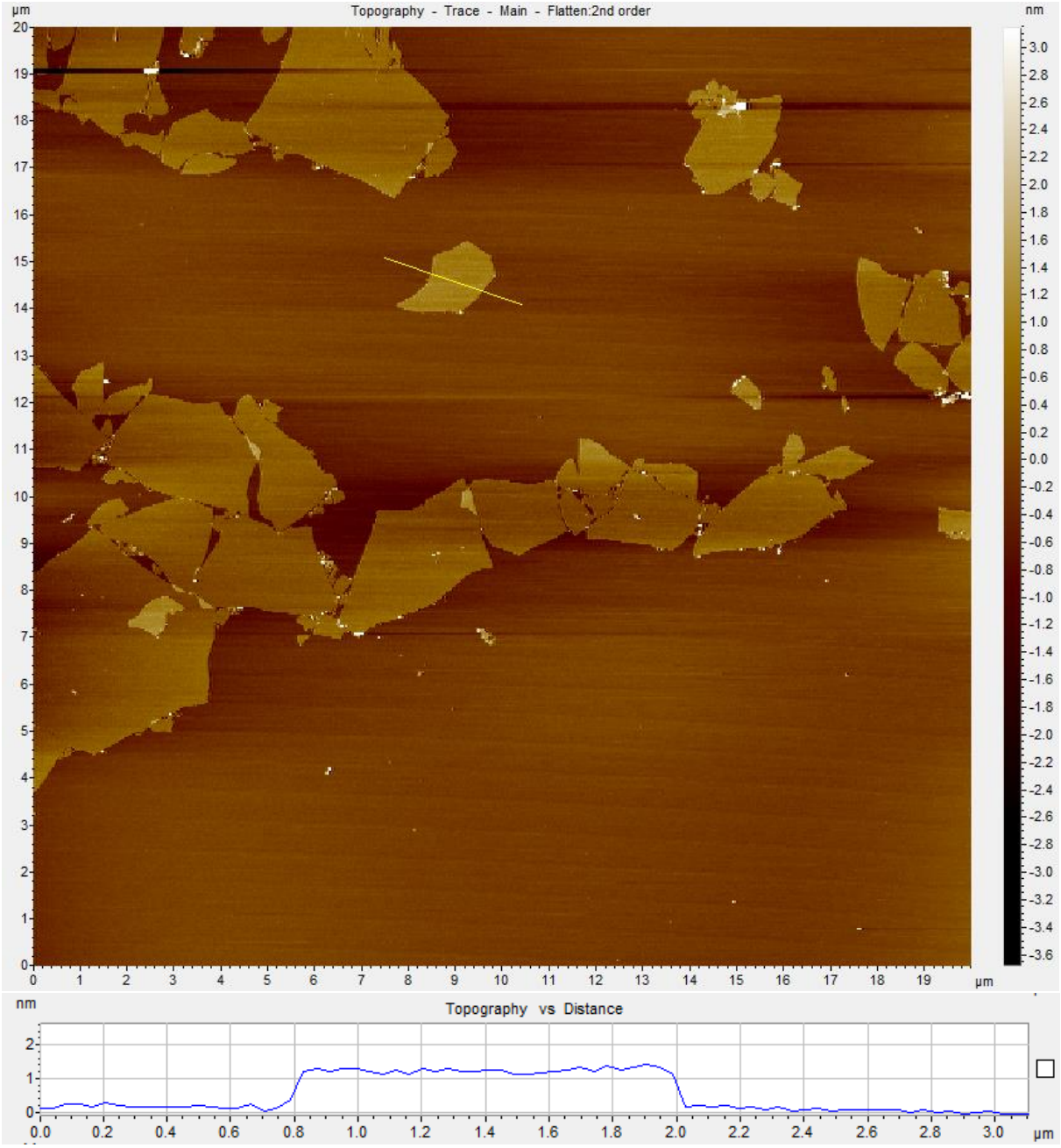

Figure S1. Atomic force microscopy (AFM) image of GO on mica. It can be seen that the GO sheets are of the sizes 1-5 µm. The topography inset at the bottom corresponds to the yellow line on the image and the height of approximately 1 nm show the single layer structure of GO. Agilent Technologies 5500 AFM in tapping mode.

Concentration

The concentration of the synthesized GO stock solutions was determined by lyophilization, as a standard on triplicate samples. Concentration of the used NMR samples were then based on the stock solution concentration and the amount of dilution.

When this method was used on the commercial GO solution, results were obtained that were in agreement with the stated concentrations.

Sample preparation

The required amount of GO was taken from the GO stock solution and centrifuged at 12,000 rpm (13,000 rcf) for 30 min. The supernatant was then exchanged with deuterated solvent and the GO dispersed by vigorous shaking. This could be repeated a number of times for higher exchange of H_2O, however with higher organic solvent concentration, clear separation of GO and supernatant became increasingly difficult. Then the dissolved compound of interest was added and after shaking the solution was transferred to a NMR tube and the sample was ready for acquisition.

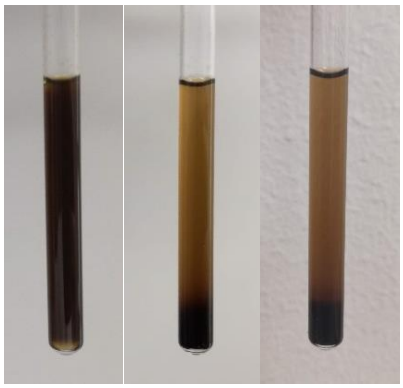

Constant after 1-3 days.

Figure S2. Sample of 4.1 mg/mL GO in DMSO-d6/D_2O 1:1. Left: when freshly prepared. Middle: after 17 days. Right: after 58 days.

The GO LC structure is sensitive to very high and low pH as well as salt concentration. The sensitivity increases with a larger fraction of organic solvent.

NMR acquisition and processing

All data acquired at 298 K in 5 mm standard NMR tubes at 800 MHz in TopSpin 3.5 pl 6 by Bruker unless otherwise stated and processed in TopSpin 3.6.1 by Bruker.

As mentioned in the main text, anisotropic samples often have shimming issues and was for this work usually done manually. We have been made aware that automatic shimming using a non-splitting proton signal have worked well for other types of alignment media. This is done in TopSpin using the command “topshim 1h o1p=4.45 selwid=0.5 rga”, here using the residual water signal at 4.45 ppm and the selective excitation of 0.5 ppm width. This method have only been tried sparingly on GO samples, but seems to provide good results.

2D CLIP-HSQC, J_{CH} = 145.0 Hz, relaxation delay 1.5 s, size of FID 2k (F2) x 512 (F1), zero-filled to 4k x 1k, window function QSINE, line broadening 1.0 Hz (F2) and 0.3 Hz (F1).
No line broadening in deuterium spectra of aligned samples to see small quadrupolar splittings.
Dipolar couplings manually measured from 1D slices of 2D CLIP-HSQC spectra.

RDCs found by $T_{CH}=J_{CH} + D_{CH}$, where $^1T_{CH}$ was measured from the aligned samples and $^1J_{CH}$ from a corresponding isotropic menthol sample.

Calculations

Maestro suite version 11.6.013(2018-2) by Schrödinger using program MacroModel to perform conformational search. Force field MMFFs, modelled in water, PRCG minimization, mixed torsional/low-mode sampling, 10’000 steps and an energy cutoff of 21 kJ/mol.

DFT calculations in Gaussian version 09 revision B01. Used for geometry optimization with B3LYP/6-31G(d) for output structures from conformational search and subsequent calculations of NMR shielding tensors with MPW1PW91/6-311+G(d,p) using GIAO. All calculations used the PCM-SCRF model for implicit solvent water.

MSpin version 2.3.4-776, 2019, by MestReLab Research S. L. used for RDC back-calculation using SVD and single tensor computation. Averaging used for distinguishable methyl groups. Example of MSpin input and output files provided below.

Assignment of menthol

Table S1. Assignment of (-)-menthol, 8 mM in D_2O:DMSO-d6 1:1. The solvent mixture results in broad peaks making extraction of J-coupling constants difficult. Referenced to DMSO at 2.50 ppm (^1H) and 39.51 ppm (^{13}C).

#	δ_H [ppm] (int, mult., *J* [Hz])	δ_C [ppm]
1	3.20 (1H, td, 11.1, 4.4)	71.8
2a	1.77 (1H, d, 14.1)	45.5
2b	0.79 (1H, m)	
3	1.26 (1H, m)	32.5
4a	1.52 (1H, d, 14.1)	35.4
4b	0.68 (1H, m)	
5a	1.46 (1H, m)	23.9
5b	0.82 (1H, m)	
6	0.95 (1H, m)	50.5
7	1.98 (1H, sep.d, 7.3, 2.2)	26.4
8	0.77 (3H, d, 7.2)	22.2
9	0.63 (3H, d, 7.3)	16.9
10	0.77 (3H, d, 7.2)	23.2

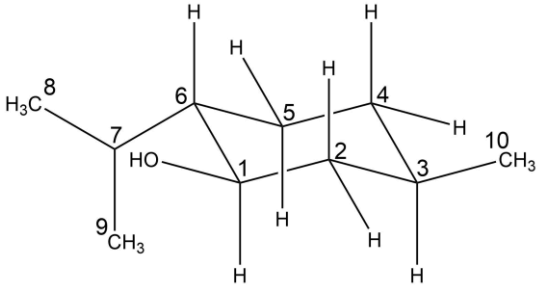

Figure S3. Structure of (-)-menthol as assigned in Table S1. For methylene groups Xa refers to equatorial protons and Xb to axial protons.

Example spectra

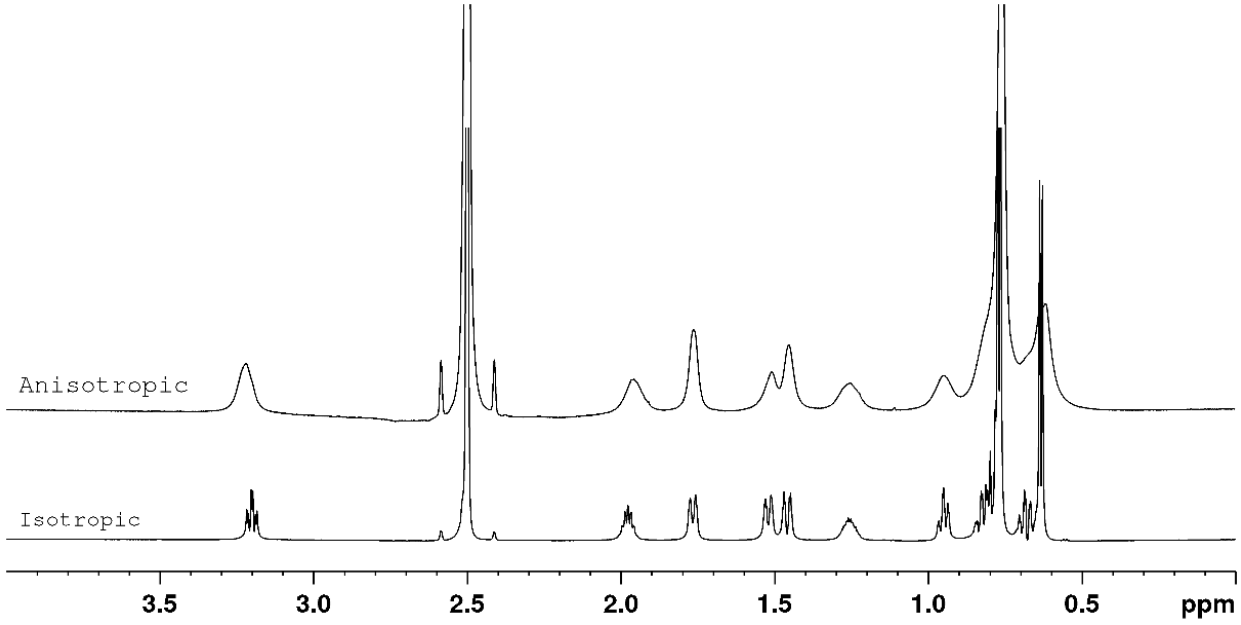

*Figure S4. 1D ^{1}H spectrum of menthol compared to a sample with 1.6 mg/mL **commercial** GO. Both samples in 1:1 D_2O:DMSO-d6, making also the isotropic peaks broader than what is usually observed.*

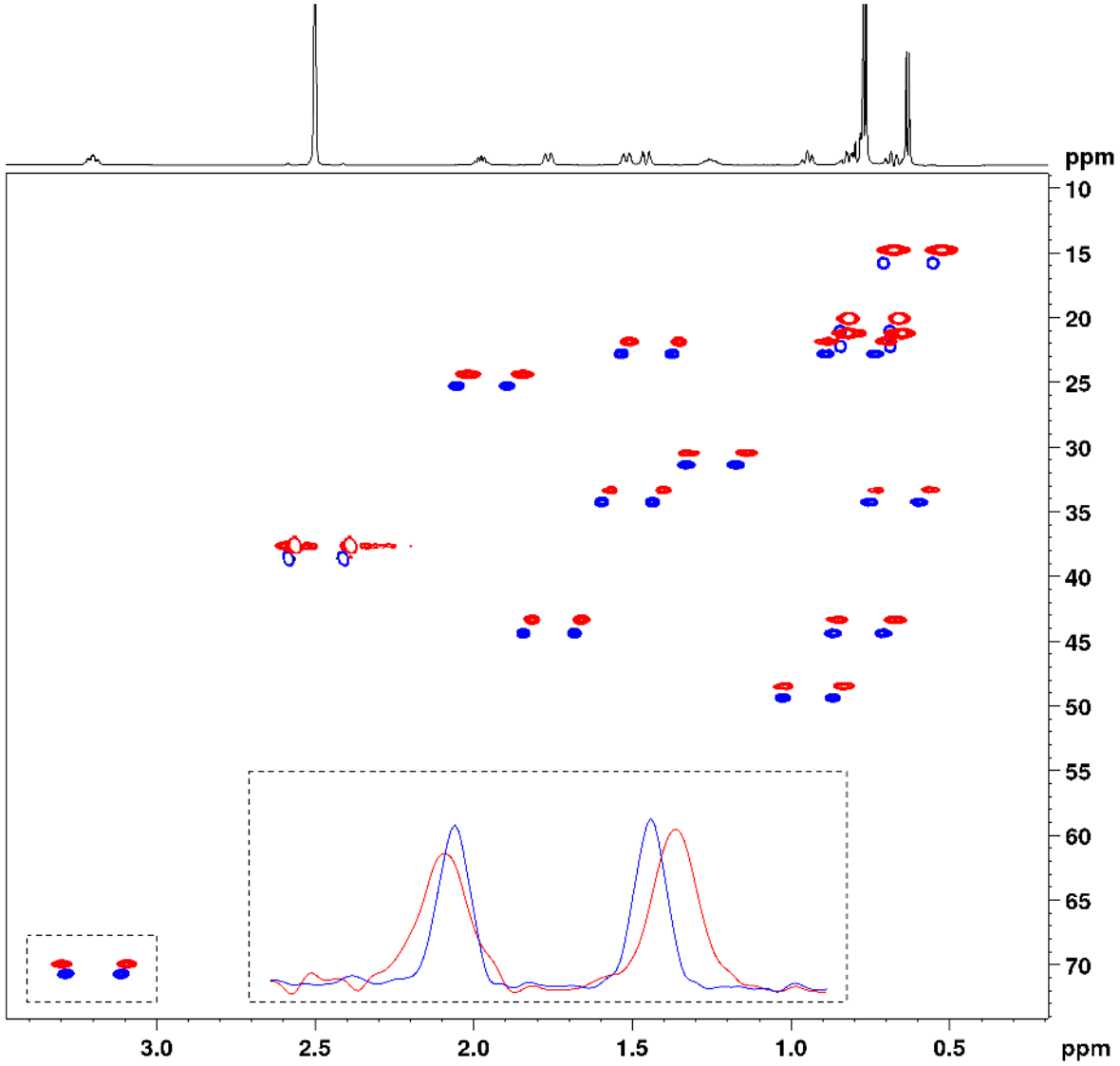

Figure S5. CLIP-HSQC spectrum of menthol (blue) and with 1.6 mg/mL commercial GO added (red). 1D slices of the boxed signals are shown. J_{CH} and T_{CH} were measured between the peak maxima. Both samples were in 1:1 D_2O:DMSO-d6. Red spectrum has been shifted slightly upwards for clarity.

Stability

Table S2: RDCs over time and the associated Q factors. 4.1 mg/mL GO, 1:1 D_2O:DMSO-d6, 6 mM menthol. All values are in Hz. Gray and white cells refer to the "dark" and "light" sample from Figure 2, respectively.

Days	17	27	37	47	56	76	139	175	216	279	Average	StDev
1	8.78	6.62	7.74	8.24	7.98	8.96	8.03	7.95	9.50	10.83	8.46	1.14
2a	-0.91	-1.26	-0.64	-0.97	-1.79	-1.41	-1.56	-3.04	-1.74	-0.59	-1.39	0.72
2b	10.00	10.49	12.54	10.55	10.12	11.69	12.69	10.57	10.32	15.53	11.45	1.73
3	9.14	9.32	9.78	8.76	9.94	7.78	10.09	9.73	9.81	15.19	9.95	1.97
4a	1.69	1.37	1.55	0.97	1.80	1.21	1.51	0.37	-0.73	-0.92	0.88	0.99
4b	7.75	7.08	7.79	7.79	8.88	7.15	7.09	8.58	10.03	11.31	8.35	1.40
5a	-0.59	-0.83	-0.54	-0.27	-0.55	-0.33	-0.94	-0.96	0.62	-1.22	-0.56	0.51
5b	9.30	12.00	11.78	9.92	11.70	12.39	11.7	11.63	11.63	13.29	11.53	1.14
6	7.12	8.06	7.39	8.99	9.59	5.80	7.00	5.65	9.63	6.85	7.61	1.43
7	2.28	2.70	3.06	2.77	3.67	3.09	2.27	2.27	3.83	-0.37	2.56	1.17
8	0.78	0.86	0.82	0.77	0.49	0.80	0.65	0.72	0.68	0.63	0.72	0.11
9	-1.90	-1.69	-1.43	-1.81	-1.77	-1.72	-2.05	-1.98	-1.07	-2.18	-1.76	0.32
10	2.48	2.79	3.05	2.11	1.76	2.51	2.93	2.69	2.95	2.66	2.59	0.40
Q	0.072	0.072	0.103	0.036	0.083	0.149	0.102	0.173	0.082	0.161	0.103	0.044
1	8.85	10.38	8.71	9.69	10.64	9.22	10.61	10.75	10.85	10.64	10.03	0.84
2a	-1.95	-1.17	-1.64	-1.08	-1.69	-1.50	-1.64	-2.84	-3.20	-3.15	-1.99	0.79
2b	10.71	10.62	12.20	12.81	11.38	13.03	13.02	12.81	12.86	15.88	12.53	1.50
3	9.62	8.46	11.87	11.06	12.12	12.42	14.18	12.56	13.22	15.34	12.09	2.03
4a	1.48	1.90	1.60	1.72	1.50	1.86	1.18	1.61	0.85	-0.79	1.29	0.80
4b	7.69	8.60	8.43	9.08	9.69	7.38	9.63	10.07	8.62	12.76	9.20	1.52
5a	0.42	-0.69	-0.93	-0.43	-1.09	-1.17	-2.10	-0.88	-0.69	-2.43	-1.00	0.81
5b	10.99	12.30	13.17	13.20	14.28	11.65	14.25	11.77	11.94	14.91	12.85	1.32
6	9.08	9.06	9.44	9.07	7.78	8.15	9.71	11.11	12.08	9.39	9.49	1.28
7	2.45	3.37	2.28	2.12	2.74	2.13	3.48	0.99	0.92	3.70	2.42	0.96
8	0.64	0.70	0.26	-1.79	0.36	0.81	0.69	0.71	0.71	0.66	0.38	0.78
9	-1.68	-1.72	-2.28	0.35	-1.92	-1.08	-2.23	-1.97	-2.19	-2.21	-1.69	0.80
10	2.42	2.73	2.97	2.92	2.78	2.92	2.85	2.84	2.86	2.90	2.82	0.16
Q	0.071	0.057	0.061	0.074	0.140	0.080	0.109	0.056	0.075	0.149	0.087	0.034

Solvent

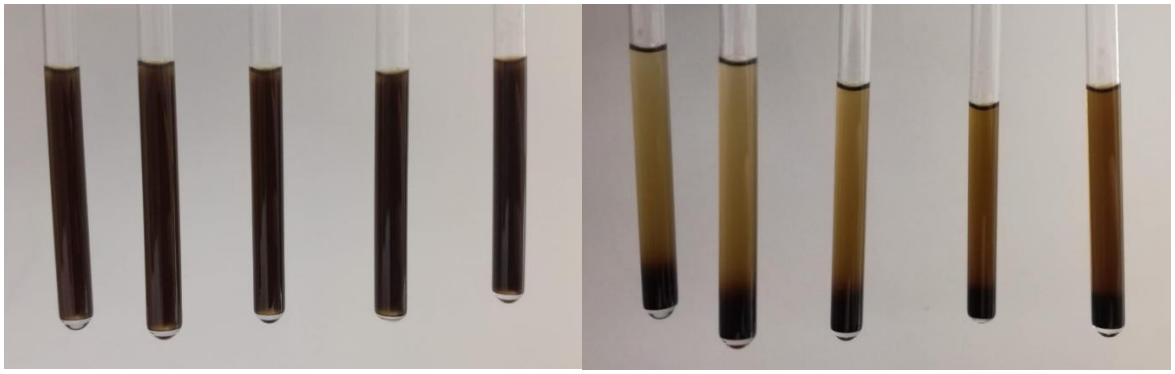

Figure S6. Left: Freshly prepared samples of equal GO concentration with increasing amounts of D_2O, 30% to 70% going left to right. Samples with low amounts of D_2O looked slightly lighter to the naked eye. Right: Same samples 17 days later after standing undisturbed. With increasing amounts of D_2O, the solution clearly becomes darker in agreement with GO being less dispersible in DMSO.

Table S3. RDCs in Hz dependent on D_2O:DMSO-d6 solvent mixture. 4.1 mg/mL GO, 6 mM menthol. Percentages refer to D_2O ratio. Blank cells is due to distorted peaks.

#	30 %	40 %	50 %	60 %	70 %
1	1.54	2.79	6.36	15.48	24.46
2a	2.25	-0.12	-1.93	-3.12	-3.96
2b	1.49	1.15	9.81	16.88	23.70
3	1.58	3.18	7.69	12.91	29.87
4a	1.35	0.77	3.65	4.77	-1.65
4b	1.49	4.57	7.62	12.83	
5a	-0.89	1.72	-1.36	-0.46	-3.40
5b	2.28	1.88	10.57	16.38	30.26
6	0.60	2.73	6.94	13.54	23.55
7	0.75	-0.17	1.86	6.63	8.65
8	-0.05	0.77	0.69	-0.10	1.36
9	0.60	-0.54	-1.42	-1.75	-4.90
10	0.82	1.22	1.64	7.72	9.85
Q	0.478	0.218	0.102	0.105	0.106

*Table S4. RDCs dependent on D_2O:Acetone-d6 solvent mixture. 1.2 mg/mL **commercial** GO, 16 mM menthol. Percentages refer to D_2O ratio.*

#	30 %	50 %	60 %	80 %
1	0.45	6.24	9.62	23.79
2a	0.96	-0.56	-0.85	-2.75
2b	1.15	6.42	9.62	22.72
3	1.17	5.59	8.47	24.33
4a	2.46	1.52	1.94	4.73
4b	1.58	8.30	9.68	20.09
5a	-1.14	-1.28	-1.46	-2.32
5b	1.17	9.91	11.21	24.11
6	2.32	6.64	8.58	19.43
7	-0.32	2.22	3.97	10.30
8	0.35	-0.57	-0.42	-0.05
9	0.00	-2.36	-1.54	-3.65
10	0.91	1.73	3.68	10.06
Q	0.447	0.126	0.059	0.068

*Table S5. RDCs dependent on D_2O:Acetonitrile-d3 solvent mixture. 1.6 mg/mL **commercial** GO, 16 mM menthol. Percentages refer to D_2O ratio. Blank cells are due to distorted peaks.*

#	30 %	50 %	70 %
1	2.53	6.89	23.23
2a	-0.05	0.02	-2.29
2b	1.32	7.80	24.20
3	2.46	6.96	22.87
4a	2.58	-0.02	2.81
4b	3.57	8.33	21.44
5a	1.83	-1.28	-1.43
5b		8.49	22.92
6	1.94	7.80	21.16
7	0.27	1.51	6.78
8	-0.42	0.54	0.93
9	-0.27	-2.08	-2.70
10	0.03	2.37	9.45
Q	0.333	0.079	0.047

*Table S6. RDCs dependent on D_2O:Methanol-d4 solvent mixture. 1.2 mg/mL **commercial** GO, 16 mM menthol. Percentages refer to D_2O ratio. Blank cells are due to distorted peaks.*

#	30 %	50 %	70 %
1	4.50	9.53	30.01
2a	0.20	-1.52	-3.87
2b	3.61	11.01	29.81
3	4.01	8.68	24.73
4a	-0.14	5.19	3.06
4b	5.68	12.32	22.12
5a	-0.13	-1.45	-1.33
5b	4.03	14.23	
6	4.02	10.10	
7	0.18	1.79	9.66
8	-0.13	0.11	0.79
9	-0.22	-1.95	-4.33
10	0.84	3.11	11.60
Q	0.0702	0.0968	0.1029

*Table S7. RDCs dependent on D_2O:Ethanol-d6 solvent mixture. 1.2 mg/**mL commercial** GO, 16 mM menthol. Percentages refer to D_2O ratio.*

#	30 %	50 %	70 %
1	2.55	6.63	20.01
2a	0.85	0.44	-2.14
2b	3.22	11.00	19.31
3	0.66	8.19	20.32
4a	2.03	2.58	4.62
4b	2.94	8.74	17.23
5a	0.29	-0.70	-2.40
5b	3.06	13.13	21.22
6	2.27	6.89	20.05
7	0.45	1.35	6.57
8	-0.14	-0.67	0.50
9	-0.47	-1.92	-2.98
10	0.38	1.82	9.24
Q	0.063	0.131	0.138

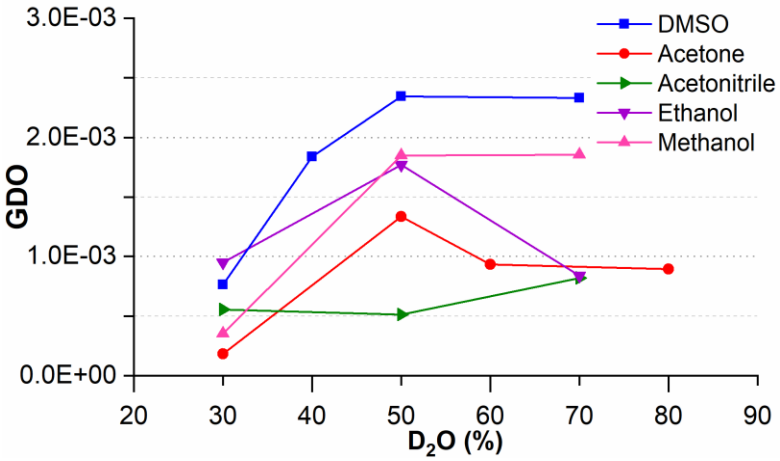

Figure S7. The generalized degree of order (GDO[1]) for the data shown in Figure 4. This is another way of expressing the alignment strength and here correlates to the behavior expressed via the Q factors. The GDO is printed directly in the output from MSpin.

Table S8. Generalized angle[1] in degrees between alignment tensors for the solvents tested here. Calculated between tensors for 1:1 mixtures of D_2O and the listed solvents. The small values show that the alignment direction does not change with the change of solvents

	DMSO	ACETONE	ACETONITRILE	ETHANOL	METHANOL	DMF
DMSO	0					
ACETONE	18.49	0				
ACETONITRILE	10.06	19.43	0			
ETHANOL	16.25	4.79	16.80	0		
METHANOL	14.16	13.97	18.02	14.79	0	
DMF	16.95	19.54	11.84	24.93	15.47	0

[1] Kramer, F., Deshmukh, M., Kessler, H. and Glaser, S. (2004), Residual dipolar coupling constants: An elementary derivation of key equations. Concepts Magn. Reson., 21A: 10-21.

Concentration

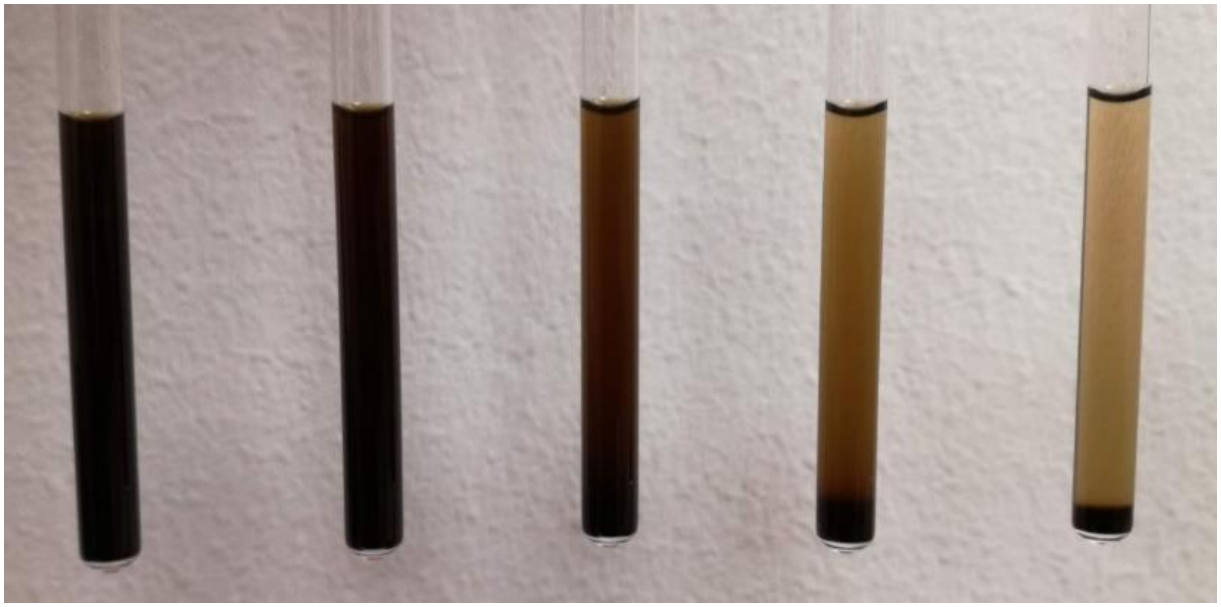

Figure S8. 2 days after sample preparation, from left concentrations of 8.3, 6.6, 5.0, 3.3 and 1.7 mg/mL GO.

Table S9. Size of measured RDCs as a function of the amount of GO in solution, 1:1 D_2O:DMSO-d6, 6 mM menthol. Blank cells are due to distorted peaks.

#	1.65 mg/mL	3.31 mg/mL	4.96 mg/mL	6.61 mg/mL	8.27 mg/mL
1	2.92	5.20	10.33	22.19	28.14
2a	0.27	-2.05	-2.05	-3.15	-4.18
2b	4.62	6.97	14.99	23.02	31.04
3	3.83	5.40	13.04	25.17	21.11
4a	-0.17	0.38	1.83	3.58	7.79
4b	0.99	6.99	11.83		17.80
5a	0.44	0.00	-0.44	-0.24	0.99
5b	1.47	8.32	13.60	25.90	35.27
6	1.42	4.58	10.05	24.24	28.77
7	0.30	0.18	3.89	8.23	11.58
8	0.32	0.12	-0.31	0.94	0.48
9	-1.25	-1.59	-2.93	-4.62	-5.24
10	0.91	0.85	4.04	8.47	11.17
Q	0.363	0.162	0.099	0.054	0.101

*Table S10. Size of measured RDCs as a function of the amount of GO in solution in **3 mm** NMR tubes, 1:1 D_2O:DMSO-d6, 6 mM menthol. Blank cells are due to distorted peaks.*

#	1.65 mg/mL	3.31 mg/mL	4.96 mg/mL	6.61 mg/mL	8.27 mg/mL
1	3.04	4.38	11.52	24.26	24.35
2a	-0.51	-1.61	-2.83	-2.97	-3.80
2b	2.99	6.52	13.13	24.51	26.49
3	4.71	4.35	12.50	25.88	32.71
4a	1.21	1.13	1.99	3.36	
4b	9.43	6.94	9.70	14.80	
5a	1.04	0.43	-1.21	0.48	-0.20
5b	3.50	2.96	12.46	25.49	46.03
6	2.27	4.11	11.10	19.76	36.91
7	1.15	1.51	3.99	9.74	11.40
8	-0.25	0.05	-0.02	0.33	0.95
9	-0.76	-0.97	-2.26	-2.41	-7.40
10	0.60	0.42	4.58	8.28	12.00
Q	0.347	0.279	0.062	0.124	0.185

*Table S11. Size of measured RDCs as a function of the amount of **commercial GO** in solution, 1:1 D_2O:DMSO-d6, 6 mM menthol. Blank cells are due to distorted peaks.*

#	0.4 mg/mL	0.8 mg/mL	1.2 mg/mL	1.6 mg/mL	2.0 mg/mL
1	4.02	11.04	16.14	25.03	24.76
2a	-0.35	-2.40	-4.04	-4.94	-5.73
2b	3.13	11.52	17.33	19.32	23.90
3	2.84	13.63	13.22	23.80	
4a	3.18	3.96	3.08	1.62	
4b	6.48	10.07	20.46		
5a	-0.82	-1.39	-1.08	-2.21	-2.83
5b	2.67	14.21	20.27	25.02	32.23
6	3.90	11.33	13.62	25.03	28.45
7	1.49	3.72	5.05	9.80	5.95
8	0.05	0.11	0.79	0.73	1.25
9	-0.95	-1.53	-1.65	-1.80	-2.61
10	1.38	5.06	7.45	10.15	10.85
Q	0.137	0.079	0.147	0.099	0.086

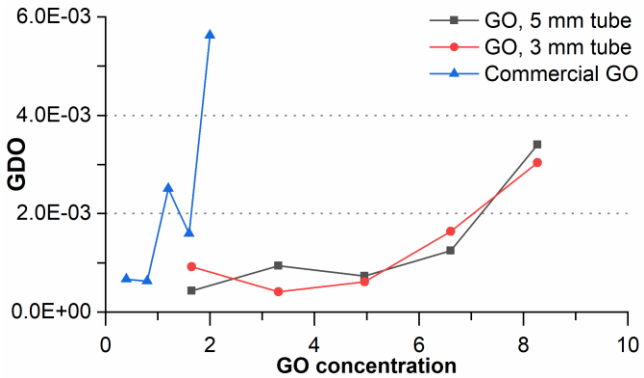

Figure S9. The generalized degree of order (GDO^1) for the data shown in Figure 5. This gives a more nuanced view of the alignment strength of especially the commercial GO samples than the Q factors alone. The GDO is printed directly in the output from MSpin.

*Table S12. RDCs of 16 mM menthol with approximately 0.4 mg/mL **re-dissolved commercial GO** in 1:1 D_2O:DMSO-d6.*

#	0.4 mg/mL re-dissolved commercial GO
1	21.51
2a	-4.99
2b	26.18
3	16.98
4a	8.96
4b	15.34
5a	-2.44
5b	30.52
6	29.93
7	11.25
8	0.62
9	-3.58
10	10.27
Q	0.088

Pinanediol

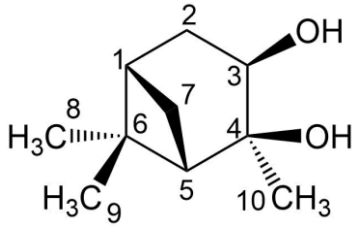

Figure S10. (+)-pinanediol with the used assignment scheme.

*Table S13. Assignment table for (+)-pinanediol in DMSO-*d6*.*

#	δ_H [ppm] (int, mult., *J* [*Hz*])	δ_C [ppm]
1	1.80 (1H, m) (1H, tdd, 5.8, 3.6, 2.3)	40.0
2	2.27 (1H, dddd, 13.7, 9.4, 3.6, 2.3) 1.50 (ddd, 13.7, 5.4, 2.3)	37.7
3	3.80 (1H, dt, 9.4, 5.8)	67.7
3 OH	4.95 (1H, d, 6.3)	-
4	-	72.2
4 OH	4.28 (1H, s)	-
5	1.83 (1H, t, 5.8)	53.7
6	-	38.1
7	2.03 (1H, dtd, 9.9, 5.8, 2.3) 1.36 (1H, d, 9.9)	27.9
8	0.89 (3H, s)	24.0
9	1.21 (3H, s)	27.9
10	1.13 (3H, s)	29.9

*Table S14. Size of measured RDCs as a function of the amount of GO in solution, 1:1 D_2O:DMSO-*d6*, 4 mM (+)-pinanediol.*

#	***2.07 mg/mL***	***4.13 mg/mL***	***6.20 mg/mL***	***8.27 mg/mL***
1	-0.27	-0.21	-0.78	-0.46
2a	0.75	0.65	2.99	5.98
2b	0.21	-0.26	-0.63	-0.66
3	-0.48	1.08	2.81	6.65
5	-0.35	0.19	0.72	2.21
7a	0.11	0.93	-0.31	-2.41
7b	-0.24	-1.30	-3.37	-6.23
8	-0.09	0.59	1.44	1.93
9	-0.38	-0.28	-0.45	-0.74
10	-0.04	-0.52	-1.00	-1.52
Q	0.886	0.201	0.151	0.043

Methyl-α-D-glucopyranoside

Table S15. Assignment table for methyl-α-D-glucopyranoside (Me-α-Glc) in D_2O.

#	δ_H [ppm] (int, mult., *J* [*H*z])	δ_C [ppm]
1	4.73 (1H, d, 3.9)	99.3
2	3.48 (1H, dd, 9.8, 3.8)	71.2
3	3.59 (1H, t, 9.6)	73.1
4	3.32 (1H, t, 9.3)	69.5
5	3.56 (1H, ddd, 10.0, 5.6, 2.2)	71.6
6	3.79 (1H, dd, 12.3, 2.3) 3.68 (1H, dd, 12.3, 5.6)	60.5
Me	3.34 (3H, s)	55.0

*Table S16. RDCs of 4.56 mg (Me-α-Glc) with app. 4 mg/mL **commercial** concentrated GO in D_2O. Averaging of the methylene group used.*

#	***RDC [Hz]***	***Calc***
1	7.58	7.76
2	10.84	13.23
3	9.99	10.63
4	13.56	14.21
5	15.93	12.39
6a	-0.09/7.87	6.44
6b	15.82/7.87	6.44
Me	2.73	0.94
Q		0.177

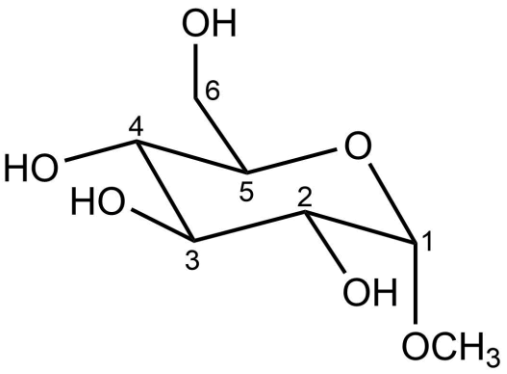

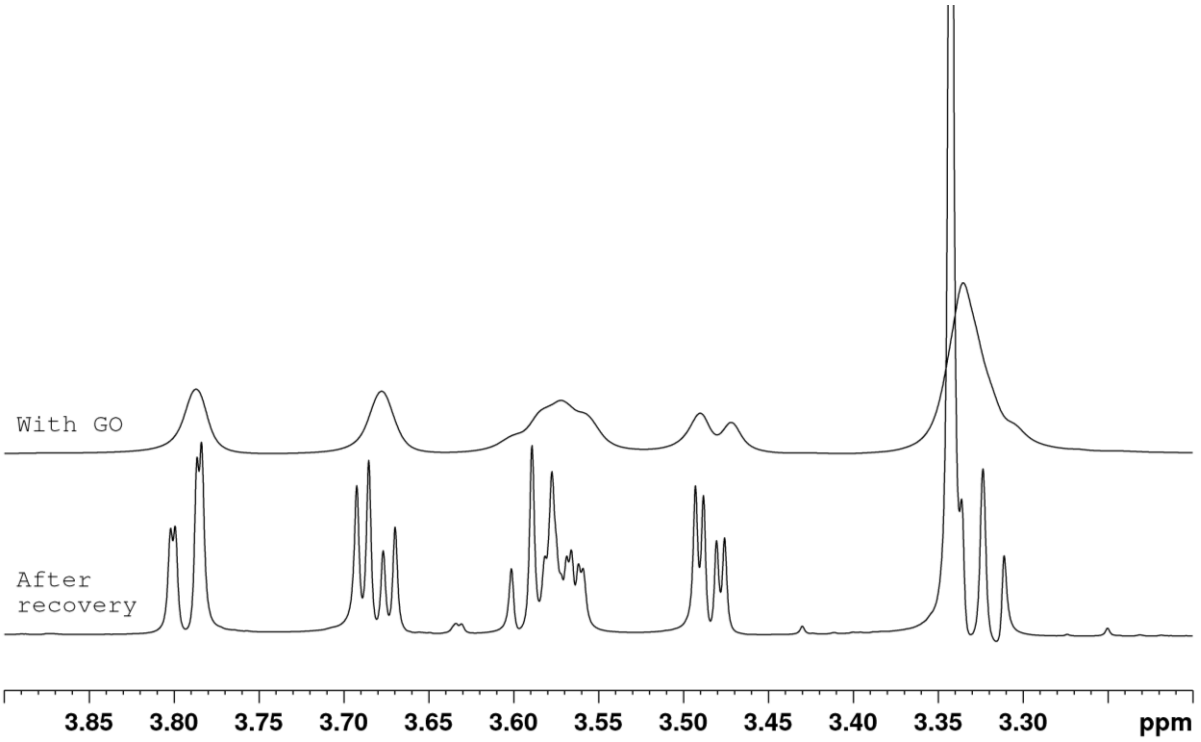

*Figure S11. Overlay of ^{1}H spectra of Me-α-Glc in D_2O with 4 mg/mL **commercial** concentrated GO and after recovery of Me-α-Glc. The signal at 4.73 ppm is excluded as it overlaps with water.*

Calculation scripts

Examples of MSpin input and output. 8 DFT optimized conformers were used and superimposed by the commands “world.eckarttransform()“ or “world.superimpose("1, 2, 3, 4, 5, 6")”.

MSpin calculation settings used:

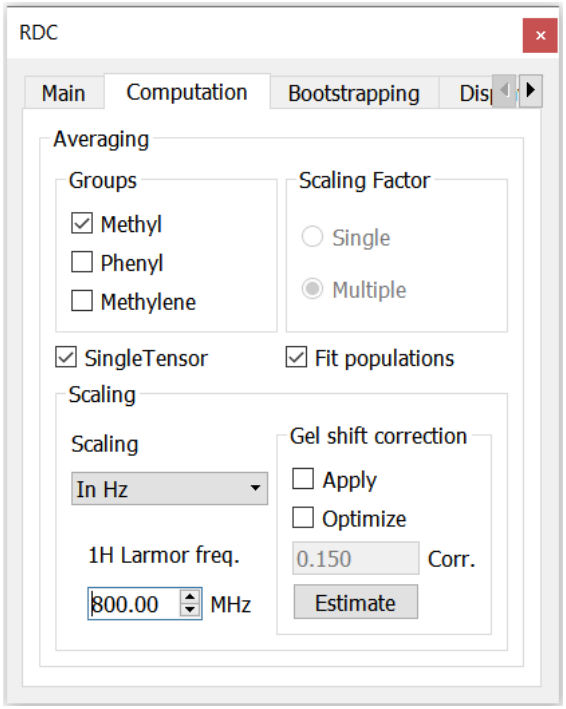

Example of content from MSpin input txt file. First and second column is PDB C and H numbers respectively. Third column is the RDC in Hz. Methylene protons could be individually assigned based on *J*-coupling constants.

```
rdc_data    {
4           17          8.78
5           19          -0.91
5           18          10.00
6           20          9.14
1           13          1.69
1           12          7.75
2           15          -0.59
2           14          9.3
3           16          7.12
7           24          2.28
9           21          2.48
9           22          2.48
9           23          2.48
}
```

MSpin output. The distribution between conformers varied between different sets of data.

```
!* MSpin-RDC Plugin *!
********
!* Computation flags *!
Method: SVD
Scaling mode: Hz
Field (T): 18.7893
1H Larmor Frequency: 800
Scale QCSA with axial component: False
Include CSA gel shift (isotropic) correction:False
Optimize CSA gel shift (isotropic) correction scale:False
Estimate CSA gel shift (isotropic) correction scale:False
Gel Shift Correction Scale: 0.15
Single Tensor: True
Optimize populations: True
Grid search points: 16
Superimpose: False
Average methyl groups: True
Average methylene groups: False
Average phenyl groups: False
Bootstrapping: False
RDC Std. Error [ppm]: 1
CSA Std. Error [ppm]: 0.01
PCS Std. Error [ppm]: 0.01
DQ Std. Error [Hz]: 1
********
!* Permutations *!
There are no permutations on the original data set
********
Data set: #1
Computed data for frame #1
RDC Data:
I    J     Exp. [Hz]  Comp. [Hz]
C4   H17   8.78       8.39
C5   H19   -0.91      2.04
C5   H18   10.00      8.60
C6   H20   9.14       8.88
C1   H13   1.69       -1.34
C1   H12   7.75       8.15
C2   H15   -0.59      2.01
C2   H14   9.30       8.50
C3   H16   7.12       8.06
C7   H24   2.28       -1.73
C9   H21   2.48       2.84
C9   H22   2.48       2.84
C9   H23   2.48       2.84

Cornilescu Quality factor: 0.307344
Computed data for frame #2
RDC Data:
I    J     Exp. [Hz]  Comp. [Hz]
C4   H17   8.78       8.27
C5   H19   -0.91      1.76
C5   H18   10.00      8.38
C6   H20   9.14       8.83
C1   H13   1.69       -1.03
C1   H12   7.75       8.11
C2   H15   -0.59      1.65
C2   H14   9.30       8.54
C3   H16   7.12       7.96
C7   H24   2.28       -1.79
C9   H21   2.48       2.84
C9   H22   2.48       2.84
C9   H23   2.48       2.84

Cornilescu Quality factor: 0.293021
Computed data for frame #3
RDC Data:
I    J     Exp. [Hz]  Comp. [Hz]
C4   H17   8.78       8.54
C5   H19   -0.91      1.93
C5   H18   10.00      8.68
C6   H20   9.14       9.03
C1   H13   1.69       -1.26
C1   H12   7.75       8.24
C2   H15   -0.59      1.81
C2   H14   9.30       8.58
C3   H16   7.12       7.96
C7   H24   2.28       -1.49
C9   H21   2.48       2.84
C9   H22   2.48       2.84
C9   H23   2.48       2.84

Cornilescu Quality factor: 0.291071
Computed data for frame #4
RDC Data:
I    J     Exp. [Hz]  Comp. [Hz]
C4   H17   8.78       8.53
C5   H19   -0.91      3.31
C5   H18   10.00      8.44
```

C6	H20	9.14	8.74
C1	H13	1.69	-3.39
C1	H12	7.75	8.11
C2	H15	-0.59	3.67
C2	H14	9.30	8.03
C3	H16	7.12	8.29
C7	H24	2.28	-0.68
C9	H21	2.48	2.58
C9	H22	2.48	2.58
C9	H23	2.48	2.58

Cornilescu Quality factor: 0.401653
Computed data for frame #5
RDC Data:

I	J	Exp. [Hz]	Comp. [Hz]
C4	H17	8.78	8.73
C5	H19	-0.91	3.09
C5	H18	10.00	8.57
C6	H20	9.14	8.96
C1	H13	1.69	-3.25
C1	H12	7.75	8.28
C2	H15	-0.59	3.33
C2	H14	9.30	8.23
C3	H16	7.12	8.25
C7	H24	2.28	-0.82
C9	H21	2.48	2.58
C9	H22	2.48	2.58
C9	H23	2.48	2.58

Cornilescu Quality factor: 0.385125
Computed data for frame #6
RDC Data:

I	J	Exp. [Hz]	Comp. [Hz]
C4	H17	8.78	8.44
C5	H19	-0.91	-0.55
C5	H18	10.00	9.01
C6	H20	9.14	9.03
C1	H13	1.69	1.49
C1	H12	7.75	8.00
C2	H15	-0.59	-0.60
C2	H14	9.30	8.75
C3	H16	7.12	8.62
C7	H24	2.28	4.09
C9	H21	2.48	2.93
C9	H22	2.48	2.93
C9	H23	2.48	2.93

Cornilescu Quality factor: 0.124893
Computed data for frame #7
RDC Data:

I	J	Exp. [Hz]	Comp. [Hz]
C4	H17	8.78	8.09
C5	H19	-0.91	-0.71
C5	H18	10.00	8.63
C6	H20	9.14	8.82
C1	H13	1.69	1.78
C1	H12	7.75	7.81
C2	H15	-0.59	-0.74
C2	H14	9.30	8.58
C3	H16	7.12	8.47
C7	H24	2.28	4.71
C9	H21	2.48	2.93
C9	H22	2.48	2.93
C9	H23	2.48	2.93

Cornilescu Quality factor: 0.152202
Computed data for frame #8
RDC Data:

I	J	Exp. [Hz]	Comp. [Hz]
C4	H17	8.78	8.85
C5	H19	-0.91	-0.67
C5	H18	10.00	9.21
C6	H20	9.14	9.25
C1	H13	1.69	1.71
C1	H12	7.75	8.02
C2	H15	-0.59	-0.82
C2	H14	9.30	8.74
C3	H16	7.12	8.14
C7	H24	2.28	2.08
C9	H21	2.48	2.93
C9	H22	2.48	2.93
C9	H23	2.48	2.93

Cornilescu Quality factor: 0.0716639
!Conformationally averaged data

!Populations
Frame #1: 0.0%
Frame #2: 0.0%
Frame #3: 0.0%
Frame #4: 0.0%
Frame #5: 0.0%
Frame #6: 0.0%
Frame #7: 0.0%
Frame #8: 100.0%

RDC Data:

I	J	Exp. [Hz]	Comp. [Hz]
C4	H17	8.78	8.85
C5	H19	-0.91	-0.67
C5	H18	10.00	9.21
C6	H20	9.14	9.25
C1	H13	1.69	1.71
C1	H12	7.75	8.02
C2	H15	-0.59	-0.82
C2	H14	9.30	8.74
C3	H16	7.12	8.14
C7	H24	2.28	2.08
C9	H21	2.48	2.93
C9	H22	2.48	2.93
C9	H23	2.48	2.93

Cornilescu Quality factor: 0.0716657
Alignment tensor information:
A'x= 2.412e-05
A'y= 1.511e-04
A'z=-1.753e-04
Saupe tensor
S'x= 3.617e-05
S'y= 2.267e-04
S'z=-2.629e-04
Alignment tensor eigenvectors
e[x]=(0.361, 0.921,-0.145)
e[y]=(-0.879, 0.388, 0.276)
e[z]=(0.311, 0.028, 0.950)

Alignment tensor in laboratory coordinates:
[1.030e-04,-4.511e-05,-8.976e-05]
[-4.511e-05,4.312e-05,8.315e-06]
[-8.976e-05,8.315e-06,-1.461e-04]

SVD condition number is 2.530e+01
Axial component Aa = -2.629e-04
Rhombic component Ar = -1.270e-04
Field=18.79 Teslas[2.27]
rhombicity R = 0.483
Asimmetry parameter etha =7.248e-01
GDO = 3.411e-04

ZY'Z'' Euler Angles (degrees)
Set 1
(5.2,18.2,62.2)
Set 2
(-174.8,-18.2,-117.8)
****
MSpin-RDC pluginma okt 26 19:55:31 2020

Triculamin: an unusual lassopeptide with potent anti-mycobacterial activity

Introduction

Almost 80 years after Albert Schatz discovered streptomycin, the first antibiotics used to treat tuberculosis, infections with mycobacteria still constitutes a major challenge for human health with multidrug resistance (MDR) and extensively drug-resistant (XDR) tuberculosis rising in several part of the world. Treatment of tuberculosis is special in the sense that it extends over several month and contains up to four drugs in combination. Moreover, many of the compounds used – such as isoniazid, pyrazinamide, and ethambutol - are only used in TB treatment. Several papers over the past decade have focused on the discovery of new compounds selective for mycobacteria among these are compounds such as lassomycin and kitamycobactin – lassopeptides that binds and stimulates ClpC1 ATPase activity, amycobactin – a macrolactone that inhitbits protein secreation through the Sec machinery, and streptomycobactin – a depsipeptide with a still unknown molecular target.(ref: Quigley&Lewis, mBio 2020, Gawrish&Lewis, Cell Chemistry&Biology, 2014) All of these were isolated following a screening campaign of 10.000 isolates against *M. tuberculosis*, but removing hits that also showed activity against *S. aureus*. Another example from the past decade is griselimycin, a cyclic depsipeptide described by Terlain and Thomas in 1971 (ref: Terlain&Thomas, Bull. Soc. Chim. Fr. 1971), but discarded as the pharmacokinetics proved unfavorable. The natural product was revived by the Müller Lab and they discovered that a minor alteration in the structure improved the stability when exposed to human liver microsomes. They also identified the molecular target as the DnaN sliding clamp. We were intrigued by two compounds discovered in the 1958 and 1967- alboverticilin and triculamin - described as very potent against *M. phlei* and *M. smegmatis* while showing neglectable activity against other microorganisms. (ref Maeda 1958, Suzuki 1967) They did not, however, show favourable results in mouse model, when compared to kanamycin. (ref Kanei 1967) The compounds were reported as being similar, but not identical , and while their structure is unknown, degradation studies had clearly established a peptide basis containing at least 17 amino acids (L-Asp (1), L-Ser (2), L-Pro (1), Gly (5), L-Val (1), L-Ile (1), L-Lys (4), L-Arg (2)) and a three fragments (GIRG, KGVRG, SKPG) that established at least part of the order of the final compound. (ref Anzai 1969) We could not match these with known antimycobacterial compounds and were intrigued by the selectivity. We therefor set out to isolate the compounds, solve the structure and investigate the basis for the biosynthesis.

Results

Bioinformatic tools can provide a strong basis for structural elucidation and are particularly good at predicting peptide-based natural products from genome sequences, so we acquired the two strains reported to produce alboverticilin and triculamin (*Streptomyces alboverticillium* NRRL 24281 and *Streptomyces triculaminicus* JCM 4242) and sequenced their genomes using a combination of illumina and nanopore sequencing. *S. triculaminicus* resulted in a 7.560.338 on 13 contigs, *S. alboverticillium* contained 7.340.446 bases on 1 contig and both had an expected high GC content. Both genomes were submitted to antiSMASH 6 Beta (ref) to identify potential biosynthetic gene clusters (BGCs) and the output manually inspected and compared. As seen in figure 1a, the two strains share most of their BGCs. Naturally, we chose to focus on the BGCs associated with non-ribosomal peptides (NRP) and ribosomally-synthesized and posttranslationally-modified peptides (RiPPs). We could not identify any NRP BGC large enough to accommodate for 17 amino acids in either strain. Neither could we find any RiPP BGCs with a predicted precursor peptide compatible with the amino acid composition reported. Finally, we searched all possible reading frames for the peptide fragments and found all in both strains in an identical ORF – from here on named *triA* and *albA*. The regions surrounding the ORFs were detected by antiSMASH and contained both genes associated with polyketide and lasso peptide biosynthesis. The two regions are compared in figure 1b. Lasso peptide biosynthesis has been reviewed elsewhere (CheungLee2019) and from major genome mining studies, we known that the typical BGC will include a precursor peptide composed of a leader and a core, a lasso cyclase homologous to asparagine synthetase, a leader peptidase homologous to transglutaminase, and often also a transporter. (Tietz, Chekan) The region found in both strains contained two separate putative BGCs. The first BGC (shaded in blue in Figure 1b) had a canonical precursor peptide with a leader containing a Tyr-17, Pro-14, and Thr-2, as well as a Gly1 and Glu8 in the predicted core peptide. The BGC had a macrocyclase, an RiPP precursor recognition element (RRE), and a peptidase. The second BGC appeared incomplete. It had a short macrocyclase (424 aa against the more typical 513-617 see supporting figure X for an alignment), an ABC transporter, but more curiously, a 52 aa predicted peptide with the 17 amino acids we found situated in the N-terminal (**figure 2**). While some RiPPs have follower peptides instead of leader peptides this has not been observed for lasso peptides. Using the short macrocyclase as a query in a BLAST search, we identified similar BGCs in *Streptomyces lydicus* (strain WYEC108 and SW_ACT1) and *Norcardia beijingensis* (NBRC 16342). In *S. lydicus* our putative lasso peptide BGC was also located in the vicinity of another lasso peptide BGC, but further away (approx. 20 kb) - for *N. beijingensis* this was not the case (supporting figure 1). Interestingly the predicted N-terminal core peptide is conserved, while the C-terminal of the precursor peptide is sequence-divergent, except

for a LAET(L/V) motif. To investigate if triculamine and alboverticilin were in fact lasso peptides, we proceeded with a bioactivity-guided isolation of both compounds.

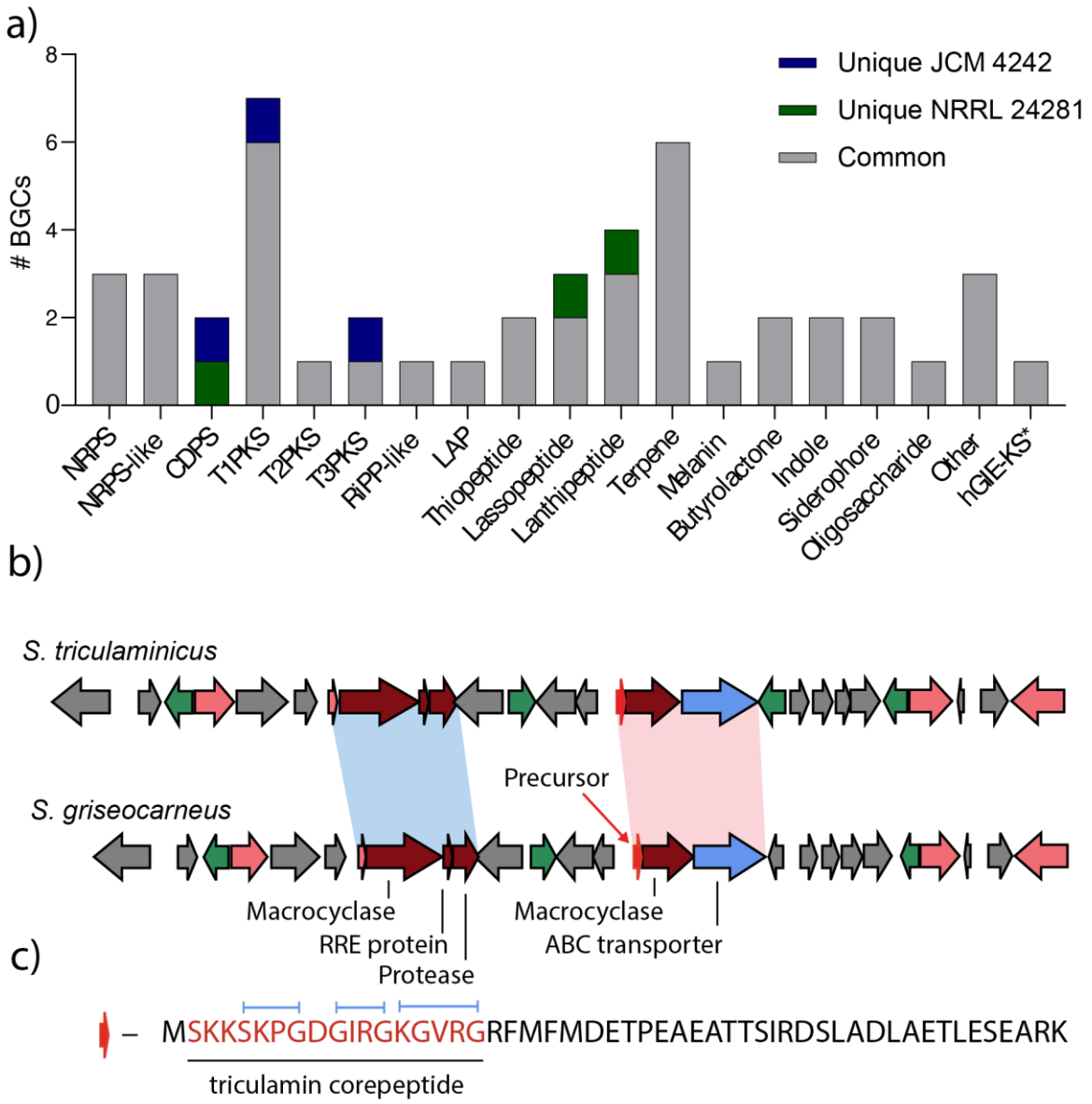

Figure 1: Comparison and analysis of biosynthetic gene clusters in S. triculaminicus JCM 4242 and S. griseocarneus NRRL 24281. ***a)*** *When comparing the antiSMASH analysis of both genomes it is evident that they share most of their biosynthetic gene cluster (the genes found in hGIE-KS is present in both genomes, but antiSMASH only identifies it as a cluster in one).* ***b)*** *One shared genomic region has a predicted lassopeptide biosynthetic gene cluster (light blue shading) containing a predicted precursor peptide, a macrocyclase, a RRE protein, and a protease. Separated by less than 4 kb fragments of another lassopeptide biosynthetic gene cluster is present (light red shading). This contains a smaller macrocyclase, an ABC transporter and a short open reading frame (red).* ***c)*** *The predicted amino acid sequence of the short open reading frame. All 17 amino acids (highlighted in red) known from triculamin and alboverticilin is present in the N-terminal. The three peptide fragments used to identify the ORF is indicated with light blue lines.*

Both strains were cultivated on ISP-2 agar plates and showed a distinct colony morphology and a pronounced tendency to produce pellets in liquid medium. Testing the bioactivity against

Mycobacterium phlei DSM 43239, it was clear that the active compound was secreted into the medium. The concentration increased over the course of approximately eight days before reaching a steady level. The active compound could not be extracted into neither EtOAc nor *n*-BuOH, but was retained by HP20 resin. We isolated both alboverticilin and triculamin from cultures (10 L) by first removing the biomass by centrifugation and absorbing the compounds from the supernatant on HP-20 resin. After eluding from resin, the extract was passed over an active carbon column, fractionated on a C18 column, before a final purification on a C18 polar column. The addition of TFA (0.1%) was critical for ensuring retention on the HPLC columns. Both compounds were analyzed using HRMS. As can be seen in supporting figure X, we observed a series of m/z values (+2, +3, +4, +5) and based on these, calculated a molecular weights of 1709.0074 for both compounds. This matches the calculated molecular weight 1708,9856 of amino acid 2-18 of the predicted peptide encoded by *triA* and *albA* with a loss of one molecule of H_2O as expected if triculamin and alboverticilin are in fact lasso peptides. To solve the structure of triculamin, a series of 2D- and 3D spectra were recorded on a 950 MHz NMR. ^{1}H, ^{13}C and ^{15}N chemical shifts were assigned using a combination of 1D ^{1}H, ^{1}H-^{13}C HSQC, ^{1}H-^{13}C HSQC-TOCSY, HMBC and ^{1}H-^{15}N HSQC, see Table XX. 2D NOESY spectra aided in confirming the sequential assignment of the backbone. The isopeptide bond formation closing the macrolactam ring between Ser1 and Asp8 was confirmed by a HMBC correlation from Ser1Hα to Asp8Cγ, in addition to NOESY correlations between Ser1NH and Asp8Hβ's. Several long-range NOE's between the macrolactam ring and the tail were signs of the lasso structure, among these correlations from Lys2NH to Gly14NH and Val15Hα. Figure X1 shows key long-range NOE's observed.

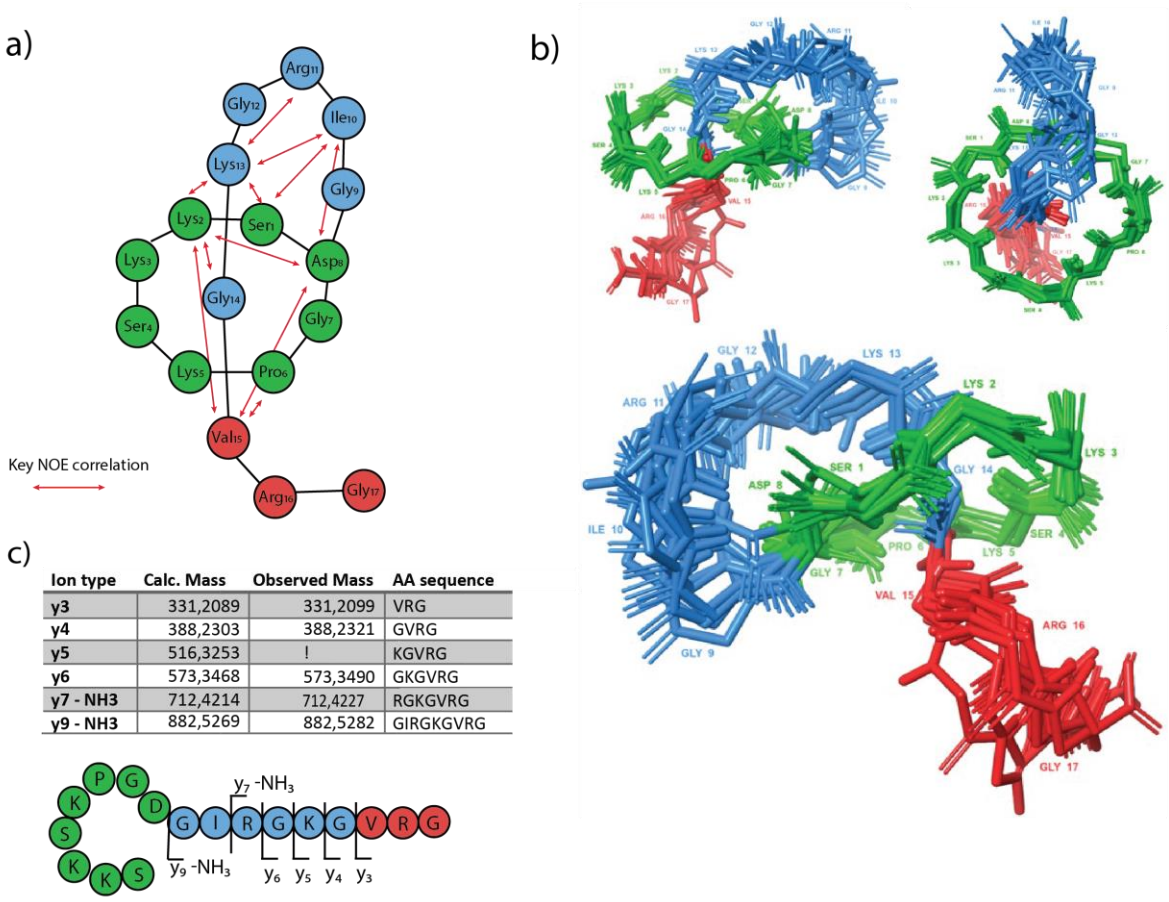

Ion type	Calc. Mass	Observed Mass	AA sequence
y3	331,2089	331,2099	VRG
y4	388,2303	388,2321	GVRG
y5	516,3253	!	KGVRG
y6	573,3468	573,3490	GKGVRG
y7 - NH3	712,4214	712,4227	RGKGVRG
y9 - NH3	882,5269	882,5282	GIRGKGVRG

Figure 2

An initial 3D structure was made in the modelling suite Maestro and conformations generated using the program MacroModel using a total of 19 distance constraints related to the backbone or the lasso structure. The distances were derived from integrated NOE cross-peaks seen in NOESY spectra at 120 ms mixing time using the NOE cross-peak between the beta protons of Asp8 as a reference set to 1.78 Å. This resulted in a large set of 1498 conformers, which was subsequently used as input to the DICONO program developed by Casper Hoeck[1]. The program iteratively adds structures from the set of conformers provided to form the best fit as an average of all the added structures. Here the program was given all 118 trusted NOE derived distances to find the best, combined fit for the experimental data. This approach allows for a more dynamic set of conformers representing the 3D structure of a molecule. The output was a set of 11 conformers with a combined average deviation of 0.61 Å. This set of conformers represent the 3D structure in solution of this lasso peptide. From the overlay in Figure X2 is seen how Gly14 is situated in the middle of the macrolactam ring with Lys13 and Val15 placed just above and below the ring, respectively.

Subjecting triculamin to MS/MS fragmentation reveal a series of y-ions matching the C-terminal of the peptide following Asp8 – a characteristic feature of many other lassopeptides (examples and refs).

The spectras recorded for alboverticilin identical (see supporting figure X).

To assess the biological activity of both compounds we determined their MIC values against a panel of microbial pathogens and three human cell lines in microtiter plates. The results are presented in figure XX and clearly demonstrates a remarkable selectivity against mycobacteria over both other microorganism as well as human cell lines. This mirrors the original studies and indicates that the target of triculamin and alboverticilin could be a promising lead for anti-mycobacterial drugs. We also tested the time-dependent killing of triculamin against *M. smegmatis* in either mid-exponential and late-exponential phase and observed efficient killing comparable to kanamycin.

Discussion

Methods

Fermentation:

Streptomyces triculaminicus JCM 4242 and *Streptomyces griseocarneus* NRRL 24281 were grown on ISP-2 agar (glucose 4 g/L, yeast extract 4 g/L, malt extract 10 g/L, agar 15 g/L, pH 7.3) at 28 ˚C. Spores were harvested after 8 days, stored in 25% glycerol, and used as inoculum. Seed cultures were prepared in 100 ml ISP-2 in 500 ml baffled flasks equipped with stainless steel springs and cultured at 28 ˚C and 200 RPM. Growth was monitored by OD_{600} measurements. For antibiotic production, actively growing seed cultures were diluted 5% (v/v) into 2 L triculamin production medium (TPM) (glucose 22 g/L, yeast extract 2.5 g/L, NH_4NO_3 4 g/L, $CaCO_3$ 2 g/L, NaCl 2 g/L, pH X (Suzuki, 1967)) in 5 L baffled flasks. Production cultures were incubated at 28 ˚C and 200 RPM. The maximum production was attained in 8 days.

Isolation of triculamin

The fermentation broth of JCM 4242 (12 L) and NRRL 24281 (10 L) was centrifuged and supernatant was collected. HP-20 resin was added (10% (w/v)) and washed with deionized water before eluting with 100% MeOH. The MeOH extract was dried *in vacuo* and re-dissolved in water. The mixture was further separated on an active carbon column (). After washing with water, triculamin was eluted with a hydrochloric acid/acetone solution of 80% acetone and HCl concentration of 0.1 M. The eluate was dried *in vacuo* to remove acetone, lyophilized and dissolved in water. The mixture was extracted twice with an equivalent volume of *n*-butanol. The *n*-butanol was discarded and the aqueous layer was lyophilized, dissolved in DMSO, and fractionated by HPLC on a C18 column ()

using the following gradient with solvents acidified with 0,1% trifluoroacetid acid (TFA): 0-5 minutes, 5% MeCN/H_2O; 5-20 minutes, linear gradient from 5% MeCN/H_2O to 40% MeCN/H_2O; 25-29 minutes, 95% MeCN/H_2O. Fractions containing triculamin were pooled and lyophilized. The resulting powder was dissolved in DMSO and fractionated by HPLC on a C18 polar column () using the following gradient with solvents acidified with 0,1% TFA: 0-2 minutes, 5% MeCN/H_2O; 2-25 minutes, linear gradient from 5% MeCN/H_2O to 25% MeCN/H_2O; 25-30 minutes, 95% MeCN/H_2O. Fractions containing triculamin were pooled and lyophilized. (top 1, 2,3?). Antibiotic activity was monitored by disc diffusion assays with *Mycobacterium phlei* DSM 43239 as test organism and M250 media (proteose peptone no. 3 5 g/L, meat extract 3 g/L, glycerol 20 mL/L, agar 15.0 g/L, pH 7.0) as assay medium.

Genome sequencing and assembly:

(JCM 4242 and NRRL 24281 were grown in TPM and cells were harvested by centrifugation. DNA was extracted using the NucleoSpin® Tissue kit from Macherey-Nagel following standard protocols. The recommend pretreatment with lysozyme was used as well as overnight incubation with proteinase K.)
The genomes were deposited in in GenBank as GCA_017349075.1 for JCM4242 and GCA_017356985.1 for NRRL B-24281. They were both analyzed using antiSMASH 6 beta to using standard settings to identify potential biosynthetic gene clusters.

MS/MS:

Samples of triculamin and alboverticilin were analyzed in on a Dionex Ultimate 3000 UHPLC coupled to a Bruker Maxis Impact using an Ascentis Express C18 column (100 x 2.1, 2 µm). The compounds were eluted using a H2O:MeCN gradient containing 0.1% Formic acid. The spectra were calibrated using an internal calibrant of Na-Formate. Fragmentation was attempted at 20, 30 and 40 eV.

NMR:

Freeze-dried powder of Triculamin (purified from Streptomyces triculaminicus JCM 4242) (10-12 mg) was dissolved in a 0.5 mL H2O/D2O 90:10 solution. All NMR data were acquired at 298K on a Bruker Avance III+ spectrometer at a 1H frequency of 950 MHz equipped with a cryogenically cooled triple resonance probe.

The following spectra were acquired with the listed parameters and processed using Topspin 4.0.6 with linear prediction to double the resolution and zero-filling to another doubling of the points.

NMR processing and NOESY data integration in Topspin 3.6.1 (2018) from Bruker. The modelling suite Maestro version 2018-2 from Schrödinger, LLC, used to model the initial structure. Program MacroModel version 12.0 from Schrödinger, LLC, used to perform conformational search using the force field OPLS, an energy cutoff of 50kJ/mol, 10’000 steps and water as solvent.

Thermal and proteolytic stability:

Minimum inhibitory concentration (MIC):

MIC was determined by broth microdilution (<32 µg/ml) in Müller-Hinton broth (MHB) and Middlebrook 7H9 broth with 0.05% Tween-80 and ADC (0.5% BSA, 0.2% dextrose, 0.085% NaCl, 0.003 g catalase/L) used for mycobacterial strains. The inoculum was standardized to approximately $5x10^5$ CFU/ml. Plates were incubated for 3 days (*M. phlei* DSM 43239, *M. smegmatis* DSM 43080) or 20 hours (*B. cereus* DSM 31*, A. baumannii DSM* 300007*, S. aureus* DSM 20231*, E. cloacae* DSM 30054*, E. faecium* DSM 20477*, K. oxytoca* DSM 5175*, P. aeruginosa* DSM 19880) at 37°C. The MIC was defined as the lowest concentration of antibiotic with no visible growth. Experiments were performed with biological replicates.

Minimum bactericidal concentration (MBC):

After MIC determination cells were pelleted and resuspended in fresh media. Aliquots from wells with MIC, 2X MIC, and 4X MIC concentrations of compound were plated on Müller-Hinton agar (MHA) and incubated for 3 days at 37°C. The MBC was defined as the lowest concentration of antibiotic that resulted in a 99.9% decrease in colony count. Experiments were performed with biological replicates.

Time-dependent killing:

Exponential phase (42 hours) and stationary phase (72 hours). Experiments were performed with biological replicates.

Cell viability assay:

Human osteosarcoma cells, U-2OS (ATCC HTB-96), were grown in McCoy's 5A Medium (Sigma M9309) supplemented with 10% FBS (Gibco, cat. no. A3160802) and 1% penicillin/streptomycin. Human pancreatic cancer cells, PANC1 (ATCC CRL-1496) and non-cancer skin fibroblasts BJ (ATCC CRL-2522) were grown in high glucose Dulbecco's Modified Eagle Medium (DMEM) (Sigma, cat. no. D6546) supplemented with 1% GlutaMax (Gibco, cat. no. 35050061), 1% penicillin/streptomycin and 10% FBS. All cell lines were cultured at 37 °C in a humidified atmosphere (5% CO2) and passaged when 90% confluence was reached. All cell lines were validated via STR-analysis.

U-2OS, PANC-1 and BJ cells were seeded in black 96 well plates (Thermo Scientific, 137101) at a density of 2,000 cells/well in complete medium (75 µL/well). After seeding, the cells were left to adhere to the substratum overnight. Compounds dissolved in MQ-water were first diluted to 100X in sterile MQ-water before 25 times dilution to 4X in cell culture media (final MQ-water = 1%). Compounds were then dosed in the designated culture plates in triplicates in 25 µL medium, and the plates were placed at 37 °C in a humidified atmosphere containing 5% CO2. After 46.5 h, 20 µL CellTiter-Blue (Promega G8081) was added to each well and incubated for 1.5 h, after which the plates were analysed in a Tecan Spark 10M multimode plate reader for fluorescence (552 ± 10 nm excitation; 598 ± 10 nm emission). Replicate measurements were performed in distinct wells. The average growth of treated cells was calculated by correcting fluorescence values for background fluorescence and subsequently normalized to the average of cells treated with 1% MQ-water. Data were plotted and fitted to a four-parameter dose−response curve using Prism v.8.4.2 for Windows (GraphPad Software, www.graphpad.com).